

JOINT TRANSPORTATION RESEARCH PROGRAM

INDIANA DEPARTMENT OF
TRANSPORTATION AND PURDUE UNIVERSITY



New Repair Strategies for Life-Cycle Extension of Corroded Steel Girder Bridges



**Anna Tarasova, Deven Kanakamedala,
Jungil Seo, Amit H. Varma, Robert J. Connor**

RECOMMENDED CITATION

Tarasova, A., Kanakamedala, D., Seo, J., Varma, A. H., & Connor, R. J. (2024). *New repair strategies for life-cycle extension of corroded steel girder bridges* (Joint Transportation Research Program Publication No. FHWA/IN/JTRP-2024/15). West Lafayette, IN: Purdue University. <https://doi.org/10.5703/1288284317748>

AUTHORS

Anna Tarasova

Graduate Research Assistant
Lyles School of Civil and Construction Engineering
Purdue University
(765) 409-6901
atarasova@hntb.com
Corresponding Author

Deven Kanakamedala

Graduate Research Assistant
Lyles School of Civil and Construction Engineering
Purdue University

Jungil Seo

Senior Principal Research Scientist
Lyles School of Civil and Construction Engineering
Purdue University

Amit H. Varma, PhD

Karl H. Kettelhut Professor of Civil Engineering
Director of Bowen Laboratory of Large-Scale CE Research
Purdue University

Robert J. Connor, PhD

Jack and Kay Hockema Professor in Civil Engineering Director of CAI and S-BRITE
Lyles School of Civil and Material Engineering
Purdue University

JOINT TRANSPORTATION RESEARCH PROGRAM

The Joint Transportation Research Program serves as a vehicle for INDOT collaboration with higher education institutions and industry in Indiana to facilitate innovation that results in continuous improvement in the planning, design, construction, operation, management and economic efficiency of the Indiana transportation infrastructure. https://engineering.purdue.edu/JTRP/index_html

Published reports of the Joint Transportation Research Program are available at <http://docs.lib.purdue.edu/jtrp/>.

NOTICE

The contents of this report reflect the views of the authors, who are responsible for the facts and the accuracy of the data presented herein. The contents do not necessarily reflect the official views and policies of the Indiana Department of Transportation or the Federal Highway Administration. The report does not constitute a standard, specification or regulation.

TECHNICAL REPORT DOCUMENTATION PAGE

1. Report No. FHWA/IN/JTRP-2024/15	2. Government Accession No.		3. Recipient's Catalog No.	
4. Title and Subtitle New Repair Strategies for Life-Cycle Extension of Corroded Steel Girder Bridges			5. Report Date February 2024	
			6. Performing Organization Code	
7. Author(s) Anna Tarasova, Deven Kanakamedala, Jungil Seo, Amit H. Varma, and Robert J. Connor			8. Performing Organization Report No. FHWA/IN/JTRP-2024/15	
9. Performing Organization Name and Address Joint Transportation Research Program Hall for Discovery and Learning Research (DLR), Suite 204 207 S. Martin Jischke Drive West Lafayette, IN 47907			10. Work Unit No.	
			11. Contract or Grant No. SPR-4635	
12. Sponsoring Agency Name and Address Indiana Department of Transportation (SPR) State Office Building 100 North Senate Avenue Indianapolis, IN 46204			13. Type of Report and Period Covered Final Report	
			14. Sponsoring Agency Code	
15. Supplementary Notes Conducted in cooperation with the U.S. Department of Transportation, Federal Highway Administration.				
16. Abstract <p>Steel girder ends are susceptible to corrosion damage due to deicing salts, water, and other contaminants leaking from failed expansion joints. When corrosion becomes significant, it leads to a reduction in the sectional properties of steel girders and consequently reduces bearing and shear resistance. Conventional repair methods, although effective, require substantial time and resources to complete, causing public inconvenience from necessary traffic closures. Therefore, there is a need for practical, rapid, and robust repair methods suitable for implementation by local Department of Transportation (DOT) maintenance personnel. In this study, five innovative repair methods were systematically evaluated through a selection process called the House of Quality Matrix. After completing the comprehensive evaluation and additional numerical simulations, the "sandwich panel" repair method was selected for further investigation. The "sandwich panel" repair method encased the corroded region with a filler material reinforced by threaded rods. Two thin steel plates installed on both girder sides served as stay-in-place formwork. This expedited the installation process and eliminated the labor-intensive steps of jacking, welding, and formwork disassembly, thus making the repair more cost-effective and less time-consuming.</p> <p>The structural performance of the repair method was evaluated experimentally by conducting seven large-scale tests. Various test parameters were considered in the tests, including (1) threaded rod layout, (2) filler material, and (3) support condition. The experimental results indicated that the method was effective in restoring their original design strength. A parametric study complemented the experimental evaluation, using the finite element models benchmarked with experimental results. Design guidelines and recommendations were developed based on the experimental and numerical results.</p>				
17. Key Words steel bridges, corrosion, bridge rehabilitation, bridge maintenance, bridge preservation			18. Distribution Statement No restrictions. This document is available through the National Technical Information Service, Springfield, VA 22161.	
19. Security Classif. (of this report) Unclassified	20. Security Classif. (of this page) Unclassified		21. No. of Pages 190 including appendices	22. Price

EXECUTIVE SUMMARY

Introduction

Steel girder ends are susceptible to corrosion damage due to deicing salts, water, and other contaminants that leak from failed expansion joints. When corrosion becomes significant, it leads to a reduction in the sectional properties of steel girders, thus reducing bearing and shear resistance. Conventional repair methods, although effective, require substantial time and resources to complete, which causes public inconvenience from necessary traffic closures. Therefore, there is a need for practical, rapid, and robust repair methods suitable for implementation by local Department of Transportation (DOT) maintenance personnel.

In this study, five innovative repair methods were systematically evaluated through a selection process called the House of Quality Matrix. After the comprehensive evaluation and additional numerical simulations, the sandwich panel repair method was selected for further investigation. The core concept of the proposed sandwich panel repair method involved the encasement of the corroded region with a filler material reinforced by threaded rods. Two thin steel plates installed on both girder sides served as stay-in-place formwork, expediting the installation process and eliminating the labor-intensive steps of jacking, welding, and formwork disassembly, thus making it more cost-effective and less time-consuming.

The structural performance of the repair method was evaluated experimentally by conducting seven large-scale tests. Various test parameters were considered in the tests, including (1) threaded rod layout, (2) filler material, and (3) support condition. The test specimens were obtained from the corrosion-damaged steel girders of the North-Split Reconstruction Project in Indiana. The experimental results indicated that the method was effective in restoring the original design strength. A parametric study complemented the experimental evaluation by using the finite element models benchmarked with experimental results. Design guidelines and recommendations were developed based on the experimental and numerical results.

This study focused on achieving the following three objectives.

1. Developing innovative method(s) to repair corrosion-damaged steel girder bridges.
2. Verifying the structural robustness of the developed innovative repair method(s) through experimental testing and numerical simulations.

3. Preparing design guidelines and recommendations for the Indiana Department of Transportation (INDOT).

Findings

Seven large-scale experiments revealed a complete recovery of the design bearing capacity and retention of at least 85% of the design shear capacity in all repaired specimens, except for Specimen 3. Specimen 3 exhibited improved capacity and performance compared to the non-repaired girder, but it did not reach the design bearing capacity. This confirmed the effectiveness of the sandwich panel method for rehabilitating corroded steel bridge girders. Experimental data was utilized to validate the results of finite element simulations. Finite element models reasonably predicted the behavior of specimens, deviating from the experimental data by no more than 10% in terms of the maximum applied load. Additionally, the developed finite element models accurately captured the failure modes of web local crippling and threaded rod rupturing; therefore, they were used to conduct further parametric study.

A numerical parametric study comprised of three cases with over 30 finite element models was performed. The parametric study clarified the effects of three parameters: (1) the number of threaded rods used in repair, (2) their layout, and (3) material properties on the post-repair strength of the girder. Recommendations on the optimal threaded rod layout, location, and filler material selection were provided—acknowledging their impact on failure modes, load-carrying capacity, and cracking patterns. In addition, an equation to estimate the minimum required number of threaded rods was formulated and verified based on numerical and experimental studies that considered post-repair capacity, residual capacity of the corroded girder, and sectional and material properties of the threaded rod.

Implementation

The proposed novel repair method, known as the sandwich panel, demonstrated effectiveness for the rehabilitation of corroded steel girder bridges. The developed equations and recommendations offer comprehensive guidance for successful implementation in the field. Additionally, by incorporating this repair method, traffic closure can be either significantly reduced or eliminated. The sandwich panel repair method, by excluding labor-intensive steps of jacking, welding, and formwork disassembly, could be more cost-effective, competitive, and less time-consuming compared to traditional repair methods.

TABLE OF CONTENTS

1. INTRODUCTION	1
1.1 Background	1
1.2 Research Objectives	1
1.3 Report Layout	1
2. LITERATURE REVIEW	2
2.1 Influence of Corrosion on the Residual Capacity of Steel Girders	2
2.2 Conventional Repair Methods	3
2.3 Innovative Repair Methods	3
3. EVALUATION OF INNOVATIVE REPAIR METHODS	8
3.1 Overview of Innovative Repair Methods	8
3.2 Evaluation Method: House of Quality Matrix	12
4. MATERIAL TESTING	16
4.1 Material Level Testing (Phase I)	17
4.2 Evaluation of Filler Materials Using House of Quality Matrix	34
4.3 Material Level Testing: Derivation of Stress-Strain Curves (Phase II)	36
4.4 Finite Element Modeling	38
5. EXPERIMENTAL EVALUATION AND OBSERVATIONS	49
5.1 Test Matrix	49
5.2 Test Setup	49
5.3 Material Properties	53
5.4 Sensor Layout	53
5.5 Specimen Details	63
6. EXPERIMENTAL RESULTS	70
6.1 Specimen 1	70
6.2 Specimen 2	73
6.3 Specimen 3	78
6.4 Specimen 4	80
6.5 Specimen 5	83
6.6 Specimen 6	90
6.7 Specimen 7	96
6.8 Summary and Observations	102
7. FINITE ELEMENT MODELING	112
7.1 Modeling Approach: Specimen 1–Specimen 2	112
7.2 Modeling Approach: Specimen 3–Specimen 7	114
7.3 Results	117
8. PARAMETRIC STUDY	134
8.1 Parametric Study: Case I	134
8.2 Parametric Study: Case II	140
8.3 Parametric Study: Case III	145
8.4 Summary	149
9. RECOMMENDATIONS FOR DESIGN AND APPLICATION	151
9.1 Selection of the Repair Configuration	151
9.2 Calculation of Required Number of Threaded Rods	152
9.3 Development of Threaded Rod Layout	155
9.4 Selection of the Infill Material	155
9.5 Components Required for Sandwich Panel Repair	156
9.6 Fabrication Guidelines	160
9.7 Assembly Guidelines	160
9.8 Long-Term Performance	160
10. SUMMARY AND CONCLUSIONS	162
REFERENCES	162
APPENDICES	
Appendix A. Evaluation Results for Innovative Repair Methods	165
Appendix B. Section Loss Measurements for Specimens 1–7	165
Appendix C. Sandwich Panel Repair Details	165

LIST OF TABLES

Table 3.1	Requirements set by the customer	14
Table 3.2	Definitions of the novel repair method requirements	15
Table 3.3	Requirements, importance levels, and severity rates	15
Table 3.4	Calculation of absolute importance factor for the sandwich panel repair method	16
Table 3.5	Final assessment of innovative repair methods using the House of Quality Matrix	16
Table 4.1	Properties of NS Grout produced by Euclid Chemical	20
Table 4.2	Properties of TammsgROUT Supreme Grout produced by Euclid Chemical	22
Table 4.3	Properties of Hi-Flow Grout produced by Euclid Chemical	24
Table 4.4	Properties of Hybrid Grout produced by Five Star Products	27
Table 4.5	Properties of Kwik Bond PPC-1121 produced by Kwik Bond Polymers	28
Table 4.6	Properties of Kwik Bond HCSC produced by Kwik Bond Polymers	32
Table 4.7	Properties of UHPC produced by Steelike	36
Table 4.8	Requirements, importance levels, and severity rates	36
Table 4.9	Assessment criteria for the infill material	37
Table 4.10	Results of material level testing	37
Table 4.11	Results of evaluation using the House of Quality Matrix	38
Table 4.12	Material properties: modulus of elasticity and compressive strength	48
Table 5.1	Test matrix	50
Table 6.1	Experimental results	111
Table 6.2	Test setup and bearing arrangement details	111
Table 7.1	Comparison between FE simulations and experimental data	133
Table 8.1	Parametric study matrix	134
Table 9.1	Shear and bearing capacities of $W24 \times 68$ girder	153

LIST OF FIGURES

Figure 1.1 Typical corrosion pattern	1
Figure 2.1 Conventional repair method: replacing the corroded part by welding (a) before repair, and (b) after repair	3
Figure 2.2 Conventional repair method: bolting steel angles and plates	4
Figure 2.3 Artificial section loss	5
Figure 2.4 Welded stud arrangement	5
Figure 2.5 UHPC repair panel	5
Figure 2.6 Stud sizing and layout and UHPC panel size	6
Figure 2.7 Completed UHPC panels after formwork removal	7
Figure 2.8 The details of the CFRP bonding method on the corroded webs	7
Figure 3.1 Corroded girder after shear studs welding	9
Figure 3.2 Repaired girder after UHPC curing and disassembling the formwork	10
Figure 3.3 Strengthening the corroded part with CFRP sheets	10
Figure 3.4 Sandwich panel repair method (isometric view)	11
Figure 3.5 Sandwich panel repair method (front view)	11
Figure 3.6 Improved bolted angles method (isometric view)	12
Figure 3.7 Improved bolted angles method (front view)	12
Figure 3.8 Web strengthening with diagonally oriented angles (isometric view)	13
Figure 3.9 Web strengthening with diagonally oriented angles (side view)	14
Figure 4.1 Flow cone with 0.5" orifice	17
Figure 4.2 Bronze and plastic molds for 2 × 2" cubes and plastic molds for 4 × 8" cylinders	18
Figure 4.3 Cube NS-1.1 $f'_c = 3,362$ psi	18
Figure 4.4 Cube NS-1.2 $f'_c = 3,273$ psi	18
Figure 4.5 Cube NS-1.3 $f'_c = 3,464$ psi	18
Figure 4.6 Strength gain over time for NS Grout (fluid consistency)	19
Figure 4.7 Modulus of elasticity test: test setup	19
Figure 4.8 Modulus of elasticity test results for NS Grout (7-day curing time)	20
Figure 4.9 Cube HS-1.1 $f'_c = 4,756$ psi	20
Figure 4.10 Cube HS-1.2 $f'_c = 4,768$ psi	21
Figure 4.11 Cube HS-1.3 $f'_c = 4,792$ psi	21
Figure 4.12 Strength gain over time for Tammsgrout Supreme (fluid consistency)	21
Figure 4.13 Modulus of elasticity test for Tammsgrout Supreme (8-day curing time)	22
Figure 4.14 Cube HF-1.1 $f'_c = 3,438$ psi	22
Figure 4.15 Cube HF-1.2 $f'_c = 3,508$ psi	23
Figure 4.16 Cube HF-1.3 $f'_c = 3,363$ psi	23
Figure 4.17 Strength gain over time for Hi-Flow Grout (fluid consistency)	23
Figure 4.18 Modulus of elasticity test for Hi-Flow Grout (35-day curing time)	24
Figure 4.19 Modified flow table test setup	24
Figure 4.20 Measuring the diameter of the grout spread	25
Figure 4.21 Cube HY-1.1 ($f'_c = 6,713$ psi)	25
Figure 4.22 Cube HY-1.2 ($f'_c = 6,255$ psi)	25

Figure 4.23 Strength gain over time for Hybrid Grout (flowable consistency)	26
Figure 4.24 Modulus of elasticity test for Hybrid Grout (7-day curing time)	27
Figure 4.25 Slump flow test; $d_{avg} = 12.25$ in.	27
Figure 4.26 Cylinders after casting (bleeding of resin)	28
Figure 4.27 Cylinder PPC-3.1; $f'_c = 6,585$ psi	28
Figure 4.28 Cylinder PPC-3.2; $f'_c = 6,980$ psi	28
Figure 4.29 Strength gain over time for Kwik Bond PPC-1121	29
Figure 4.30 Modulus of elasticity test for Kwik Bond PPC-1121 (7-day curing time)	29
Figure 4.31 Slump flow test; $d_{avg} = 19.06$ in.	30
Figure 4.32 HCSC cylinders after casting (bleeding of resin)	30
Figure 4.33 HCSC-1.1; $f'_c = 8,478$ psi	30
Figure 4.34 HCSC-1.2; $f'_c = 8,444$ psi	31
Figure 4.35 HCSC-1.3; $f'_c = 8,267$ psi	31
Figure 4.36 Strength gain over time for Kwik Bond HCSC	31
Figure 4.37 Modulus of elasticity test for Kwik Bond HCSC (7-day curing time)	32
Figure 4.38 Hobart mixer with a vertical shaft	33
Figure 4.39 UHPC mixing process	33
Figure 4.40 Cylinders after casting	33
Figure 4.41 Modified flow table test setup	33
Figure 4.42 Measuring the diameter after the test; $d_1 = 9.25$ in.	33
Figure 4.43 Cylinder UHPC-3.1; $f'_c = 14,936$ psi	34
Figure 4.44 Cylinder UHPC-3.2; $f'_c = 14,595$ psi	34
Figure 4.45 Strength gain over time for Steellike UHPC	35
Figure 4.46 Modulus of elasticity test for Steellike UHPC (7-day curing time)	36
Figure 4.47 Sensor layout	39
Figure 4.48 Test setup	40
Figure 4.49 Details of LVDT installation	40
Figure 4.50 Stress-strain curve for NS Grout. Curing time = 3, 28 days	40
Figure 4.51 Stress-strain curve for Hi-Flow Grout. Curing time = 3, 28 days	41
Figure 4.52 Stress-strain curve for Kwik Bond-PPC 1121. Curing time = 3, 28 days	41
Figure 4.53 Stress-strain curve for Steellike UHPC. Curing time = 3, 28 days	42
Figure 4.54 Strength gain over time for NS Grout	42
Figure 4.55 Strength gain over time for Hi-Flow Grout	43
Figure 4.56 Strength gain over time for Kwik Bond-PPC 1121	43
Figure 4.57 Strength gain over time for Steellike UHPC	44
Figure 4.58 FE model: boundary conditions and applied load	44
Figure 4.59 FE model: standard mesh. Mesh size = $1/4"$	44
Figure 4.60 Stress-strain curves for Abaqus input: NS Grout	45
Figure 4.61 Stress-strain curves for Abaqus input: Hi-Flow Grout	45
Figure 4.62 Stress-strain curves for Abaqus input: KB-PPC 1121	46
Figure 4.63 Stress-strain curves for Abaqus input: Steellike UHPC	46

Figure 4.64 Comparison of FE simulations and experimental data: NS Grout	47
Figure 4.65 Comparison of FE simulations and experimental data: Hi-Flow Grout	47
Figure 4.66 Comparison of FE simulations and experimental data: Kwik Bond-PPC 1121	48
Figure 4.67 Comparison of FE simulations and experimental data: Steelike UHPC	48
Figure 5.1 Corroded girder end	49
Figure 5.2 Additional bearing placement	49
Figure 5.3 Threaded rod layout for Specimens 3–5: AutoCAD drawing	50
Figure 5.4 Threaded rod layout for Specimens 6–7: AutoCAD drawing	50
Figure 5.5 3D model of the test setup: front view	51
Figure 5.6 3D model of the test setup: back view	52
Figure 5.7 3D model of the test setup: top view	52
Figure 5.8 3D model of the test setup: isometric view	53
Figure 5.9 3D model of the test setup: side view	53
Figure 5.10 Steel angle (lateral bracing): spreader beam connection	54
Figure 5.11 (a) Spreader beam: top flange connection. (b) Top flange: steel angle connection	54
Figure 5.12 Roller support at the far end	54
Figure 5.13 Pin support at the corroded end	55
Figure 5.14 Test setup for Specimens 4–5	55
Figure 5.15 Additional bearing (tack welded)	55
Figure 5.16 Test setup assembly in Bowen Laboratory	56
Figure 5.17 Strain gauge layout (side elevation): Specimen 1	56
Figure 5.18 Example of installed strain gauge rosette (SR9)	57
Figure 5.19 Displacement sensor layout (side elevation): Specimen 1	57
Figure 5.20 Example of installed displacement transducers	58
Figure 5.21 Strain gauge layout (side elevation): Specimen 2	58
Figure 5.22 Displacement sensor layout (side elevation): Specimen 2	59
Figure 5.23 Strain gauge layout (side elevation): Specimens 3, 6, and 7	59
Figure 5.24 Displacement sensor layout (side elevation): Specimens 3, 6, and 7	60
Figure 5.25 Strain gauge before applying sealant	60
Figure 5.26 Strain gauge after applying sealant	60
Figure 5.27 Strain gauge layout: threaded rods	61
Figure 5.28 Strain gauge installation process: (a) Step 1, (b) Step 2, and (c) Step 3	61
Figure 5.29 Strain gauge layout (side elevation): Specimens 4 and 5	62
Figure 5.30 Displacement sensor layout (side elevation): Specimens 4 and 5	62
Figure 5.31 Example of DT2 installation for Specimens 4 and 5	63
Figure 5.32 Standard section loss profile	63
Figure 5.33 Specimen 1: isometric view	64
Figure 5.34 Specimen 1: front view	64
Figure 5.35 Specimen 2: isometric view	65
Figure 5.36 Specimen 2: side view	65
Figure 5.37 Specimen 3: artificial corrosion in the studied end	66

Figure 5.38 Specimen 3: bearing stiffener welded to far girder end	66
Figure 5.39 Specimen 4: isometric view	66
Figure 5.40 Specimen 4: front view	67
Figure 5.41 Specimen 5: isometric view	67
Figure 5.42 Specimen 5: front view	68
Figure 5.43 Specimen 6: isometric view	68
Figure 5.44 Specimen 6: front view	68
Figure 5.45 Specimen 7: isometric view	69
Figure 5.46 Specimen 7: front view	69
Figure 5.47 Specimen 7 bearing stiffener welded to far girder end	69
Figure 6.1 Load—vertical displacement plot for Specimen 1	71
Figure 6.2 Load—OOP displacement plot for Specimen 1	71
Figure 6.3 Load—strain (bottom flange) plot for Specimen 1	72
Figure 6.4 Load—vertical strain (support) plot for Specimen 1	72
Figure 6.5 Load-maximum principal strain (west side) for Specimen 1	73
Figure 6.6 Specimen 1: deformed shape, front view	74
Figure 6.7 Specimen 1: deformed shape, locations of SP1 and SP4	74
Figure 6.8 Specimen 1: deformed shape, view from the east side	74
Figure 6.9 Load-vertical displacement plot for Specimen 2	75
Figure 6.10 Load-OOP displacement plot for Specimen 2	75
Figure 6.11 Load-strain (bottom flange) plot for Specimen 2	76
Figure 6.12 Load-vertical strain (support) plot for Specimen 2	76
Figure 6.13 Specimen 2: deformations in the corroded region	77
Figure 6.14 Load-maximum principal strain (west side) for Specimen 2	77
Figure 6.15 Specimen 2: deformed shape	78
Figure 6.16 Specimen 2: deformed shape. Locations of SP1 and SP4	78
Figure 6.17 Rupture in the artificially corroded web	78
Figure 6.18 Load-vertical displacement plot for Specimen 3	79
Figure 6.19 Load-OOP displacement plot for Specimen 3	79
Figure 6.20 Load-strain (bottom flange) plot for Specimen 3	80
Figure 6.21 Load-vertical strain (support) plot for Specimen 3	81
Figure 6.22 Load-maximum principal strain (west side) for Specimen 3	81
Figure 6.23 Specimen 3: deformed shape, front view	82
Figure 6.24 Specimen 3: deformed shape, front view (enlarged)	82
Figure 6.25 Specimen 3: deformed shape, view from the west side	83
Figure 6.26 Specimen 3: deformed shape, view from the east side	83
Figure 6.27 Specimen 3: cracks in grout panel	84
Figure 6.28 Specimen 3: detachment of stay-in-place formwork from grout panel	84
Figure 6.29 Load: vertical displacement plot for Specimen 4	85
Figure 6.30 Load: OOP displacement plot for Specimen 4	85
Figure 6.31 Load: strain (bottom flange) plot for Specimen 4	86

Figure 6.32 Load: vertical strain (support) plot for Specimen 4	86
Figure 6.33 Load: maximum principal strain (east side) for Specimen 4	87
Figure 6.34 Load: strain in threaded rods for Specimen 4	87
Figure 6.35 Instrumented threaded rods	88
Figure 6.36 Specimen 4: deformed shape, front view	88
Figure 6.37 Specimen 4: deformed shape, enlarged view	89
Figure 6.38 Specimen 4: deformed shape, view from the east side	89
Figure 6.39 Specimen 4: deformed square washer, view from the west side	90
Figure 6.40 Specimen 4: cracks in west panel (top view)	90
Figure 6.41 Specimen 4: cracking in west panel (elevation view)	91
Figure 6.42 Specimen 4: threaded rod deformations (grout panel removed)	91
Figure 6.43 Specimen 4: cross-section of ruptured rods	92
Figure 6.44 Specimen 4: three ruptured rods	92
Figure 6.45 Load: vertical displacement plot for Specimen 5	92
Figure 6.46 Load: OOP displacement plot for Specimen 5	93
Figure 6.47 Load: strain (bottom flange) plot for Specimen 5	93
Figure 6.48 Load: vertical strain (support) plot for Specimen 5	94
Figure 6.49 Load: maximum principal strain (west side) for Specimen 5	94
Figure 6.50 Load: strain in threaded rods for Specimen 5	95
Figure 6.51 Specimen 5: deformed shape, front view	95
Figure 6.52 Specimen 5: deformed shape, enlarged front view	96
Figure 6.53 Specimen 5: deformed shape, view from the west side	96
Figure 6.54 Specimen 5: deformed shape, view from the east side	97
Figure 6.55 Specimen 5: deformed shape, east side view	97
Figure 6.56 Specimen 5: cracking in the west Kwik Bond panel	98
Figure 6.57 Load: vertical displacement plot for Specimen 6	98
Figure 6.58 Load: OOP displacement plot for Specimen 6	99
Figure 6.59 Load: strain (bottom flange) plot for Specimen 6	99
Figure 6.60 Load: vertical strain (support) plot for Specimen 6	100
Figure 6.61 Load: maximum principal strain (east side) for Specimen 6	100
Figure 6.62 Load: strain in threaded rods for Specimen 6	101
Figure 6.63 Specimen 6: deformed shape, front view	101
Figure 6.64 Specimen 6: deformed shape, enlarged front view	102
Figure 6.65 Specimen 6: deformed shape and failure	102
Figure 6.66 Specimen 6: cracking in the west panel	103
Figure 6.67 Specimen 6: deformations in threaded rods and grout panels cracking	103
Figure 6.68 Specimen 6: web crippling behind grout panel	104
Figure 6.69 Load: vertical displacement plot for Specimen 7	104
Figure 6.70 Load: OOP displacement plot for Specimen 7	105
Figure 6.71 Load: strain (bottom flange) plot for Specimen 7	105
Figure 6.72 Load: vertical strain (support) plot for Specimen 7	106

Figure 6.73 Load: maximum principal strain (west side) for Specimen 7	106
Figure 6.74 Load: strain in threaded rods for Specimen 7	107
Figure 6.75 Specimen 7: deformed shape	107
Figure 6.76 Specimen 7: deformed shape, enlarged front view	108
Figure 6.77 Specimen 7: deformed shape, east side view	108
Figure 6.78 Specimen 7: cracking in a west panel	109
Figure 6.79 Specimen 7: buckling and bulging of steel sheets	109
Figure 6.80 Specimen 7: web crippling deformations, front view	110
Figure 6.81 Specimen 7: web crippling deformations behind the concrete panel	110
Figure 7.1 Assembly in Abaqus, elevation view	112
Figure 7.2 Section loss profile	112
Figure 7.3 Boundary conditions (BC) of the FE model, side elevation view	113
Figure 7.4 BC of the FE model, front view	113
Figure 7.5 Standard mesh: Specimen 1	114
Figure 7.6 Stress-strain curve for steel	115
Figure 7.7 First modeshape (Specimen 1)	115
Figure 7.8 Second modeshape (Specimen 2)	116
Figure 7.9 Specimen 3 assembly, elevation view	116
Figure 7.10 Specimen 3 assembly, front view	117
Figure 7.11 Specimen 3 assembly, isometric view	117
Figure 7.12 Specimen 4 and 5 assemblies	118
Figure 7.13 Specimen 6 and 7 assemblies	118
Figure 7.14 Specimen 3–Specimen 7: boundary conditions	119
Figure 7.15 Standard meshing approach for Specimen 3–Specimen 7	119
Figure 7.16 Comparison of load-vertical displacement relationship for Specimen 1	120
Figure 7.17 Comparison of load-vertical displacement relationship for Specimen 2	120
Figure 7.18 Deformed shape of Specimen 1 (FE model, post-peak load = 162.1 kips)	121
Figure 7.19 Deformed shape of Specimen 1 (experiment)	121
Figure 7.20 Deformed shape of Specimen 2 (FE model, post-peak load = 21.5 kips)	122
Figure 7.21 Deformed shape of Specimen 2 (experiment)	122
Figure 7.22 Comparison of load-vertical displacement relationship for Specimen 3	123
Figure 7.23 Deformed shape of Specimen 3 (FE model, post-peak load = 55.6 kips)	123
Figure 7.24 Deformed shape of Specimen 3 (experiment)	124
Figure 7.25 Specimen 3: corroded web yielding (FE model, post-peak load = 55.6 kips)	124
Figure 7.26 Stress distribution in threaded rods. No yielding was observed (post-peak load = 55.6 kips)	125
Figure 7.27 Comparison of load-vertical displacement relationship for Specimen 4	125
Figure 7.28 Deformed shape of Specimen 4 (FE model, peak load = 310.2 kips)	125
Figure 7.29 Deformed shape of Specimen 4 (experiment)	126
Figure 7.30 Specimen 4: corroded web yielding (FE model, peak load = 310.2 kips)	126
Figure 7.31 Specimen 4: threaded rod deformations (FE model, peak load = 310.2 kips)	127
Figure 7.32 Comparison of load-vertical displacement relationship for Specimen 5	127

Figure 7.33 Deformed shape of Specimen 5 (FE model, peak load = 307.3 kips)	128
Figure 7.34 Deformed shape of Specimen 5 (experiment)	128
Figure 7.35 Specimen 5: corroded web yielding (FE model, peak load = 307.3 kips)	129
Figure 7.36 Specimen 5: threaded rod deformations (FE model, peak load = 307.3 kips)	129
Figure 7.37 Comparison of load-vertical displacement relationship for Specimen 6	130
Figure 7.38 Specimen 6: stress distribution (FE model, peak load = 228.7 kips)	130
Figure 7.39 Specimen 6: corroded web yielding (FE model, peak load = 228.7 kips)	131
Figure 7.40 Specimen 6: stress distribution in threaded rods (FE model, peak load = 228.7 kips)	131
Figure 7.41 Comparison of load-vertical displacement relationship for Specimen 7	132
Figure 7.42 Specimen 7: stress distribution (FE model, peak load = 271.4 kips)	132
Figure 7.43 Specimen 7: corroded web yielding (FE model, peak load = 271.4 kips)	133
Figure 7.44 Specimen 7: deformations in threaded rods (FE model, peak load = 271.4 kips)	133
Figure 8.1 Case I: threaded rod layout with 16 effective threaded rods (I-G-16)	135
Figure 8.2 Case I: threaded rod layout with 11 effective threaded rods (I-G-11)	135
Figure 8.3 Case I: threaded rod layout with 7 effective threaded rods. Option 7: Middle (I-G-7.1)	136
Figure 8.4 Case I: threaded rod layout with 7 effective threaded rods. Option 7: bottom	136
Figure 8.5 Impact of threaded rod material on the repair capacity (Case I: 16 effective threaded rods)	137
Figure 8.6 Impact of threaded rod material on the repair capacity (Case I: 11 effective threaded rods)	137
Figure 8.7 Impact of threaded rod material on the repair capacity (Case I: 7 effective threaded rods, Option 7: middle)	138
Figure 8.8 Impact of threaded rod material on the repair capacity (Case I: 7 effective threaded rods, Option 7: bottom)	138
Figure 8.9 Impact of the number of threaded rods on the repair capacity (Case I: $F_u = 60$ ksi)	139
Figure 8.10 Impact of the number of threaded rods on the repair capacity (Case I: $F_u = 125$ ksi)	139
Figure 8.11 Impact of the number of threaded rods on the repair capacity (Case I: $F_u = 150$ ksi)	140
Figure 8.12 Case II: threaded rod layout with 16 effective threaded rods (II-G-16)	141
Figure 8.13 Case II: threaded rod layout with 11 effective threaded rods (II-G-11)	141
Figure 8.14 Case II: threaded rod layout with 7 effective threaded rods. Option 7: middle (II-G-7.1)	142
Figure 8.15 Case II: threaded rod layout with 7 effective threaded rods. Option 7: bottom (II-G-7.2)	142
Figure 8.16 Impact of threaded rod material on the repair capacity (Case II: 16 effective threaded rods)	143
Figure 8.17 Impact of threaded rod material on the repair capacity (Case II: 11 effective threaded rods)	143
Figure 8.18 Impact of threaded rod material on the repair capacity (Case II: 7 effective threaded rods. Option 7: middle)	144
Figure 8.19 Impact of threaded rod material on the repair capacity (Case II: 7 effective threaded rods. Option 7: bottom)	144
Figure 8.20 Impact of the number of threaded rods on the repair capacity (Case II: $F_u = 60$ ksi)	145
Figure 8.21 Impact of the number of threaded rods on the repair capacity (Case II: $F_u = 125$ ksi)	145
Figure 8.22 Impact of the number of threaded rods on the repair capacity (Case II: $F_u = 150$ ksi)	146
Figure 8.23 Case III: threaded rod layout with 15 effective threaded rods (III-G-15)	147
Figure 8.24 Case III: threaded rod layout with 9 effective threaded rods (III-G-9)	147
Figure 8.25 Case III: threaded rod layout with 6 effective threaded rods (III-G-6)	148
Figure 8.26 Impact of threaded rod material on the repair capacity (Case III: 15 effective threaded rods)	148
Figure 8.27 Impact of threaded rod material on the repair capacity (Case III: 9 effective threaded rods)	149
Figure 8.28 Impact of threaded rod material on the repair capacity (Case III: 6 effective threaded rods)	149
Figure 8.29 Impact of the number of threaded rods on the repair capacity (Case II; $F_u = 60$ ksi)	150

Figure 8.30 Impact of the number of threaded on the repair capacity (Case II; $F_u = 125$ ksi).	150
Figure 8.31 Impact of the number of threaded rods on the repair capacity (Case III: $F_u = 150$ ksi)	151
Figure 9.1 Non-corroded diaphragm in a steel bridge	152
Figure 9.2 Severely corroded diaphragms	152
Figure 9.3 Placement of an additional bearing	154
Figure 9.4 Definition of d_1 and d_2 values	154
Figure 9.5 Definition of the bearing region	155
Figure 9.6 Polyester binder resin	156
Figure 9.7 MEKP catalyst	157
Figure 9.8 KBP	157
Figure 9.9 KBP blended PPC sand	157
Figure 9.10 Process of adding MEKP catalyst to binder resin	157
Figure 9.11 Mixing MEKP catalyst and binder resin (15 seconds)	157
Figure 9.12 Mixing aggregates with catalyzed binder resin (2 minutes)	158
Figure 9.13 Water required for NS Grout mixing (5 lb.)	158
Figure 9.14 NS Grout powder (25 lb.)	158
Figure 9.15 Mixing of NS Grout	158
Figure 9.16 Cracking pattern: Kwik Bond-PPC 1121	158
Figure 9.17 Cracking pattern: NS Grout	158
Figure 9.18 Sandwich panel repair mock-up specimen. Clamped stay-in-place formwork	159
Figure 9.19 Square washers and hex nuts used in the repair (outer side)	159
Figure 9.20 Standard washers and hex nuts used in the repair (inner side)	159
Figure 9.21 Connection of threaded rods to steel girder web and to stay-in-place formwork	159
Figure 9.22 Sealed stay-in-place formwork, side view	161
Figure 9.23 Sealed stay-in-place formwork, front view	161
Figure 9.24 Elevation view. Girder at end-bent support	161
Figure 9.25 Caulk bead detail	161

1. INTRODUCTION

1.1 Background

Transportation infrastructure across the United States currently faces an enormous challenge as 42% of all bridges have reached their 50-year design life. According to the ASCE 2021 Report Card for America's Infrastructure, the estimated total number of bridges in the United States is approximately 617,000, and 7.5% of those bridges are classified as structurally deficient, with a recent estimate of the nation's backlog of repair needs of \$125 billion (ASCE, 2021). A bridge is classified as structurally deficient when one of the key structural elements—the decks, superstructure, or substructure, is rated as poor or worse. During the inspection, the conditions of various bridge elements are rated on a scale of 0 (failed condition) to 9 (excellent condition); a rating of 4 is considered a "poor" condition (AASHTO, 2018/2020).

The Indiana Department of Transportation (INDOT) maintains and owns approximately 5,700 of 19,300 bridges in Indiana. Based on the Federal Highway Administration's (FHWA) inventory data, 116 bridges are rated as structurally deficient and must be repaired (FHWA, n.d.). This is approximately 2% of all bridges currently maintained by INDOT. Structural deficiency in steel bridges is often caused by the deterioration of steel girder ends due to corrosion (Figure 1.1). Deterioration of girder ends usually occurs because deicing salts, water, and other contaminants leak through the failed deck expansion joints. When corrosion becomes significant, it can decrease the sectional properties of end steel girders and eventually reduce structural resistance against bearing and shear, which could result in structural deficiency or total failure of the bridge.

Conventional repair methods for corrosion-damaged steel girders require a substantial amount of time and resources to complete and often cause public inconvenience due to traffic lane closure. The major drawbacks of conventional repair methods include lead paint removal, sandblasting, grinding, jacking of the structure, lane closure, and extended repair time. Therefore, there is a need for practical, rapid, and robust repair strategies that can be implemented by bridge maintenance personnel.

In the following subsections, studies that evaluated the effect of corrosion on the performance of steel girders are discussed. Furthermore, conventional methods that the INDOT generally implements, and

innovative repair methods proposed by other researchers were reviewed.

1.2 Research Objectives

This study concentrated on achieving the following three objectives.

1. Developing innovative method(s) to repair corrosion-damaged steel girder bridges.
2. Verifying the structural robustness of the developed innovative repair method(s) through experimental testing and numerical simulations.
3. Preparing design guidelines and recommendations for the Indiana Department of Transportation (INDOT).

The research objectives stated above were achieved by taking the following actions.

1. Identifying existing conventional and innovative repair methods
2. Developing and evaluating novel repair methods
3. Performing material testing
4. Performing a series of large-scale experiments
5. Conducting numerical investigations
6. Completing a parametric study
7. Developing design guidelines for novel repair method(s)

1.3 Report Layout

The layout of the report is as follows.

- *Chapter 2: Literature Review*

This chapter summarizes the research that has been completed on the development of novel repair methods. In addition, conventional repair methods are described in detail as well as the research that has been conducted to investigate the effect of girder end corrosion on shear and bearing capacities.

- *Chapter 3: Evaluation of Innovative Repair Methods*

This chapter provides a detailed description of innovative repair methods, followed by an introduction to the tool called the House of Quality Matrix (HQM) used for evaluation. In addition, evaluation process results for novel repair methods using HQM are provided.

- *Chapter 4: Material Testing*

This chapter presents the results of material testing of prospective filler materials for the sandwich panel repair method. Furthermore, the developed material models for application in finite element simulations are shown.

- *Chapter 5: Experimental Evaluation and Observations*

This chapter discusses the experimental program developed

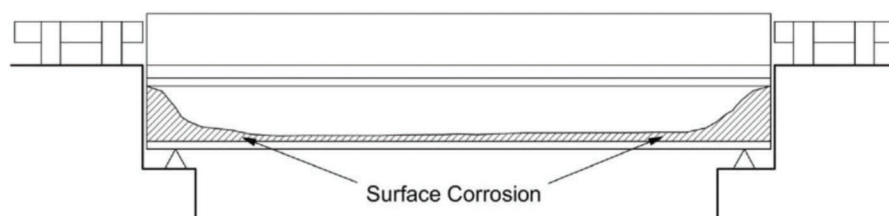


Figure 1.1 Typical corrosion pattern.

for this study. It comprises the test matrix, test setup, specimen details, and sensor layouts.

- *Chapter 6: Experimental Results*

This chapter presents the results of seven large-scale tests completed. For every experiment, load-vertical displacement, load-out-of-plane displacement, load-strain responses, and failure modes are shown.

- *Chapter 7: Finite Element Modeling*

This chapter describes modeling approaches for the specimens, including meshing techniques, boundary conditions, interactions, constraints, and buckling analysis. In addition, a comparison between load-vertical displacement responses obtained through experimental evaluation and numerical simulations is shown.

- *Chapter 8: Parametric Study*

This chapter presents the results of a parametric study investigating the impact of different threaded rod layouts and their tensile strengths on the sandwich panel repair capacity. The parametric study results were used to develop design recommendations and validate the proposed design equations.

- *Chapter 9: Recommendations for Design and Application*

This chapter contains the guidelines and recommendations for performing the sandwich panel design, including the selection of filler material and threaded rod calculations.

- *Chapter 10: Summary and Conclusions*

This chapter summarizes the experimental and numerical investigations conducted for the sandwich panel repair method and the most significant conclusions. Additionally, the limitations of the study and the future research scope are outlined.

2. LITERATURE REVIEW

2.1 Influence of Corrosion on the Residual Capacity of Steel Girders

Multiple studies have been conducted in the US to evaluate the effect of steel girder end corrosion on the residual capacity. Kayser (1988) studied the impact of corrosion on the capacity and reliability of steel bridges. To estimate the effect of section loss on the flexural, shear, and bearing capacities, plate theory was used. Bearing and shear failures are generally governed in corrosion-damaged steel girders. The full-depth stiffeners significantly increased the girder's bearing capacity and primarily impacted short-span bridges because thinner structural members were used. Capacity curves were developed for several stiffened and unstiffened W-sections ($W24 \times 76$, $W30 \times 116$, $W36 \times 182$, and $W36 \times 230$) that indicated a combination of linear and nonlinear correlation between section loss and residual loading capacity. A corrosion damage model was devised by incorporating information about the form and rate of corrosion in different environments. Furthermore, reliability theories and structural analysis were employed to estimate the residual load-carrying capacity and safety of the bridge.

Kayser and Nowak (1989) discussed capacity reduction in steel girder bridges caused by corrosion. This study investigated the relationship between residual

flexural capacity and section loss in a bottom for composite and non-composite girders. In addition to flexural capacity, analogous curves were generated for residual shear and bearing capacities. Bearing capacity correlated nearly linearly with section loss for stiffened girders with full-depth bearing stiffeners and nonlinearly with section loss for unstiffened girders. However, the correlation between shear capacity and section loss was always nonlinear despite the use of full-depth transverse stiffeners. One of the most important findings presented in this study was the more significant tolerance that girders with bearing stiffeners had toward section loss in the end region caused by corrosion.

Tzortzinis, Gerasimidis, Brena, and Knickle (2019) examined 216 bridge inspection reports that contained 808 beam ends to identify typical corrosion patterns for unstiffened steel beams. Consequently, 18 patterns were finalized for beams with and without diaphragms because of the strong influence of the diaphragm on the corrosion pattern. In this study, six naturally corroded beams were tested in the laboratory because no previous research has considered naturally corroded beams. By comparing the capacity estimations calculated using the *MassDOT 2019 Bridge Manual* with experimental data, it was observed that in some cases the manual overestimated the actual capacity. In addition, initial imperfections affected the residual capacity of the beam, and the current procedures described in the manual do not account for this. After completing the experimental investigation, high-fidelity finite element models were benchmarked with experimental data, and a parametric study with over 2000 models with various corrosion patterns was performed to specify the parameters that influence the residual bearing capacity. One of the most essential findings was the insignificance of the hole size if it was located just above the bearing. Finally, equations for calculating the bearing capacity of the deteriorated girders were developed that accounted for different levels of imperfections ($0.1t_w$, $0.5t_w$, $1t_w$) and the N/d (bearing length/overall depth of the girder) ratio. The proposed equations consider local and global web buckling as possible failure modes.

Javier, Hebdon, and Provines (2021) conducted 17 full-scale tests on unstiffened hot-rolled steel beams delivered to the laboratory from decommissioned bridges in Virginia. A shear load was applied close to the deteriorated area to induce shear failure in the end region. Strain, displacement, and applied load were recorded during large-scale testing. The strain was recorded using a digital image correlation system (DIC); displacement was recorded using string potentiometers, and the applied load was recorded using a pressure transducer. The experimental results were compared with estimations based on equations provided in AISC 360, AASHTO LRFD, and the equations proposed by other researchers. It was proven that the AASHTOWare Bridge Rating (BrR) can accurately determine a corroded beam's residual capacity.

A flowchart to estimate the residual shear capacity was developed for the webs with and without through-web holes caused by corrosion. For the cases of webs with holes, the reduction factor presented in the *MassDOT LRFD Bridge Manual 2020*, Part I, Section 7.2.9.2 was implemented.

Gerasimidis, Breña, and Tzortzinis (2021) analyzed inspection reports provided by the Massachusetts Department of Transportation) that contained 210 corroded stiffened beam ends. Based on that examination, two groups of girders were identified: girders that had two bearing stiffeners and girders with only one bearing stiffener. The corrosion patterns were provided for each configuration. In this study, stiffener deterioration due to corrosion was also considered. Two specimens were experimentally evaluated and failed because of large out-of-plane displacements of the web. After the experimental part of the project, a parametric study was conducted to specify the parameters that influence the residual bearing capacity. Three different corrosion patterns were considered during the parametric study, which contained 1,000 high-fidelity finite element models. The deterioration of the bearing stiffener was also accounted for (30%, 50%, and 70% section loss in the bearing stiffener) in the parametric study. It was concluded that section loss in the stiffener had a detrimental effect on the bearing capacity of the beam and, therefore, should be examined and documented more cautiously during field inspections. It was discovered that if the corroded area is greater than the bearing length (N) plus 10% of the web depth (d), it does not decrease the bearing capacity any further. In general, existing procedures overestimate the capacity of stiffened corroded girders. Therefore, a set of equations was developed to estimate the residual capacity of the beams that aligned well with the parametric study results.

2.2 Conventional Repair Methods

Two conventional repair methods are generally used in the United States to repair beam-end corrosion. The first traditional method involves cutting the corroded part and welding a new section to replace it (FDOT, 2018; WisDOT, 2024). Depending on the corrosion damage in the girder end, it could be either a tee section or an entire W-section cut from a matching girder

(Figure 2.1). However, the following repair method requires multiple steps, such as traffic closure to eliminate the live load and jacking the beam end to relieve it from the dead load. Welding of bearing stiffeners may be required at locations where temporary supporting members and calibrated jacks would be installed. Finally, protective paint should be applied to the region where the repairs were installed.

The second conventional repair method widely used in the US requires bolting additional steel cover plates and angle sections in the deteriorated region with severe corrosion (FDOT, 2018; GDOT, 2012; IDOT, 2017). This repair method is more cost-effective than replacing the deteriorated part by welding because neither jacking nor field welding is typically required (Figure 2.2). Before installation, it is necessary to clean the corroded area of loose paint and corrosion debris. Once the holes are drilled, the entire cleaned area must be painted. After the steel plates and angle sections were bolted together and tightened, the repaired region must also be painted (including bolts) to prevent further deterioration. Depending on the state, welding of the legs of the angle section to the steel plate using fillet welds might be required (GDOT, 2012).

2.3 Innovative Repair Methods

2.3.1 Early Research

Numerous researchers have initiated the development of novel repair methods that could be easily implemented on-site, avoiding traffic closure and expensive labor to address difficulties associated with conventional repair methods. In this subsection, the early research that originated further studies is reviewed.

For example, Nakamura and Narita (2003) studied how partial concrete encasement of undamaged I-girders can improve shear and flexural capacities. This study primarily focused on the encasement of continuous girders where hogging moments occur (at intermediate supports), resulting in the bottom and web being subjected to compression. Two cases were evaluated in which the vertical rebars were welded to the top and bottom flanges (BC) and welding was not performed (BC-N). Additionally, the already buckled girder (BC-R) was encased in concrete with rears

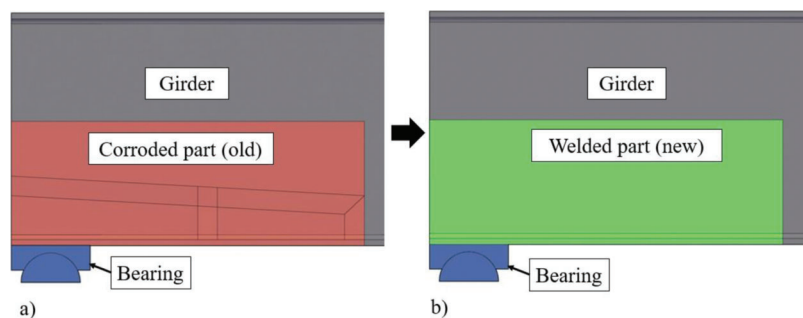


Figure 2.1 Conventional repair method: replacing the corroded part by welding (a) before repair, and (b) after repair.

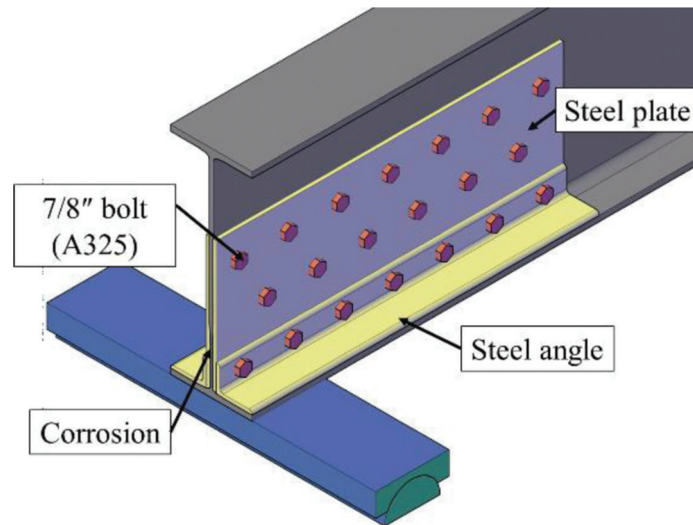


Figure 2.2 Conventional repair method: bolting steel angles and plates.

welded to flanges to investigate whether the encasement could also be used for rehabilitation. It was found that after encasement, the flexural and shear capacities increased 2 and 3 times, respectively, for the BC case. In contrast, the flexural capacity increased 1.75 times for the BC-N specimen, indicating that welding affects the load-carrying capacity. Finally, the already damaged BC-R specimen showed significantly improved behavior after the repair, exhibiting 1.9 times increase in capacity compared with the intact specimen. The authors also proposed an analytical approach to calculate the composite I-girders' shear and flexural capacities. Although the primary focus of the research was not the rehabilitation of corroded steel girders, the application of concrete encasement as a potential repair technique inspired future studies.

He, Liu, Chen, and Yoda (2012) discussed the performance of partially encased I-girders with flat and corrugated webs subjected to shear loading. Seven girders were tested in the laboratory: two specimens without concrete encasement (S-0 and S-1 with flat and corrugated web, respectively), and the remaining five specimens that were encased in concrete with shear studs welded to the web. In addition, vertical and horizontal rebars were welded to flanges and stiffeners to prevent concrete spalling. The corrugated web added approximately 10% to the ultimate shear capacity of the girder without concrete encasement. However, after reaching the first peak load, the capacity of the girder with a flat web continued to increase because of the development of tension field action. The authors found no significant difference in failure modes between composite specimens (SC-0 and SC-1) with corrugated and flat webs, which could have been attributed to the lateral restraint provided by concrete. All encased specimens exhibited improved shear performance by 60% and 40% for flat and corrugated webs, respectively. Finally, the authors proposed equations to calculate the shear capacity of partially encased I-

girders considering steel tension and concrete compression strut contributions.

He, Liu, Lin, Chen, and Yoda (2012) conducted a numerical study using finite element (FE) models validated using experimental data. The FE models had geometric and material nonlinearities. An extensive parametric study was conducted once the FE models were benchmarked to investigate the effect of thickness, height, concrete, and steel strengths. It was concluded that every abovementioned parameter affects the shear capacity of the partially encased girder, except for the headed stud stiffness.

Ogami, Fujii, Yamada, and Iwashaki (2015) suggested a repair method for corroded beam ends by welding shear studs to the web, attaching rebars, and encasing the deteriorated region in resin. Six specimens were tested, including non-corroded, corroded, and four repaired beams with artificial corrosion. While the corrosion profile remained the same, the stud layout (A and B) and resin thickness varied to examine their effect on the repaired specimen's strength. It was found that every repaired specimen could achieve the capacity of the intact specimen and even exceed it. To conclude, different stud layouts and resin thicknesses did not affect the capacity; therefore, Type B repair was preferable due to the ease of implementation.

2.3.2 Beam End Repair Using Ultra-High-Performance Concrete (UHPC)

Zmetra, McMullen, Zaghi, and Wille (2017) proposed a novel repair method to rehabilitate corroded girder ends by encasing the corroded region in ultra-high-performance concrete (UHPC) with high tensile and compressive strengths, superb durability, and flowability. Shear studs were welded to the undamaged portion of the web and flange to facilitate force transfer and ensure composite action with UHPC (Figure 2.3 through Figure 2.6). Three half-scale tests were performed at

the University of Connecticut Structures Laboratory on an undamaged hot-rolled W21 55 girder (baseline specimen), an artificially corroded girder, and a repaired girder using UHPC. The test results demonstrated the effectiveness of the proposed novel repair by fully restoring bearing capacity and eliminating bearing failure.

McMullen and Zaghi (2020) examined the performance of the UHPC repair method by conducting four full-scale experiments on steel plate girders. The experiments included testing the baseline (unrepaired) girder alongside two full-height and one half-height retrofitted specimens. Section loss in all girders was induced by metal grinding and sandblasting. All three repaired specimens (full-height-1, full-height-2, and half-height) were able to fully recover and even increase the original design shear capacity of the girder by 46%, 38%, and 31%, respectively. Additionally, it was proven that this repair method could be implemented under live load vibrations without traffic closure. The full-height-2 specimen was cured under simulated vibrations induced by the mass shaker. Although the loading capacity of the half-height specimen was lower than that of the two full-height repaired specimens, the shear studs welded to the girder web used only 15% of their ultimate slip-displacement capacity. However, the studs in full-height repairs used approximately 60%–80% of the maximum slip capacity, having less capacity reserve. The baseline specimen failed in web local crippling of the corroded region; all three repaired specimens failed in web shear buckling, and very little cracking of the UHPC panels was observed.

Kruszewski, Wille, and Zaghi (2018a) conducted an extensive experimental study on the push-out behavior of shear studs welded to a thin 9.5-mm web cut from a salvaged girder built in 1958. Shear studs had different diameters, layouts, and horizontal and vertical spacings; additionally, the compressive strength of the UHPC varied. It was found that the shear stud layout did not have a significant effect on the repair capacity. However, the UHPC strength was directly correlated



Figure 2.3 Artificial section loss (Zmetra et al., 2017).

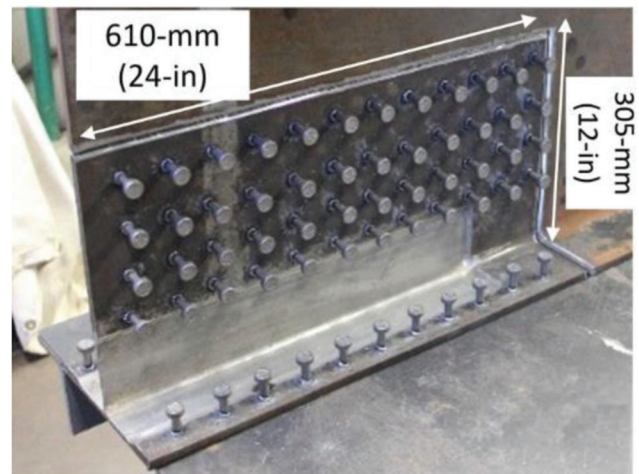


Figure 2.4 Welded stud arrangement (Zmetra et al., 2017).



Figure 2.5 UHPC repair panel (Zmetra et al., 2017).

with the shear capacity of the stud and yield/ultimate slip. Ultra-high-performance concrete with a larger compressive strength increased the capacity of the single shear stud and decreased the yield slip, resulting in a less ductile composite connection. Overall, the existing equations in AASHTO and Eurocode-4 under-predicted a stud's capacity by 2%–21% and 27%–43%, respectively. The authors proposed an updated equation to calculate the shear capacity of a headed stud that considered the compressive strength of UHPC, which agreed well with the experimental data.

Kruszewski, Wille, and Zaghi (2018b) performed an additional 16 push-out tests to evaluate design parameters such as the effect of eccentric load, different concrete mixes (with and without reinforcement/fibers), shear stud clear and side covers, surface preparation requirements, and vehicle vibrations. It was found that eccentric loading significantly reduced the capacity. The instantaneous center of rotation (ICR) method, which accounts for both the translation and rotation of the stud, could be used. However, steel fibers or reinforcement in UHPCs are vital for the ductile behavior of

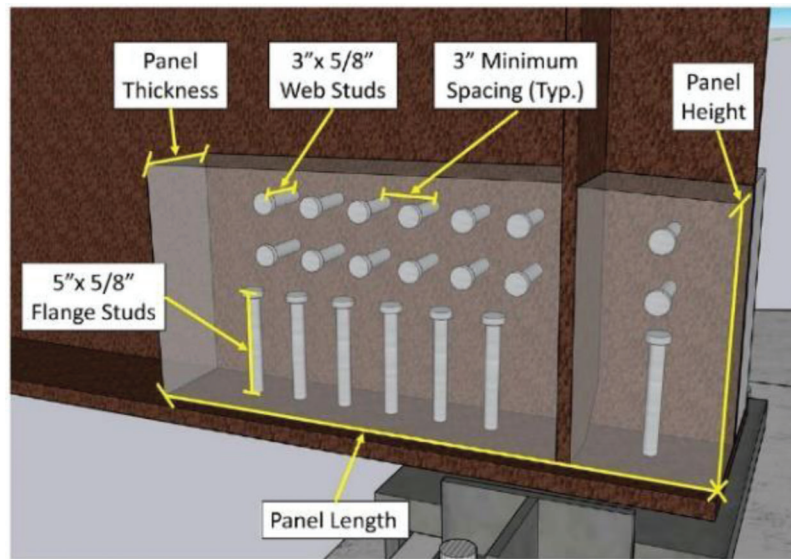


Figure 2.6 Stud sizing and layout and UHPC panel size (Lassy et al., 2023).

headed studs. For mixes without steel fibers (UHPC-B, HSC), the observed failure mode was concrete panels splitting instead of stud rupture. Therefore, at least 1% of the steel fibers should be used to enhance the tensile properties of UHPC/HSC. Additionally, vertical ferrules generated larger weld collars and increased the bearing surface, thus improving the stud capacity. Finally, removing the paint, at least in the shear stud locations, was essential to achieve good-quality welding.

Through push-out tests, Kruszewski and Zaghi (2019) experimentally examined three options for shear connectors, including threaded bars, headed studs, and UHPC dowels. An actual bridge constructed in 1960 was selected to present various arrangements of shear connectors that could restore the required strength based on live load (HS-93), strength I, and capacity design scenarios and illustrate the flexibility of the repair. The installation process for the threaded bar involved drilling a normal-sized hole in the web, followed by tightening the high-strength nuts to a torque of 100 lb.-ft. For headed studs, a stud welding gun and a conventional ferrule were used for attachment to the web. Finally, 1.5-in. holes were drilled in the web to examine the feasibility of UHPC dowels as shear connectors. Overall, all three connectors were found to be suitable for restoring the required capacity. However, the UHPC dowel exhibited more brittle failure than the threaded bar of the shear stud.

Kruszewski, Zaghi, and Wille (2019) conducted a numerical parametric study using high-fidelity finite element models. First, the numerical models were benchmarked using experimental data obtained by performing a series of push-out tests. The push-out specimens included eccentrically and concentrically loaded shear stud groups with 12-, 16-, and 19-mm diameters welded to a 9.5-mm web plate. Material models for steel and concrete materials were developed

based on material testing of steel coupons and concrete cylinders. To capture the actual behavior of the push-out specimens, it was essential to develop material models, including damage parameters. In conclusion, it was found that the web thickness-to-stud diameter ratio governs the failure mode of the specimen. Therefore, for a shear stud to fully develop its plastic shear strength, this ratio should be 0.5. For lower values, web bearing or global shear failures are observed. In addition, it was found that an increase in eccentricity significantly decreases the bearing capacity of a group of studs. This equation was proposed to calculate the capacity of shear studs subjected to eccentric loading based on the elastic rotation method.

Hain and Zaghi (2021) presented the results of the first field implementation of a novel UHPC repair that used full-depth encasement of a corroded end due to corrosion pattern and geometric limitations. Because of the full-depth encasement, a complicated system of PVC pipes was developed to cast UHPC directly from the top of the deck. It was vital to ensure adequate working time of the UHPC mix to prevent clogging of pipes and premature curing before the casting was completed. During this study, four out of 43 beam ends were instrumented with foil strain gauges installed on the web, shear studs, and concrete to monitor the effectiveness of the repair in providing an alternate load path. The data recorded by sensors after the repair at 4 and 28 days showed a significant decrease in web strain amplitude. The strain gauges installed on the shear studs and concrete panels displayed non-zero readings under live loads. The increase in UHPC compressive strength over time was found to reduce the strain in the web. Additional complications were imposed by casting in cold weather, which required heating of the beam ends while the UHPC was being cured and keeping the mixed components in a heated truck before mixing with warm water. The repair project was completed

successfully, and knowledge transfer was performed between the University of Connecticut and Connecticut DOT.

Lassy et al. (2023) provided an example of the second successful implementation of the novel repair in the field. The bridge located in East Hartford was made from weathered steel, which introduced additional complications for shear stud welding. Because the average daily traffic (ADT) on this bridge was high, with approximately 50,000 vehicles crossing it, its closure for repair would have caused complications. Due to favorable bridge geometry and the requirement of only partial-height encasement, traffic was not stopped during the entire repair process. Overall, 49 beam ends were repaired, and two of them were instrumented to monitor the performance and effectiveness of the repair. In this repair, shear studs were welded to the bottom flange for the first time (Figure 2.7), and it was noted that they carried both axial and shear loads. However, a complete understanding of shear stud behavior requires further research to propose a formula to estimate the required number of studs to be welded on the bottom. Strain data in the girder web supported the theory of force transfer from the web to UHPC panels; therefore, web strains after repair decreased with an increase in the compression strength of UHPC. Additionally, the strain gauge installed over the existing hole in the web started carrying loads after the concrete was cured, proving that the load path was restored.

Before concrete casting, the strains in this region were close to zero because of the disruption of the load path by the perforation. To conclude, another successful example of novel repair implementation was presented (Figure 2.8), and this approach is currently being designed for 15 more bridge repairs in Connecticut.

The Connecticut Department of Transportation published design guidelines that could be used to detail beam end repair using ultra-high-performance concrete (CTDOT, 2022). The guidelines were developed in collaboration with the University of Connecticut, compiling findings obtained during previous research stages. The document includes the design loads, methodology, stud capacity calculation, shear stud layout, and panel sizing.

Fan, Huang, and Negoita (2022) presented an example of the UHPC repair successfully implemented on the Sidney Sherman Bridge in Texas, which had complicated geometry and required bearing replacements in addition to corrosion on the girder ends. In this case, additional light reinforcement was installed inside the UHPC panels because of the expected high tensile forces and to ensure the safety of the repair. The uniqueness of the repair was that the UHPC panel acted as a jacking point to allow the replacement of the rocker bearing that experienced over-rotation and shearing off the anchor bolts.

Finally, the Federal Highway Administration featured a few examples of UHPC implementation for



Figure 2.7 Completed UHPC panels after formwork removal (Lassy et al., 2023).

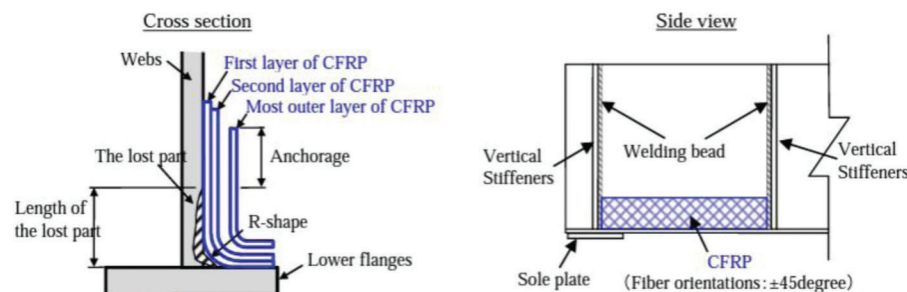


Figure 2.8 The details of the CFRP bonding method on the corroded webs (from Miyashita et al., 2015).

beam end repair conducted outside Connecticut (Haber et al., 2022). The repairs included the Masters Road-Belle River Bridge (MI), the Sidney Sherman Bridge (TX), and the interchange of Routes 6 and 10 (RI).

2.3.3 Beam End Repair Using Carbon Fiber-Reinforced Polymers (CFRP)

Zhao and Al-Mahaidi (2009) discussed the results of testing light steel beams that were strengthened using carbon fiber-reinforced polymer (CFRP) sheets and subjected to bearing loading. Overall, 21 specimens were tested that had different sizes, slenderness ratios, and strengthening methods: installation of CFRP plate on the inner side (Method 1), outer side (Method 2), or both inner and outer sides (Method 3). The most effective method was Method 3, which proposed the installation of CFRP plates on both sides of the beam web; the most significant capacity increase was observed for the slenderest beam. The authors proposed a formula to calculate the web buckling capacity of a strengthened beam based on the column design; however, the effective length factor k was reduced by two times.

Wakabayashi et al. (2012) performed a series of uniaxial compression tests on steel plates reinforced with fiber-reinforced plastics: high elasticity and high-strength carbon fibers, glass and hybrid fibers, high-strength polyethylene, and carbon fiber strand sheets. In addition, the effect of polyurea putty on the critical buckling load and failure mode was studied. FRP sheets with a lower modulus of elasticity exhibited better flexibility and performance. A more severe impact of polyurea putty application to prevent delamination was observed for stiffer FRP sheets with a higher modulus of elasticity. Finally, applying different types of FRP sheets was found to be beneficial to the overall performance of the reinforced steel plate compared to the case when the same layers were used (CSCU and 2CEU). The authors also developed a formula to predict the critical buckling load, giving accurate results with a 1.1%–7.1% error.

Ahn, Kainuma, Yasuo, and Takehiro (2013) presented the results of CFRP sheet application to repair corroded girder ends. Their study selected a highway plate girder bridge with 23.42 m (76.84 ft.) spans that experienced web corrosion and deterioration of bearing stiffeners. The corroded area was cleaned to achieve a good bond between the CFRP sheets and the girder. Furthermore, epoxy resin was applied to even out the surfaces. Multiple strain gauges were installed along the height of the girder web (four strain gauges) and a stiffener (two strain gauges) was used to monitor stresses. A truck test was conducted to measure stress ranges under the moving load, and the data before and after the repair were compared. Overall, improved behavior of the repaired girder was observed after the web and stiffeners were reinforced with CFRP sheets (fibers were oriented along the direction of maximum principal stresses). The successful experimental

evaluation of the novel repair application was followed by a finite element study to investigate the effect of corrosion on the residual capacity of the steel girder. It was found that for steel plate girders, the corrosion of stiffeners affects the residual capacity more severely than web corrosion.

Miyashita et al. (2015) described an application of CFRP sheets to recover the loading capacity of corroded girder ends. A polyurea putty layer was applied to prevent delamination of CFRP sheets from the girder surface under large deformations. CFRP sheets are widely used to restore the capacity of reinforced concrete beams and columns; however, their application to repair steel structures has not been widely studied. A transformation method was used to calculate the number of CFRP sheets required for repair. Two tests were performed on corroded girders with simulated section loss with and without through-web holes. The first compression test with vertically oriented CFRP fibers was conducted to prove the effectiveness of the repair. Once the recovery in load-carrying capacity was observed, the second shear test also exhibited a successful capacity recovery; however, in this case, the fibers were oriented at a 45° angle, accounting for the orientation of the shear stresses. Jagtap and Pore (2021) reported experimental and analytical results of strengthening corroded steel beams with two layers of CFRP laminates subjected to flexure. The experimental results showed a 90%–162% increase in load-carrying capacity (LCC) after the repair; however, because of severe corrosion, Beam-2 did not reach the LCC of an undamaged beam. However, good agreement between the FE model and the experimental data was achieved.

3. EVALUATION OF INNOVATIVE REPAIR METHODS

An assessment of novel repair strategies for corroded steel girder ends was performed, and at the end of the study, one repair method was selected for further development and experimental investigation (Tarasova et al., 2023). In the following subsections, five novel repair methods are briefly described. The repair methods include the following.

1. UHPC (ultra-high-performance concrete) beam end repair method.
2. Strengthening the corroded part with CFRP (carbon-fiber-reinforced polymer) sheets method.
3. Sandwich panel method.
4. Improved bolted angles method.
5. Web strengthening with diagonally oriented angles method.

3.1 Overview of Innovative Repair Methods

3.1.1 UHPC Beam End Repair

The first innovative repair method was developed by the research team at the University of Connecticut

(McMullen & Zaghi, 2020; Zmetra et al., 2017). The primary concept of the repair is to encase the corroded region in ultra-high-performance concrete that, after curing, restricts lateral displacements of the corroded region and prevents web local crippling failure. Headed studs need to be welded either to the web only or to both the girder's web and bottom flange to transfer the forces from the girder directly to UHPC panels, avoiding deteriorated web/flange areas. Shear studs also create a composite action between shear studs and concrete that helps to resist the shear and bearing forces. The test results showed that the loading capacity of the repaired girder successfully recovered and even surpassed its original design strength. The required steps to perform the repair could be summarized as follows.

1. Clean the steel girder end in the region where repair will be performed. Remove corrosion, paint, and debris. Grind regions ground smooth where studs will be welded.
2. Mark locations of shear studs and weld them using a stud welding gun (Figure 3.1).
3. Construct formwork from plywood and secure it using threaded bars to prepare for casting.
4. Pump UHPC to encase the corroded part.
5. Cure UHPC and disassemble the formwork (Figure 3.2).
6. Paint steel surfaces cleaned to prevent further deterioration of the girder end.

3.1.2 Strengthening the Corroded Part with CFRP Sheets

The second innovative repair method utilizes carbon-fiber-reinforced polymer (CFRP) sheets attached to the corroded region (Ahn et al., 2013; Jagtap & Pore, 2021; Miyashita et al., 2015). In this method, the steel

girder and multiple CFRP sheets resist the shear and bearing forces. The polyurea putty layer with a low modulus of elasticity is essential to prevent the delamination of CFRP sheets under large out-of-plane deformations and therefore must be installed first. Consequently, the loading capacity of the girder could exceed its original design capacity. However, removing the corrosion and paint is essential for good-quality bonding between the CFRP sheets and the girder. Strengthening corroded end with CFRP sheets repair is shown in Figure 3.3, and procedures can be summarized as follows.

1. Clean the surface for the CFRP sheet attachment. Remove corrosion, paint, and debris.
2. Apply multiple adhesion layers, including the primer layer and polyurea putty layer.
3. Attach the calculated number of CFRP sheets to the girder. CFRP laminates are attached using an adhesive made of resin and a hardener.
4. Cover the CFRP sheets with the protective layer and cure the entire system.

3.1.3 Sandwich Panel Repair Method

The third repair method, sandwich panel, has the central concept of providing lateral restraint and preventing web buckling by pouring infill material between two steel plates/sheets (Tarasova et al., 2023). Applying bent steel corrosion-resistant sheets/plates removes the requirement for formwork construction and reduces the repair time. In this method, load transfers from the web to the infill material directly through threaded rods that function as shear connectors (Figure 3.4 and Figure 3.5). Hence, threaded rods create an alternate load path for shear forces in the web of the girder. Also, there are multiple options for infill

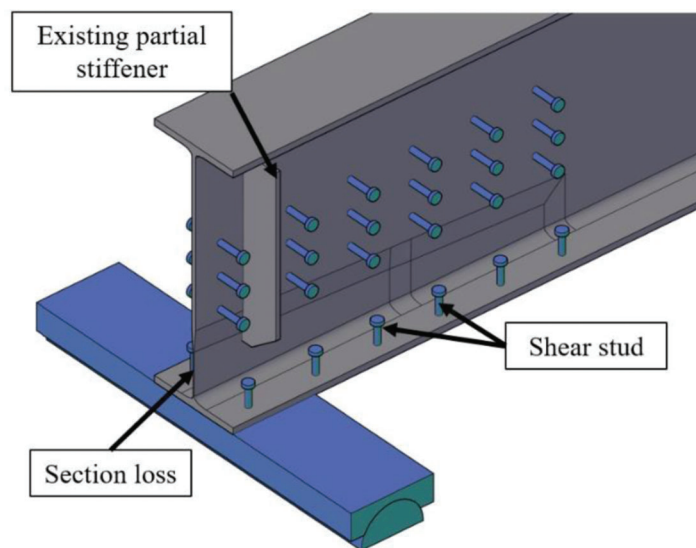


Figure 3.1 Corroded girder after shear studs welding.

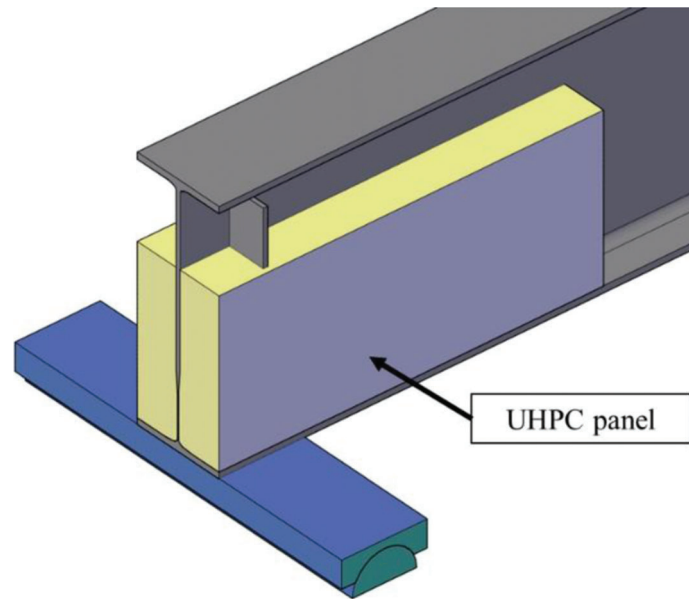


Figure 3.2 Repaired girder after UHPC curing and disassembling the formwork.

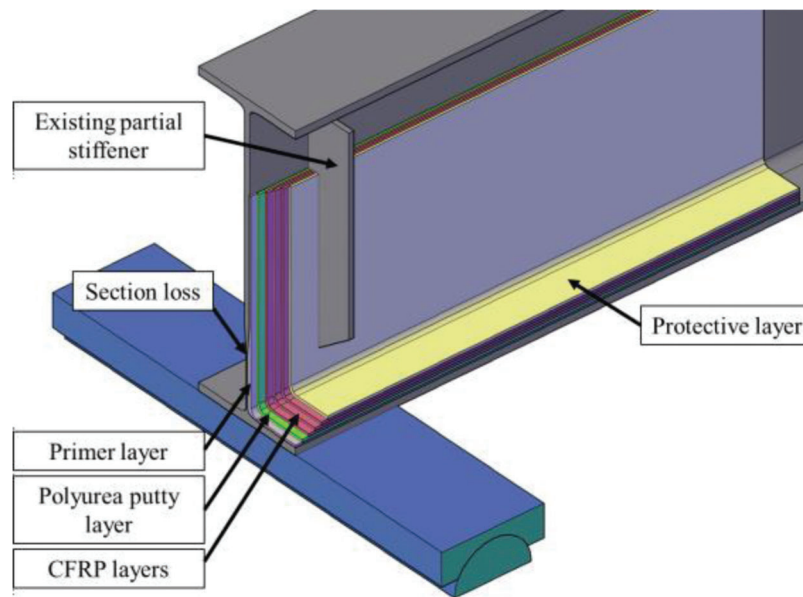


Figure 3.3 Strengthening the corroded part with CFRP sheets.

material: conventional cementitious grout, polyester polymer concrete (PPC), or ultra-high-performance concrete (UHPC). Concisely, the repair procedure could be summarized as follows.

1. Clean the surface of corrosion and debris. Removal of paint is not required.
2. Drill holes in the girder web and steel plates/sheets.
3. Install steel plates/sheets and threaded rods. Utilizing corrosion-resistant threaded rods and steel plates/sheets is recommended to prevent corrosion.
4. Cast the infill material between the steel plates and the girder web.
5. Cure infill material until it reaches design compressive strength.

3.1.4 Improved Bolted Angles Method

The fourth repair strategy, the improved bolted angles method, is developed on the traditional repair method of bolting steel plates and angles to the deteriorated region to strengthen the web and increase the bearing strength of the girder (FDOT, 2018; GDOT, 2012; IDOT, 2017). Typically, the main disadvantage of the conventional repair method is the

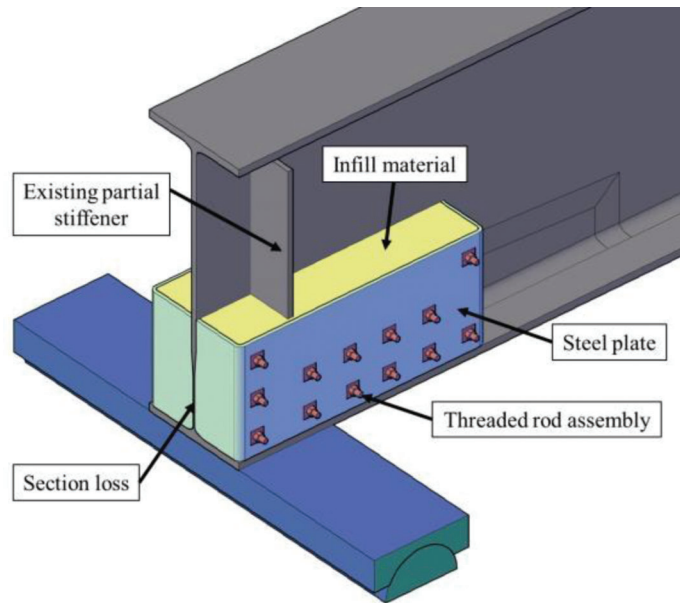


Figure 3.4 Sandwich panel repair method (isometric view).

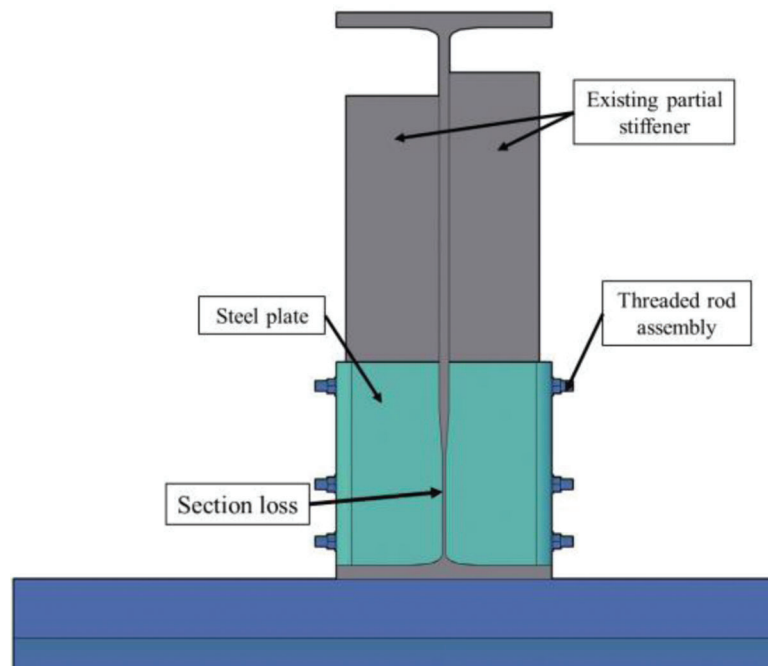


Figure 3.5 Sandwich panel repair method (front view).

presence of gaps that accumulate moisture and facilitate corrosion propagation. By applying high-viscosity epoxy resin and sealing the gaps between steel angles and a corroded girder web, the durability of the conventional repair method could be significantly enhanced (Figure 3.6 and Figure 3.7). However, proper surface preparation is necessary for an adequate bond between the steel surface and epoxy resin. The repair procedures could be listed as follows.

1. Clean the surface from paint, corrosion, and debris and prepare it for epoxy resin application.
2. Drill holes in the girder web using a magnetic drill and a prefabricated template.
3. Brush the epoxy resin on the corroded region to get a flat and smooth surface.
4. Attach angle sections and steel plates to the web and flange using bolts. The application of corrosion-resistant bolts and steel plates/angles is recommended to prevent further deterioration of newly installed members.

3.1.5 Web Strengthening with Diagonally Oriented Angles

Finally, in the fifth repair method, angle sections are bolted to both sides of the girder web parallel to the direction of the compression diagonal (Figure 3.8 and Figure 3.9). Within the corroded area, the spacing of bolts is reduced to ensure the load transfer between the girder web and the steel angle. This repair method is built upon the conventional process of strengthening the corroded region with steel angles and bolts (FDOT, 2018; GDOT, 2012; IDOT, 2017). The repair method is recommended for application on stiffened girders where the shear buckling failure is expected due to web thickness reduction. Installation of the angle sections parallel to the compression diagonal contributes to additional stiffness, preventing shear buckling failure. For unstiffened girders that do not have full depth bearing stiffeners, web crippling would usually govern. However, the proposed repair method only increases the shear strength

without substantially improving the girder's bearing capacity. The repair procedures could be summarized as follows.

1. Clean the surface of corrosion and debris.
2. Mark the location and drill holes in the girder web using a magnetic drill.
3. Paint the region that was previously cleaned to avoid further deterioration.
4. Install angle sections and bolt them. Utilizing corrosion-resistant bolts and angle sections is recommended to avoid painting and corrosion of newly installed steel members.

3.2 Evaluation Method: House of Quality Matrix

House of Quality Matrix (HQM) was used to determine the optimal repair method for steel girder bridges. House of Quality Matrix is part of a more extensive process called Quality Function Deployment

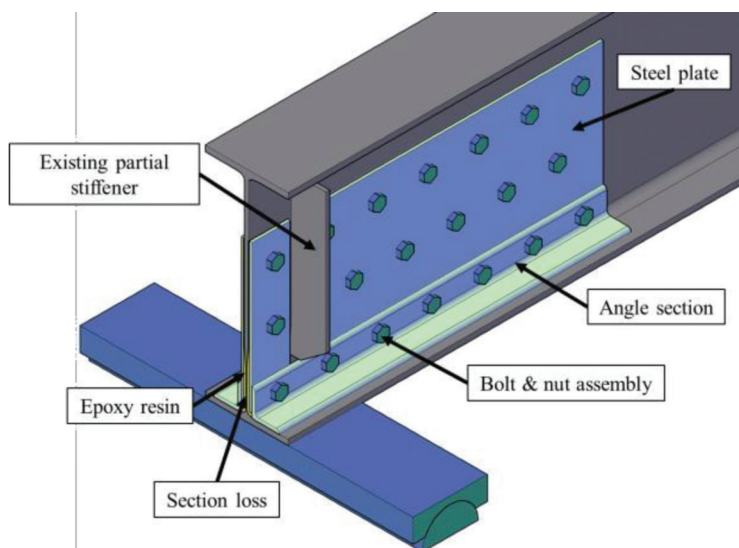


Figure 3.6 Improved bolted angles method (isometric view).

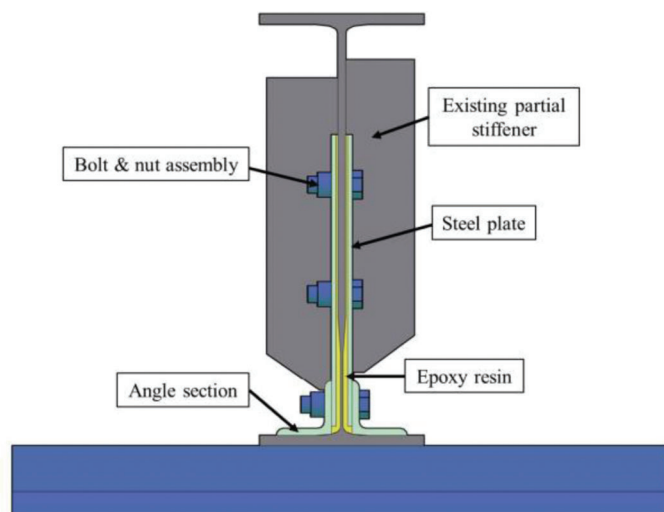


Figure 3.7 Improved bolted angles method (front view).

(QFD), a commonly used way of improving the design of products and services per customer needs (Hauser et al., 2010; Wheelwright & Clark, 1992). This type of cause-and-result analysis was developed in Japan in the 1960s. QFD was then brought to the United States approximately 20 years later. It gained early popularity due to numerous successes in the automobile industry. In QFD, customer satisfaction with a product/service can be measured by quality. QFD begins with developing the initial matrix, called the House of Quality Matrix, that visually resembles a house.

A House of Quality Matrix is a diagram that helps to determine how closely a product satisfies customer requirements. It is a process of getting feedback from customers, converting their requirements into a written plan, and prioritizing execution steps based on what is the most important to the client. A House of Quality Matrix is a six-step process.

1. Identify what the customer needs (requirements set by INDOT).
2. Identify how the product will satisfy the customer (proposed innovative repair methods).
3. Identify relationships between “how” and customers’ needs.
4. Develop importance ratings.
5. Assess competing products/services.
6. Define the desirable technical attributes.

In this study, Step 5 and Step 6 were eliminated since the primary purpose was to identify one innovative repair strategy for steel bridge girders repair. In this process, the local Department of Transportation in Indiana was a customer; innovative repair methods were the potential products, and finally, requirements were the customer’s needs. Each requirement also had a corresponding importance rating.

3.2.1 Requirements

The first step to assembling a House of Quality Matrix is identifying the customer’s requirements. In this study, the customer was the Indiana Department of Transportation (INDOT). Two meetings were held in Crawfordsville and Greenfield districts to collect feedback from the INDOT maintenance personnel regarding essential requirements for the repair. The requirements specified by the customer were categorized into four groups: capacity and durability, cost-effectiveness, construction applicability and time, and others (Table 3.1). For each category, additional subcategories were identified. For example, the capacity and durability category had four subcategories: loading capacity, corrosion prevention, and behavior under low temperatures.

A prioritization process was completed to determine the basic requirements once the customer’s needs were identified. In Table 3.2 a detailed explanation of every requirement is provided. For example, the loading capacity requirement was fully met only when the repaired girder’s strength reached (or exceeded) the original design capacity.

3.2.2 Importance Level and Severity Rate

The importance level was determined for every requirement to assess and rate each customer’s demand accurately. The importance level was assigned to every requirement based on input from the local DOT (Table 3.3). Accordingly, the “high” importance level had a severity rate of 9, “medium” had a severity rate of 6, and “low” had a severity rate of 3.

The “high” importance level was assigned to loading capacity, welding, and construction time because these requirements are the most necessary requirements for

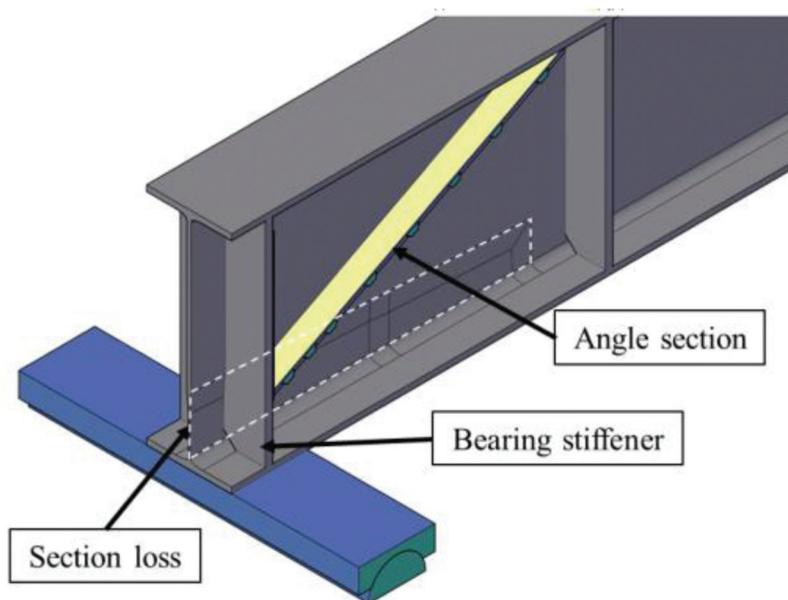


Figure 3.8 Web strengthening with diagonally oriented angles (isometric view).

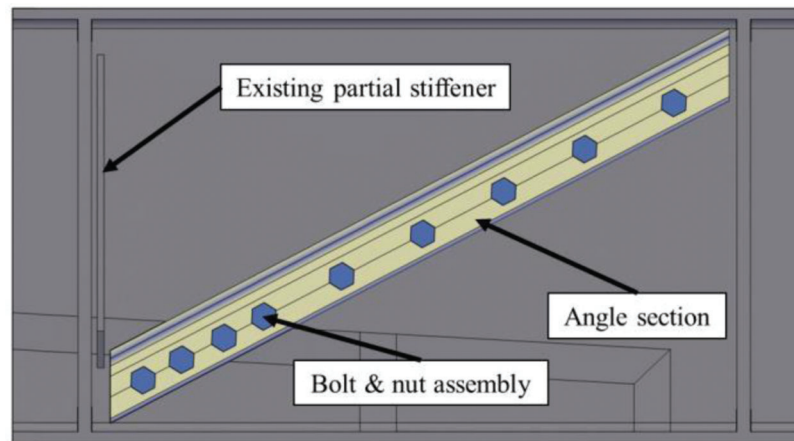


Figure 3.9 Web strengthening with diagonally oriented angles (side view).

TABLE 3.1
Requirements set by the customer

Category	Requirements
Capacity and Durability	Loading capacity Corrosion prevention Behavior under low temperature
Cost-Effectiveness	Material Fabrication and construction
Construction Applicability and Time	Jacking of the structure Corrosion removal Paint removal Drilling and bolting Welding Formwork construction Concrete or grout casting Construction time
Others	Adaptability in design Technology maturity

designing the repair method and have the ultimate impact. the “medium” importance level was assigned to corrosion prevention, behavior under low temperatures, material, fabrication, and construction, jacking of the structure, corrosion removal, paint removal, formwork construction, adaptability in design, and technology maturity because their effect on cost and schedule is less critical. The “low” importance level was assigned to drilling and bolting and concrete/grout casting since they have the most negligible impact on the design of the repair method.

3.2.3 Performance Level

The correlation between customer demands (requirements) and the product (innovative repair methods) was determined using a specific factor called performance level. The performance level factor had three levels: strong, medium, and weak, with weight factors of 9, 3, and 1, respectively. “Strong” indicates a solid relationship (weight factor of 9), and “medium” highlights a standard relationship (weight factor of 3). Finally, “weak” was given

to the poor relationship between a demand set by the customer and the product (weight factor of 1).

3.2.4 Results and Discussion

The complete correlation between requirements and five novel repair methods based on input from local DOT is presented in the following section. The five repair methods were evaluated on 15 requirements, from loading capacity to technology maturity. The findings are presented in Table A.1 through Table A.5.

3.2.4.1 Calculation of importance factors. The product of the severity rate and weight factor was computed to calculate absolute and relative importance factors. For example, the absolute importance factor for the sandwich panel repair method was calculated following an approach presented in Table 3.4. The loading capacity had a severity rate of 9 and a “strong” relationship with the sandwich panel repair method because, after the repair, the loading capacity was fully recovered. “Strong” performance level had a weight factor of 9;

TABLE 3.2
Definitions of the novel repair method requirements

Requirement	Description
Loading Capacity	The repaired girder's loading-carrying capacity equals or exceeds its original design capacity.
Corrosion Prevention	The corrosion propagation in the repaired specimen is prevented.
Behavior Under Low Temperature	The performance of the repaired girder under low temperatures is like that under average temperatures.
Material	Materials used for repair are reasonably priced and commercially available.
Fabrication and Construction	Prefabricated structural elements and an economic fabrication process are used to accelerate the construction.
Jacking of the Structure	Jacking the structure and providing alternative support during the repair is unnecessary.
Corrosion Removal	The removal of existing corrosion to prepare the surface is optional.
Paint Removal	Existing paint (especially lead paint) does not have to be removed as a part of the surface preparation process.
Drilling and Bolting	Drilling and bolting work in the repair is not required.
Welding	Hot work (such as welding) is not necessary for repair implementation.
Formwork Construction	Formwork assembly is not required.
Concrete or Grout Casting	No concrete/grout casting is associated with the repair.
Construction Time	The overall traffic closure time is minimized.
Adaptability in Design	Reference materials for the repair design, material standards, and design specifications exist that could be used.
Technology Maturity	The procedures and repair guidelines are in Department of Transportation reports or maintenance manuals.

TABLE 3.3
Requirements, importance levels, and severity rates

Requirements	Importance Level	Severity Rate
Loading Capacity	High	9
Corrosion Prevention	Medium	6
Behavior Under Low Temperature	Medium	6
Material	Medium	6
Fabrication and Construction	Medium	6
Jacking of the Structure	Medium	6
Corrosion Removal	Medium	6
Paint Removal	Medium	6
Drilling and Bolting	Low	3
Welding	High	9
Formwork Construction	Medium	6
Concrete or Grout Casting	Low	3
Construction Time	High	9
Adaptability in Design	Medium	6
Technology Maturity	Medium	6

therefore, their product was equal to 81. Following the same approach for every requirement, the value of 591 points for the absolute importance factor was calculated.

Similar calculations were performed for all five innovative repair methods, and the results are presented in Table 3.5. The values of the absolute importance

factors for all five innovative repair methods were added to get a total absolute importance factor of 2,481 points. The value of the absolute importance factor for each innovative repair method was then divided by the total absolute importance factor to obtain the relative importance factor.

3.2.5 Conclusions

Overall, the House of Quality Matrix is a powerful tool when meeting customers' requirements and choosing among multiple products is crucial. This study considered different repair methods: UHPC beam end repair, strengthening the corroded part with CFRP, sandwich panel, improved bolted angles, and web strengthening with diagonally oriented angles. The Quality Function Deployment process showed its effectiveness, and among the five methods mentioned above, the sandwich panel repair idea was chosen for further development. As a result, the sandwich panel repair method had the highest relative importance factor of 23.82% among the five discussed repair methods. Therefore, the sandwich panel repair method was selected for further experimental and numerical investigation to evaluate the structural robustness of the proposed novel repair method.

TABLE 3.4
Calculation of absolute importance factor for the sandwich panel repair method

Requirement		Severity Rate	Sandwich Panel Repair Method	Weight Factor	Product
Capacity and Durability	Loading capacity	9	Strong	9	= 81
	Corrosion prevention	6	Strong	9	= 81
	Behavior under low temperature	6	Strong	9	= 54
Cost-Effectiveness	Material	6	Strong	9	= 54
	Fabrication and construction	6	Medium	3	= 18
Construction Applicability and Time	Jacking of the structure	6	Strong	9	= 54
	Corrosion removal	6	Medium	3	= 18
	Paint removal	6	Strong	9	= 54
	Drilling and bolting	3	Weak	1	= 3
	Welding	9	Strong	9	= 81
	Formwork construction	6	Strong	9	= 54
	Concrete or grout casting	3	Weak	1	= 3
	Construction time	9	Medium	3	= 27
Others	Adaptability in design	6	Medium	3	= 18
	Technology maturity	6	Medium	3	= 18
Absolute Importance Factor					= 591

TABLE 3.5
Final assessment of innovative repair methods using the House of Quality Matrix

Requirement/Severity Rate		UHPC Beam End Repair	Strengthening the Corroded Part with CFRP	Sandwich Panel	Improved Bolted Angles	Web Strengthening with Diagonally Oriented Angles
Loading Capacity	9	Strong	Medium	Strong	Strong	Medium
Corrosion Prevention	6	Strong	Strong	Strong	Medium	Weak
Behavior Under Low Temperature	6	Medium	Medium	Strong	Strong	Medium
Material	6	Medium	Weak	Strong	Medium	Strong
Fabrication and Construction	6	Medium	Medium	Medium	Medium	Strong
Jacking of the Structure	6	Strong	Strong	Strong	Strong	Strong
Corrosion Removal	6	Medium	Weak	Medium	Medium	Medium
Paint Removal	6	Medium	Weak	Strong	Weak	Strong
Drilling and Bolting	3	Strong	Strong	Weak	Weak	Weak
Welding	9	Medium	Strong	Strong	Strong	Strong
Formwork Construction	6	Weak	Strong	Strong	Strong	Strong
Concrete or Grout Casting	3	Weak	Strong	Weak	Strong	Strong
Construction Time	9	Medium	Weak	Medium	Medium	Strong
Adaptability in Design	6	Medium	Medium	Medium	Medium	Medium
Technology Maturity	6	Medium	Medium	Medium	Medium	Medium
Absolute Importance Factor	2,481	405	423	591	495	567
Relative Importance Factor	100%	16.32%	17.05%	23.82%	19.95%	22.85%

4. MATERIAL TESTING

The experimental program for this study consisted of material-level testing and member-level testing. The material level testing included the examination of potential filler materials that could be used for the sandwich panel repair method. Parameters such as flowability, working time, setting time, compressive strength, modulus of elasticity, and price were collected

during the experimental testing. The obtained data was further used to perform the evaluation using the House of Quality Matrix tool and select only two filler materials out of seven that were tested in the laboratory conditions.

The member-level testing consisted of structural robustness evaluation of repaired specimens using the sandwich panel method with filler materials that were selected in Chapter 4. In the following subsections of Chapter 4 only material level testing was discussed.

4.1 Material Level Testing (Phase I)

The material-level testing program consisted of two phases (Phase I and Phase II). In Phase I (Section 4.1), material testing was performed to examine the material's flowability (ASTM, 2020; 2021c; 2022c), compressive strength (ASTM, 2021a; 2021b) and modulus of elasticity (ASTM, 2022c). Seven potential infill materials were tested in Phase I to evaluate their applicability to the sandwich panel repair method. The materials discussed in the following subsections included four cementitious grouts (NS Grout, Hi-Flow Grout, Tammsgrout Supreme, Hybrid Grout), two polymer-based structural concretes (HCSC and PPC-1121) produced by Kwik Bond Polymers, and, finally, premixed ultra-high-performance concrete produced by Steelike.

To examine the material's flowability following standards were used.

- Cementitious grouts that have fluid consistency (efflux time less than 35 seconds): *ASTM C939/C939M-22: Standard Test Method for Flow of Grout for Preplaced-Aggregate Concrete (Flow Cone Method)*.
- UHPC and cementitious grouts that have flowable consistency (efflux time more than 35 seconds): *ASTM C1437-20: Standard Test Method for Flow of Hydraulic Cement Mortar*.
- For polymer-based concretes: *ASTM C1611/C1611M-21: Standard Test Method for Slump Flow of Self-Consolidating Concrete*.

The material's compressive strength was determined using the following standards.

- For cementitious grouts: *ASTM C109/C109M-21: Standard Test Method for Compressive Strength of Hydraulic Cement Mortars* (using 2-in. or 50-mm cube specimens).
- For polymer-based concretes and UHPC: *ASTM C39/C39M-21: Standard Test Method for Compressive Strength of Cylindrical Concrete Specimens*.

4.1.1 Cementitious Grouts

4.1.1.1 Euclid Chemical NS Grout. NS Grout produced by Euclid Chemical is a non-shrink, non-staining, non-metallic grout that is highly flowable and gains at least 3.5 ksi strength in 3 days. One of the criteria for an infill material was its superb flowability as bridges have complicated geometry, and filling all gaps to prevent potential corrosion is vital.

4.1.1.1.1 Mixing procedures. The mixing procedures for NS Grout were simple, and instructions provided in a technical data sheet (TDS) were followed (Euclid Chemical, n.d.b). Due to the small quantities of material required, a shear mixing paddle attached to a heavy-duty power drill was utilized to mix grout in a 5-gal. bucket. Depending on the consistency (plastic, flowable, or fluid), the amount of water per 55-lb. bag varies from 0.88 gal. to 1.3 gal. according to provisions

in the TDS. It is recommended to reach at least flowable consistency when mixing grout for application in sandwich panel repair; otherwise, the flowability requirements set by the repair method will not be met. A larger water/cement ratio contributes to a longer workable time but might cause grout bleeding.

4.1.1.1.2 Flow rate test (ASTM C939). The first material test that was performed right after mixing was a flow cone test following provisions of ASTM C939 (ASTM, 2022c) to ensure no bleeding or segregation (Figure 4.1). TDS states the minimum efflux time of 20 seconds to guarantee no bleeding. The upper limit on the efflux time was equal to 35 seconds. In the following series of material tests, the fluid consistency of grout was targeted, however, the flowable consistency was also accepted. The average efflux time was found to be 29.8 seconds, and therefore, the mix was accepted for casting cube (compressive strength test) and cylinder (modulus of elasticity test) specimens (Figure 4.2).

4.1.1.1.3 Compressive strength test (ASTM C109). To determine the compressive strength of NS Grout in 1, 3, and 7 days, 2-in. cube specimens were tested according to ASTM C109 (ASTM, 2021b). The maximum permissible range was 8.7% of the average compressive strength of the three same-age specimens. The values outside the permitted range were termed outliers and were not considered in an average strength calculation. However, a minimum of two cubes was required to calculate the average strength.

The cubes were dry-cured at a normal ambient temperature, and the failure modes of 2 × 2" NS Grout



Figure 4.1 Flow cone with 0.5" orifice.



Figure 4.2 Bronze and plastic molds for 2×2" cubes and plastic molds for 4×8" cylinders.



Figure 4.4 Cube NS-1.2 $f'_c = 3,273$ psi.



Figure 4.3 Cube NS-1.1 $f'_c = 3,362$ psi.

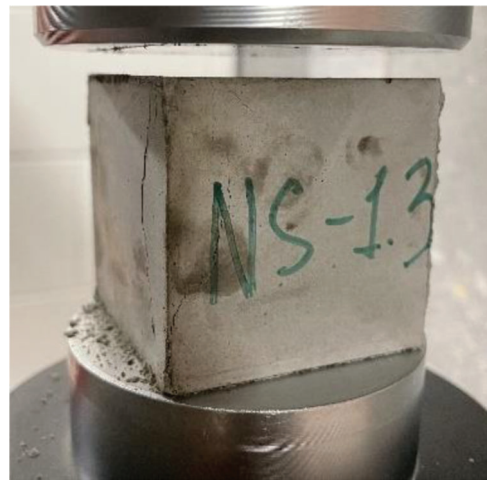


Figure 4.5 Cube NS-1.3 $f'_c = 3,464$ psi.

specimens after 24 hours of cure are shown in Figures 4.3, 4.4, and 4.5. The dry curing was selected for the simplicity of the sandwich panel repair application in the field, as it would be complicated to ensure wet curing conditions. However, it was found that all specimens reached the compressive strength specified in the technical data sheet for the fluid consistency of NS Grout.

The strength gain over time is shown in Figure 4.6, and it can be observed that the fastest rate of strength gain was recorded over the first day of curing (3.37 ksi/day) after the rate slowed down to 0.45 ksi/day.

4.1.1.1.4 Modulus of elasticity test (ASTM C469). The modulus of elasticity of grout was not provided in TDS; therefore, an additional test was

performed due to necessity of the Young's modulus for the development of a material model for the finite element simulations. According to ASTM C469 (ASTM, 2022b), the 4×8" cylinder must be loaded to only 40% of the ultimate compressive strength (f'_c) to remain in the elastic response range and prevent sensor damage (Figure 4.7). The Forney compression testing machine performed three elastic cycles to measure the average MOE = 3,050 ksi after a 7-day curing time (Figure 4.8). The modulus of elasticity is also a function of time, and therefore, it increases with curing time, resulting in a more brittle behavior. The results of the material testing, including ultimate compressive strength, flowability, and other properties such as working and setting time, and the cost per cubic feet as of 06/2022, are presented in Table 4.1.

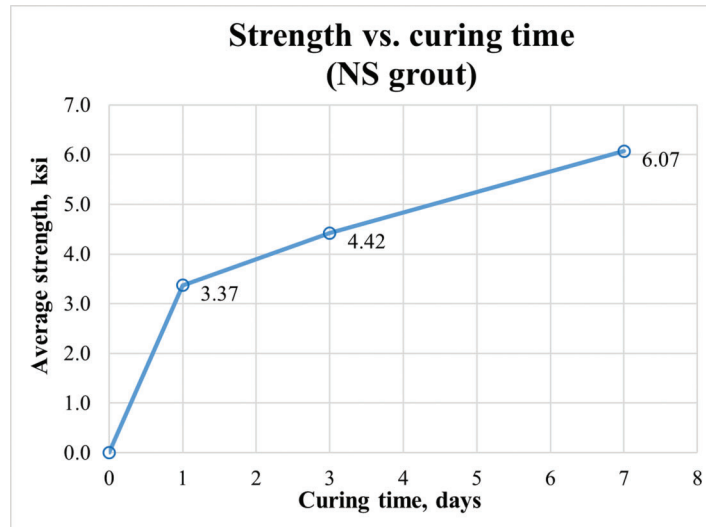


Figure 4.6 Strength gain over time for NS Grout (fluid consistency).



Figure 4.7 Modulus of elasticity test: test setup.

4.1.1.2 Euclid Chemical Tammsgrout Supreme Grout. Tammsgrout Supreme Grout, produced by Euclid Chemical, is a non-shrink, high-strength grout that is highly flowable and gains at least 5 ksi strength in 3 days. Tammsgrout Supreme does not contain any

chlorides or additives that might cause corrosion of the base structure.

4.1.1.2.1 Mixing procedures. The mixing procedures for Tammsgrout Supreme Grout were simple, and instructions provided in a technical data sheet (TDS) were followed (Euclid Chemical, n.d.c). Due to the small quantities of material required, a shear mixing paddle attached to a heavy-duty power drill was utilized to mix grout in a 5-gal. bucket. Depending on the consistency (plastic, flowable, or fluid), the amount of water per 55-lb. bag varied from 0.7 gal. to 1.1 gal.

4.1.1.2.2 Flow rate test (ASTM C939). The first material test performed right after mixing was a flow cone test following ASTM C939 (ASTM, 2022c) standard provisions to ensure no bleeding or segregation. TDS states the minimum efflux time to be 20 seconds for fluid consistency to ensure no bleeding. The upper limit on the efflux time was set by ASTM C939 (ASTM, 2022c) and is equal to 35 seconds. A flow cone test yielded an efflux time of 53.22 seconds, which exceeded the maximum efflux time by 52%. The potential reasons for increased efflux time were improper cleaning of the flow cone or insufficient amount of water in the mix, which decreased its flowability. However, no segregation or bleeding was observed, and the mix was accepted for casting cube (compressive strength test) and cylinder (modulus of elasticity test) specimens.

4.1.1.2.3 Compressive strength test (ASTM C109). To determine the compressive strength of Tammsgrout Supreme Grout in 1, 3, and 7 days according to ASTM C109 (ASTM, 2021b), 2-in. cube specimens were tested. The maximum permissible range was 8.7% of the average strength of the three specimens tested at the same age. The values outside the permitted range were

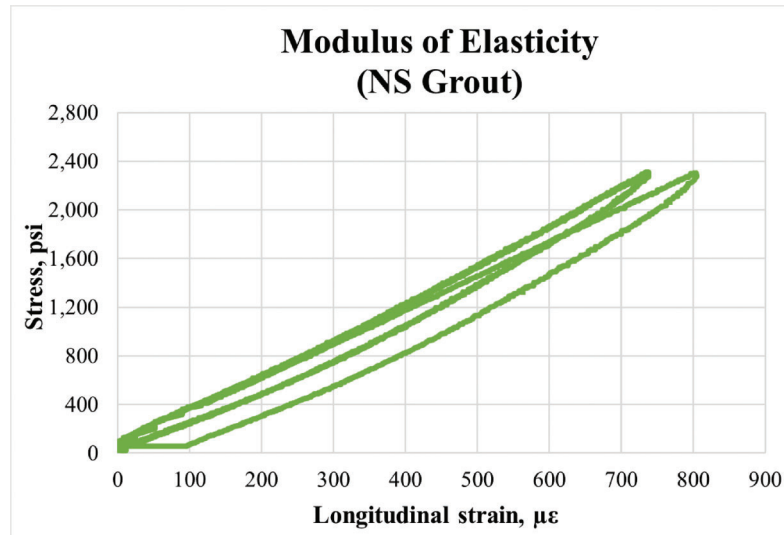


Figure 4.8 Modulus of elasticity test results for NS Grout (7-day curing time).

TABLE 4.1
Properties of NS Grout produced by Euclid Chemical

Properties	Value	Source
Flow Test	29.8 sec	Test, ASTM C939
Working time	15 min	TDS
Initial Set Time	3–5 hours	TDS
Final Set Time	4–6 hours	TDS
f'_c (1 Day)	3.37 ksi	Test, ASTM C109
f'_c (3 Days)	4.42 ksi	Test, ASTM C109
f'_c (7 Days)	6.07 ksi	Test, ASTM C109
MOE (7 Days)	3,050 ksi	Test, ASTM C469
Price (on 6/2022)	66.67 \$/ft ³	JK supply quote

named outliers and were not considered in an average strength calculation. However, a minimum of two cubes was required to calculate the average strength.

The cubes were dry-cured at an ambient temperature, and the failure modes of 2 × 2" Tammsgrout Supreme Grout specimens tested within 24 hours of curing are shown in Figures 4.9, 4.10, and 4.11. The dry curing was selected for the simplicity of the sandwich panel repair application in the field, as it would be complicated to ensure wet curing conditions. However, it was found that all specimens reached at least 95% of the compressive strength specified in the technical data sheet for Tammsgrout Supreme Grout (fluid consistency). The strength gain over time is shown in Figure 4.12, and it can be observed that the fastest rate of strength gain was recorded over the first day of curing (4.77 ksi/day). After that, the rate slowed to 1.22 ksi/day and 0.36 ksi/day for a 3-day and 7-day cure, respectively.

4.1.1.2.4 Modulus of elasticity test (ASTM C469). The modulus of elasticity of grout was not provided in the technical data sheet (TDS); therefore, an additional test in the Bowen Laboratory was

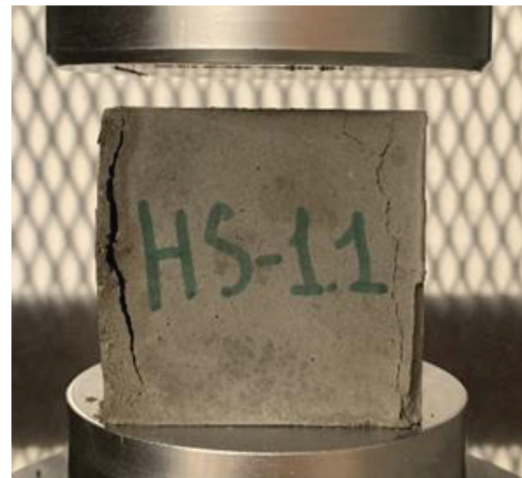


Figure 4.9 Cube HS-1.1 f'_c = 4,756 psi.

performed. According to ASTM C469 (ASTM, 2022b), the 4 × 8" cylinder must be loaded to 40% of the ultimate strength to remain in the elastic response range and avoid cracking that would damage the sensors (Figure 4.7). The Forney compression testing machine performed three elastic cycles to measure the average MOE = 3,450 ksi after 8 days of cure (Figure 4.13). The results of the material testing, including ultimate compressive strength, flowability, and other properties such as working and setting time, and the cost as of 06/2022, are presented in Table 4.2.

4.1.1.3 Euclid Chemical Hi-Flow Grout. Hi-Flow Grout produced by Euclid Chemical is a non-shrink, high-tolerance grout that is highly flowable and gains at least 3 ksi strength in 3 days. It provides consistent and exacting performance in grouting operations that are highly important.

4.1.1.3.1 Mixing procedures. The mixing procedures for Hi-Flow Grout were simple, and the instructions provided in TDS were followed (Euclid Chemical, n.d.a). Due to the small quantities of material required, a shear mixing paddle attached to a heavy-duty power drill was utilized to mix grout in a 5-gal. bucket. Depending on the consistency (plastic, flowable, or fluid), the amount of water per 50-lb. bag varies from 0.8 gal. to 1.2 gal.

4.1.1.3.2 Flow rate test (ASTM C939). The first material test performed right after mixing was a flow cone test following ASTM C939 (ASTM, 2022c) to ensure no bleeding or segregation. Technical data sheet (TDS) states the minimum efflux time should be 20 seconds to ensure no bleeding. The upper limit on

the efflux time was equal to 35 seconds. In the following series of material tests, the fluid consistency of grout was targeted. The average efflux time was 33.12 seconds, and therefore, the mix was accepted for casting cube (compressive strength test) and cylinder (modulus of elasticity test) specimens. The Hi-Flow Grout has the most extensive working time compared to other cementitious grouts, equal to 60 minutes. Based on the information in TDS, the grout mix should pass the flow cone test even 60 minutes after mixing was completed.

4.1.1.3.3 Compressive strength test (ASTM C109). To determine the compressive strength of Hi-Flow Grout in 1, 4, and 7 days according to ASTM



Figure 4.10 Cube HS-1.2 $f'_c = 4,768$ psi.

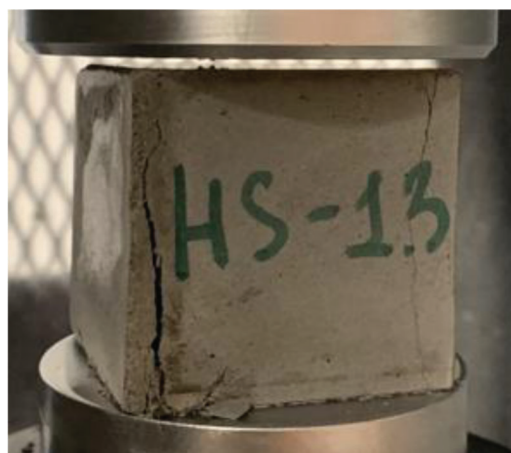


Figure 4.11 Cube HS-1.3 $f'_c = 4,792$ psi.

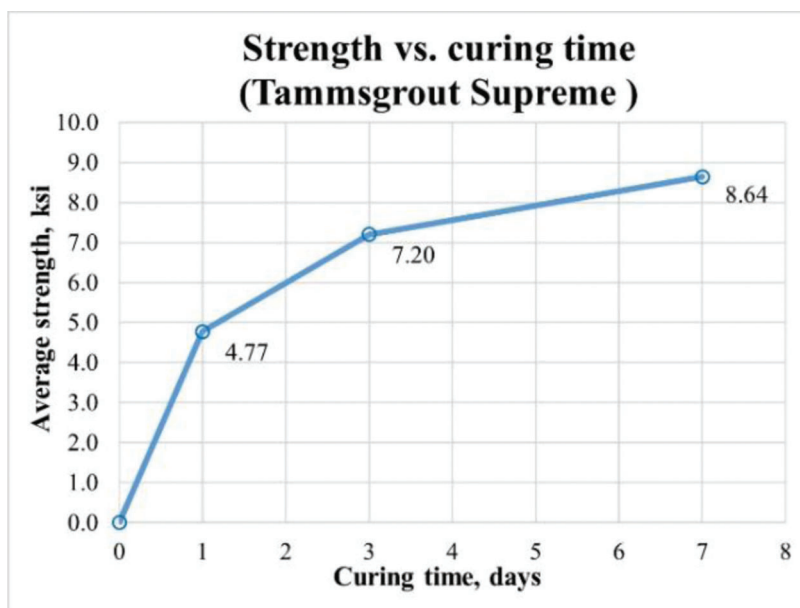


Figure 4.12 Strength gain over time for TammsgROUT Supreme (fluid consistency).

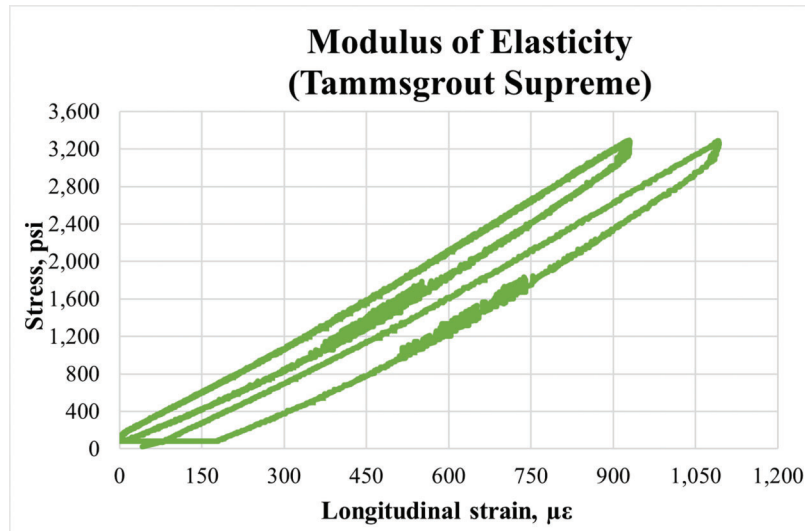


Figure 4.13 Modulus of elasticity test for TammsgROUT Supreme (8-day curing time).

TABLE 4.2
Properties of TammsgROUT Supreme Grout produced by Euclid Chemical

Properties	Value	Source
Flow Test	53.22 sec	Test, ASTM C939
Working Time	15 min	TDS
Initial Set Time	5 hours	TDS
Final Set Time	7 hours	TDS
f'_c (1 Day)	4.77 ksi	Test, ASTM C109
f'_c (3 Days)	7.20 ksi	Test, ASTM C109
f'_c (7 Days)	8.64 ksi	Test, ASTM C109
MOE (8 Days)	3,450 ksi	Test, ASTM C469
Price (on 6/2022)	82.44 \$/ft ³	JK supply quote

C109 (ASTM, 2021b), 2-in. cube specimens were tested. The maximum permissible range was 8.7% of the average strength of the three cube specimens tested at the same age. The values outside the permitted range were named outliers and were not considered in an average strength calculation. However, a minimum of two cubes was required to calculate the average strength.

The cubes were dry-cured at an ambient temperature, and the failure modes of 2 × 2" Hi-Flow Grout specimens tested within 24 hours of curing are shown in Figures 4.14, 4.15, and 4.16. The dry curing was selected for the simplicity of the sandwich panel repair application in the field, as it would be complicated to ensure wet curing conditions. However, the dry-cured specimens reached the compressive strength specified in TDS for the fluid consistency of Hi-Flow Grout.

The strength gain over time is shown in Figure 4.17, and it can be observed that the fastest rate of strength gain was recorded during the first day of curing (3.34 ksi/day) after the rate slowed down to 0.73



Figure 4.14 Cube HF-1.1 f'_c = 3,438 psi.

ksi/day and 0.11 ksi/day for a 4-day and 7-day cure, respectively.

4.1.1.3.4 Modulus of elasticity test (ASTM C469). The Hi-Flow Grout's modulus of elasticity (MOE) was not provided in the technical data sheet (TDS); therefore, an additional test was performed. According to ASTM C469 (ASTM, 2022b), the 4 × 8" cylinder must be loaded to 40% of the ultimate strength to remain in the elastic response range and avoid cracking that would damage the sensors (Figure 4.7). The Forney compression testing machine performed three elastic cycles to measure the average MOE = 2,900 ksi after 35-day curing time (Figure 4.18). The modulus of elasticity is also a function of time, and therefore, it increases with curing time, resulting in a more brittle behavior. The results of the material



Figure 4.15 Cube HF-1.2 $f'_c = 3,508$ psi.



Figure 4.16 Cube HF-1.3 $f'_c = 3,363$ psi.

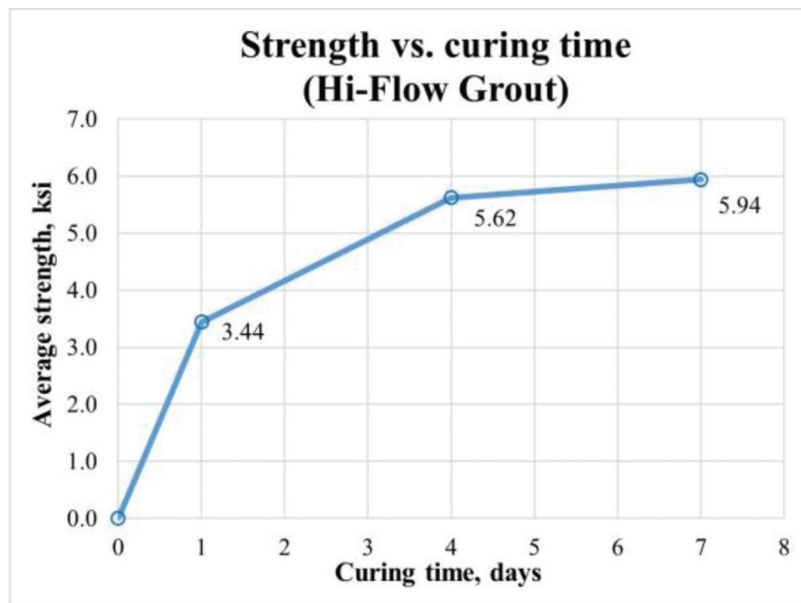


Figure 4.17 Strength gain over time for Hi-Flow Grout (fluid consistency).

testing, including ultimate compressive strength, flowability, and other properties such as working and setting time, and the cost as of 06/2022, are presented in Table 4.3.

4.1.1.4 Five-Star Hybrid Grout. Hybrid Grout produced by Five Star Products is a non-shrink, non-metallic grout highly flowable that gains at least 4 ksi strength in 8 hours when cured at average temperatures (72°F). One of the criteria for an infill material was its superb flowability because bridges have complex geometry, and filling all gaps to prevent future

corrosion is paramount. Hybrid Grout can be easily poured using buckets or pumped.

4.1.1.4.1 Mixing procedures. The mixing procedures for Hybrid Grout were more complicated, and instructions provided in a technical data sheet (TDS) were followed (Five Star Products, n.d.). Due to the small quantities of material required, a shear mixing paddle attached to a heavy-duty power drill was utilized to mix grout in a 5-gal. bucket. The amount of water can vary from 6.9 lb. to 7.5 lb. per 45-lb. bag with a maximum water/cement ratio of 0.17 to reach a

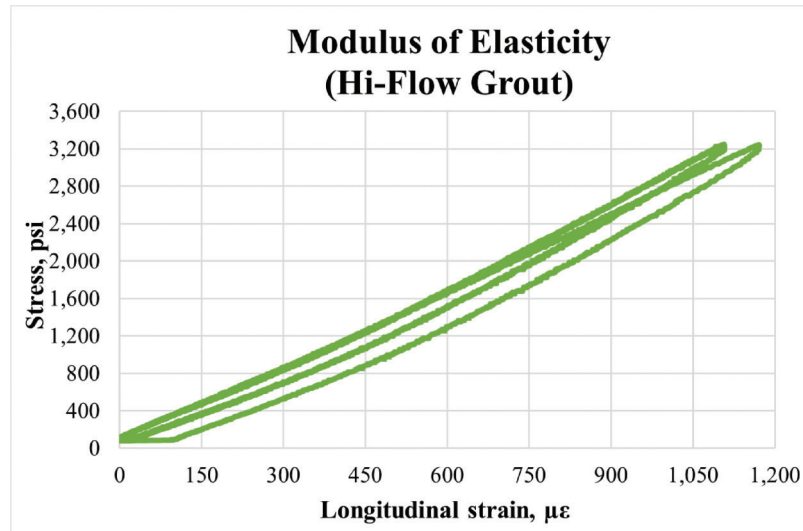


Figure 4.18 Modulus of elasticity test for Hi-Flow Grout (35-day curing time).

TABLE 4.3
Properties of Hi-Flow Grout produced by Euclid Chemical

Properties	Value	Source
Flow Test	33.12 sec	Test, ASTM C939
Working Time	60 min	TDS
Initial Set Time	3 hours 50 min	TDS
Final Set Time	4 hours 50 min	TDS
f'_c (1 Day)	3.44 ksi	Test, ASTM C109
f'_c (4 Days)	5.62 ksi	Test, ASTM C109
f'_c (7 Days)	5.94 ksi	Test, ASTM C109
MOE (35 Days)	2,900 ksi	Test, ASTM C469
Price (on 6/2022)	86.22 \$/ft ³	JK supply quote

flowable consistency. To perform the material testing, 31.12 lb. of Hybrid Grout was mixed with 6.62 lb. of water, resulting in a water/cement ratio of 0.21 that went beyond the specified in a TDS but was enforced by the complicated mixing conditions in the laboratory.

4.1.1.4.2 Flow rate test (ASTM C1437). One of the first material tests performed right after mixing was a modified flow table test following ASTM C1437 (ASTM, 2020) to ensure no bleeding or segregation. Because the mix was flowable and self-consolidating, it was decided to modify the test by excluding the requirement of dropping the table 25 times in 15 seconds to consolidate the mix. Therefore, the table was replaced with a piece of laminated black plywood installed and leveled on the floor. The bronze flow mold was placed in the center, as shown in Figure 4.19, and the diameter measurements were taken along eight lines drawn at a 45-degree angle to each other (Figure 4.20).

The technical data sheet (TDS) states the diameter of the spread should be 8–12". The average diameter of the spread was 12.75", which exceeded the upper limit stated by TDS by 6.25% due to the increased water/cement ratio. However, the mix was accepted for casting cube (compressive strength test) and cylinder



Figure 4.19 Modified flow table test setup.

(modulus of elasticity test) specimens as reasonable deviation from TDS was observed, and no bleeding or segregation was noticed. According to ASTM C1437 (ASTM, 2020), the flow is the increase in the average base diameter of the grout, expressed as a percentage of the original base diameter. The base inside diameter of the flow mold was 4", which resulted in a flow of 219%.



Figure 4.20 Measuring the diameter of the grout spread.



Figure 4.21 Cube HY-1.1 ($f'_c = 6,713$ psi).

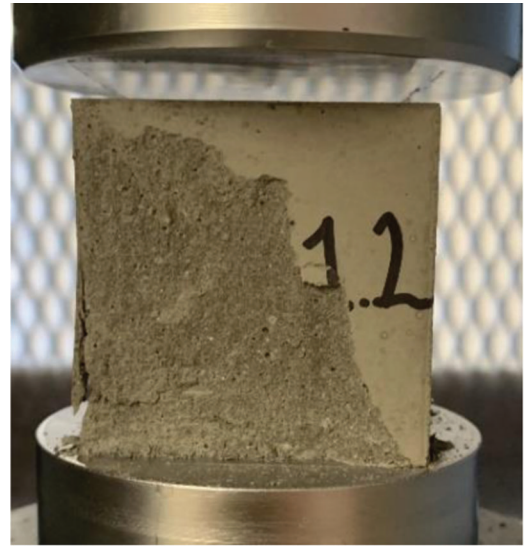


Figure 4.22 Cube HY-1.2 ($f'_c = 6,255$ psi).

4.1.1.4.3 Compressive strength test (ASTM C109). To determine the compressive strength of Hybrid Grout in 1, 3, and 7 days according to ASTM C109 (ASTM, 2021b), 2-in. cube specimens were tested. The maximum permissible range was 8.7% of the average strength of the three specimens tested at the same age. The average strength calculation did not consider the values outside the permitted range (outliers). However, a minimum of two cubes was required to calculate the average strength. The cubes were dry-cured at an ambient temperature, and the failure modes of 2 × 2" Hybrid Grout specimens tested within 24 hours of curing are shown in Figure 4.21 and Figure 4.22. The last cube, HY-1.3 ($f'_c = 5,720$ psi), was specified as an outlier and excluded from calculating the average strength in 24 hours because it was beyond the permissible range. The dry curing was selected for the simplicity of the sandwich panel repair application in the field, as it would be complicated to ensure wet curing conditions. However, all cube specimens reached 85%–90% of the compressive strength specified in the technical data sheet for Hybrid Grout because of dry curing or increased water/cement ratio during mixing.

The strength gain over time is shown in Figure 4.23, and it can be observed that the fastest rate of strength gain was recorded over the first day of curing (6.48 ksi/day); however, after the rate slowed down to 1.77 ksi/day and 0.51 ksi/day for 3-day and 7-day cure, respectively.

4.1.1.4.4 Modulus of elasticity test (ASTM C469). The modulus of elasticity test for Hybrid Grout was

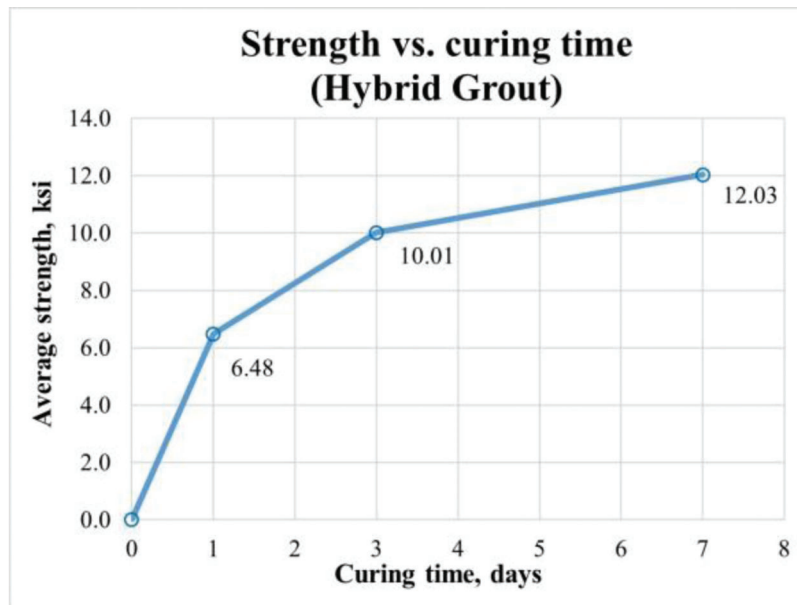


Figure 4.23 Strength gain over time for Hybrid Grout (flowable consistency).

performed in Bowen Laboratory. According to ASTM C469 (ASTM, 2022b), the 4 × 8" cylinder must be loaded to 40% of the ultimate strength to remain in the elastic response range and avoid cracking that would damage the sensors (Figure 4.7). The Forney compression testing machine performed three elastic cycles to measure the average MOE = 3,350 ksi after a 7-day curing time (Figure 4.24). The modulus of elasticity is also a function of time, and therefore, it increases with curing time, resulting in a more brittle behavior. The results of the material testing, including ultimate compressive strength, flowability, working and setting time, and a price as of 06/2022, are presented in Table 4.4.

4.1.2 Polymer-Based Concrete

4.1.2.1 Polyester polymer concrete PPC 1121. PPC 1121 polyester polymer concrete is a pre-mixed polymer concrete made of polyester binder resin and graded aggregates with a high molecular weight methacrylate (HMWM) primer system that develops true composite action at the bond line of the substrate. PPC 1121 gains at least 6 ksi ultimate compressive strength and allows for a 2-hour traffic return in a wide temperature range varying from 40°F–100°F. PPC-1121 is a self-consolidating concrete (SCC); therefore, neither rodding, tamping, nor vibration is required when casting.

4.1.2.1.1 Mixing procedures. The mixing procedures for PPC 1121 were complicated, and instructions provided in a technical data sheet (TDS) were followed alongside the recommendations provided by Kwik Bond Polymers representatives (KwikBond Polymer, n.d.b). Due to the small quantities of material required, a shear mixing paddle attached to a heavy-duty power drill was utilized to mix PPC 1,121 in 5-gal. buckets.

To cast a batch of cylinders, 4.5 lb. of binder resin was mixed with 0.75 fl. oz of MEKP (methyl ethyl ketone peroxide) for 15 seconds. MEKP is a catalyst that reacts with resin to turn it from liquid into solid and is often used in the composites industry. Once the resin was catalyzed, 25.02 lb. of sand and 12.5 lb. of coarse aggregate were added and mixed for 2 minutes until the aggregate appeared wet. The amount of MEKP catalyst added controls working time that can vary from 15 to 30 minutes. The ambient temperature also affects how fast PPC 1121 cures and gains strength over time, with the higher temperatures accelerating the curing process.

4.1.2.1.2 Slump flow (ASTM C1611). One of the first material tests performed right after mixing was a slump flow test of self-consolidating (SCC) concrete following ASTM C1611 (ASTM, 2021c). The average diameter (d_{avg}) of the Kwik Bond–PPC 1121 spread was equal to 12.25 in.; however, no data was available in the TDS to compare it with. It could be seen that the concrete started bleeding, as shown in Figure 4.25 and Figure 4.26. However, resin bleeding in polymer-based concretes is standard and should not raise concerns. Oppositely, it indicates that resin content was correctly calculated, allowing for a consolidation of Kwik Bond–PPC 1121.

4.1.2.1.3 Compressive strength test (ASTM C39). To determine the compressive strength (f'_c) of polyester polymer concrete in 1, 3, and 7 days according to ASTM C39 (ASTM, 2021a), 4 × 8" cylinders were cast. The maximum permissible range was 9% of the average strength of the two specimens tested at the same age in the laboratory conditions. The average strength calculation did not consider the values outside the permitted range (outliers). However, a minimum of two cylinders was required to calculate the

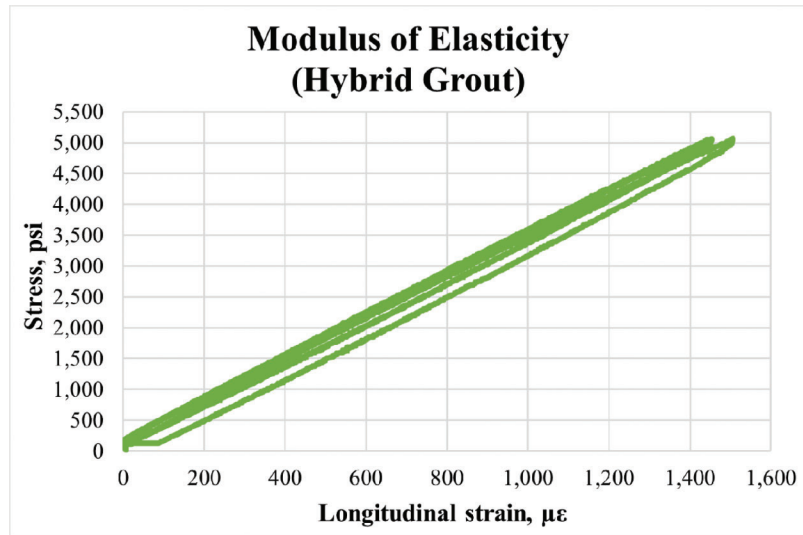


Figure 4.24 Modulus of elasticity test for Hybrid Grout (7-day curing time).

TABLE 4.4
Properties of Hybrid Grout produced by Five Star Products

Properties	Value	Source
Flow Test	12.75 in. (219%)	Test, ASTM C1437
Working Time	30 min	TDS
Initial Set Time	2 hours	TDS
Final Set Time	N/A	N/A
f'_c (1 Day)	6.48 ksi	Test, ASTM C109
f'_c (3 Days)	10.01 ksi	Test, ASTM C109
f'_c (7 Days)	12.03 ksi	Test, ASTM C109
MOE (7 Days)	3,350 ksi	Test, ASTM C469
Price (on 06/2022)	111 \$/ft ³	JK supply quote

average concrete strength. The cylinders were dry-cured at an ambient temperature, and the failure modes of 4 × 8" PPC 1121-cylinder specimens tested after 3-day curing time are shown in Figures 4.27 and 4.28. Cylinder specimens exceeded the ultimate compressive strength specified in the technical data sheet (6 ksi).

The strength gain over time is shown in Figure 4.29, and it can be observed that the fastest rate of strength gain was recorded over the first day of curing (4.92 ksi/day). However, after that, the rate slowed down to approximately 0.93 ksi/day for a 3-day curing period. After curing Kwik Bond PPC-1121 for 3 days, the compressive strength almost plateaued with an insignificant increase over time (0.07 ksi/day). One of the distinctive features of Kwik Bond PPC-1121 or polymer-based concretes in general, is the ability to gain 90% of ultimate compressive strength over the first 24 hours of curing with a diminishing rate of gain after that over the next few days depending on catalyst levels and temperature conditions.

4.1.2.1.4 Modulus of elasticity test (ASTM C469). The modulus of elasticity (MOE) was provided in the technical data sheet (TDS) for PPC1121



Figure 4.25 Slump flow test; $d_{avg} = 12.25$ in.

polyester polymer concrete; nevertheless, an additional test in the Bowen Laboratory was performed. According to ASTM C469 (ASTM, 2022b), the 4 × 8" cylinder must be loaded to 40% of the ultimate strength to remain in the elastic response range and avoid cracking that would damage the sensors. The Forney compression testing machine performed three elastic cycles to measure the average MOE = 1,850 ksi after 7 days of cure (Figure 4.30), compared well with the MOE = 1,500 ksi provided in TDS. The modulus of elasticity is also a function of time; therefore, it increases with



Figure 4.26 Cylinders after casting (bleeding of resin).

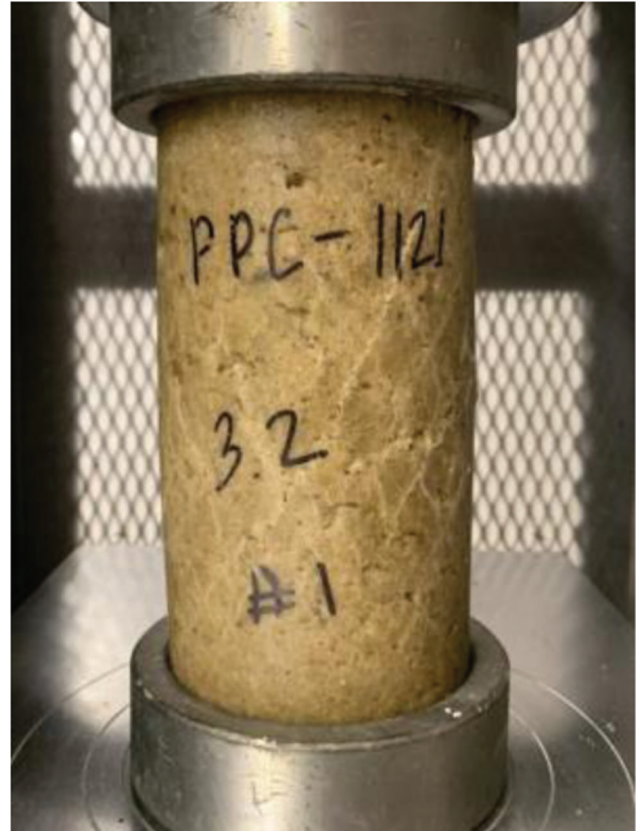


Figure 4.28 Cylinder PPC-3.2; $f'_c = 6,980$ psi.

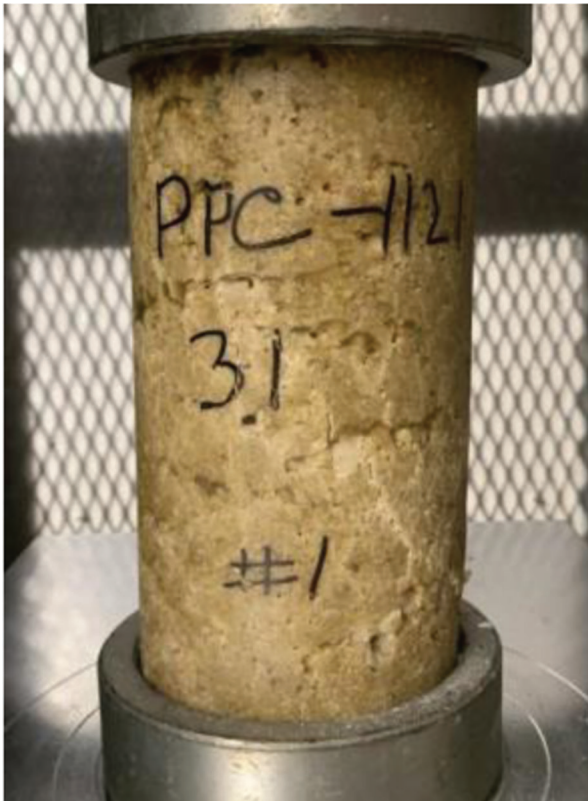


Figure 4.27 Cylinder PPC-3.1; $f'_c = 6,585$ psi.

TABLE 4.5

Properties of Kwik Bond PPC-1121 produced by Kwik Bond Polymers

Properties	Value	Source
Flow Test	12.25 in.	Test, ASTM C1611
Working Time	15–30 min ¹	TDS
Initial Set Time	N/A	N/A
Final Set Time	2 hours	TDS
f'_c (1 Day)	4.92 ksi	Test, ASTM C39
f'_c (3 Days)	6.78 ksi	Test, ASTM C39
f'_c (7 Days)	7.04 ksi	Test, ASTM C39
MOE (7 Days)	1,850 ksi	Test, ASTM C469
Price (on 06/2022)	80 \$/ft ³	Kwik Bond Polymers quote

¹Value could be adjusted based on the amount of catalyst.

curing time, resulting in a less ductile behavior of concrete specimens. The results of the material testing, including ultimate compressive strength, flowability, working and setting time, and a price as of 06/2022, are presented in Table 4.5.

4.1.2.2 Hybrid composite synthetic concrete (HCSC).

Kwik Bond HCSC is a polymer-based basalt fiber reinforced structural concrete offering enhanced mechanical efficacy, compatibility with adjacent materials, and complete elimination of degradation. HSCS gains

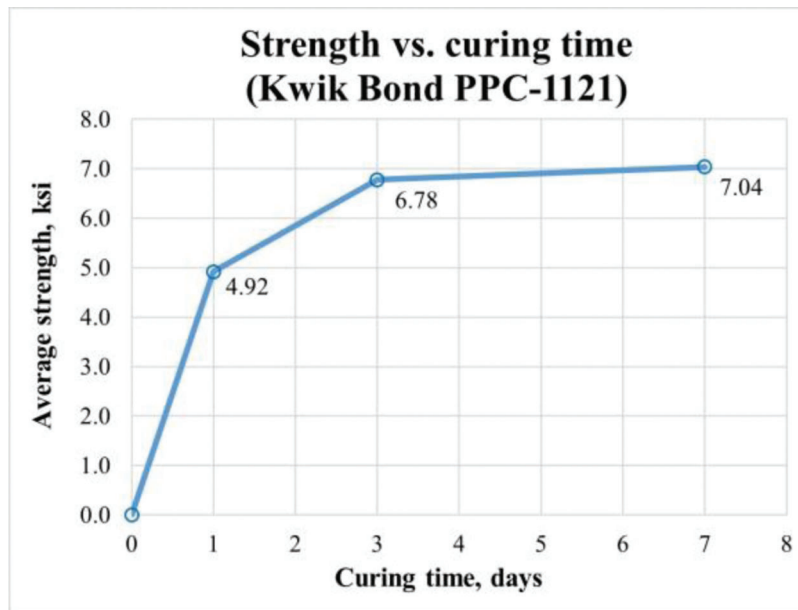


Figure 4.29 Strength gain over time for Kwik Bond PPC-1121.

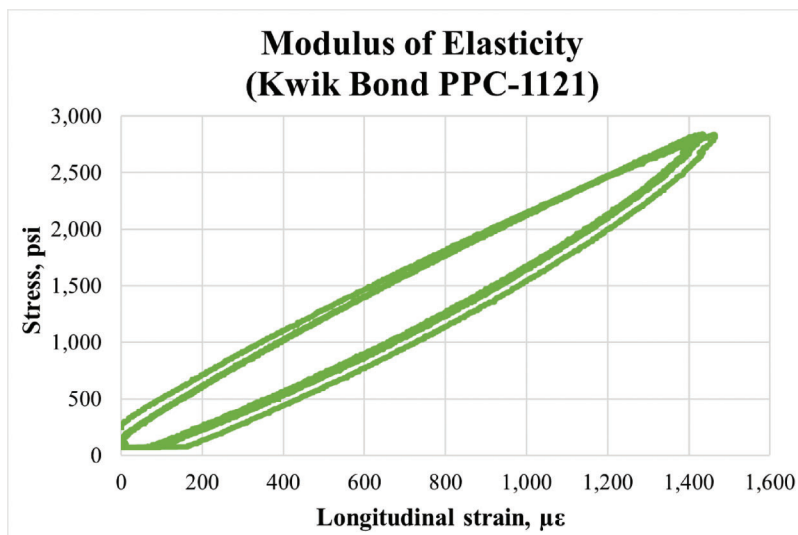


Figure 4.30 Modulus of elasticity test for Kwik Bond PPC-1121 (7-day curing time).

at least 7.5 ksi strength in 8 hours and allows for a 4-hour traffic return in a wide temperature range varying from 40°F–100°F. Also, HCSC is a self-consolidating concrete; therefore, neither rodding, tamping nor vibration is required when casting.

4.1.2.2.1 Mixing procedures. The mixing procedures for HCSC were complicated, and instructions provided in a technical data sheet (TDS) were followed alongside the recommendations provided by Kwik Bond Polymers representatives (KwikBond Polymer, n.d.a). Due to the small quantities of material required, a shear mixing paddle attached to a heavy-duty power

drill was utilized to mix HCSC in 5-gal. buckets. To cast a batch of cylinders and perform a slump flow test, 9 lb. of binder resin was combined with 1.5 fl. oz of MEKP for 15 seconds. MEKP is a catalyst that reacts with resin to turn it from liquid into solid and is often used in the composites industry. Once the resin was catalyzed, 69.25 lb. of HCSC aggregate was added and mixed for 2 minutes until the aggregate appeared wet. The amount of MEKP catalyst added controls working time that can vary from 15 to 30 minutes. The ambient temperature also affects how fast HCSC cures and gains strength over time, with the higher temperatures accelerating the curing process.



Figure 4.31 Slump flow test; $d_{avg} = 19.06$ in.



Figure 4.32 HCSC cylinders after casting (bleeding of resin).

4.1.2.2.2 Slump flow (ASTM C1611). One of the first material tests performed right after mixing was a slump flow test of self-consolidating (SCC) concrete following ASTM C1611 (ASTM, 2021c). The average diameter (d_{avg}) of the HCSC spread was equal to 19 in.; however, no data was available in the technical data sheet to compare it with. It could be seen that the concrete started bleeding, as shown in Figure 4.31 and Figure 4.32. However, resin bleeding in polymer-based concretes is a standard process. Oppositely, it indicates that resin content was correctly calculated, allowing for a consolidation of HCSC.

4.1.2.2.3 Compressive strength test (ASTM C39). To determine the compressive strength of HCSC in 1, 3, and 7 days according to ASTM C39 (ASTM, 2021a), nine 4×8 " cylinders were cast. The maximum permissible range was 10.6% of the average strength of the three specimens tested at the same age in the laboratory conditions. The average strength calculation did not consider the values outside the permitted range (outliers). However, a minimum of two cylinders was required to calculate the average concrete strength. The cylinders were dry-cured at an ambient temperature, and the failure modes of 4×8 " HCSC cylinder specimens tested within 24 hours of curing are shown in Figures 4.33, 4.34, and 4.35. Cylinder specimens reached 91% of the ultimate compressive strength specified in the technical data sheet (10 ksi), and a 9% variation was considered reasonable.

The strength gain over time is shown in Figure 4.36, and it can be observed that the fastest rate of strength gain was recorded over the first day of curing (8.4 ksi/day); however, after that, the rate slowed down to approximately 0.1 ksi/day. One of the distinctive



Figure 4.33 HCSC-1.1; $f'_c = 8,478$ psi.



Figure 4.34 HCSC-1.2; $f'_c = 8,444$ psi.



Figure 4.35 HCSC-1.3; $f'_c = 8,267$ psi.

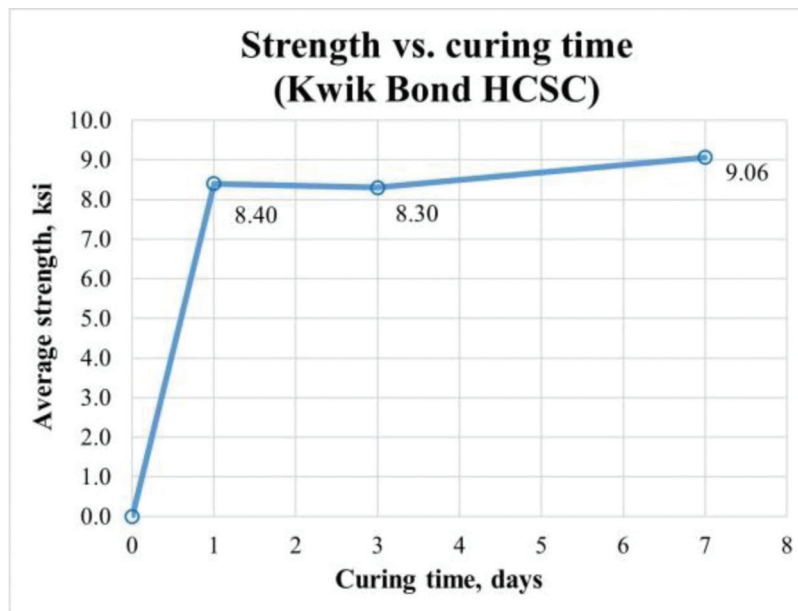


Figure 4.36 Strength gain over time for Kwik Bond HCSC.

features of Kwik Bond HCSC or polymer-based concretes in general, is the ability to gain 75% of ultimate compressive strength over the first 8 hours of curing. After 1 day of curing, the compressive strength does not change significantly with time.

4.1.2.2.4 Modulus of elasticity test (ASTM C469). The modulus of elasticity (MOE) was provided in the technical data sheet (TDS) for HCSC; nevertheless, an additional test in the Bowen Laboratory was performed. According to ASTM C469

(ASTM, 2022b), the 4×8 " cylinder must be loaded to 40% of the ultimate strength to remain in the elastic response range and avoid cracking that would damage the sensors. The Forney compression testing machine performed three elastic cycles to measure the average $MOE = 2,550$ ksi after 7 days of cure (Figure 4.37), compared well with the 2,500 ksi MOE value provided in TDS. The modulus of elasticity is also a function of time; therefore, it increases with curing time, resulting in a less ductile behavior of concrete specimens. The results of the material testing, including

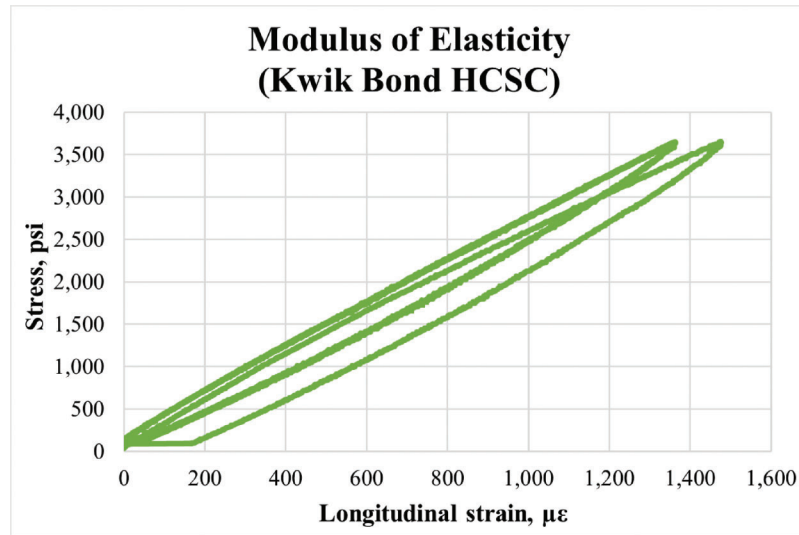


Figure 4.37 Modulus of elasticity test for Kwik Bond HCSC (7-day curing time).

TABLE 4.6
Properties of Kwik Bond HCSC produced by Kwik Bond Polymers

Properties	Value	Source
Flow Test	19.06 in.	Test, ASTM C1611
Working Time	15–30 min ¹	TDS
Initial Set Time	N/A	N/A
Final Set Time	2–4 hours	TDS
f' _c (1 Day)	8.40 ksi	Test, ASTM C39
f' _c (3 Days)	8.3 ksi	Test, ASTM C39
f' _c (7 Days)	9.06 ksi	Test, ASTM C39
MOE (7 Days)	2,550 ksi	Test, ASTM C469
Price (on 06/2022)	110 \$/ft ³	Kwik Bond Polymers quote

¹Value could be adjusted based on the amount of catalyst.

ultimate compressive strength, flowability, working and setting time, and a price as of 06/2022, are presented in Table 4.6.

4.1.3 Ultra-High-Performance Concrete (UHPC)

4.1.3.1 Steelike ultra-high-performance concrete. Ultra-high-performance concrete (UHPC) produced by Steelike has superior compressive and tensile strengths, flowability, and durability compared to conventional grout and concrete, including high-performance and very-high-performance concrete. When mixed with 2% fibers by volume, Steelike UHPC is expected to achieve at least 11 ksi compressive strength in just 1 day of cure, and, if needed, the compressive strength of 14 ksi could be reached in as little as 12 hours (Steelike Inc., 2023). The most significant advantage of Steelike UHPC is its flexibility to accommodate the project needs; for example, extending setting and working time, which is extremely important when performing a repair in the field, could be easily modified.

4.1.3.1.1 Mixing procedures. The mixing procedures for UHPC were the most complex, and, therefore, to perform the repairs in the field, Steelike representatives or third parties certified by Steelike must be present on site. To properly mix UHPC, only a vertical shaft mixer is required, and conventional concrete or paddle mixers cannot handle the complex mixing procedures that UHPC requires. Due to the small quantities of material needed, a Hobart mixer was utilized to mix small batches of concrete (Figure 4.38 and Figure 4.39). The four cylinders cast from UHPC are shown in Figure 4.40. For one batch, 17.5 lb. of concrete was mixed with 0.51 lb. of ice, 0.94 lb. of cold water, and 1.29 lb. of steel fibers. The cold water and ice were added to the mix to keep the low temperatures of the mix that extended the working time. To control the working time, 0.08 5 lb. of ZRBRA admixture was included in the mix.

In summary, the mixing procedures could be outlined as follows.

1. Add dry UHPC mix to the Hobart mixer and mix it at medium speed for 1 minute.
2. Pour cold water with ZEBRA admixture quickly followed by adding all ice.
3. Continue mixing at low speed until the mix becomes fluid.
4. Add fibers slowly and continue mixing.

While the mixing is in process, the surface temperature should be monitored not to exceed 70°F; once 80°F temperature is reached, discharge is required.

4.1.3.1.2 Flow rate test (ASTM C1437). One of the first material tests performed right after mixing was a modified flow table test following ASTM C1437 (ASTM, 2020) to ensure no bleeding or segregation. Because the mix was flowable and self-consolidating, it was decided to modify the test by excluding the requirement of dropping the table 25 times in 15 seconds to



Figure 4.38 Hobart mixer with a vertical shaft.



Figure 4.40 Cylinders after casting.



Figure 4.39 UHPC mixing process.



Figure 4.41 Modified flow table test setup.

consolidate the mix. Therefore, the table was replaced with a piece of laminated black plywood installed and leveled on the floor. The bronze flow mold was placed in the center, as shown in Figure 4.41, and the diameter measurements were taken along eight lines drawn at a 45-degree angle to each other (Figure 4.42).

The technical data sheet (TDS) states the diameter of the spread should be 7"–10". The average diameter of the spread was 9.28", which agreed well with the data provided in TDS. According to ASTM C1437 (ASTM, 2020), the flow is the increase in the average base diameter of the UHPC, expressed as a percentage of the original base diameter. The base inside diameter of the flow mold was 4", which resulted in a flow of 132%.

4.1.3.1.3 Compressive strength test (ASTM C1856/ C39). To determine the compressive strength of UHPC the provisions of ASTM C1856 (ASTM, 2017) should be followed that require the fabrication of 3 × 6" instead of 4 × 8" cylinders that are used for testing of normal concrete. However, due to the absence of 3 × 6" cylinder molds in the laboratory and the capabilities of the Forney compression machine to apply up to



Figure 4.42 Measuring the diameter after the test; $d_1 = 9.25$ in.

600,000 lbs., 4 × 8" cylinders were used. Steelike UHPC specimens were tested in 1, 3, and 7 days according to ASTM C39 (ASTM, 2021a). The maximum permissible range was 9% of the average strength of the two specimens tested at the same age in the laboratory conditions. The average strength calculation did not

consider the values outside the permitted range (outliers). However, a minimum of two cylinders was required to calculate the average compressive strength. The cylinders were dry-cured at an ambient temperature, without steam treatment, and the failure UHPC specimens tested at 3-day curing time are shown in Figure 4.43 and Figure 4.44.

The strength gain over time is shown in Figure 4.45, and it can be observed that the fastest rate of strength gain was recorded over the first day of curing (8.8 ksi/day); however, after the rate slowed down to 3 ksi/day and 0.78 ksi/day for 3-day and 7-day cure, respectively. Cylinder specimens reached 80%–94% of the compressive strength specified in the technical data sheet.

4.1.3.2 Modulus of elasticity test (ASTM C469). The static modulus of elasticity of UHPC was provided in the technical data sheet (TDS); nevertheless, an additional test in the Bowen Laboratory was performed following similar procedures previously described for cementitious grouts produced by Euclid Chemical, Five Star Products or polymer-based concrete produced by Kwik Bond Polymers. According to ASTM C469 (ASTM, 2022b), the 4 × 8" cylinder must be loaded to 40% of the ultimate strength to remain in the elastic response range and avoid cracking that would damage the sensors (Figure 4.7). The Forney compression testing machine performed three elastic cycles to measure the average MOE = 6,450 ksi after a 7-day

cure (Figure 4.46) which was significantly higher than any material previously tested. However, the modulus of elasticity is also a function of time, and therefore, it increases with curing time, resulting in a more brittle behavior. The material properties of Steelike UHPC, including ultimate compressive strength in 1, 3, and 7 days, flowability, working and setting time, and a price as of 06/2022, are presented in Table 4.7.

4.2 Evaluation of Filler Materials Using House of Quality Matrix

During Phase I, seven materials varying from inexpensive cementitious NS Grout to the most expensive material, ultra-high-performance concrete, with superb material properties were tested. However, evaluation was required to select materials that would be further used in the sandwich panel repair. A House of Quality Matrix tool was employed to determine two infill materials that would accurately satisfy the established list of requirements. A more detailed description of the House of Quality Matrix was provided earlier in Section 3.2. The requirements consisted of compressive strength in 1 day (early strength) and 7 days of curing, workability, flowability, initial set time, price, the complexity of mixing, availability on the market, and shrinkage (Table 4.8). Following a similar procedure described in Subsection 3.2.2, each requirement was assigned the importance level (high, medium, or low).



Figure 4.43 Cylinder UHPC-3.1; $f'_c = 14,936$ psi.



Figure 4.44 Cylinder UHPC-3.2; $f'_c = 14,595$ psi.

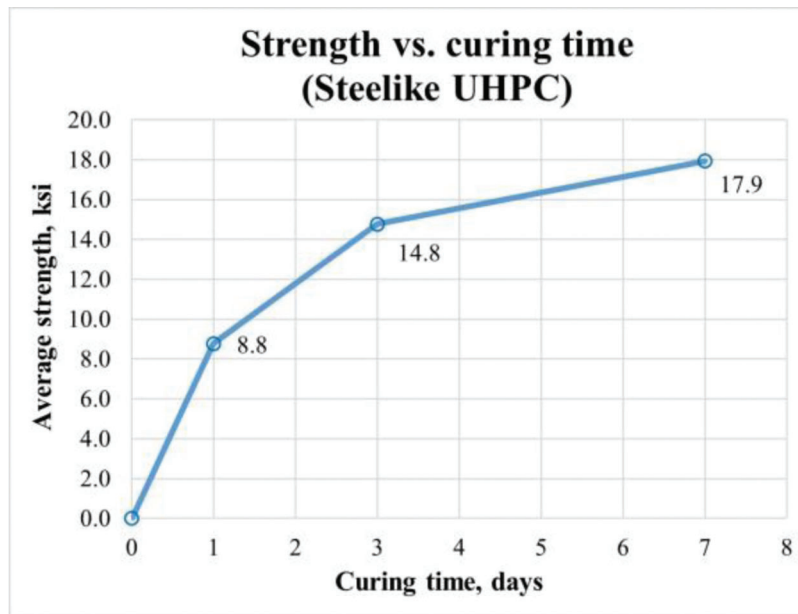


Figure 4.45 Strength gain over time for Steelike UHPC.

The “high” importance level (severity rate = 9) was assigned to workability, initial set time, and price because these requirements are the most critical requirements for infill material and have the ultimate impact. The longer working time increases the provided time slot for pouring the infill material into the stay-in-place formwork. If the workability of the mix is too short (less than 15 minutes), maintenance personnel might not have sufficient time for material placement before the material starts hardening. Additionally, the quicker initial setting time results in a faster traffic return if it is decided to close the entire bridge/one lane to decrease the number of vibrations while curing the infill material. Finally, it is essential to use reasonably priced materials to keep the repair cost-effective.

The “medium” importance level (severity rate = 6) was assigned to flowability and complexity of mixing because their effect was less critical. More flowable materials would speed up the casting process because neither tamping nor vibration would be required to evenly spread the infill material over the entire volume of stay-in-place formwork. The less complicated materials to mix, for example, cementitious grouts, would not require special maintenance personnel training. However, to mix UHPC, a construction crew should be trained appropriately by manufacturer representatives due to an elaborate mixing process that can drastically impact the quality of the mixed material.

Finally, the “low” importance level (severity rate = 3) was assigned to early compressive strength, compressive strength, market availability, and shrinkage since they have the most negligible impact on the repair. The compressive strength could be neglected if the material reaches 3 ksi in 1 day of curing because the force

transfer mechanism is elaborated, and the grout/concrete panels would not be subjected to pure compression. The threaded rods are expected to carry the shear and tensile forces, whereas the grout/concrete panels have the main purpose of encasing the corrosion and preventing the out-of-plane displacement of the corroded web. Most materials described are not available for purchase in home improvement stores. However, they could be purchased directly from the manufacturer or distributors.

In Table 4.9, the assessment criteria are provided that were used for material evaluation. The relationship between demands (requirements) and the products (filler materials) was determined using a factor called performance level. The performance level had three levels: strong, medium, and weak, with weight factors of 9, 3, and 1, respectively. “Strong” indicated a solid relationship (weight factor = 9), and “medium” highlighted a standard relationship (weight factor = 3). Finally, “weak” was given to the poor relationship between a demand set by the customer and the product (weight factor = 1). The data from Table 4.10 contained necessary information about strength, workability, flowability, set time, price, and shrinkage to perform an assessment. The description of the mixing process provided in Section 4.1.1 to Section 4.1.3 was utilized to estimate the complexity of mixing.

The results of the assessment of seven materials tested during Phase I of material testing are shown in Table 4.11. The values of the absolute importance factors for all seven infill materials were added up to get a total absolute importance factor of 1,869 points. The value of the absolute importance factor for each infill material was then divided by the total absolute importance factor to obtain the relative importance factor.

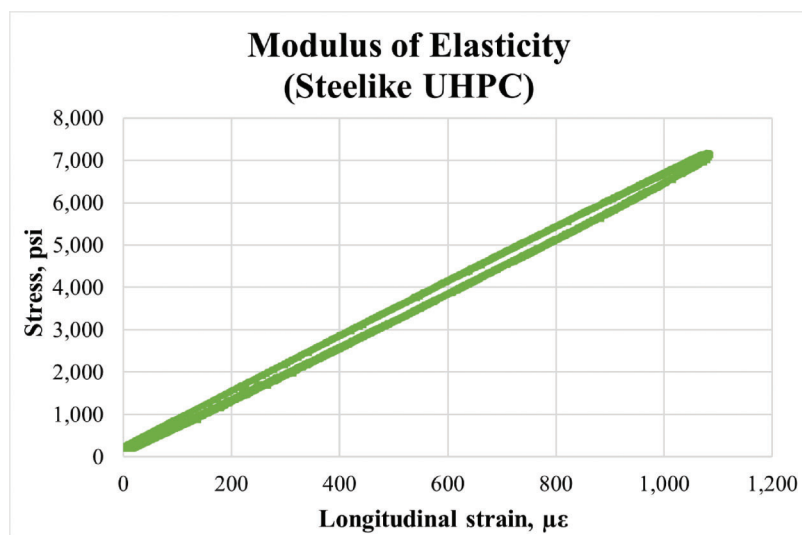


Figure 4.46 Modulus of elasticity test for Steelike UHPC (7-day curing time).

TABLE 4.7
Properties of UHPC produced by Steelike

Properties	Value	Source
Flow Test	9.28 in. (132%)	Test, ASTM C1437
Working Time	As needed ¹	TDS
Initial Set Time	75 minutes ¹	TDS
Final Set Time	87 minutes ¹	TDS
f'_c (1 Day)	8.8 ksi	Test, ASTM C39
f'_c (3 Days)	14.77 ksi	Test, ASTM C39
f'_c (7 Days)	17.94 ksi	Test, ASTM C39
MOE (7 Days)	6450 ksi	Test, ASTM C469
Price (on 06/2022)	133 \$/ft ³	Steelike, Inc. quote

¹Could be adjusted. Contact the manufacturer.

TABLE 4.8
Requirements, importance levels, and severity rates

Requirements	Importance Level	Severity Rate
Early Strength (1 Day Curing Time)	Low	3
Compressive Strength (7 Days Curing Time)	Low	3
Workability	High	9
Flowability	Medium	6
Initial Set Time	High	9
Price	High	9
Complexity of Mixing	Medium	6
Availability on the Market	Low	3
Shrinkage	Low	3

To conclude, four materials, NS Grout, Hi-Flow Grout, Kwik Bond PPC-1121, and UHPC, got the highest relative importance factors of 16.9%, 16.9%, 15.9%, and 14.3%, respectively. It was decided to investigate these four materials more thoroughly and derive stress-strain curves in Phase II of the material-level testing program. A final decision regarding the selection of only two infill materials that would be recommended for further implementation in the sandwich panel repair method was made later.

4.3 Material Level Testing: Derivation of Stress-Strain Curves (Phase II)

A more elaborate investigation was conducted in Phase II (Section 4.3), including the installation of sensors on 4×8 " cylinders to derive the stress-strain relationship for tested materials. Cylinders were instrumented with strain gauges and displacement transducers. The instrumented cylinders were tested after 3-day and 28-day curing time. Only four selected infill materials were tested in Phase II: NS Grout, Hi-Flow Grout, PPC-1121, and Steelike UHPC.

4.3.1 Sensor Layout and Test Setup

In Phase II, 4×8 " concrete and grout cylinders were instrumented and tested following provisions of ASTM C39 (ASTM, 2021a) to derive the stress-strain curve up to the failure load. The sensor layout included two strain gauges installed vertically to measure axial compressive strain. Additionally, two linear variable differential transformers (LVDTs) were installed on both sides of the cylinders to verify the readings taken by strain gauges (Figure 4.47). Whereas strain gauges were bonded to the concrete surface, more complicated procedures were followed to attach two LVDTs: a glue gun attached two high-strength magnets to the concrete cylinder. The LVDT was similarly connected to a metal strip with a glue gun; after that, the metal strip was placed over the magnet. In summary, the high-strength magnet ensured a secure and tight attachment of a metal strip, guaranteeing no relative displacement between a strip and a magnet. As a result, the LVDT measured the vertical displacement of a cylinder subjected to compression. Based on the drawing presented in Figure 4.47, the gauge length used to

TABLE 4.9
Assessment criteria for the infill material

Requirement	Performance Level		
	Strong	Medium	Weak
Early Strength (1 Day Curing Time)	≥ 3 ksi	3 ksi–1 ksi	≤ 1 ksi
Compressive Strength (7 Days Curing Time)	≥ 5 ksi	5 ksi–3 ksi	≤ 3 ksi
Workability	≥ 30 minutes	15–30 minutes	≤ 15 minutes
Flowability	The material has a fluid consistency and can be poured easily (grouts)	The material is flowable or self-consolidating concrete	The material has plastic consistency or not self-consolidating concrete
Initial Set Time	≤ 75 minutes	75–180 minutes	≥ 180 minutes
Price	≤ 80 \$/ft ³	80\$–100 \$/ft ³	≥ 100 \$/ft ³
Complexity of Mixing	No expensive equipment is needed, and mixing procedures are easy to follow	No expensive equipment is needed. However, mixing procedures are complex	Expensive equipment is required, and (or) the mixing process is challenging
Availability on the Market	The material could be bought in the store	Material should be ordered. Lead time < 1 month	Material should be ordered. Lead time ≥ 1 month
Shrinkage	Non-Shrink	≤ 500 $\mu\epsilon$	> 500 $\mu\epsilon$

TABLE 4.10
Results of material level testing

	NS Grout	TammsgROUT Supreme	Hi-Flow Grout	Hybrid Grout	Kwik Bond–PPC 1121	Kwik Bond–HCSC	SteeLike UHPC
f'_c (1 Day)	3.4 ksi	4.8 ksi	3.4 ksi	6.5 ksi	4.9 ksi	8.4 ksi	8.8 ksi
f'_c (3 Days)	4.4. ksi	7.2 ksi	5.6 ksi	10 ksi	6.8 ksi	8.3 ksi	14.8 ksi
f'_c (7 Days)	6.1 ksi	8.6 ksi	5.9 ksi	12 ksi	7 ksi	9.1 ksi	17.9 ksi
MOE, ksi	3,050	3,450	2,900	3,350	1,850	2,550	6,450
Workability, Min	15	15	60	30	15–30	15–30	As needed ¹
Flowability	29.8 sec	53.22 sec	33.12	219%	N/A	19.06 in.	132%
Initial Set Time, Min	180–300	300	230	120	60 ¹	60 ¹	75 ¹
Shrinkage	Non-Shrink	Non-Shrink	Non-Shrink	Non-Shrink	$< 500\mu\epsilon$	$< 500\mu\epsilon$	427 $\mu\epsilon$
Price, pcf	\$67	\$82	\$86	\$111	\$80	\$110	\$133

¹Could be adjusted. Contact the manufacturer.

transform displacement measured by LVDT into strain was equal to 4.3 in. Equation 4.1 was used to transform the displacement measured by LVDT into concrete strain, where L – gauge length of 4.3 in.; ΔL – the displacement measured by the displacement sensors.

To measure a surface concrete strain, wire strain gauges utilizing polyester resin backing, PL-60-11 type, produced by Tokyo Measuring Instruments Laboratory (n.d.) were used. Additional operations were performed to fill the voids to bond the strain gauge to the irregular porous concrete surface. The instructions included degreasing the surface and applying M-Bond AE-10 adhesive to fill the voids and form a smooth surface (Vishay Precision Group, n.d.). An example of the installed concrete strain gauge is shown in Figure 4.48 and Figure 4.49. It can be seen from the figures, that the cylinder had a few large

voids that were filled with the AE-10 adhesive to achieve a smooth surface applicable for strain gauge installation.

$$\epsilon_c = \Delta L / L \quad (\text{Eq. 4.1})$$

4.3.2 Experimental Results

After 3 and 28 days of curing, the cylinders were instrumented and tested for NS Grout, Hi-Flow Grout, Kwik Bond-PPC 1121, and SteeLike UHPC. The analogous process previously described in Section 4.1 was used for mixing and casting cylinders. Figures 4.50, 4.51, 4.52, and 4.53 presents the stress-strain curves for four tested materials. The average strain values recorded by SG1 and SG2 were used in all four stress-strain curves. However, the data from LVDTs was used

TABLE 4.11
Results of evaluation using the House of Quality Matrix

Requirement/Severity Rate		Cementitious Grout				Polymer-Based Concrete		
		NS Grout	Hi-Flow Grout	Tammsgrout Supreme	Hybrid Grout	Kwik Bond–PPC 1121	Kwik Bond–HCSC	UHPC
Early Strength (1 Day)	3	Strong	Strong	Strong	Strong	Strong	Strong	Strong
Compressive Strength (7 Days)	3	Strong	Strong	Strong	Strong	Strong	Strong	Strong
Workability	9	Medium	Strong	Medium	Medium	Medium	Medium	Strong
Flowability	6	Strong	Strong	Strong	Medium	Medium	Medium	Medium
Initial Set Time	9	Weak	Weak	Weak	Medium	Strong	Strong	Strong
Price	9	Strong	Medium	Medium	Weak	Strong	Weak	Weak
Complexity of Mixing	6	Strong	Strong	Strong	Medium	Medium	Medium	Weak
Availability on the Market	3	Medium	Medium	Medium	Medium	Medium	Medium	Medium
Shrinkage	3	Strong	Strong	Strong	Strong	Medium	Medium	Medium
Absolute Importance Factor	1,869	315	315	261	189	297	225	267
Relative Importance Factor, %	100%	16.9%	16.9%	14.0%	10.1%	15.9%	12.0%	14.3%

only to validate the values recorded by strain gauges and was not used in the average strain calculation. Additionally, it could be observed that every material except Kwik Bond–PPC 1121 stress-strain relationship was obtained only up to a failure caused by concrete cracking that damaged the strain gauges. However, polyester polymer concrete, Kwik Bond–PPC 1121, had a different behavior after reaching its ultimate compressive strain, exhibiting insignificant cracking (Figure 4.27 and Figure 4.28) that allowed to capture a post-peak behavior because a concrete strain gauge was not damaged. It could be seen that ultra-high-performance concrete had the largest compressive strength of 19.98 ksi after a 28-day curing. However, the Kwik Bond–PPC 1121 had notably higher ductility with the ultimate compressive strain at failure of 9,000 $\mu\epsilon$ that was twice as high as UHPC. The observed superb ductility of Kwik Bond–PPC 1121 and minor cracking was considered beneficial characteristics for a material intended for use in the sandwich panel repair method.

In addition to cylinder testing after 3 and 28-day cure, they were also tested in 7 and 14-day to capture a strength gain rate over time. It could be observed from Figure 4.54 through Figure 4.57 that Kwik Bond–PPC 1121 gained the majority of its compressive strength after just 1 day of curing. In contrast, Hi-Flow Grout's compressive strength kept increasing over 28 days of curing with a decreasing rate of strength gain over time.

4.4 Finite Element Modeling

4.4.1 Modeling Approach

4.4.1.1 Assembly, boundary conditions and mesh. The finite element model consisted of only one part, a 4×8 " solid cylinder. To represent the boundary conditions imposed by the Forney testing machine, the bottom of

the cylinder was restrained from displacing vertically ($U_2 = 0$). In addition, only one node at the center of the bottom surface was restrained from rotating along the vertical axis (UR2). The load was evenly applied to the top surface of the cylinder using the displacement control ($U_2 = 0.05$ in.), as shown in Figure 4.58.

Finite element models were developed using solid eight-node brick linear order elements with reduced integration (C3D8R). Usually, the solid elements with one integration point (C3D8R) are susceptible to the hourglass effects due to the reduced stiffness of the elements. Enhanced hourglass control was used to prevent the appearance of zero energy modes, also known as hour glassing. In addition, distortion control with a default length ratio of 0.1 was used to avoid the appearance of negative element volumes. The cylinder was meshed using fine elements (0.25" mesh size). The standard mesh is shown in Figure 4.59.

4.4.1.2 Concrete damaged plasticity model. To model grout and concrete behavior in Abaqus, the Concrete Damaged Plasticity (CDP) model was implemented (Lee & Fenves, 1998; Lubliner et al., 1989). The CDP model can accurately predict the inelastic behavior of concrete in both tension and compression by incorporating failure modes of tensile cracking and concrete crushing (Abaqus, 2006a). Compressive stress-strain curves were obtained through material testing to simulate the behavior of NS Grout, Hi-Flow Grout, Kwik Bond–PPC 1121, and Steelike UHPC. For stress-strain definition in CDP, inelastic strain must be inputted; therefore, the values of engineering strain were transformed using experimentally obtained MOE presented in Table 4.12. The inelastic stress-strain curves for all four materials that were used as an input to Abaqus are presented in Figures 4.60, 4.61, 4.62, and 4.63.

The simplified experimental compressive stress-strain curves were developed by connecting the (0,0) node

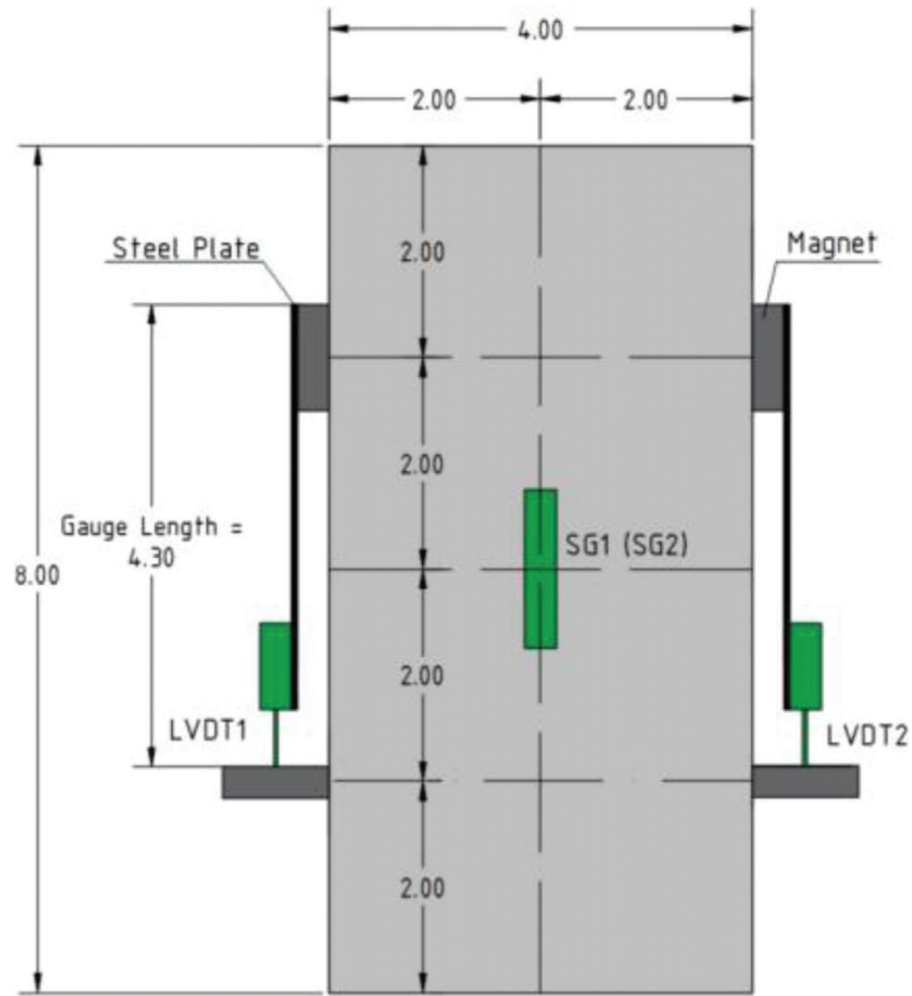


Figure 4.47 Sensor layout.

with $(0.4 f'_c, \epsilon)$. The secant modulus of elasticity was calculated as the slope of the inclined line. Figures 4.64, 4.65, 4.66, and 4.67 shows that no strain was recorded for every material test up to 500–1,000 lbf due to the concrete cylinder settlement in the neoprene pads used to cap cylinders according to ASTM C39 (ASTM, 2021a). However, that stress-strain curve would have caused an error message in Abaqus due to zero stiffness at the beginning. Therefore, the behavior was assumed to be elastic up to 40% of f'_c . The experimentally obtained data represented the plastic behavior of the material after reaching $0.4 f'_c$.

Modeling the concrete in tension using the CDP model requires the input of yield stress after failure and crack width opening. Because performing the direct tensile test on concrete and grout materials is highly challenging, the constitutive material model presented in the fib Model Code for Concrete Structures 2010 was used (International Federation for Structural Concrete, 2013). The fib Bulletin No. 42 (Müller, 2008) was used for constitutive modeling of UHPC and Kwik Bond-PPC 1121, which had more considerable tensile strength than conventional concrete.

Finally, the plasticity parameters were defined after compressive and tensile behaviors were identified. The dilation angle of 30 degrees, 0.1 eccentricity, and K_c value of 0.667 were used. The default ratio of equibiaxial to uniaxial compressive yield strengths f_{bo}/f_{co} equal to 1.16 was utilized (Bilal et al., 2023).

4.4.2 Results

The comparison of experimental data and numerical simulations for 4×8 " cylinders cast from NS Grout, Hi-Flow Grout, Kwik Bond-PPC 1121, and Steelike UHPC is shown in Figures 4.64, 4.65, 4.66, and 4.67. It could be seen that the numerical simulations aligned well with experimental data, fully matching the stiffness up to the peak load. Compressive stress-strain curves that were input in Abaqus did not have post-peak behavior, except for Kwik Bond. Therefore, due to a lack of post-peak behavior data, the FE model could not accurately capture post-peak behavior. Nevertheless, the developed material models were further implemented in finite element models assembled for specimens repaired using the sandwich panel method.

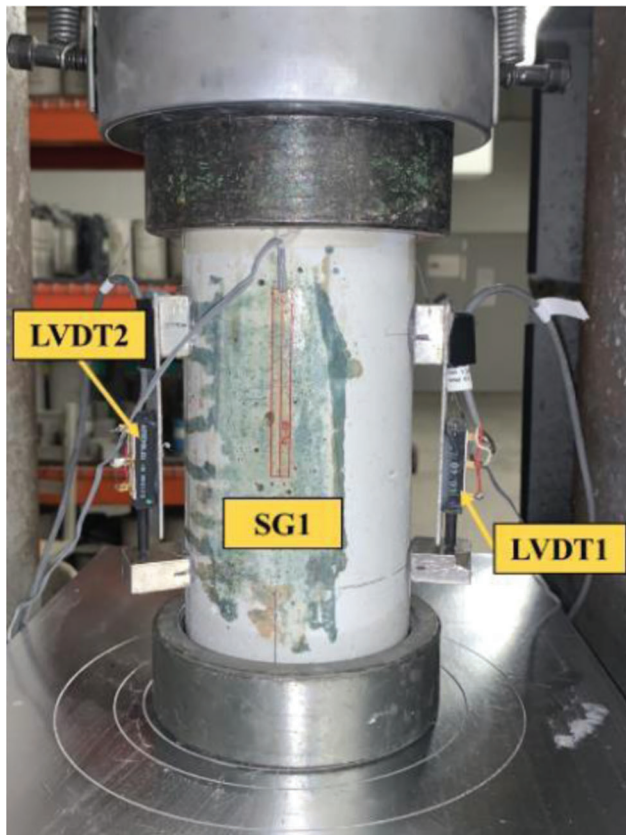


Figure 4.48 Test setup.

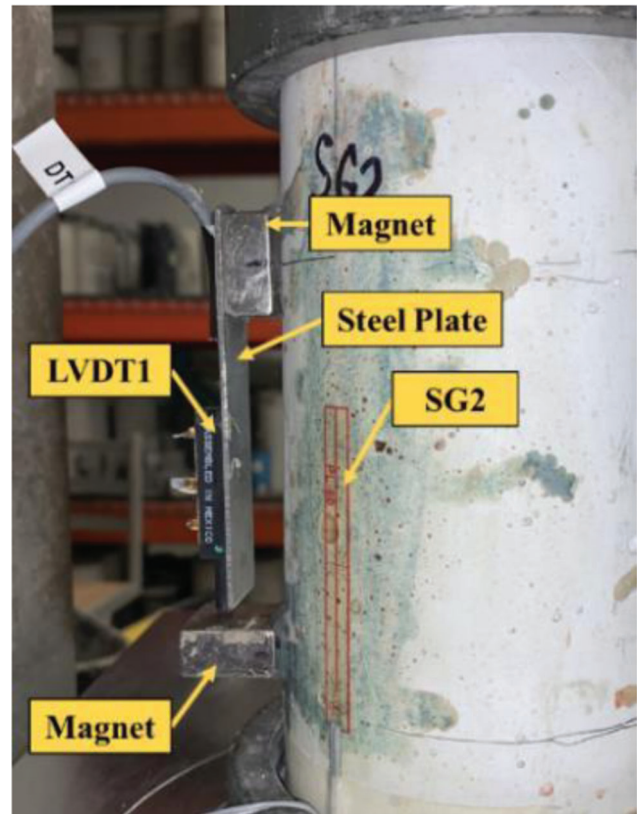


Figure 4.49 Details of LVDT installation.

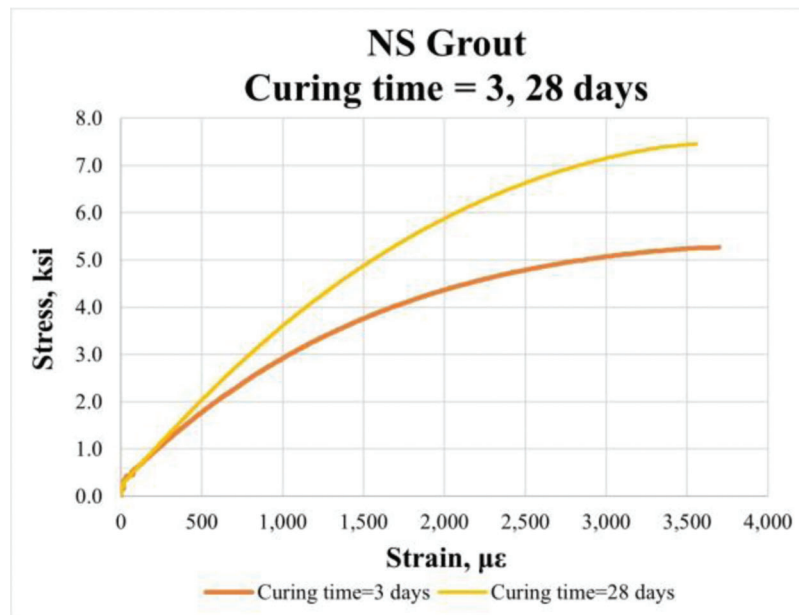


Figure 4.50 Stress-strain curve for NS Grout. Curing time = 3, 28 days.

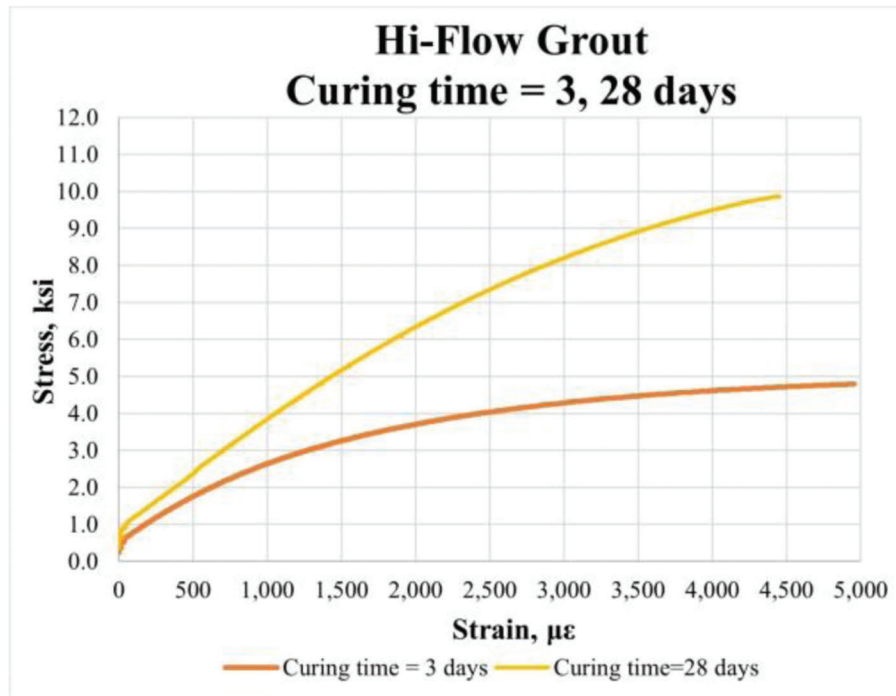


Figure 4.51 Stress-strain curve for Hi-Flow Grout. Curing time = 3, 28 days.

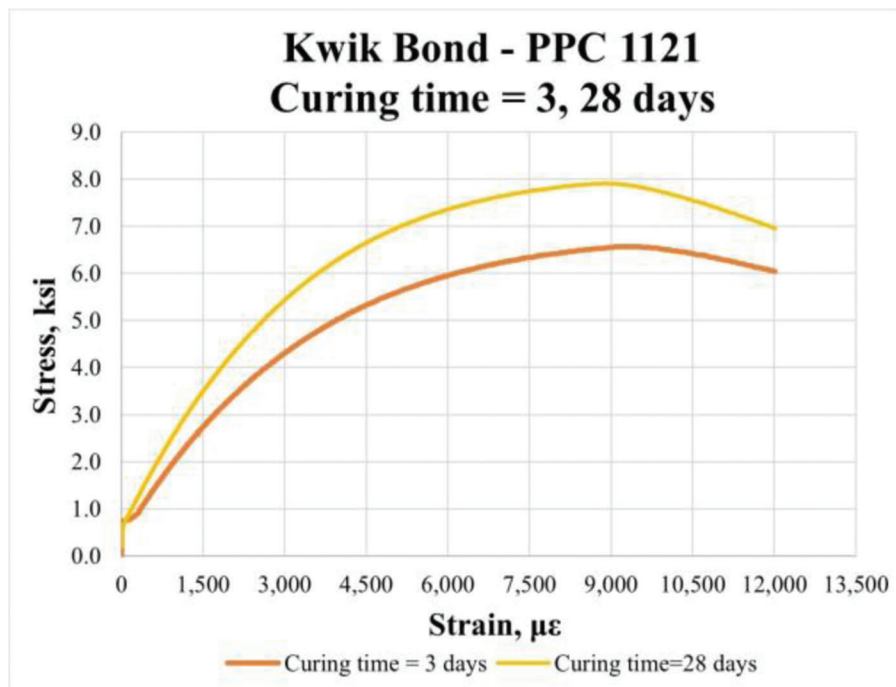


Figure 4.52 Stress-strain curve for Kwik Bond-PPC 1121. Curing time = 3, 28 days.

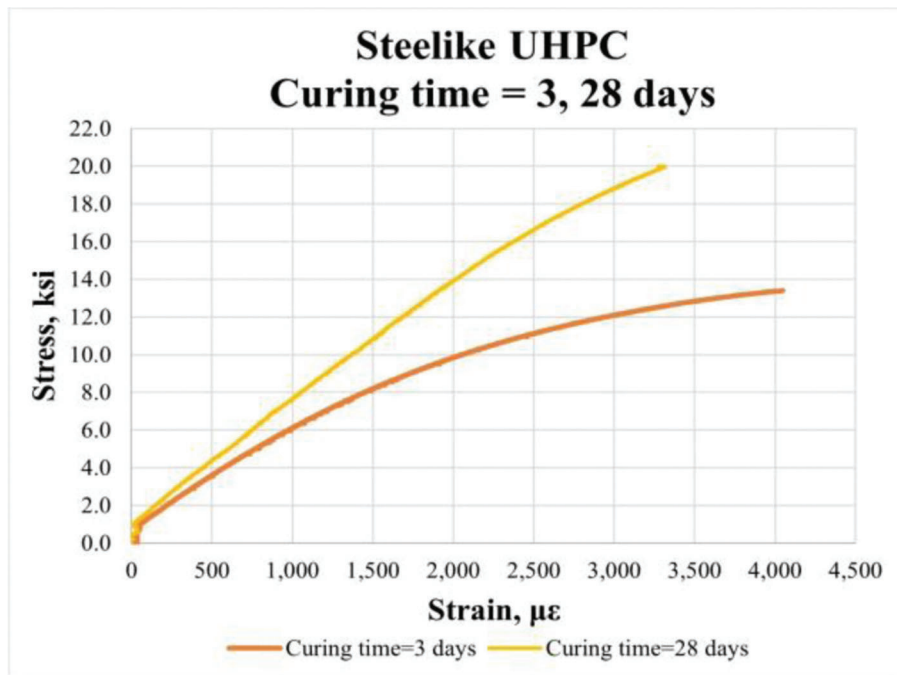


Figure 4.53 Stress-strain curve for Steelike UHPC. Curing time = 3, 28 days.

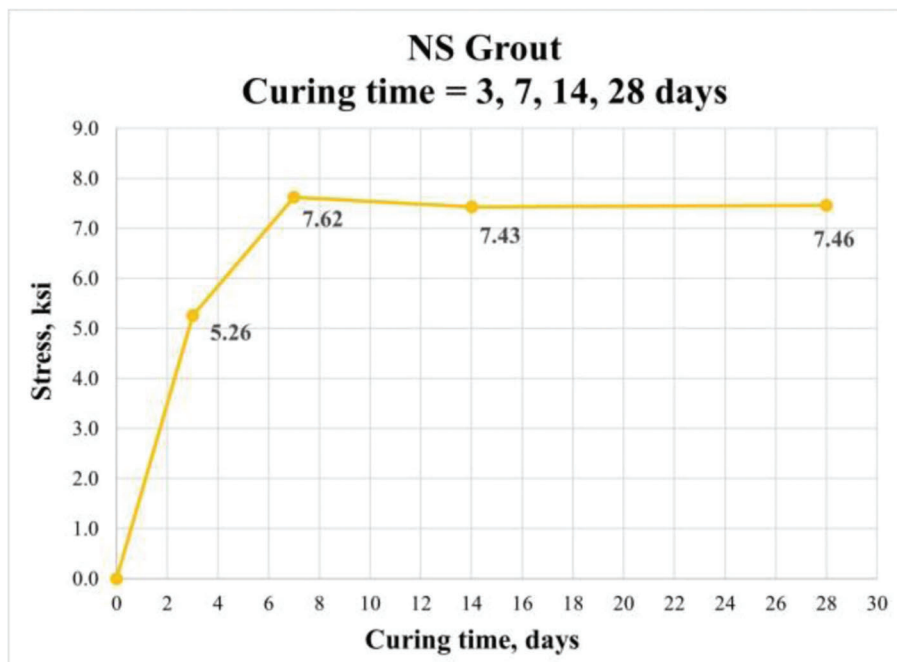


Figure 4.54 Strength gain over time for NS Grout.

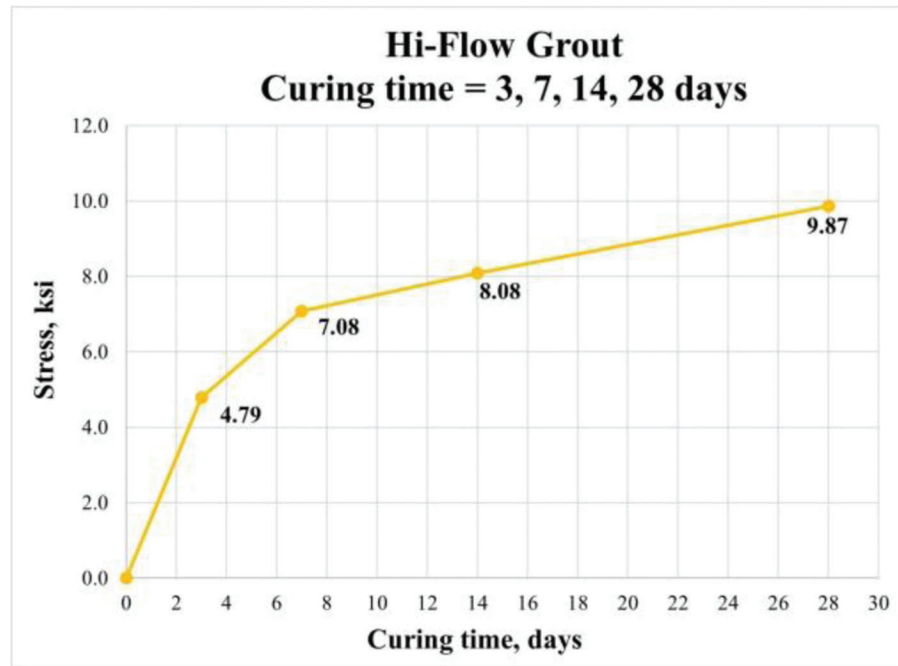


Figure 4.55 Strength gain over time for Hi-Flow Grout.

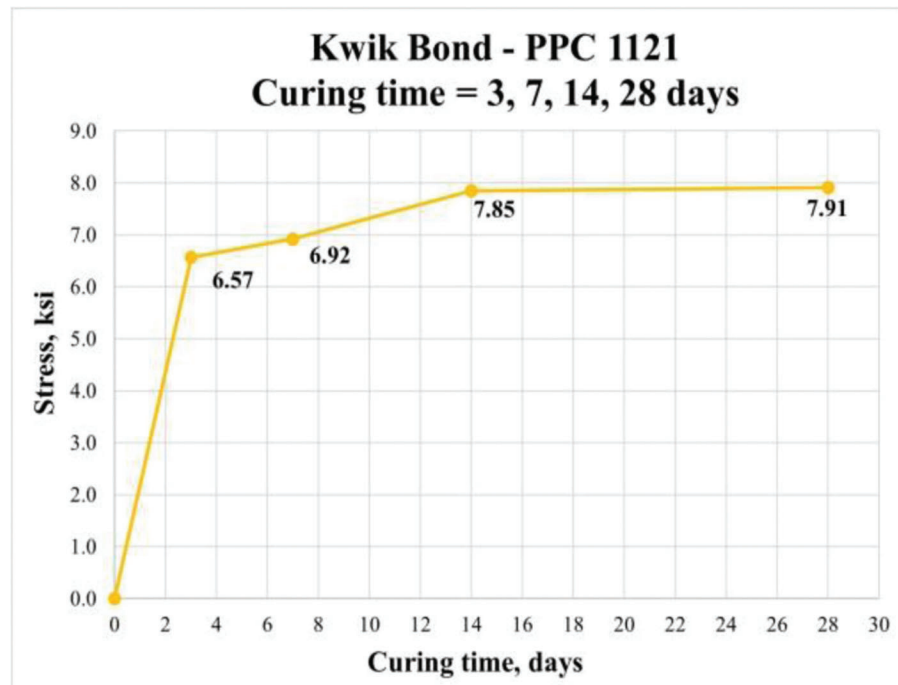


Figure 4.56 Strength gain over time for Kwik Bond-PPC 1121.

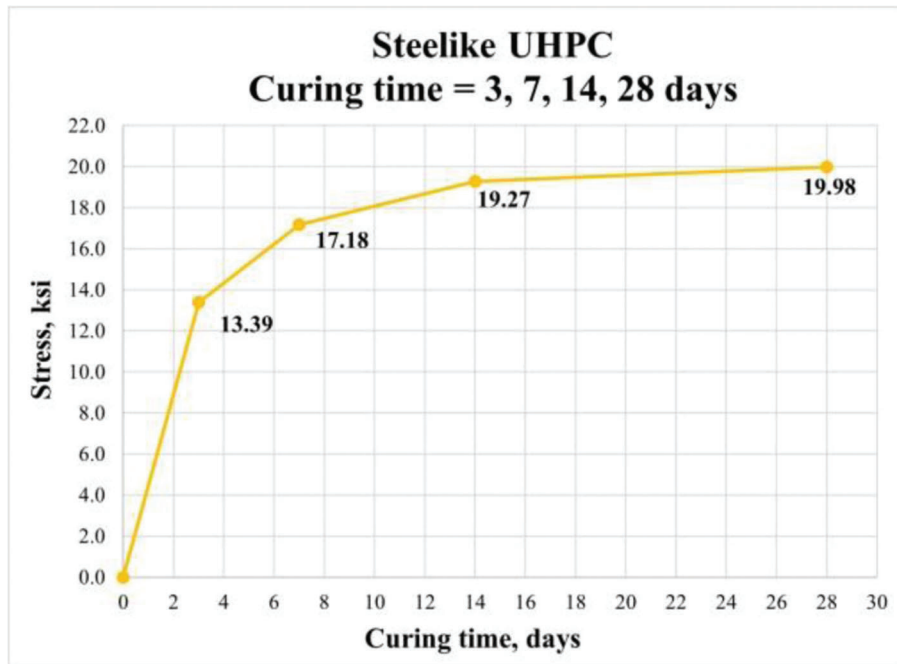


Figure 4.57 Strength gain over time for Steelike UHPC.

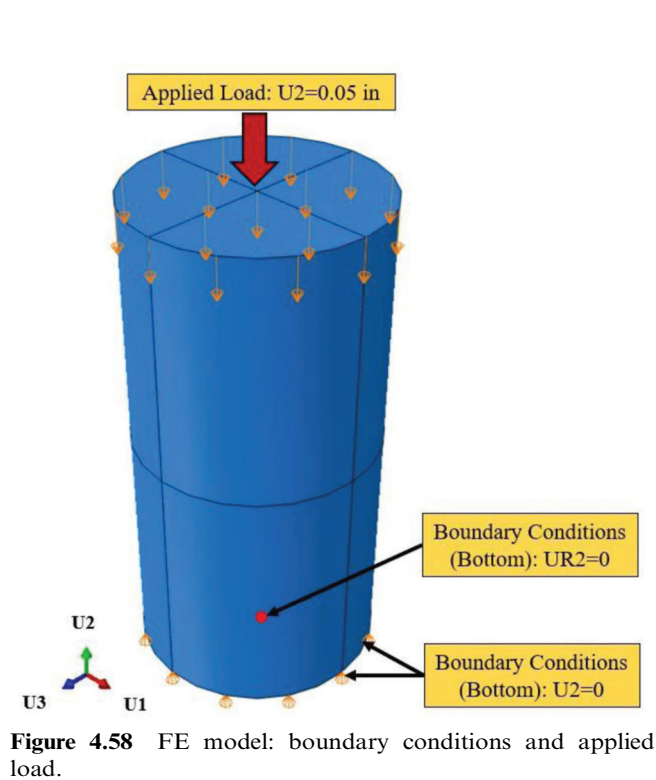


Figure 4.58 FE model: boundary conditions and applied load.

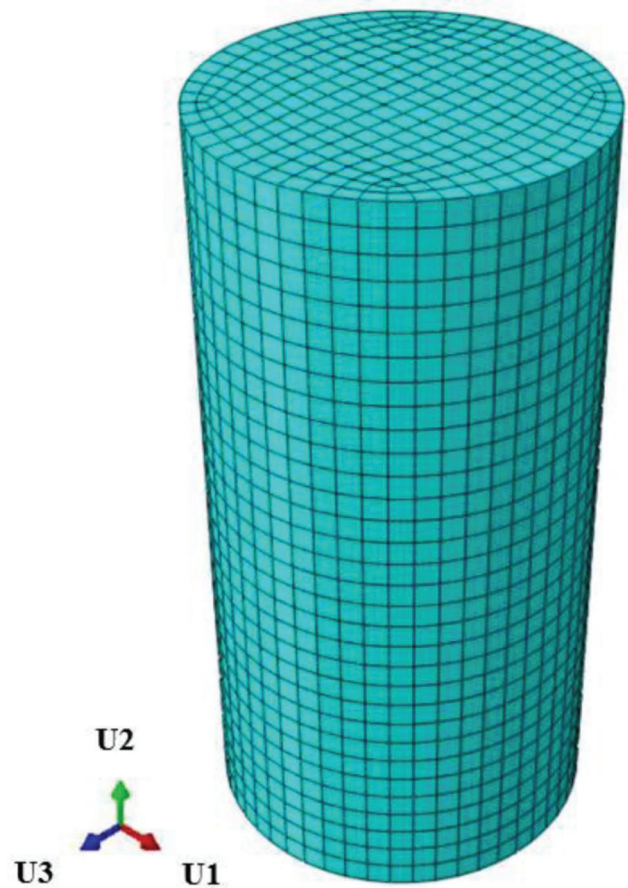


Figure 4.59 FE model: standard mesh. Mesh size = $1/4"$.

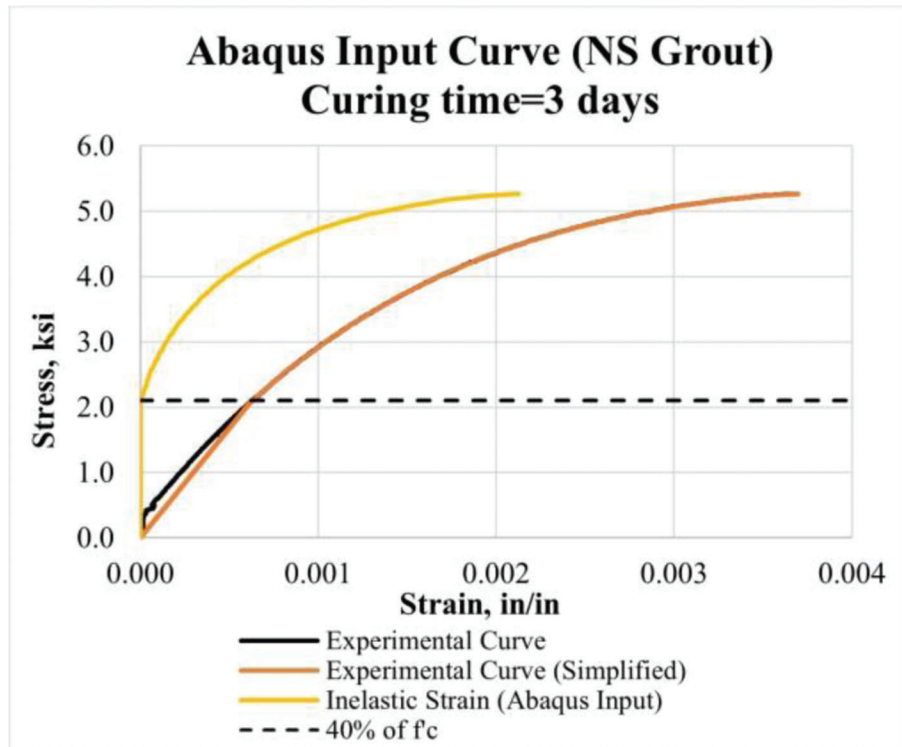


Figure 4.60 Stress-strain curves for Abaqus input: NS Grout.

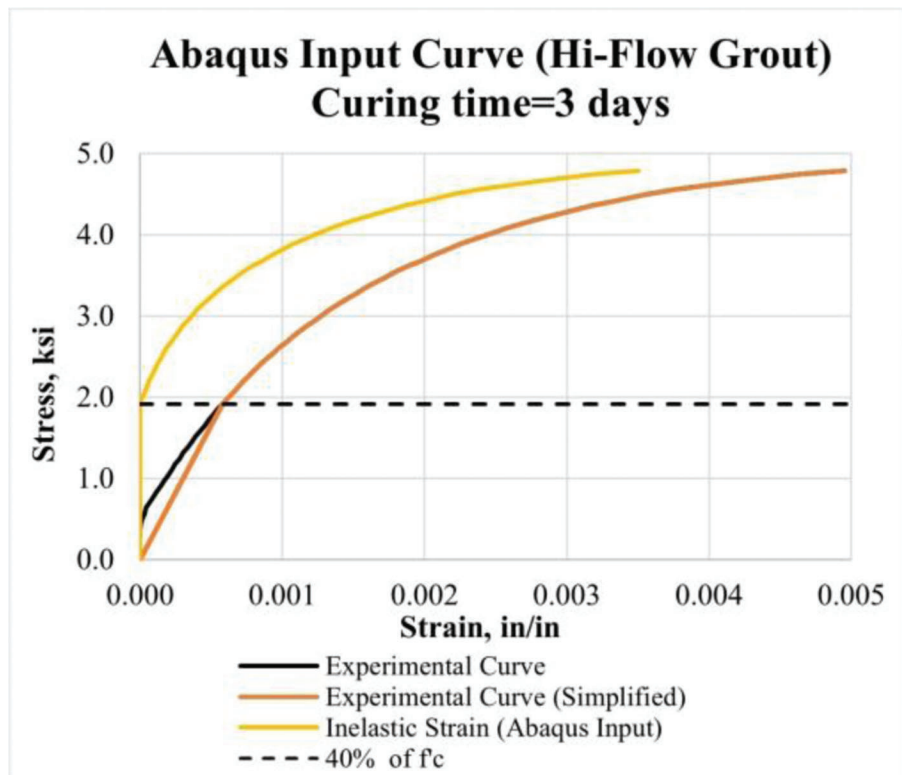


Figure 4.61 Stress-strain curves for Abaqus input: Hi-Flow Grout.

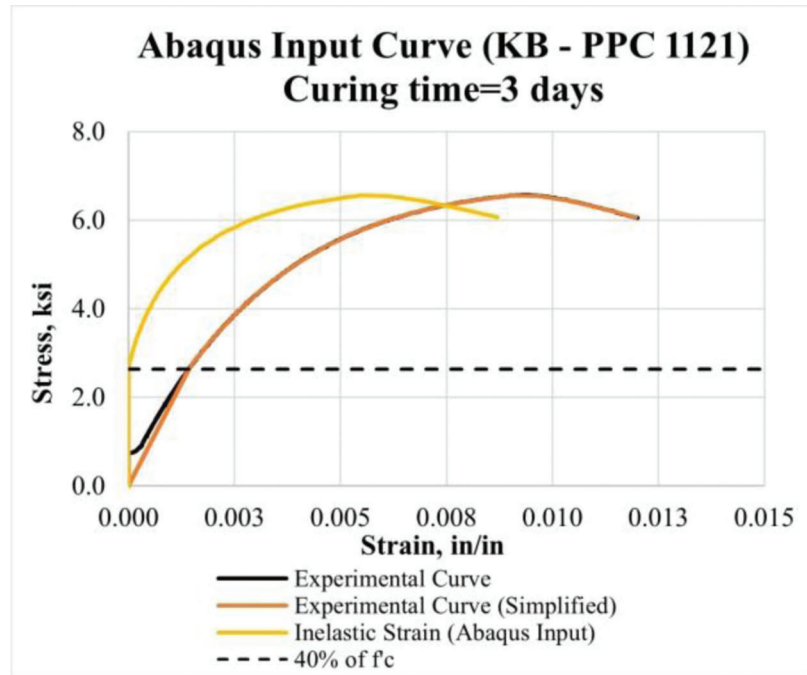


Figure 4.62 Stress-strain curves for Abaqus input: KB-PPC 1121.

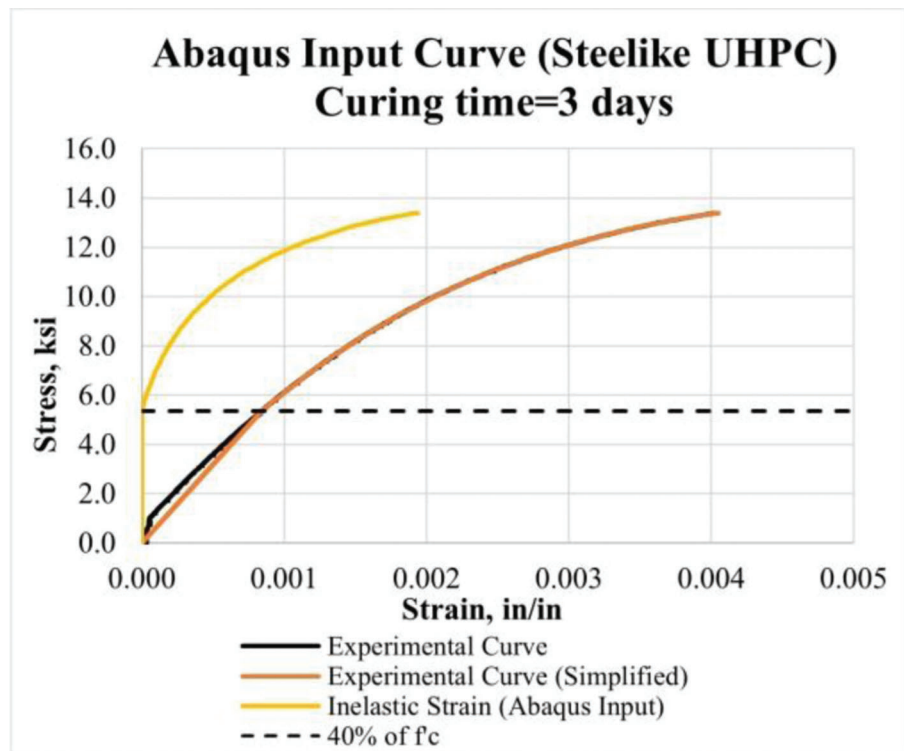


Figure 4.63 Stress-strain curves for Abaqus input: Steelike UHPC.

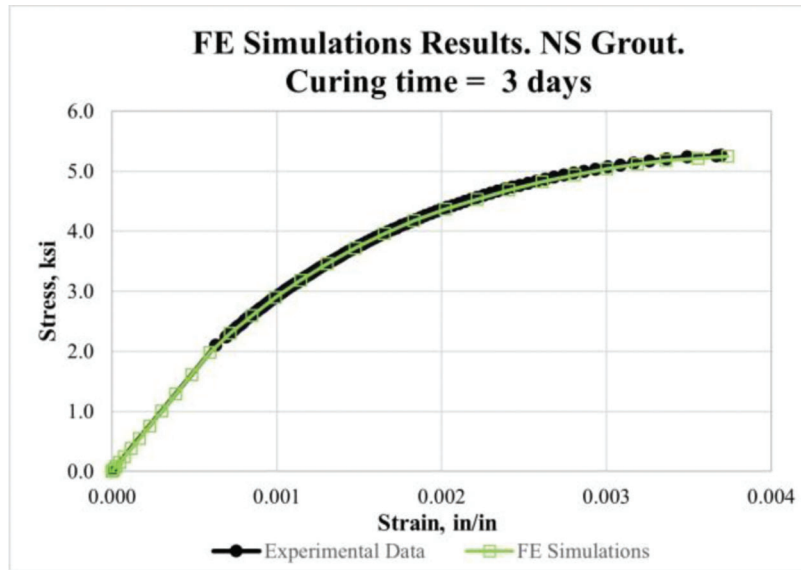


Figure 4.64 Comparison of FE simulations and experimental data: NS Grout.

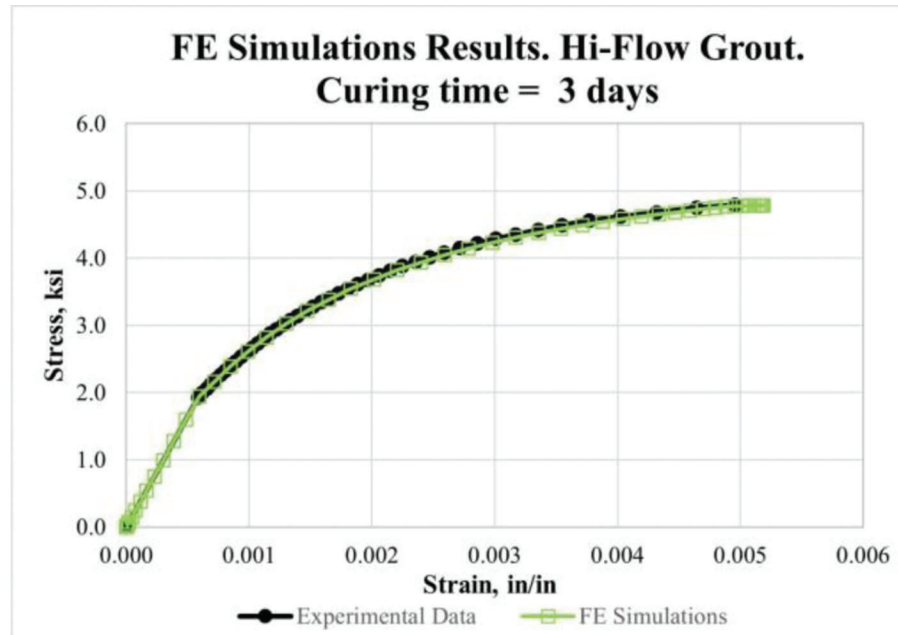


Figure 4.65 Comparison of FE simulations and experimental data: Hi-Flow Grout.

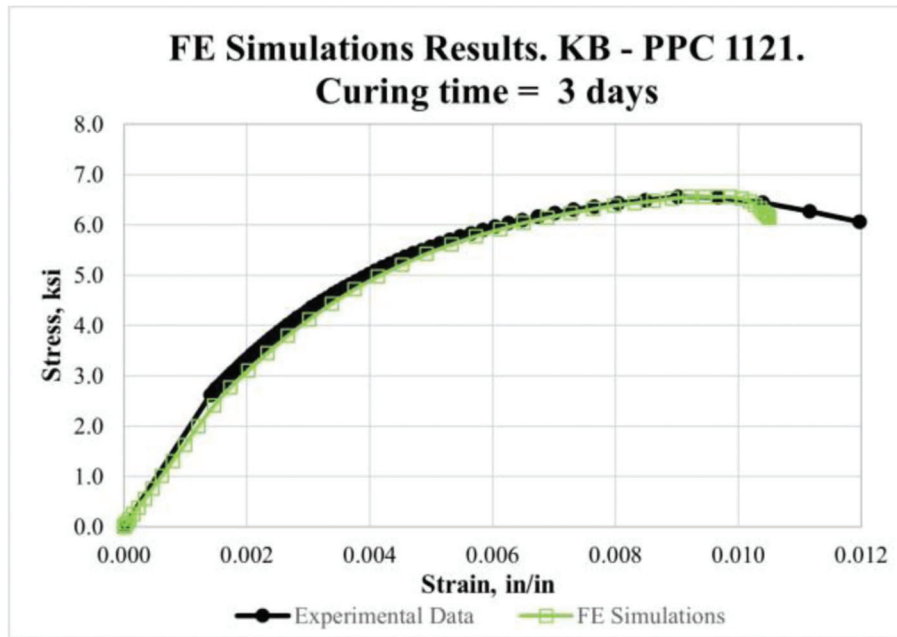


Figure 4.66 Comparison of FE simulations and experimental data: Kwik Bond-PPC 1121.

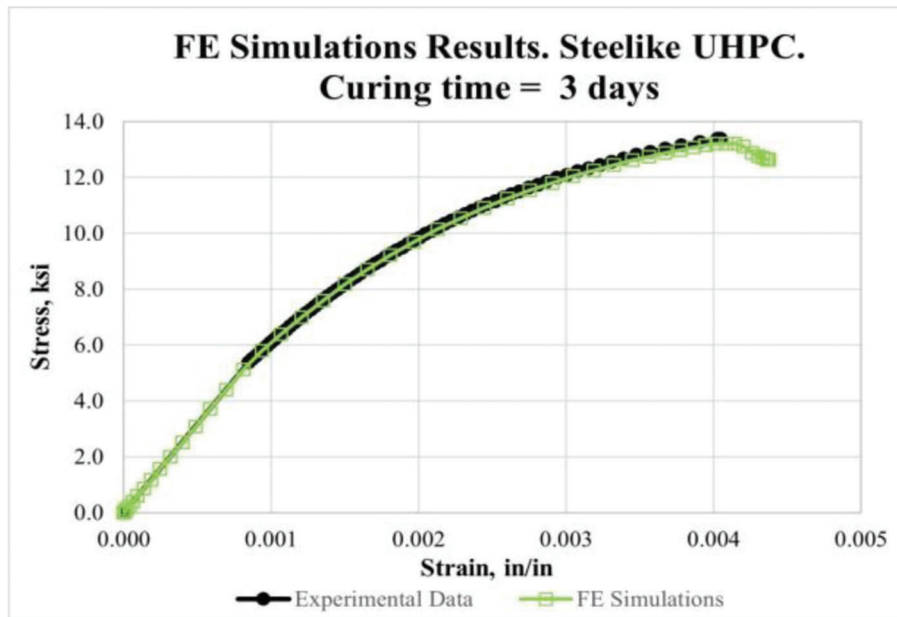


Figure 4.67 Comparison of FE simulations and experimental data: Steelike UHPC.

TABLE 4.12
Material properties: modulus of elasticity and compressive strength

Material	Modulus of Elasticity, ksi	Compressive Strength f'_c , ksi	$0.4 f'_c$, ksi
NS Grout	2,650	5.26 ksi	2.11 ksi
Hi-Flow Grout	3,300	4.79 ksi	1.92 ksi
Kwik Bond-PPC 1121	1,650	6.57 ksi	2.63 ksi
UHPC	6,350	13.39 ksi	5.36 ksi

5. EXPERIMENTAL EVALUATION AND OBSERVATIONS

Seven large-scale experiments were performed on hot-rolled W24×68 steel girders with section loss, in the Bowen Laboratory at Purdue University. These girders were retrieved from the demolished bridges that were part of the North Split Reconstruction project in downtown Indianapolis. The experimental program consisted of testing non-corroded, corroded, and five repaired steel girders using the sandwich panel repair method. This repair method was selected from five proposed novel repair methods using the House of Quality Matrix (Section 3.2). The obtained experimental data was used to validate numerical models and create a design approach for the sandwich panel repair method. The test matrix, test setup details, sensor layouts, specimen details, and experimental data with observations are described in the following sections.

5.1 Test Matrix

The test program comprised seven experiments, two on non-corroded and corroded girders without repair and five on repaired specimens with variations in bearing length, infill material, and location and length of grout/concrete panels. The parameters such as section loss profile, girder length, sectional and material properties of a girder, threaded rod diameter, and filler material properties remained constant.

Field inspections revealed challenges in accessing areas behind partial depth transverse stiffener making the encasement behind them unfeasible without detaching the diaphragm (Figure 5.1). However, instances of severe diaphragm corrosion, illustrated in Figure 5.2, may necessitate diaphragm replacement, thereby creating an opportunity for the practicality of encasement behind the partial stiffener. In such situations, the newly installed diaphragm can be strategically designed with reduced depth to facilitate the implementation of the sandwich panel repair method.

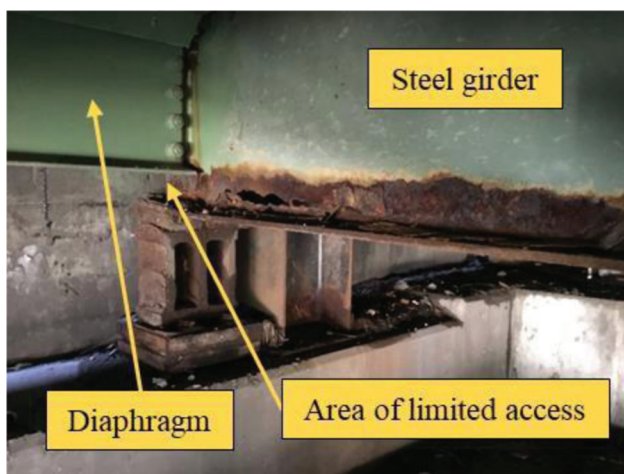


Figure 5.1 Corroded girder end.

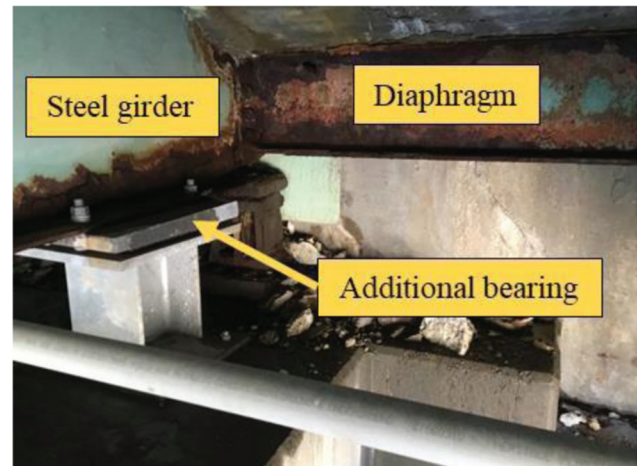


Figure 5.2 Additional bearing placement.

Moreover, an alternative approach involves providing additional support, a technique successfully employed by INDOT (Figure 5.2). Preliminary finite element simulations indicate that the additional bearing alone does not significantly enhance the bearing capacity of the corroded girder. However, when combined with the sandwich panel repair method, the synergy of the additional support proved to be efficient.

The test matrix presented in Table 5.1 summarizes essential information about each of the seven specimens. The bearing length varied and was equal to either 8 in. (one support) or 17 in. (two supports with a 1-in. gap in between). For repaired specimens, Specimen 3–Specimen 7, the number of threaded rods was constant and equal to 13 with the threaded rod layouts shown in Figure 5.3 and Figure 5.4. The threaded rods used were medium-strength Grade B7 with nominal ultimate and yield strengths of 125 ksi and 105 ksi, respectively, and were uniformly distributed over the entire length and height of the grout/concrete panel. A design approach that was developed for the calculation of the required number of rods is explained in Chapter 9. The infill material used for the repair varied between Specimen 3 to Specimen 7. A detailed description of the material properties that were derived for filler materials, NS Grout and Kwik Bond PPC-1121, can be found in Chapter 4.

5.2 Test Setup

Five out of seven large-scale tests were performed using the test setup illustrated in Figures 5.5 through 5.9. The test setup comprised a loading frame and a bracing frame. The loading frame was post-tensioned to the strong floor using four 1.75" DYWIDAG threaded bars ($F_u = 150$ ksi) to resist the uplift of the frame during the static load application. Each of the four DYWIDAG bars was post-tensioned to 125 kips. Initial finite element simulations indicated an anticipated maximum applied load not exceeding 500 kips. Therefore, a 250-ton (550 kips) ENERPAC actuator

TABLE 5.1
Test matrix

Specimen Number	Corrosion Level	Bearing Length (in.)	Number of Rods	Strength of a Rod, F_y (ksi)	Strength of a Rod, F_u (ksi)	Encasement Behind a Partial Stiffener	Infill Material
1	Light	8	N/A	105	125	N/A	N/A
2	Medium	8	N/A	105	125	N/A	N/A
3	Medium	8	13	105	125	No	Grout
4	Medium	17	13	105	125	No	Grout
5	Medium	17	13	105	125	No	Kwik Bond
6	Medium	8	13	105	125	Yes	NS Grout
7	Medium	8	13	105	125	Yes	Kwik Bond

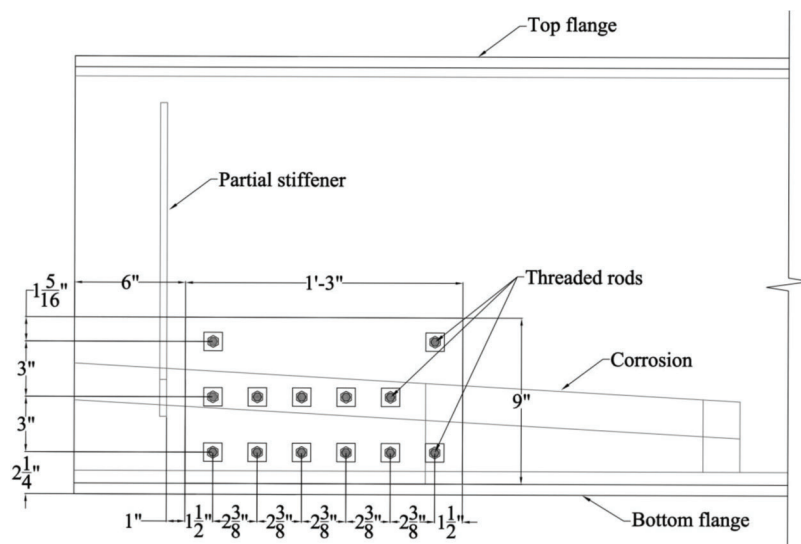


Figure 5.3 Threaded rod layout for Specimens 3–5: AutoCAD drawing.

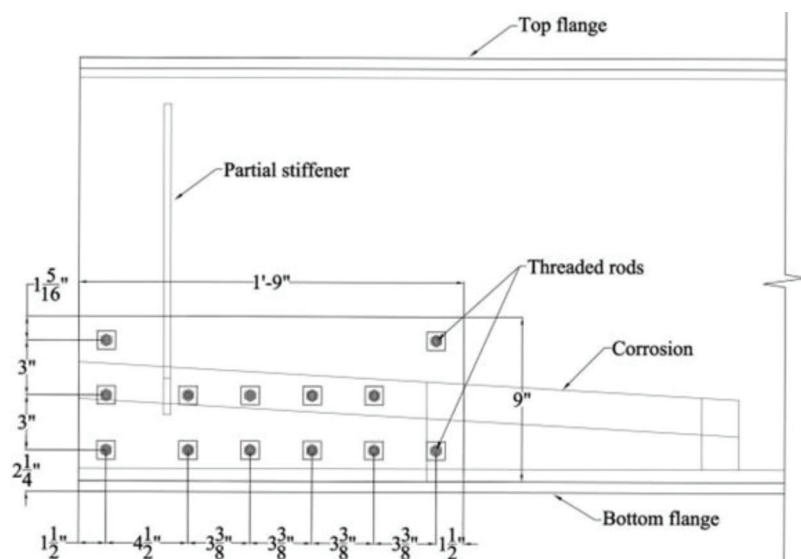


Figure 5.4 Threaded rod layout for Specimens 6–7: AutoCAD drawing.

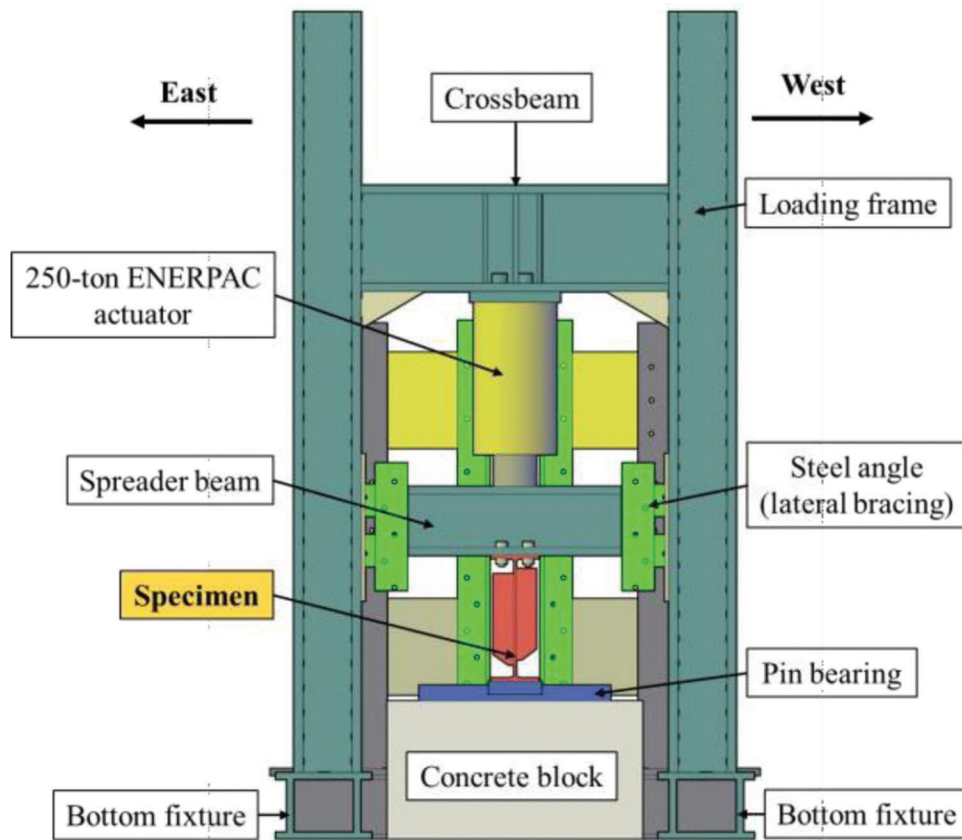


Figure 5.5 3D model of the test setup: front view.

(Model No. CLRG-25012) was attached to the crossbeam of the loading frame to apply load to the specimens.

The lateral bracing frame was located 3 ft. behind the loading frame (center to center) to prevent out-of-plane movement of the specimen and mitigate lateral torsional buckling effects on the anticipated bearing failure (Figure 5.9). The bracing frame assembly comprised the bottom fixture, two columns, three channel sections, and two angle sections as shown in Figure 5.6. The bracing frame was post-tensioned using 1.25" DYWIDAG threaded bars ($F_u = 150$ ksi). Based on preliminary structural analysis performed in Abaqus and SAP 2000, the two DYWIDAG bars were post-tensioned to 100 kips. Teflon plates were provided at the contact locations between the specimen and the steel angles (bolted to the bracing frame), ensuring smooth and frictionless interaction.

As seen in Figure 5.8, the 250-ton actuator was attached to the crossbeam of the loading frame that had three bearing stiffeners welded at the location of the attachment to prevent bearing failure. The load was applied to the top flange of the girder using a spreader beam connected to the top flange using four high-strength bolts. Hydro-stone gypsum cement was used to level the spreader beam to ensure the load was applied vertically, and this connection detail can be found in

Figure 5.11. The girder was restrained to displace out-of-plane in mid-span, which prevented lateral torsional buckling. Angles were bolted to the bracing frame with the Teflon plate placed in between to ensure non-friction sliding along the surface of the steel angle (Figure 5.12).

Two concrete blocks were positioned at both ends of the specimen, and bearings were subsequently installed on top of them. Hydro-stone gypsum cement was meticulously applied to ensure the leveling of both bearings and concrete blocks. The bearings comprised of a bottom half-cylindrical steel block and an upper component that allowed rotation (Figures 5.13 and 5.14). The half-cylindrical component of the near-end bearing (the closest to the applied load) was welded to the bottom steel plate to prevent any translational movement, effectively making the bearing assembly serve as a pinned support. In contrast, the far-end bearing functioned as a roller with translation movement in the Y-Z plane and rotation along the Y-axis.

For the last two experiments, an additional bearing was installed near the corroded end as shown in Figure 5.15 and Figure 5.16, effectively increasing the bearing length from 8" to 17". This increase in the bearing length significantly contributed to enhancing the web crippling capacity of the specimen. The fully assembled test setup in Bowen Laboratory is shown in Figure 5.17.

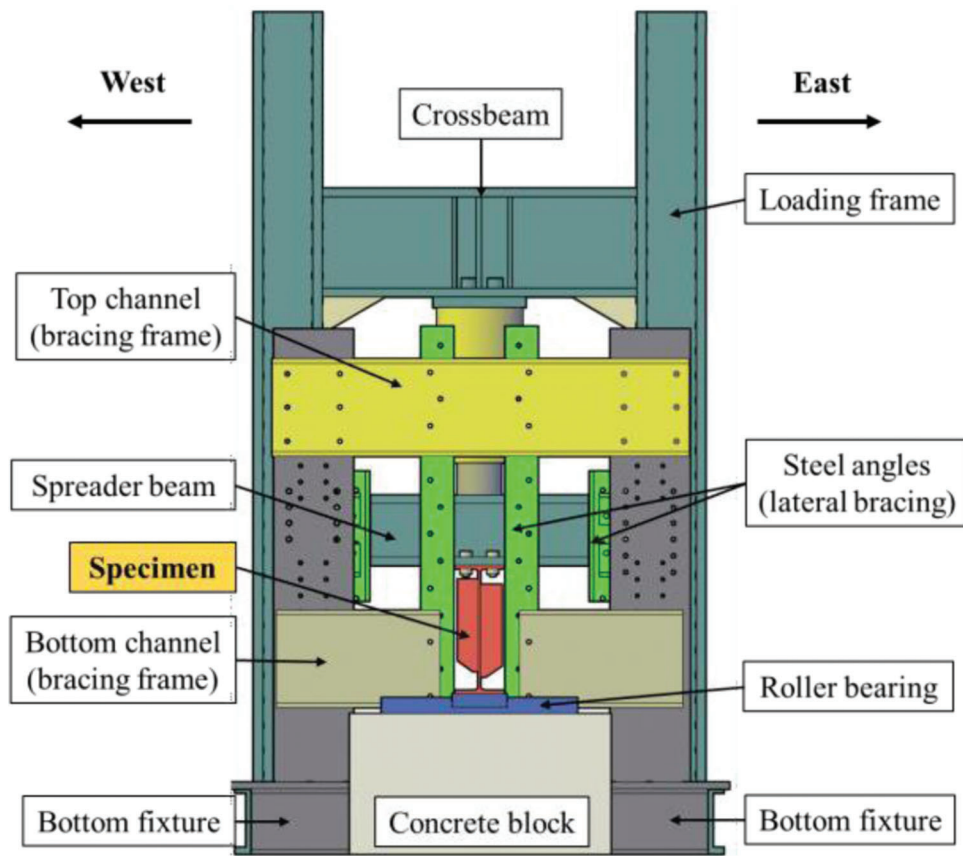


Figure 5.6 3D model of the test setup: back view.

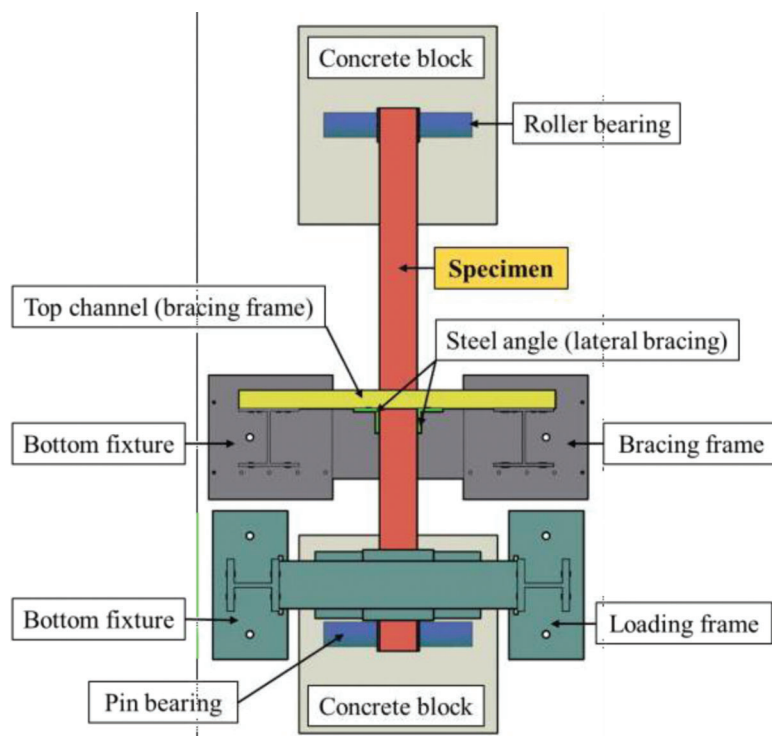


Figure 5.7 3D model of the test setup: top view.

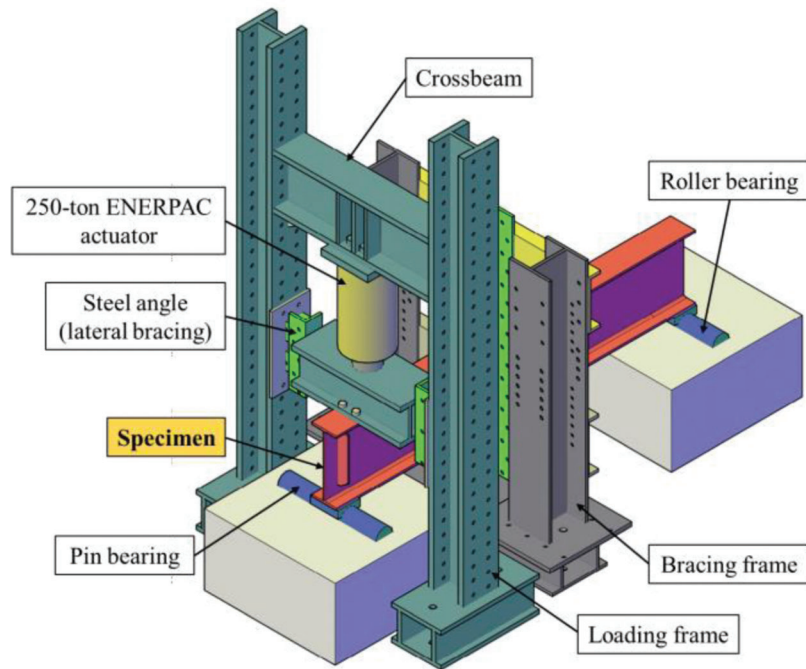


Figure 5.8 3D model of the test setup: isometric view.

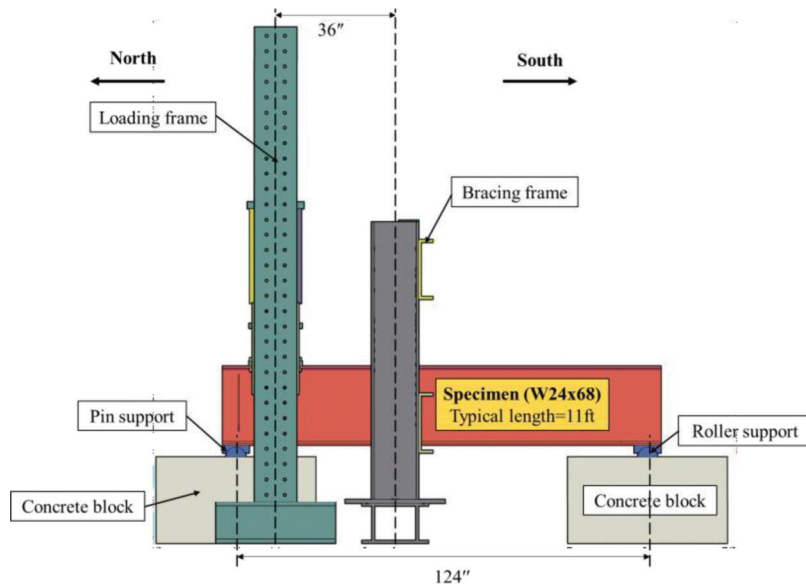


Figure 5.9 3D model of the test setup: side view.

5.3 Material Properties

The specimens used in the experimental investigation were obtained from the same bridge as the specimens investigated by Kanakamedala, Seo, Varma, Connor, and Tarasova (2023). Therefore, identical material properties were expected. In the above study, the material properties of structural steel were obtained by performing tensile coupon tests following ASTM E8-22 (ASTM, 2022a) specifications. Tensile coupons were cut from steel girders in directions longitudinal and transverse to bending stresses and tested using the

INSTRON machine. The measured yield strength (F_y) and measured ultimate strength (F_u) were determined to be 45 ksi and 66 ksi, respectively. These values were used to calculate the expected web crippling capacities by AASHTO (AASHTO, 2020) provisions.

5.4 Sensor Layout

Standard sensor layouts for Specimens 1–7 are presented in Figure 5.18 through Figure 5.25, and Figure 5.28. The number of strain gauges (SG), displacement transducers (DT), and string potentiometers

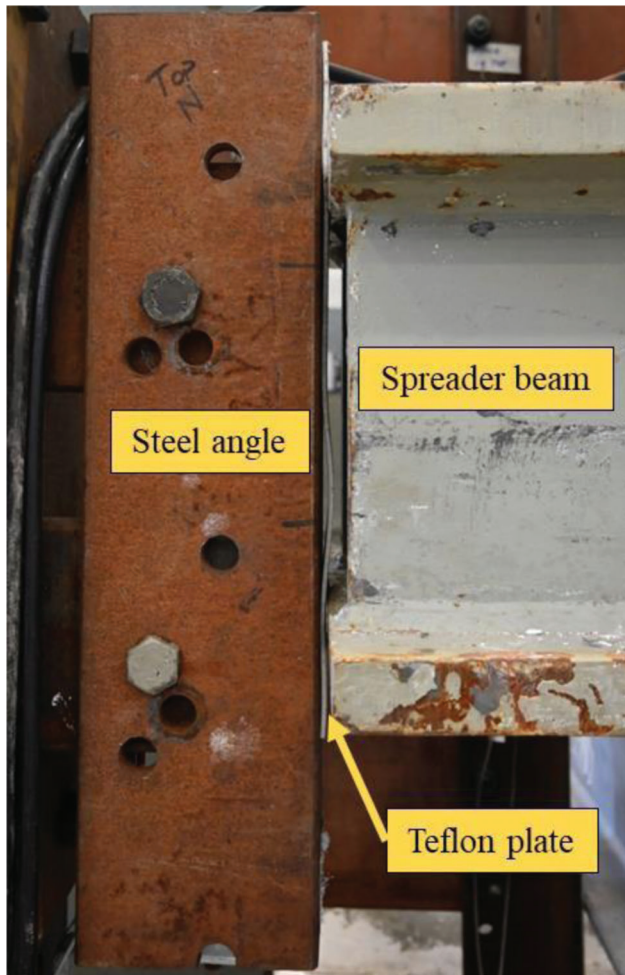
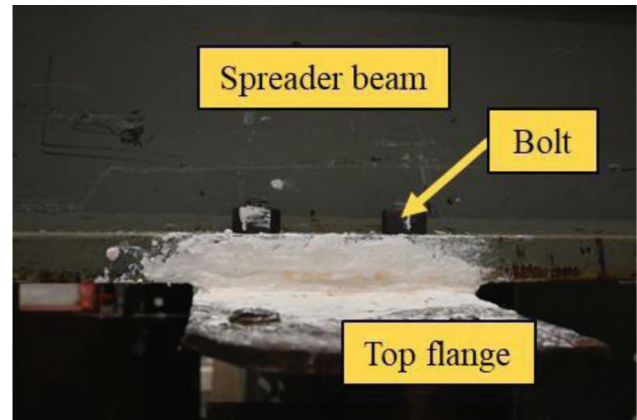
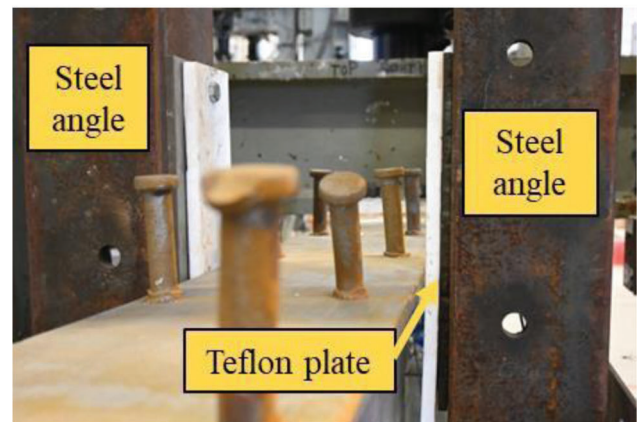


Figure 5.10 Steel angle (lateral bracing): spreader beam connection.



(a)



(b)

Figure 5.11 (a) Spreader beam: top flange connection. (b) Top flange: steel angle connection.



Figure 5.12 Roller support at the far end.

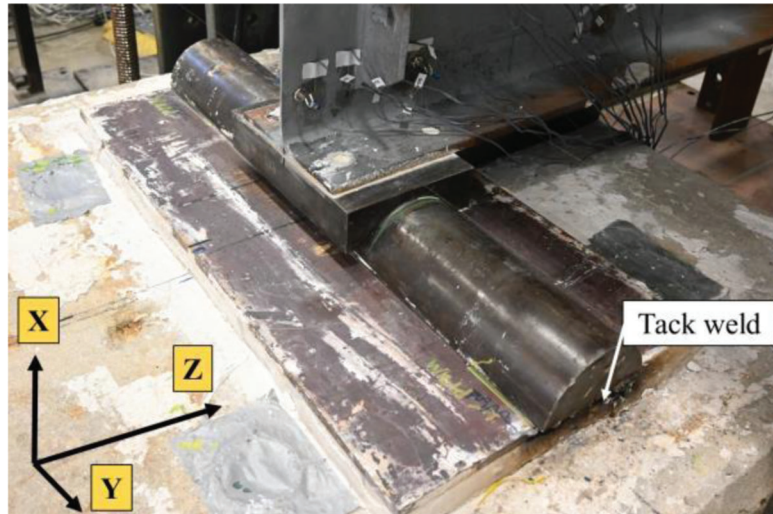


Figure 5.13 Pin support at the corroded end.

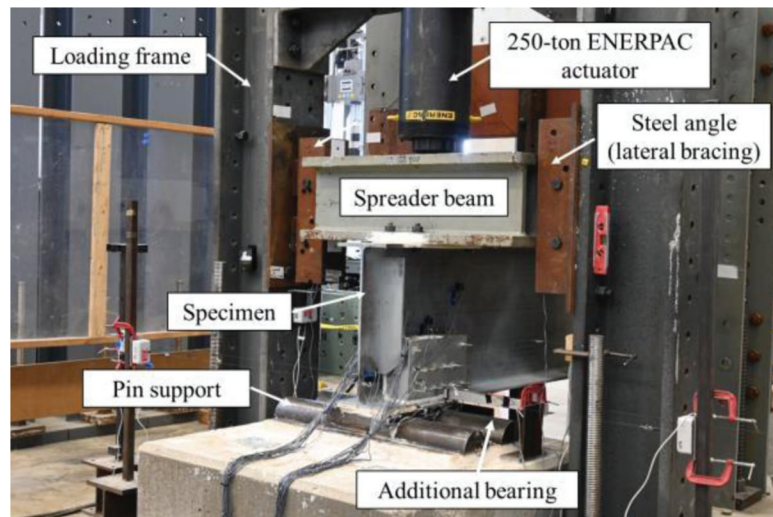


Figure 5.14 Test setup for Specimens 4-5.



Figure 5.15 Additional bearing (tack welded).

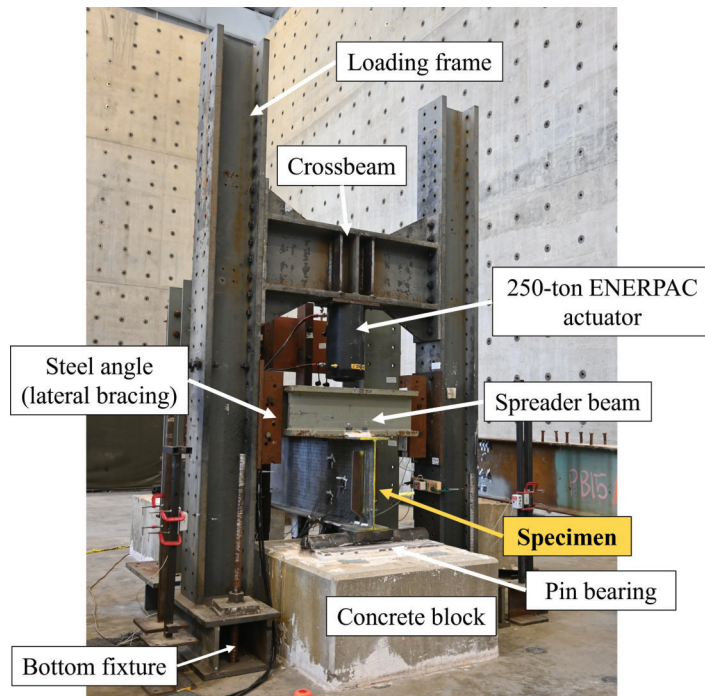


Figure 5.16 Test setup assembly in Bowen Laboratory.

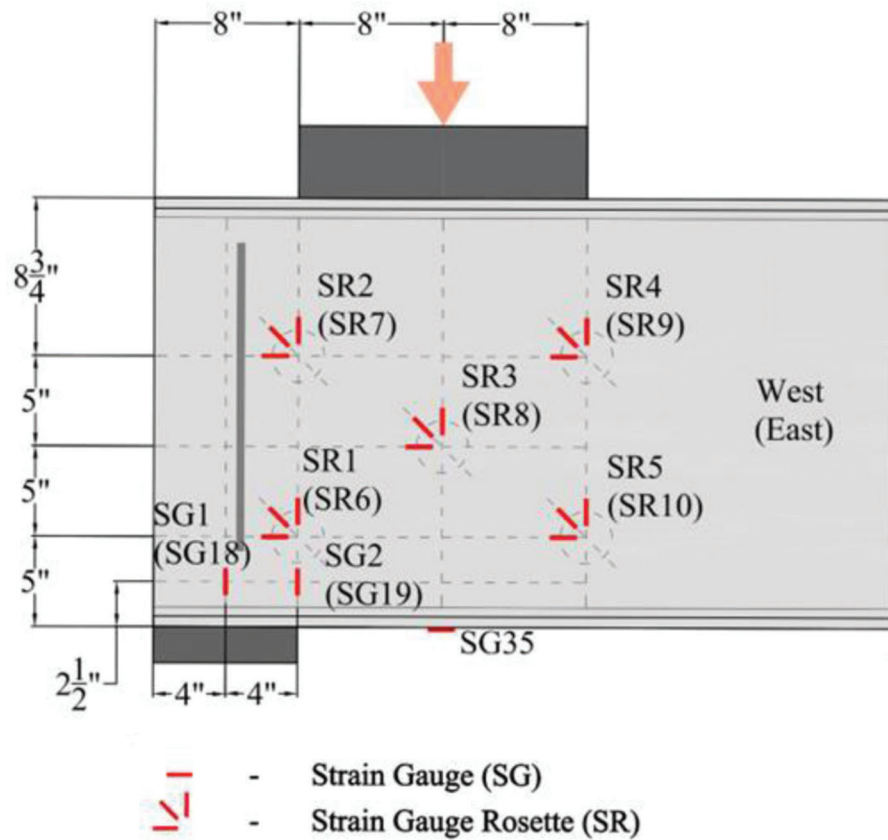


Figure 5.17 Strain gauge layout (side elevation): Specimen 1.

(SP) varied from test to test and therefore sensor layouts were divided into different subsections.

- Specimen 1
- Specimen 2

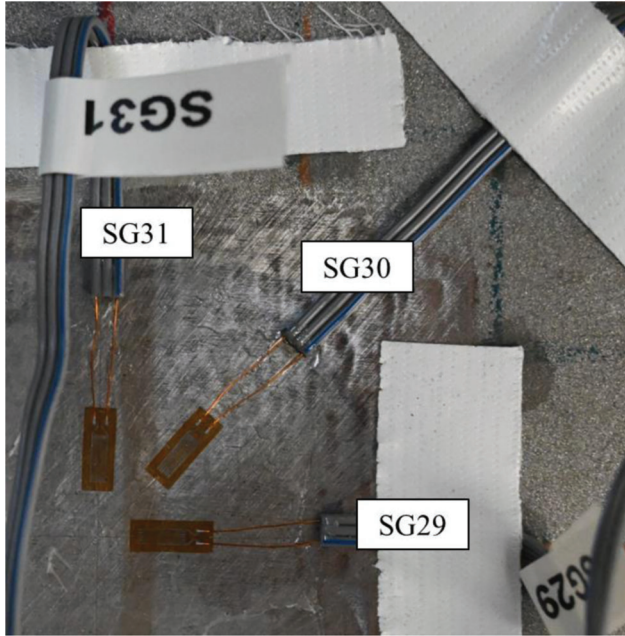


Figure 5.18 Example of installed strain gauge rosette (SR).

- Specimens 3, 6–7
- Specimens 4–5

5.4.1 Specimen 1

Specimen 1, representing a non-corroded W24 × 68 girder had 35 strain gauges (SG), 7 string potentiometers (SP), and 3 displacement transducers (DT) (Figure 5.18). The anticipated failure mode for this specimen was web local crippling, and accordingly, the sensor placement was strategically aligned with the expected behavior. Specifically, strain gauges SG1, SG 2, SG18, and SG19 were positioned above the bearing at distances of 4" and 8" from the near end of the specimen. These strain gauges were oriented vertically, aligning with the expected failure mode of web local crippling. Additionally, five strain gauge rosettes (SR2–SR10) were placed on each side of the web to calculate maximum and minimum principal strains (Figure 5.19).

Furthermore, a strain gauge (SG35) was installed on the bottom flange underneath the point of the applied load to monitor the occurrence of flexural yielding. Strain gauges used for instrumentation were post-yield, single-axis YEFLAB-5-5LJCT-F series with a gauge length of 5 mm that could record large strains up to 15%. CN adhesive was used for strain gauge attachment to an adequately prepared steel surface.

Additionally, a total of ten displacement sensors were installed to capture displacement both in-plane

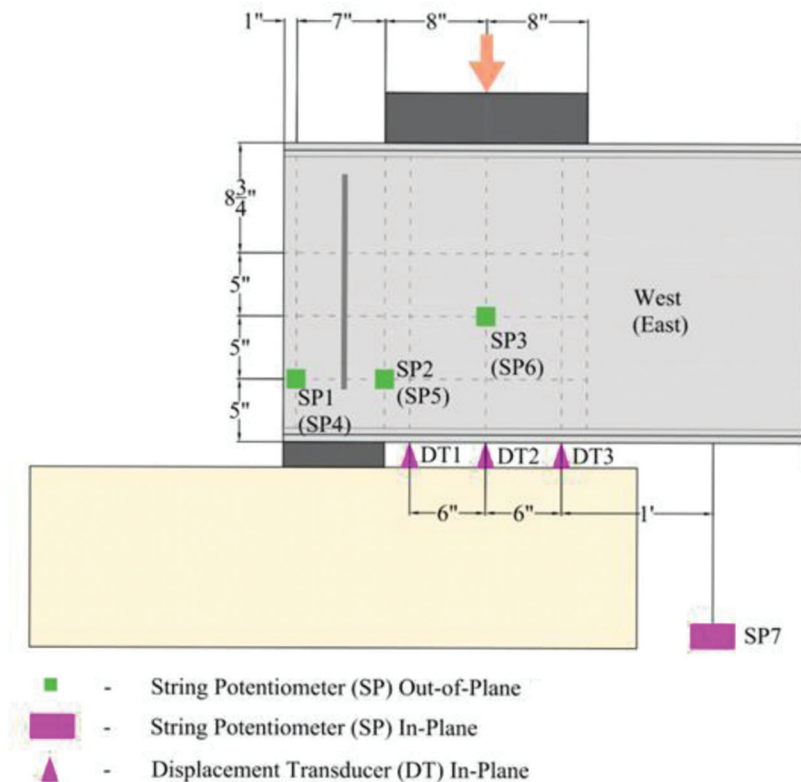


Figure 5.19 Displacement sensor layout (side elevation): Specimen 1.

and out-of-plane. This displacement sensor array comprised seven string potentiometers with strokes of 5"–10" and three displacement transducers with 1" stroke (Figure 5.20 and Figure 5.21). The critical sensor, DT2, located on the bottom flange at 16 in. from the girder end, recorded the vertical displacement of the bottom flange during the experiment. String potentiometers SP1, SP2, and SP3 were installed on the

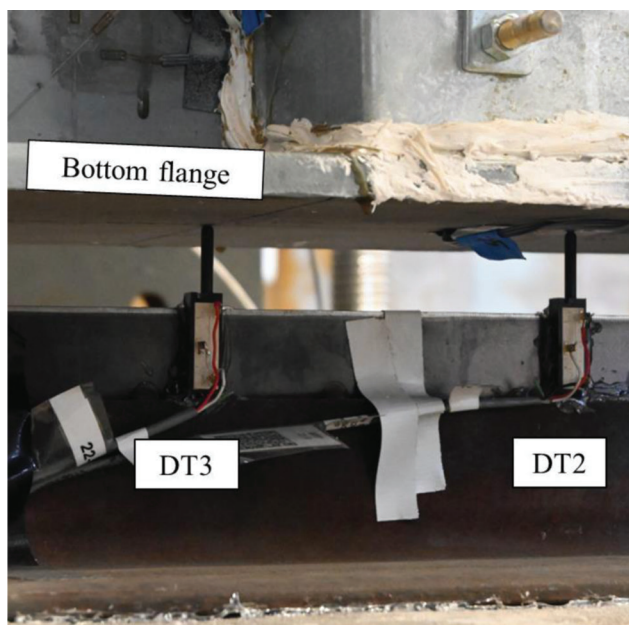


Figure 5.20 Example of installed displacement transducers.

web at 1", 8", and 16" away from the girder end, respectively, to capture the out-of-plane displacement.

5.4.2 Specimen 2

Sensor layouts for the remaining specimens remained consistent; therefore, only a few adjustments were made to the sensor layout of Specimen 2. Section loss in the specimens affected their deformed shape, leading to slight changes in the location of the displacement sensors. The anticipated failure mode for this specimen was web local crippling, and accordingly, the sensor placement was strategically aligned with the expected behavior. Based on the data obtained through numerical simulations, SP1 (SP4) and SP2 (SP5) were moved downward because the maximum out-of-plane displacements occurred approximately 3.5 in. from the bottom flange.

To account for section loss and to install strain gauge rosettes in regions with uniform thickness, the strain gauge rosettes were also relocated. Additionally, SG1(SG18) and SG2(SG19) were shifted closer to the girder end—2 in. and 4 in. away from it, respectively. The updated sensor layouts are presented in Figure 5.22 and Figure 5.23.

5.4.3 Specimen 3, Specimen 6, 7

The next group of specimens (Specimen 3, 6, and 7) had an identical sensor layout (Figure 5.24 and Figure 5.25). The anticipated failure modes for these specimens were web local crippling, concrete/grout crushing, and

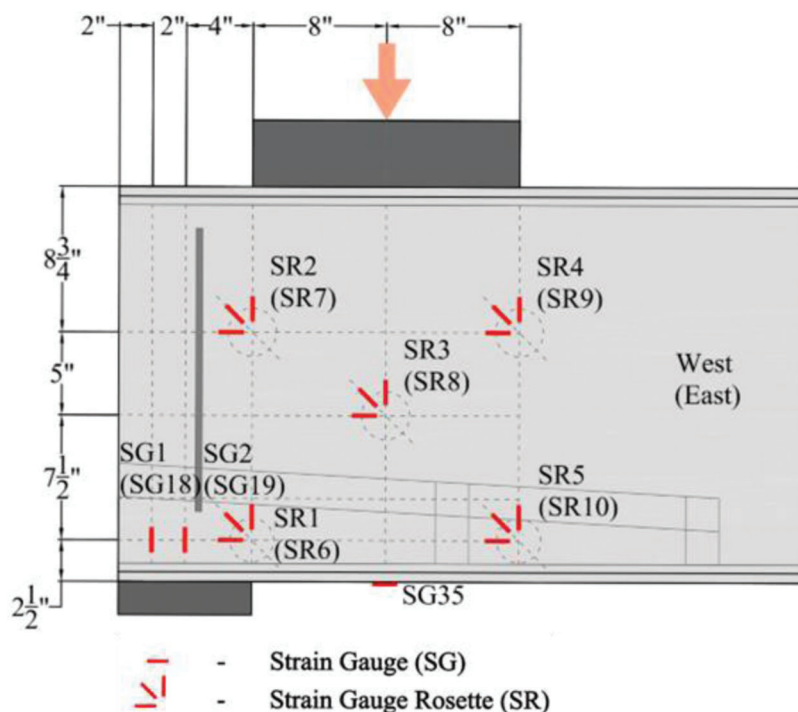


Figure 5.21 Strain gauge layout (side elevation): Specimen 2.

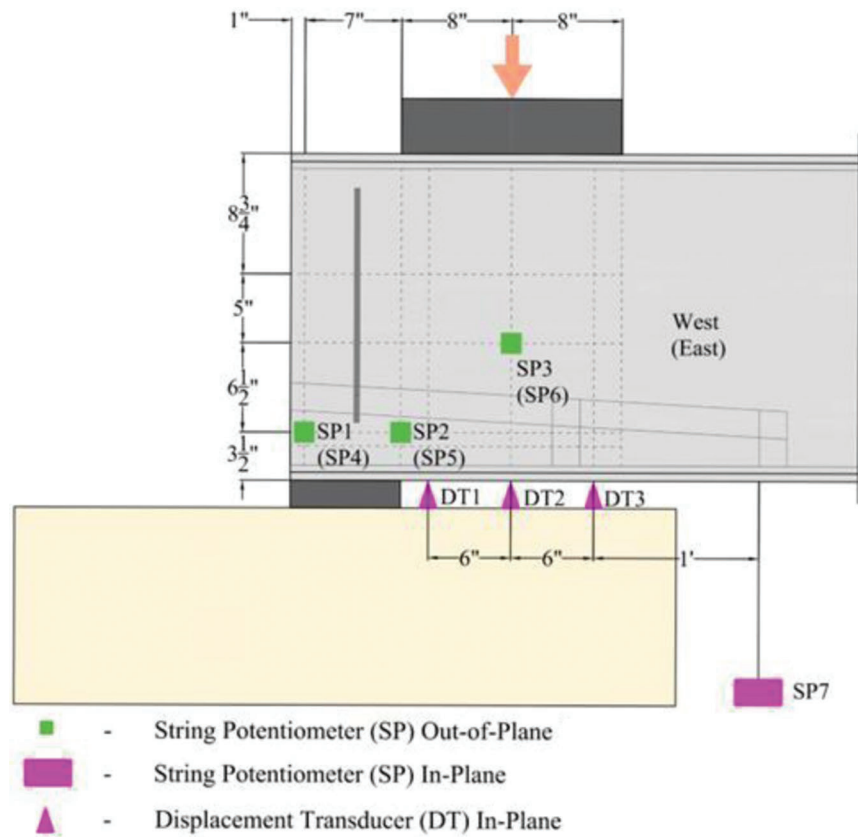


Figure 5.22 Displacement sensor layout (side elevation): Specimen 2.

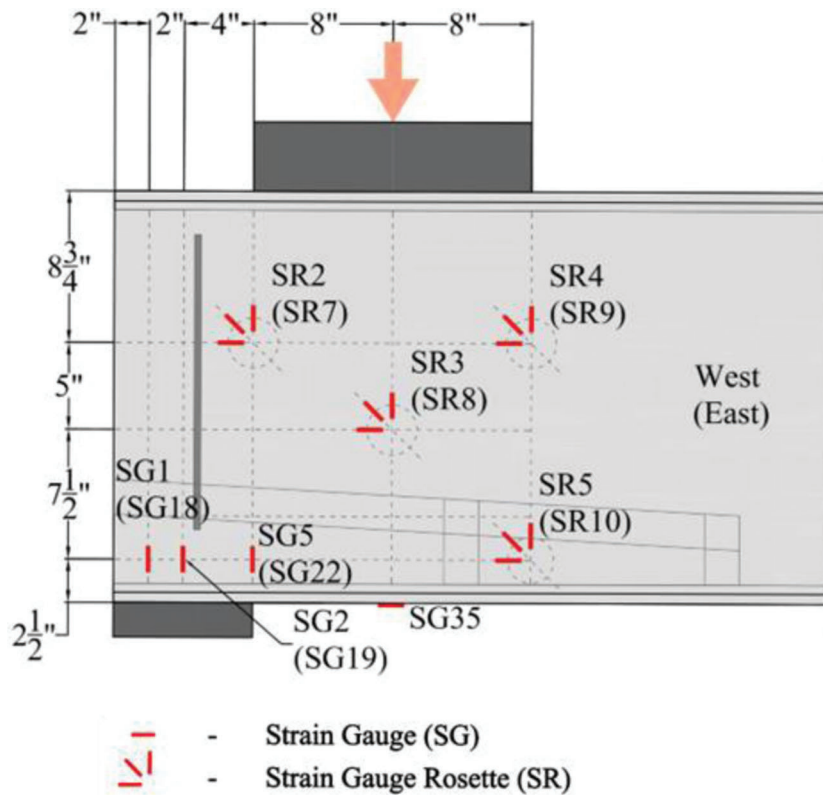


Figure 5.23 Strain gauge layout (side elevation): Specimens 3, 6, and 7.

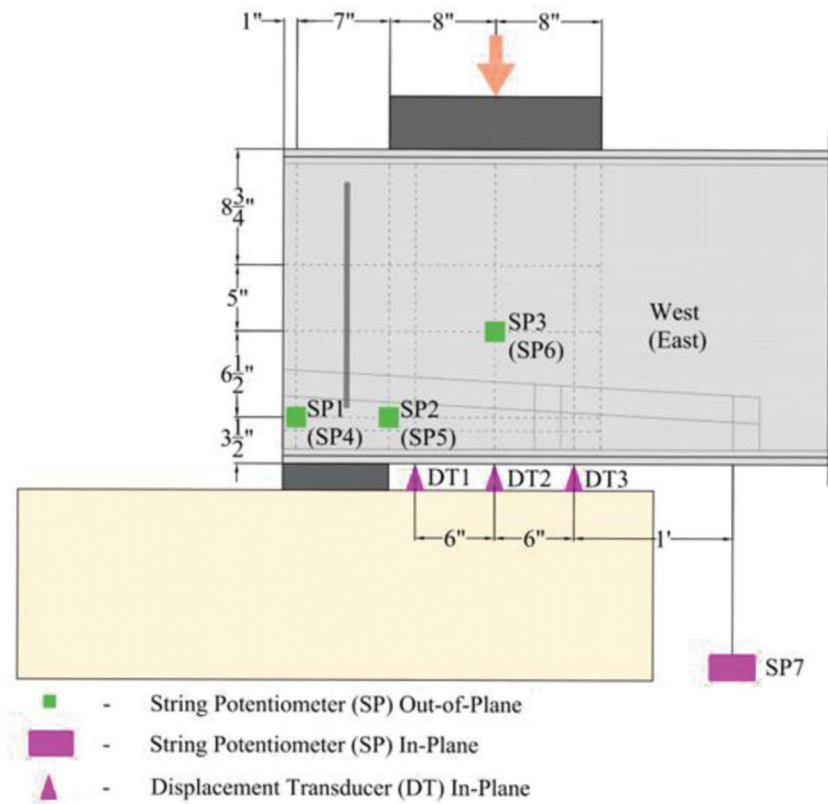


Figure 5.24 Displacement sensor layout (side elevation): Specimens 3, 6, and 7.

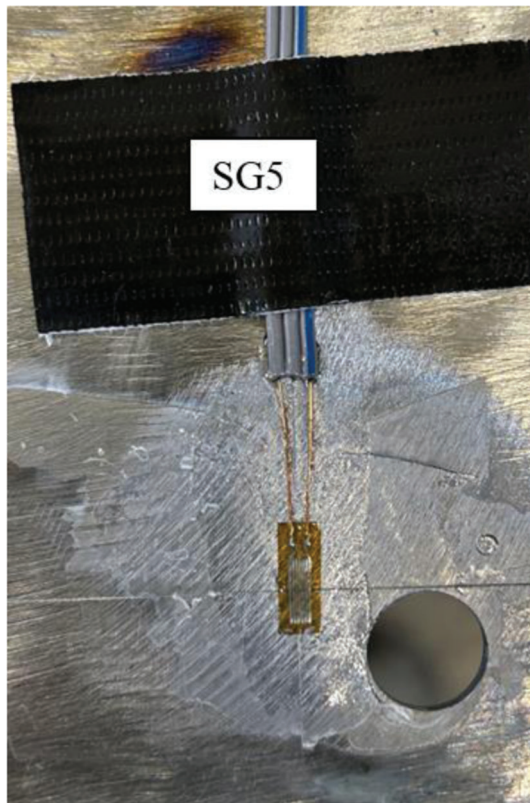


Figure 5.25 Strain gauge before applying sealant.

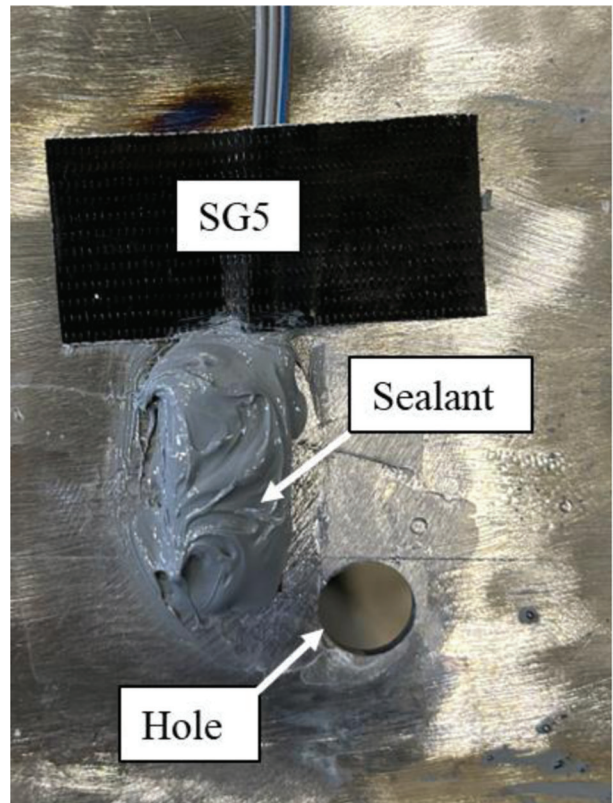


Figure 5.26 Strain gauge after applying sealant.

threaded rod rupturing, and accordingly, the sensor placement was strategically aligned with the expected behavior. Besides section loss, these specimens also had holes in the web (for the installation of threaded rods) and the grout/concrete encasement. Due to a drilled hole close to the area where SR1 and SR6 were initially installed, it was decided to replace the strain gauge rosette with one vertical strain gauge on each side (SG5 and SG22). Furthermore, because of the grout/concrete encasement, strain in this region was mainly vertical, and a strain gauge rosette was redundant.

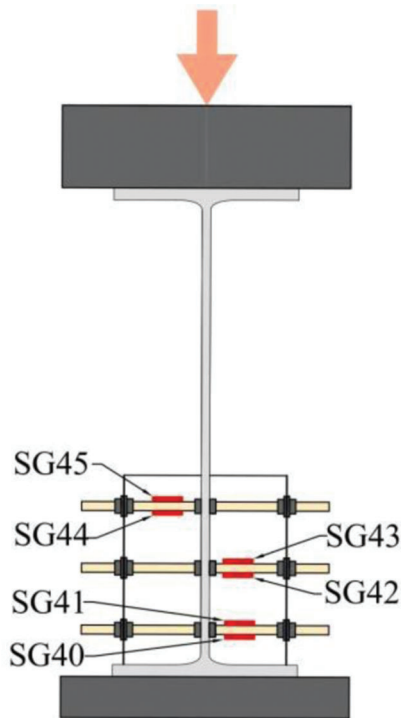


Figure 5.27 Strain gauge layout: threaded rods.

Additional measures to protect the strain gauge SG5 (SG22) were taken because of cementitious grout/polymer concrete encasement. For instance, DOWSIL™ 3145 RTV Mil-A-46146 Adhesive/Sealant was spread on top of the strain gauge and two lead wires to protect them from moisture and aggregates that the grout/concrete contained (Figure 5.26 and Figure 5.27).

5.4.3.1 Threaded rods instrumentation. The strain gauge layout for threaded rods was the same for all repaired steel girders, from Specimen 3 to Specimen 7, as shown in Figure 5.28. Both the top and bottom surfaces of the threaded rod were instrumented to accurately capture expected bending and tensile deformations. The installation process of strain gauges on the threaded rods consisted of three steps (Figure 5.29). Before cleaning the surface, the threads were ground off to get a smooth surface on which a strain gauge could be installed (Step 1). This was followed by a standard procedure of surface cleaning and the application of CN adhesive to attach the strain gauge to the steel surface. Furthermore, DOWSIL sealant was applied on top to protect the strain gauge from aggregates and moisture in the concrete (Step 2). Once the sealant was cured, the surface was wrapped in electrical tape for additional protection (Step 3).

5.4.4 Specimens 4 and 5

Finally, the last set of sensor layouts was developed for Specimen 4 and Specimen 5. The anticipated failure modes for these specimens were web local crippling, concrete/grout crushing, and threaded rod rupturing, and accordingly, the sensor placement was strategically aligned with the expected behavior. Additionally, the development of sensor layouts was governed by the geometry of the repair and available space. Therefore,

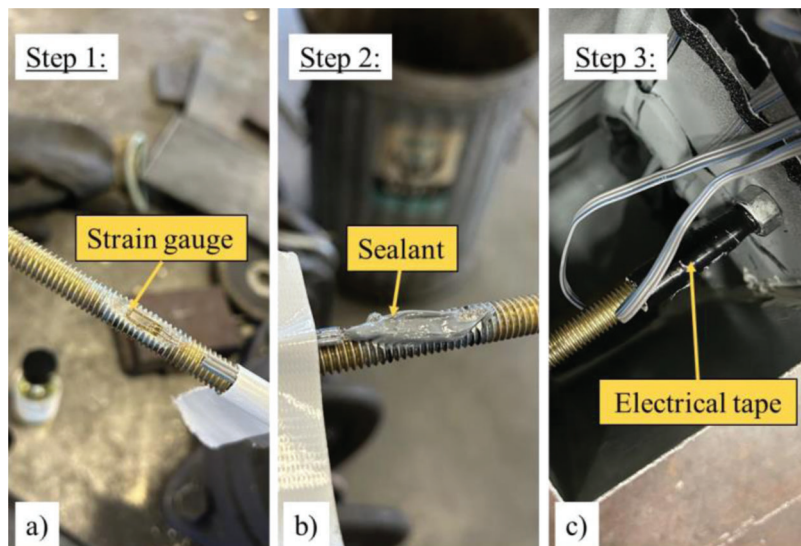


Figure 5.28 Strain gauge installation process: (a) Step 1, (b) Step 2, and (c) Step 3.

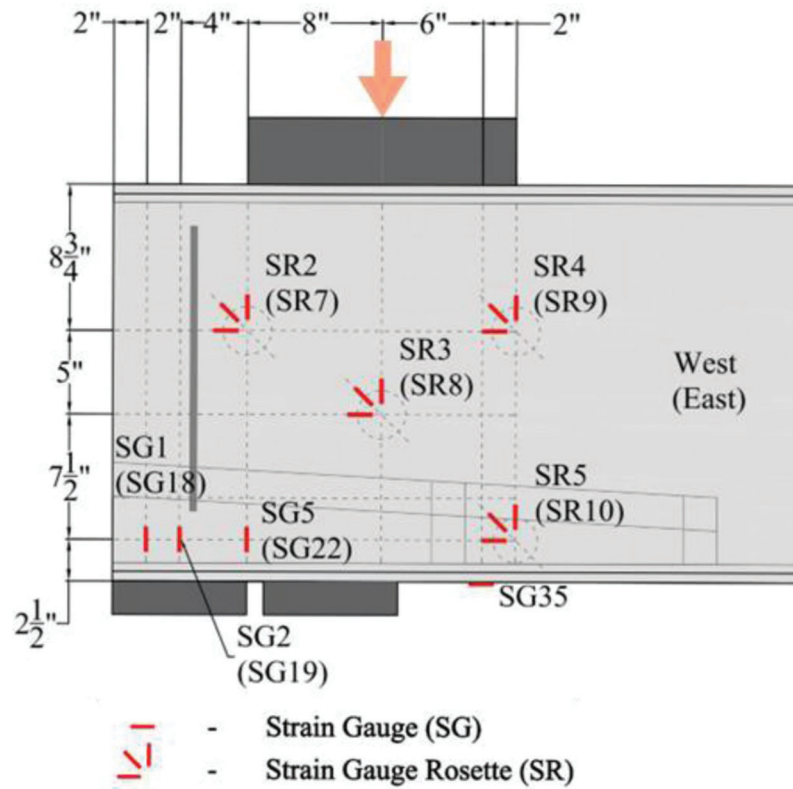


Figure 5.29 Strain gauge layout (side elevation): Specimens 4 and 5.

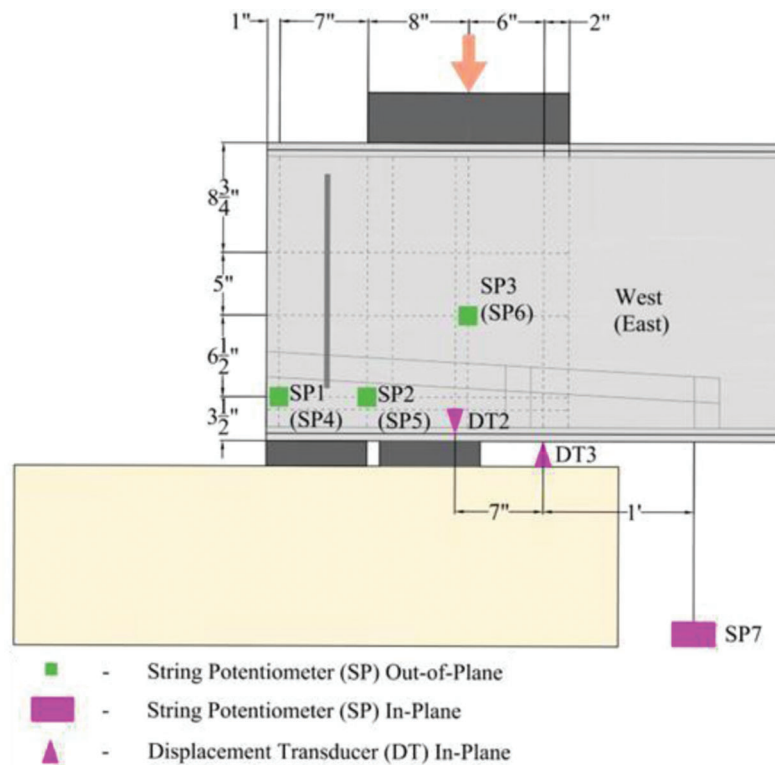


Figure 5.30 Displacement sensor layout (side elevation): Specimens 4 and 5.

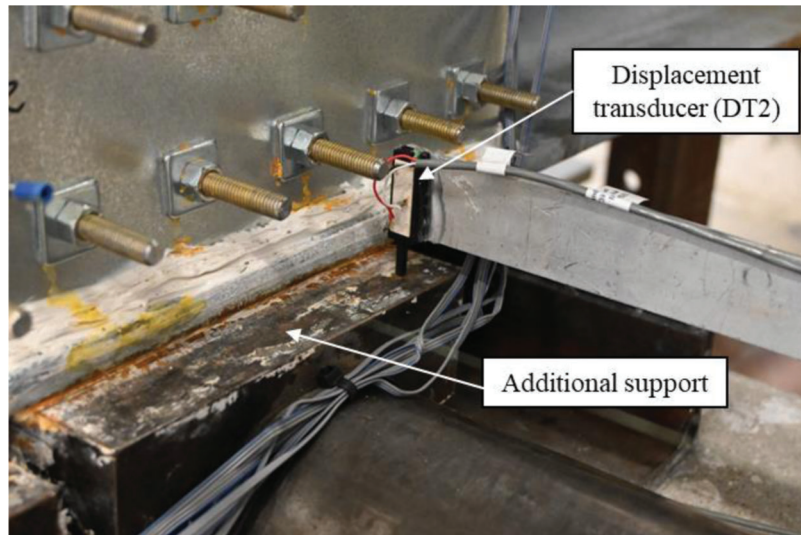


Figure 5.31 Example of DT2 installation for Specimens 4 and 5.

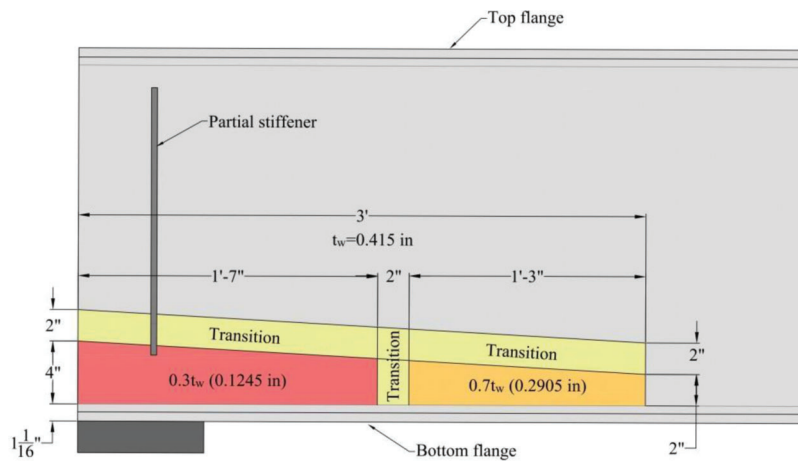


Figure 5.32 Standard section loss profile.

one of the significant changes was shifting SG35 further away from the girder end by 6 in. Due to the additional support placement, access to the previous location was restricted (Figure 5.30). Similarly, because of the lack of space and insignificant expected vertical displacements, DT1 was removed. The approach for DT2 installation changed: in the updated sensor layout, DT2 measured the displacement of the upper part of the bearing (Figure 5.31). In addition, DT2 was moved 1" closer to the girder end due to space limitations produced by threaded rods. A comparison could be made between the previously installed displacement transducer DT2 (Figure 5.21) and the updated version (Figure A.1).

5.5 Specimen Details

5.5.1 Corrosion Profile

The section loss profile utilized in this study was derived by Kanakamedala et al. (2023) based on the

section loss analysis of naturally corroded girders. The derived section loss profile had a trapezoidal shape characterized by two different corrosion levels: medium ($0.7t_w$) and light ($0.3t_w$), with transition regions between them. The girder-end close to the expansion joint area usually exhibits severe corrosion. Consequently, a 70% section loss was induced over the first 19", followed by the transition region, and finally, a 30% section loss over the remaining 15". A similar section loss profile was later introduced in all the specimens except Specimen 1 for consistency, as shown in Figure 5.32. The artificial corrosion was introduced through manual grinding and machine milling, meticulously monitoring the thickness during the process. Measurements were taken every 5–10-minute intervals using a UT gauge.

Accurate section loss measurements were obtained using a high-precision UT gauge (R7900, 0.002 in accuracy) manufactured by REED Instruments. A detailed grid of 1×1 in. was marked over a 4-ft-long segment starting from the corroded girder end. At each grid point, measurements were meticulously obtained,

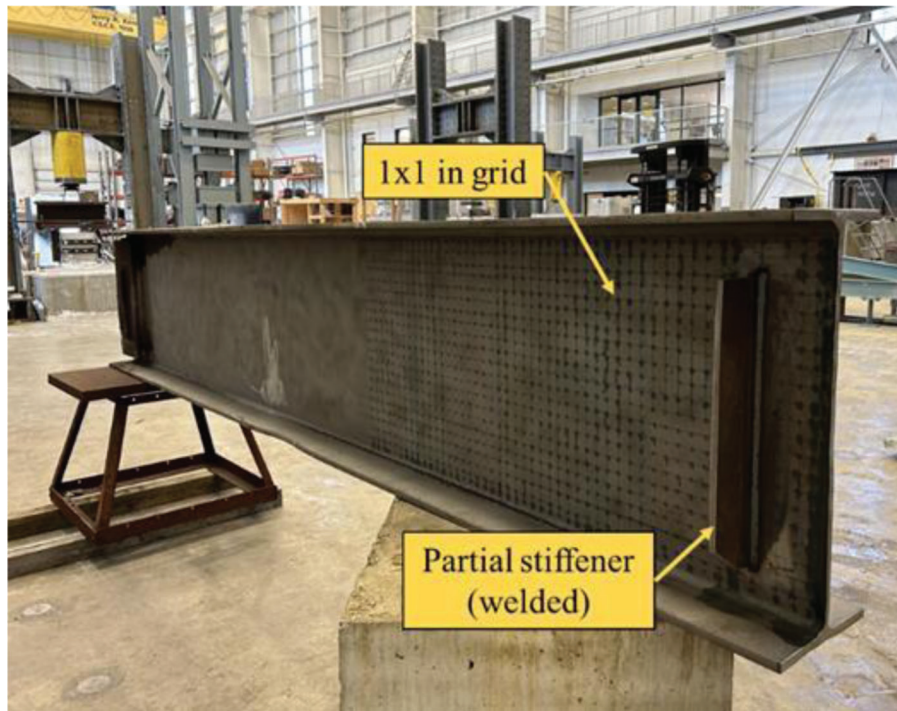


Figure 5.33 Specimen 1: isometric view.



Figure 5.34 Specimen 1: front view.

resulting in an extensive dataset of approximately 1,000 readings. The results of section loss measurements for Specimen 1–7 can be found in Figures B.1 through B.7 in Appendix B. In the contour plots, the deep brown color represents a 50%–75% loss in thickness, the light

brown color represents only a 15%–30% loss, while the grey-filled region indicates a section loss exceeding 75% of the nominal web thickness (t_w). The contour plots were thoughtfully configured to align with the visual hierarchy, where the deeper color directly correlates with the severity of the corrosion.

5.5.2 Specimen 1

The girders obtained from the corroded steel girder bridges in the North Split Reconstruction project were originally 22-ft-long. The girders were cut in half using a plasma cutter resulting in two specimens for testing two girder ends.

Specimen 1 was lightly corroded, 11-ft-long, W24×68 rolled steel girder without partial stiffeners. Therefore, prefabricated partial stiffeners were subsequently welded on both sides of the girder web to simulate conditions representative of an actual steel bridge. Visual inspection, as shown in Figure 5.33 and Figure 5.34, indicated that Specimen 1 exhibited no significant corrosion.

5.5.3 Specimen 2

Specimen 2 was the moderately corroded 11-ft-long steel W24×68 girder with existing partial-depth stiffeners. It could be seen from Figure 5.35 that Specimen 2 had natural (upper part of the girder web) and artificial (the bottom part of the web) corrosion. In the naturally corroded area, a patch was welded behind the partial stiffener to prevent failure as the load was applied in high proximity to this region (Figure 5.36).

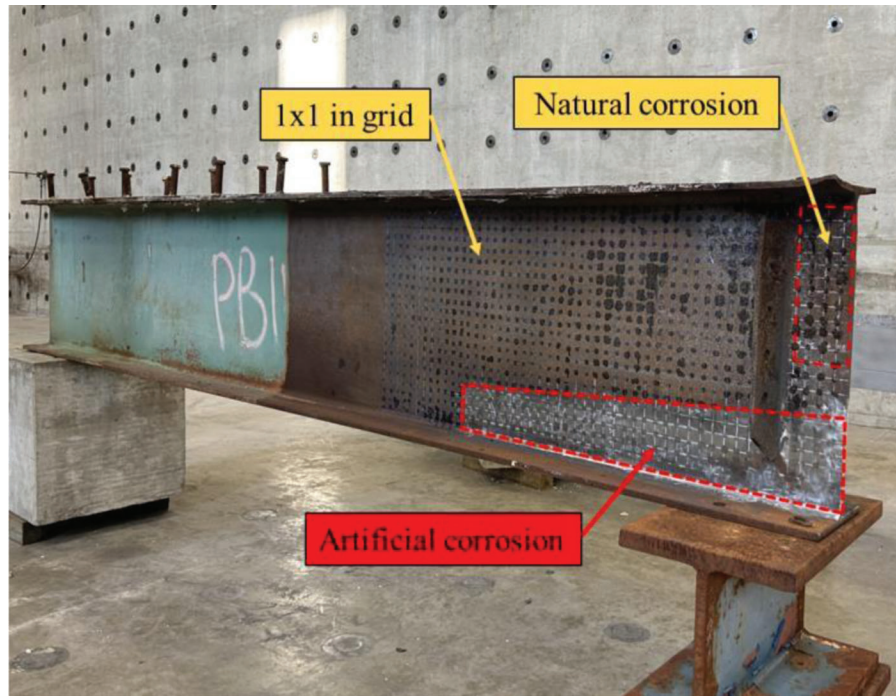


Figure 5.35 Specimen 2: isometric view.

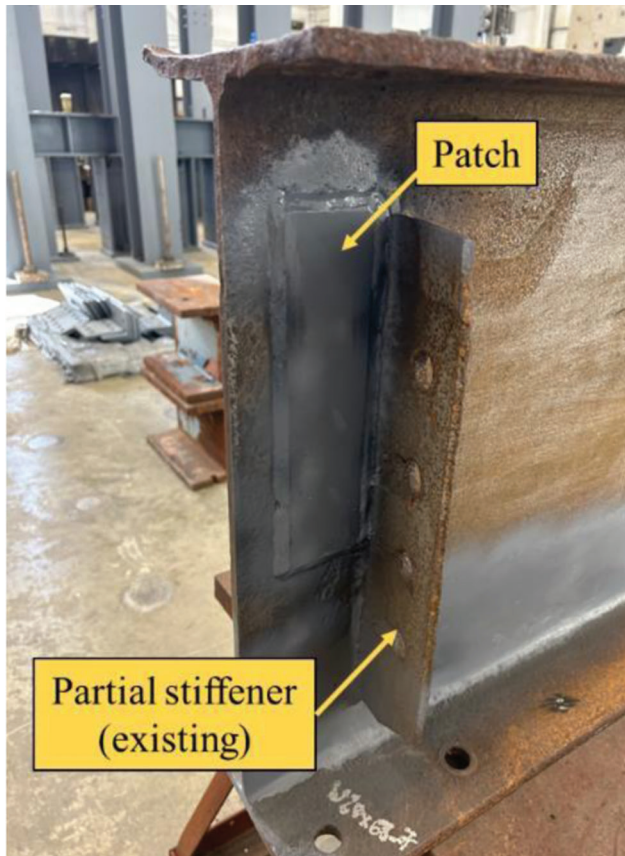


Figure 5.36 Specimen 2: side view.

The artificial corrosion was induced through grinding, and during this process, the thickness of the web was controlled by taking measurements using a UT gauge every 5–10 minutes.

5.5.4 Specimen 3

Specimen 3 was an 11-ft-long W24×68 steel girder with existing partial-depth stiffeners. One girder end was undamaged, whereas the opposite end had already crippled, and had severe corrosion and holes in the web. To maintain consistency in the section loss profile in Specimen 2–Specimen 7, it was decided to introduce artificial section loss to the undamaged end, as shown in Figure 5.32. The artificial corrosion was introduced through manual grinding, meticulously monitoring the thickness. Measurements were taken every 5 to 10 minutes using a UT gauge. The opposite end, with deterioration but without repair, was strengthened by welding 0.75-in.-thick full-depth bearing stiffeners on both sides of the web. Welding the bearing stiffeners at the opposite end (without repair) prevented potential deformations in this region because the experiment's core objective was to investigate the behavior of the repaired corroded girder end using the sandwich panel method. The final fabricated specimen after inducing artificial corrosion, welding partial stiffeners at the studied end (consistent with Specimen 1), and bearing stiffeners at the far end is shown in Figure 5.37 and Figure 5.38.



Figure 5.37 Specimen 3: artificial corrosion in the studied end.



Figure 5.38 Specimen 3: bearing stiffener welded to far girder end.

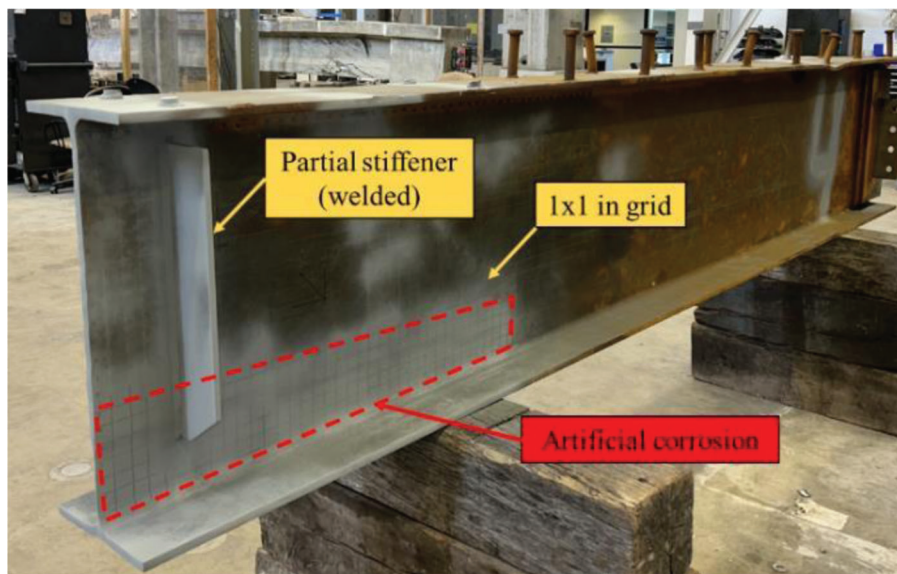


Figure 5.39 Specimen 4: isometric view.

5.5.5 Specimen 4

Specimen 4 initially was an undamaged 11-ft-long W24 \times 68 steel girder without existing partial-depth stiffeners. The artificial corrosion was introduced to the

intact end following the pattern shown in Figure 5.32. Grinding and machine milling were used to speed up inducing section loss. Most of the web thickness was removed using milling equipment, whereas the angle grinder was primarily used to make smooth transition

regions. The final fabricated specimen after inducing section loss and welding partial depth stiffeners but before the repair is shown in Figure 5.39 and Figure 5.40.

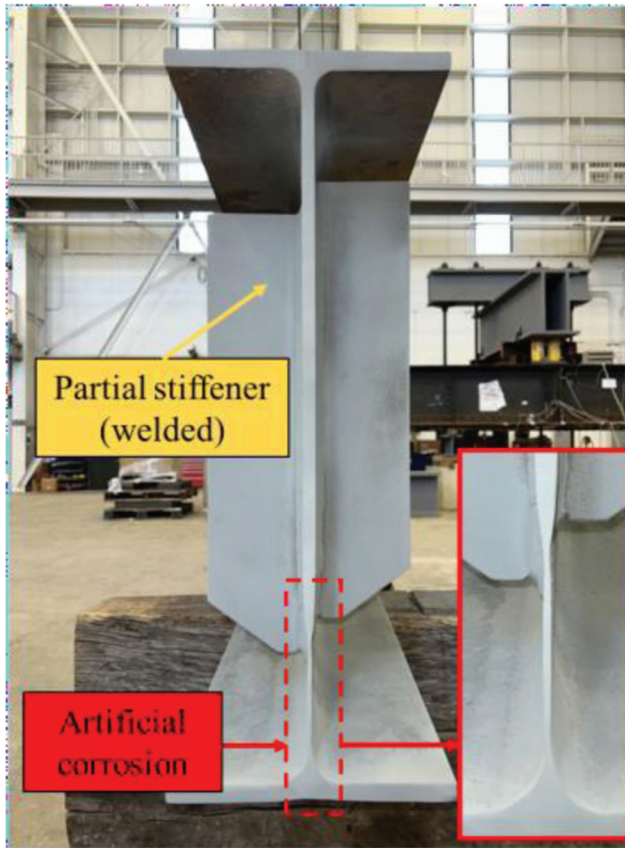


Figure 5.40 Specimen 4: front view.

5.5.6 Specimen 5

Specimen 5 initially was an undamaged 11-ft-long W24×68 steel girder without existing partial-depth stiffeners. The artificial corrosion was introduced to the undamaged end following the pattern shown in Figure 5.32. For this specimen, grinding, and machine milling were used to speed up inducing section loss. Most of the web thickness was removed using milling equipment, whereas the angle grinder was primarily used to make smooth transition regions. The studied artificially corroded end was further repaired using the sandwich panel method. The final fabricated specimen after inducing section loss and welding partial depth stiffeners, but before the repair is shown in Figure 5.41 and Figure 5.42.

5.5.7 Specimen 6

Specimen 6 initially was an undamaged 11-ft-long W24×68 steel girder without existing partial-depth stiffeners. The section loss was introduced to the undamaged end following the pattern shown in Figure 5.32. For this specimen, grinding, and machine milling were used to speed up inducing section loss. Most of the web thickness was removed using milling equipment, whereas the angle grinder was primarily used to make smooth transition regions. The studied artificially corroded end was further repaired using the sandwich panel method. The final fabricated specimen after inducing artificial section loss and welding partial depth stiffeners, but before the repair, is shown in Figure 5.43 and Figure 5.44.

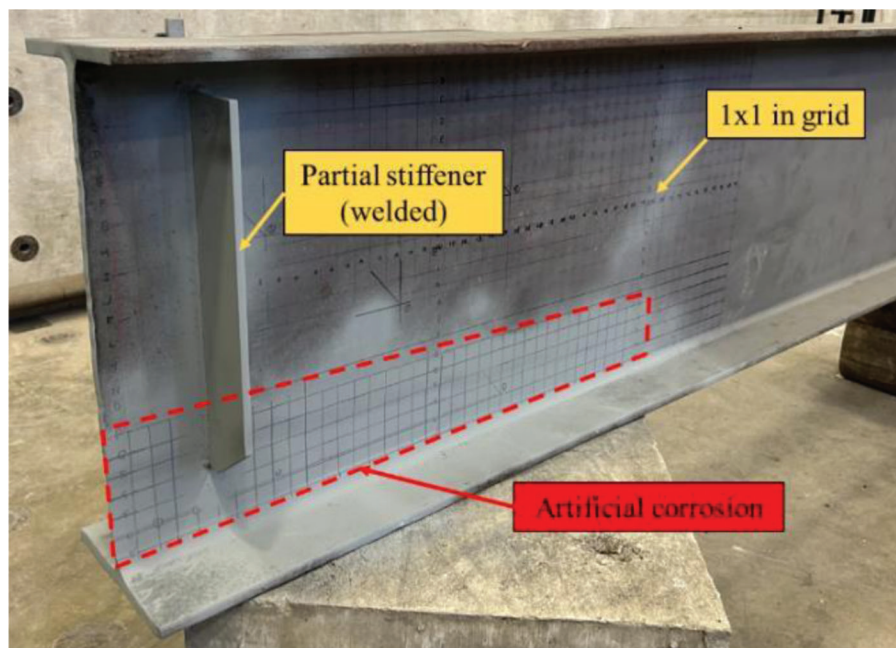


Figure 5.41 Specimen 5: isometric view.

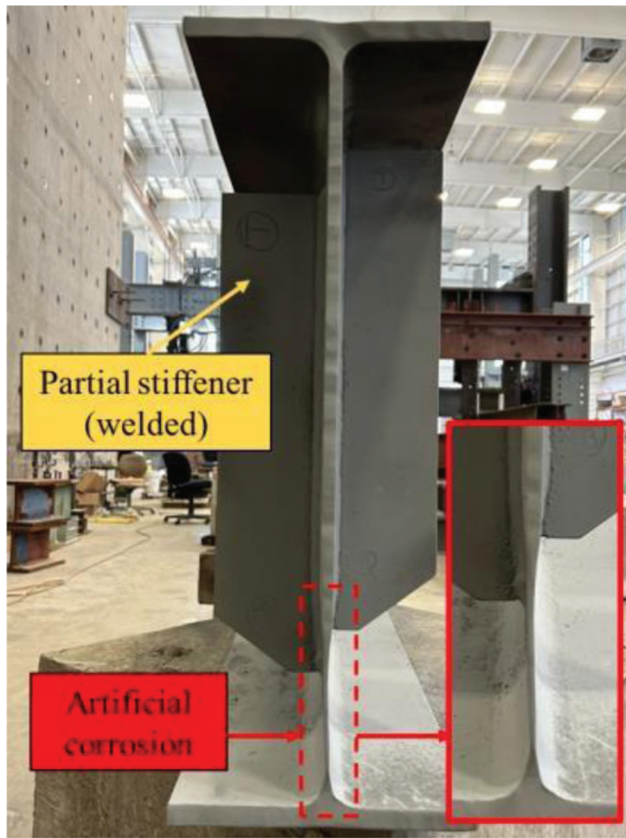


Figure 5.42 Specimen 5: front view.

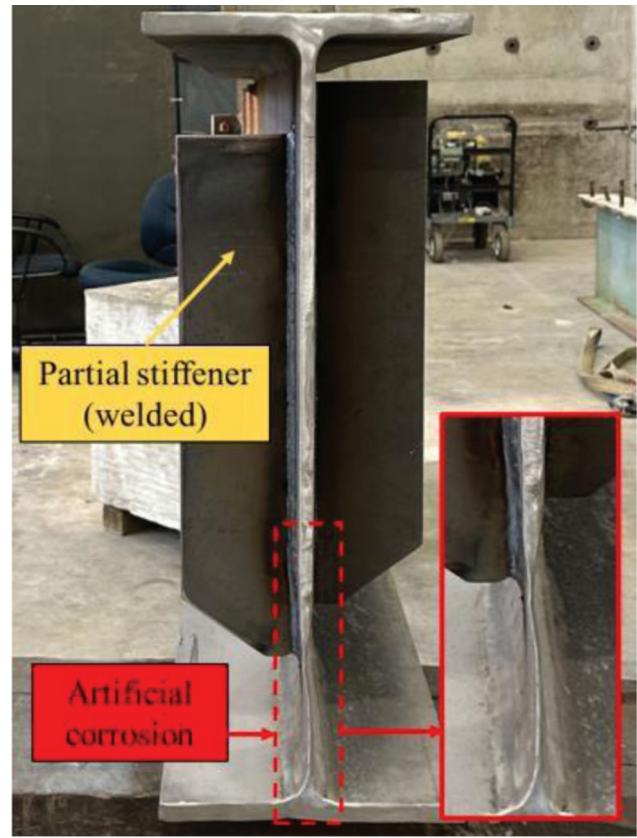


Figure 5.44 Specimen 6: front view.

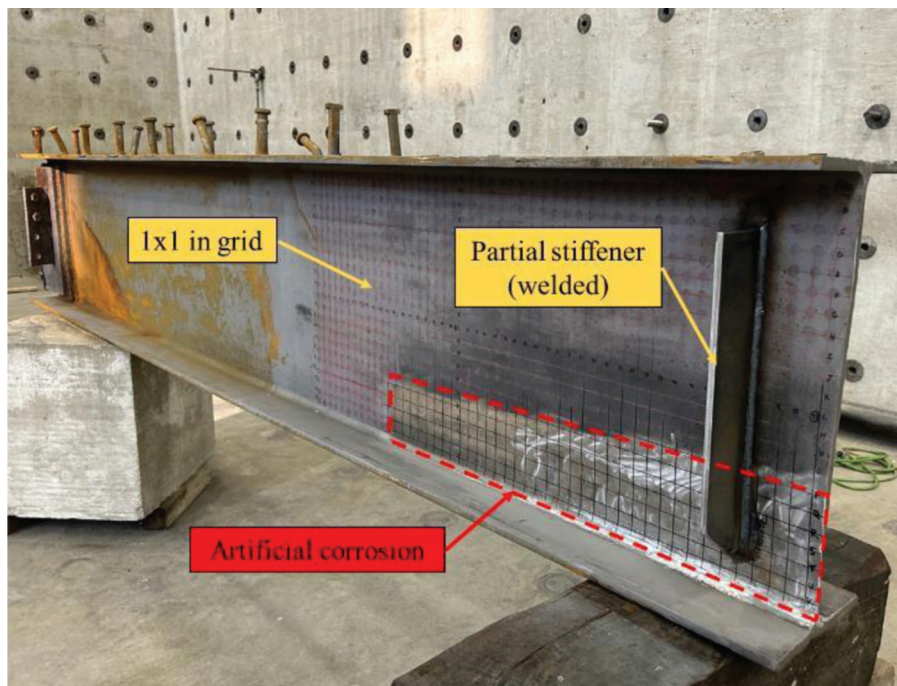


Figure 5.43 Specimen 6: isometric view.

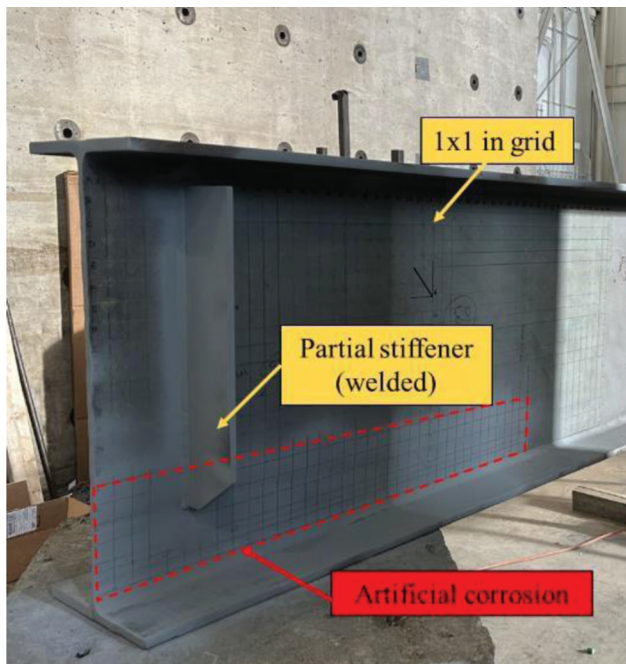


Figure 5.45 Specimen 7: isometric view.

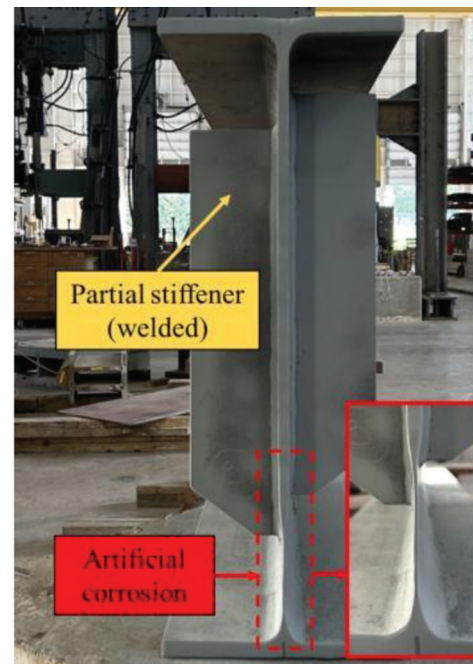


Figure 5.46 Specimen 7: front view.

5.5.8 Specimen 7

Specimen 7 was an 11-ft-long W24×68 steel girder with existing partial-depth stiffeners. The girder had one undamaged end, whereas the other end had already crippled due to severe corrosion. It was decided to introduce section loss to the undamaged end following the profile shown in Figure 5.32 so Specimen 2 through Specimen 7 would have a consistent section loss profile. For this specimen, grinding, and machine milling were used to speed up inducing section loss. Most of the web thickness was removed using milling equipment, whereas the angle grinder was primarily used to make smooth transition regions.

The excessively corroded far end was strengthened by welding 1-in-thick full-depth bearing stiffeners on both sides of the web. Welding the bearing stiffener at the far end eliminated potential deformations in this region. The final fabricated specimen after inducing artificial section loss and welding partial stiffeners at the studied end (same as for Specimen 1) and bearing stiffeners at the far end is shown in Figures 5.45, 5.46, and 5.47.

5.5.9 Implementation of Sandwich Panel Repair Method

Specimen 3 was the first application of the sandwich panel repair method, employing Euclid NS Grout as the infill material. Detailed information on its properties, mixing procedures, and stress-strain curves were provided in Subsections 4.1.1.1 and 4.3.2. To execute the repair, the following materials were acquired for constructing stay-in-place formwork and installing threaded rods.

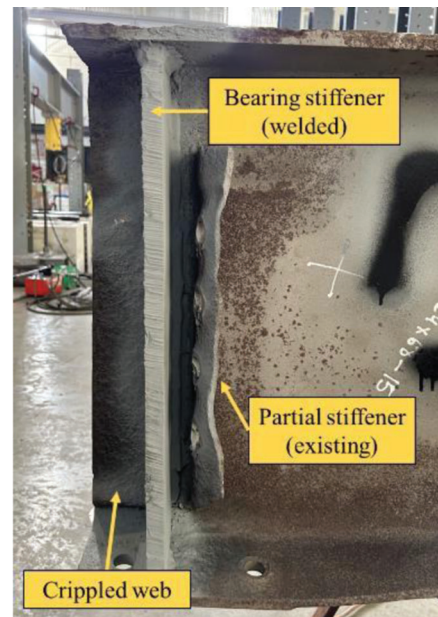


Figure 5.47 Specimen 7 bearing stiffener welded to far girder end.

1. *Zinc-Galvanized Low-Carbon 0.024-in. Steel Sheet*
These steel sheets were utilized to fabricate corrosion-resistant stay-in-place formwork.
2. *Grade B7 Medium-Strength Steel Threaded Rod*
Zinc yellow-chromate plated; 3/8"-16 thread size. Threaded rods constituted a pivotal repair component, and their tensile strength directly impacted the repair's capacity.
3. *Medium-Strength Steel Hex Nut*
Grade 5, zinc-plated, 3/8"-16 thread size. Hex nuts

were employed to fasten threaded rods on the girder web, ensuring their stability.

4. *Zinc-Plated Steel Square Washer For 3/8" Screw Size, 1" Wide*
Square washers were used for stress redistribution on the outer side of a stay-in-place formwork.
5. *Grade 9 Steel Washer*
Zinc yellow chromate plated for 3/8" screw size. Conventional washers were installed within the formwork to minimize the localized deformations in the steel sheets.

The selection of corrosion-resistant materials was paramount for a wet environment. The general procedures for implementing the sandwich panel repair were as follows.

1. Mark the location of the center of the holes on the girder web in accordance with the drawing (Figure 5.3 and Figure 5.4). The hole diameter must be 1/16" plus the diameter of the threaded rod to satisfy tolerance requirements (Equation 5.1). Use a magnetic drill to drill the holes.

$$d_{hole,web} = d_{rod} + 1/16'' \quad (\text{Eq. 5.1})$$

2. Mark the hole locations on steel sheets before bending them. It is recommended to ensure the diameter of the holes be 1/4" larger to accommodate greater tolerance during the assembly of the repair (Equation 5.2). A cordless 20V drill can be utilized drill holes in the steel sheet as the material is thin.

$$d_{hole,sheet} = d_{rod} + 1/4'' \quad (\text{Eq. 5.2})$$

3. Bend the steel sheet by using a hydraulic press or bench vise and applying pressure on the other to achieve a 90-degree angle.
4. Secure threaded rods by affixing one hex nut on each side of the girder web, as shown in Figure A.10, and ensuring a snug-tight condition. No pretension is required, and slight adjustments are permissible for the alignment of threaded rods.
5. Install steel sheets on both sides of the girder web utilizing nuts and washers (Figure A.10).
6. Ensure the snug-tight condition of all the nuts and utilize a square washer on the outer side for effective pressure redistribution. A standard circular washer is sufficient for the inside of the steel sheet.
7. Seal any existing gaps with fast-curing, heavy-duty construction adhesive. The repaired girder before casting the infill material is shown in Figure A.11.
8. Mix the infill material following the guidelines in the technical data sheet or as described in Chapter 4. Pour the mixed material inside the stay-in-place formwork, prevent any leakage, and allow it to cure to attain the design strength.

The result of the implemented sandwich panel repair for Specimens 3 to 7 is shown in Figure C.4 through Figure C.8 in Appendix C.

6. EXPERIMENTAL RESULTS

6.1 Specimen 1

The lightly corroded Specimen 1 reached the maximum load of 231 kips and ultimately failed in web local crippling. At maximum applied load, the vertical displacement at DT2 and out-of-plane displacement at SP1 were 0.208" and 0.263", respectively. Observations during the test revealed that the girder's capacity exceeded the design web crippling capacity calculated according to AASHTO LRFD 2020 (Equation D6.5.3-2), by 65% attributed to the presence of partial stiffeners.

The force-vertical displacement relationship is shown in Figure 6.1. Due to the loading applied close to the bearing region, vertical displacements recorded remained below 1" throughout the test. Therefore, linear variable differential transformers (LVDT) were used for precise data recording. Figure 6.1 illustrates a soft load-vertical displacement response up to 25 kips attributed to the initial settling of bearings and concrete blocks. Beyond 25 kips, Specimen 1 exhibited a significantly stiffer behavior, with an initial stiffness of 2,955 kips/in. up to the load of 100 kips, followed by softening due to steel yielding. At the peak load of 231 kips, Specimen 1 underwent deformations but with negative stiffness.

Since failure mode was web local crippling, large out-of-plane (OOP) displacements relative to the vertical displacement were recorded. Based on the data from SP1, SP2, and SP3 (Figure 6.2), the most significant out-of-plane displacement occurred at the girder end (SP1) while lower values were recorded by SP2 and SP3 (away from the girder end). Maximum out-of-plane displacement of 1.05" was recorded at SP1 following which the experiment was terminated due to large out-of-plane displacements.

Strain in the bottom flange was recorded by a longitudinally oriented strain gauge (SG35). Figure 6.3 shows that the bottom flange remained within the elastic range, with strain not exceeding the yielding strain $\epsilon_y = 1,550 \mu\epsilon$. However, the web area on top of the bearing began yielding at 118 kips (SG1), followed by the yielding of SG2 at 184 kips (Figure 6.4). Overall, all vertical strain gauges were subjected to compression during the test, with the most significant strains recorded by SG1(SG18) and SG2(SG19), located in the bearing region.

Both the east and west sides of Specimen 1 were instrumented for redundancy and to compare the accuracy of the recorded data. Data from five strain gauge rosettes (SR) on the west side of the girder web revealed that SR1 yielded at 146 kips while SR2–SR5 experienced only elastic deformations (Figure 6.5). In summary, the yielding first was recorded by SG1, followed by SR1, and finally SG2.

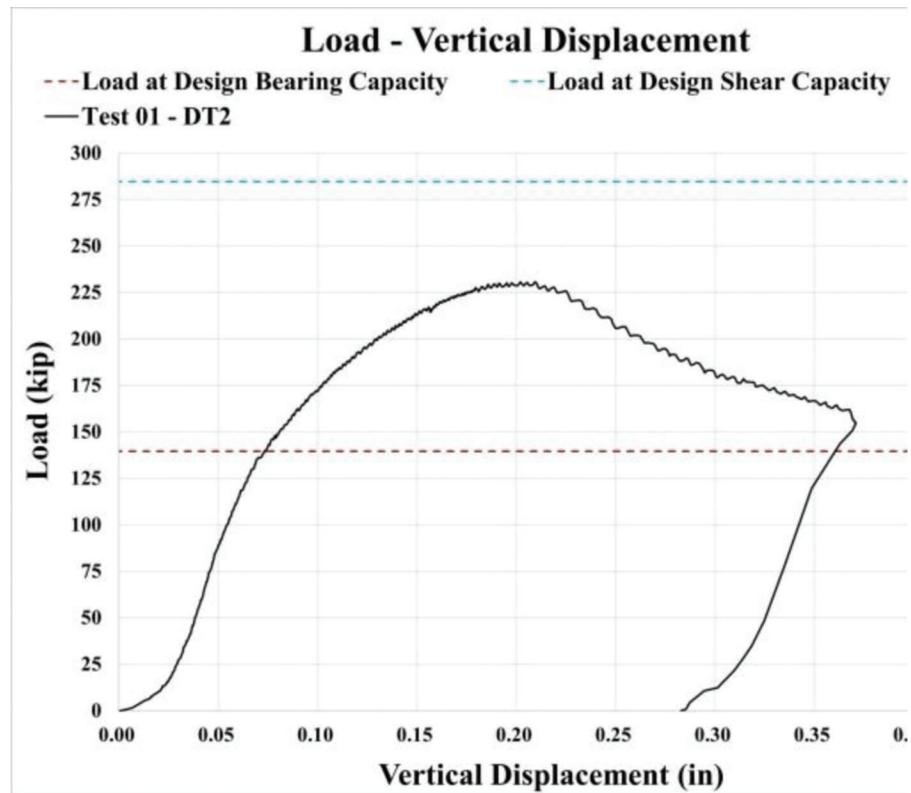


Figure 6.1 Load–vertical displacement plot for Specimen 1.

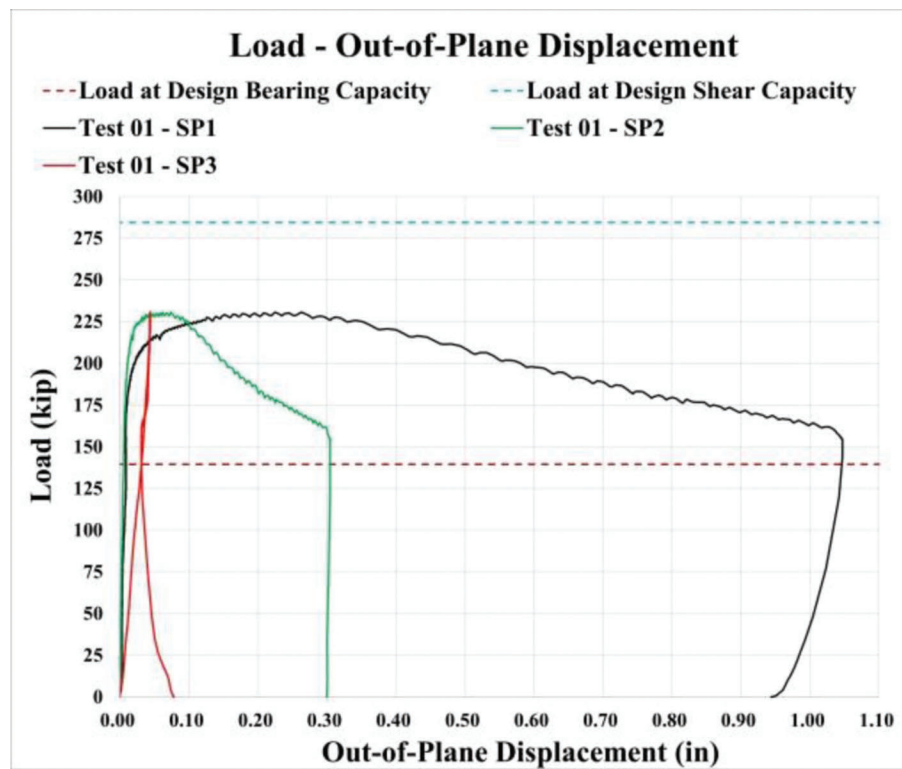


Figure 6.2 Load–OOP displacement plot for Specimen 1.

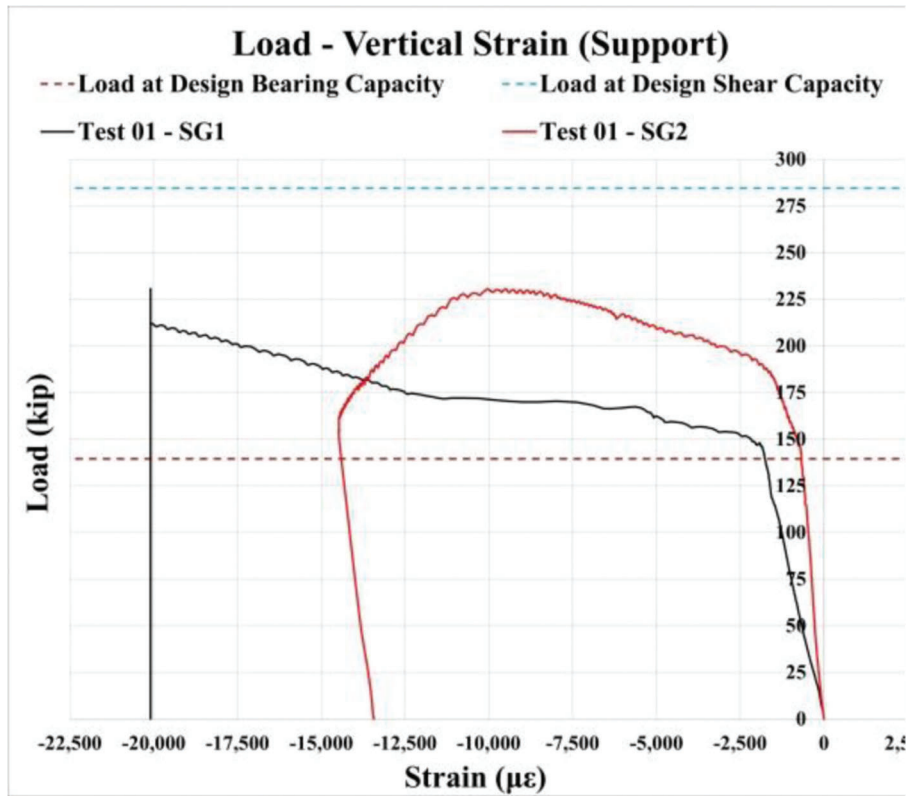


Figure 6.3 Load-strain (bottom flange) plot for Specimen 1.

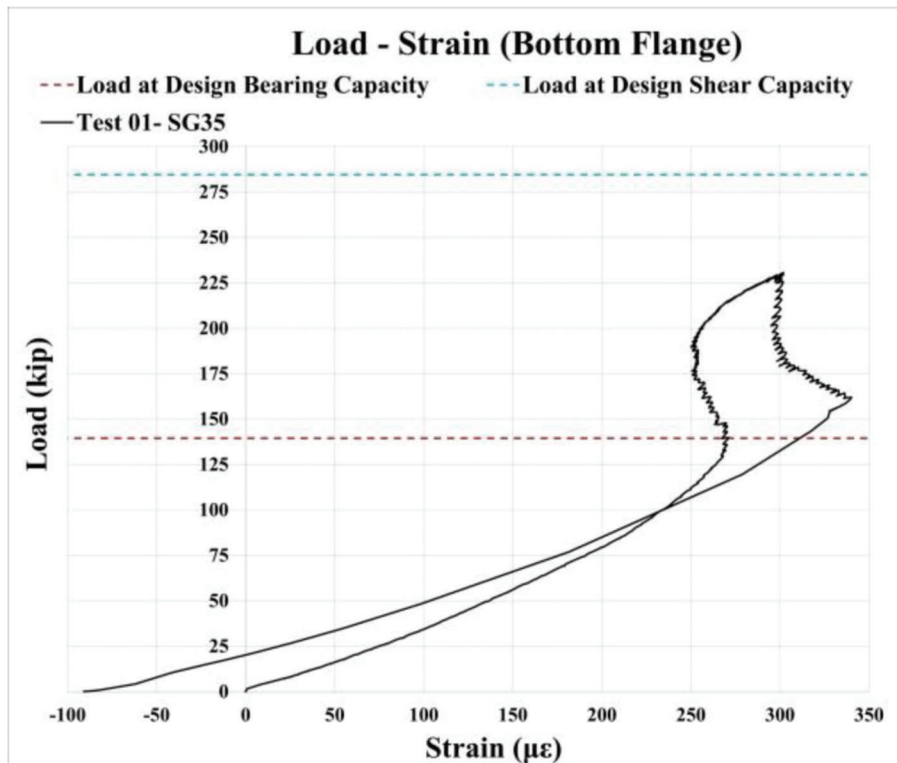


Figure 6.4 Load-vertical strain (support) plot for Specimen 1.

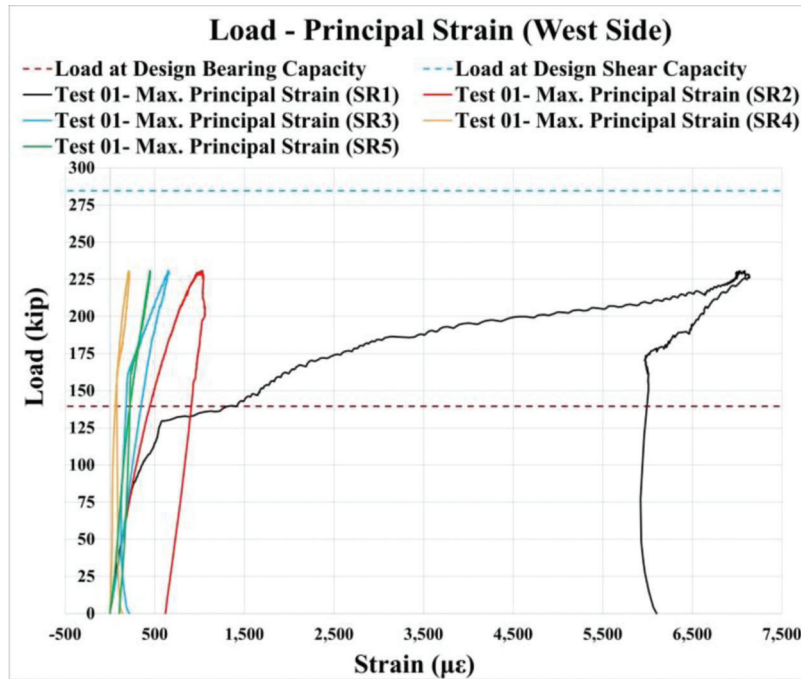


Figure 6.5 Load-maximum principal strain (west side) for Specimen 1.

The deformed shape of Specimen 1 is shown in Figure 6.6 through Figure 6.8. As expected, the specimen failed in web local crippling, a governing failure mode in unstiffened hot-rolled steel girders.

6.2 Specimen 2

The moderately corroded Specimen 2 reached the maximum load of 39 kips and ultimately failed in web local crippling. At the maximum applied load, the vertical displacement of 0.023" (DT2) and out-of-plane displacement of 0.020" (SP1) were documented. The design bearing capacity was calculated using equations provided in AASHTO LRFD 2020 (D6.5.3-2) and a significant 72% decrease in the design bearing capacity was observed due to moderate corrosion in the specimen.

The force-vertical displacement plot is shown in Figure 6.9. The displacement transducer DT2 was located right under the point of applied loading, 16" from the girder end, measuring the displacement of the bottom flange. From the force-vertical displacement plot, it could be observed that up to the peak load of 39 kips, the behavior of the girder was linear-elastic, and no softening behavior was observed before a sudden failure. Specimen 2 had a constant stiffness of 1,939 kips/in. up to the peak load; after reaching it, the girder continued to endure deformations but with a negative stiffness.

Since failure mode was web local crippling, large out-of-plane (OOP) displacements relative to the vertical displacement were recorded. Based on the data from sensors SP1, SP2, and SP3 (Figure 6.10), the most significant OOP displacement occurred at the girder

end (SP1), while lower values were recorded by SP2 and SP3 (away from the girder end). Maximum out-of-plane displacement of 0.57" was recorded by SP1 at 22 kips. The experiment was terminated due to substantial out-of-plane displacements and a significant decrease in the capacity of the specimen.

Strains in the bottom flange were recorded by a longitudinally oriented strain gauge (SG35). From Figure 6.11, it could be seen that the bottom flange remained within the elastic range, with strains not exceeding the yielding strain $\epsilon_y = 1,550 \mu\epsilon$. However, the corroded area in the bearing region started yielding at 37 kips (SG2), followed by post-peak yielding of SG1 at 34 kips (Figure 6.12). In the beginning, all vertical strain gauges were subjected to compression. Nonetheless, after reaching the peak load, SG2 continued to undergo compressive deformations, whereas SG1 switched to tensile deformations. The behavior was caused by web crippling deformations that occurred in the girder. The deformed shape of this region is shown in Figure 6.13. Overall, the most significant strains were recorded by SG1(SG18) and SG2(SG19), located in the corroded region close to the bearing.

Data from five strain gauge rosettes (SR) located on the west side of the girder web, revealed that SR1 yielded at 39 kips, a few time steps before Specimen 2 reached its capacity. The rest of the strain gauge rosettes (SR2–SR4, and SR10) experienced only elastic deformations (Figure 6.14). The SR5 was replaced by data from SR10 due to the strain gauges in this rosette not functioning correctly. To conclude, the yielding first was recorded by SG2, followed by the yielding of SR1, and finally SG2.

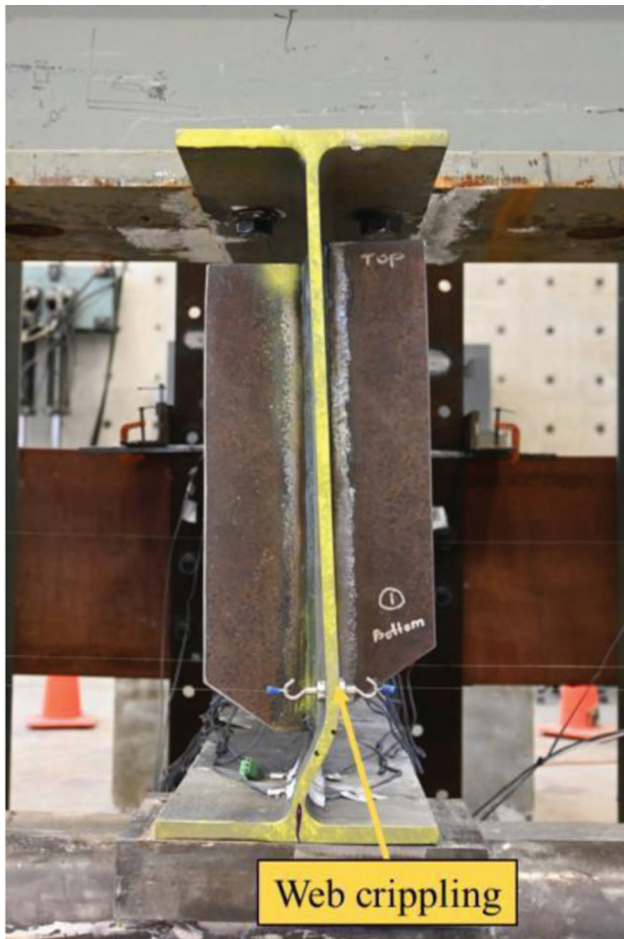


Figure 6.6 Specimen 1: deformed shape, front view.

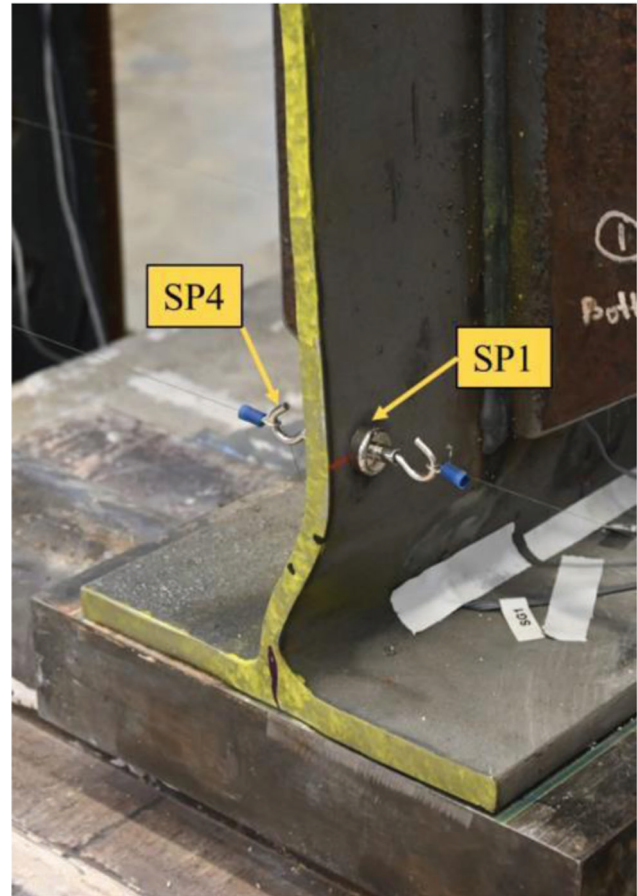


Figure 6.7 Specimen 1: deformed shape, locations of SP1 and SP4.

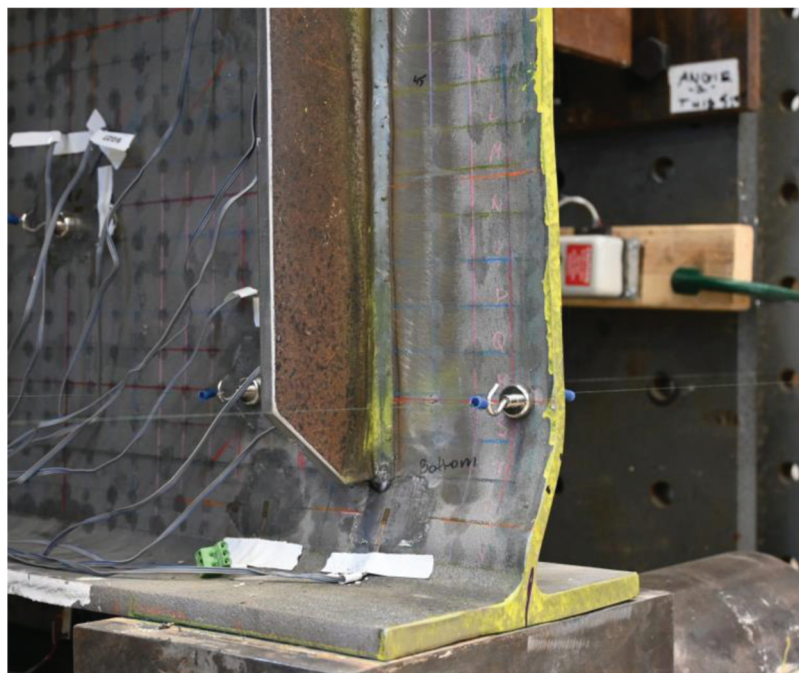


Figure 6.8 Specimen 1: deformed shape, view from the east side.

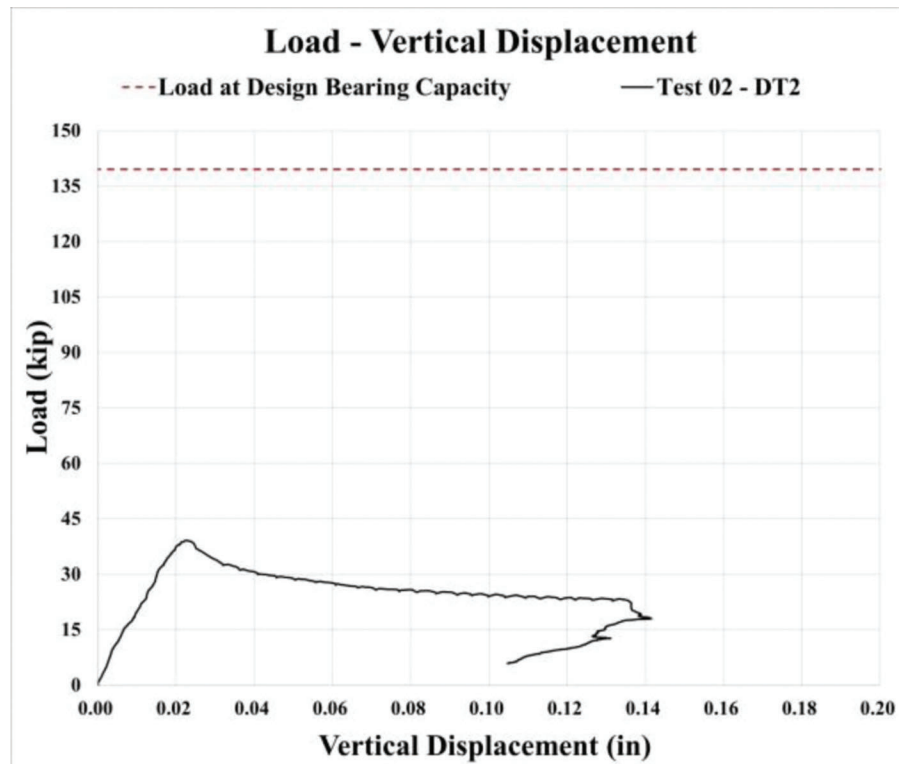


Figure 6.9 Load-vertical displacement plot for Specimen 2.

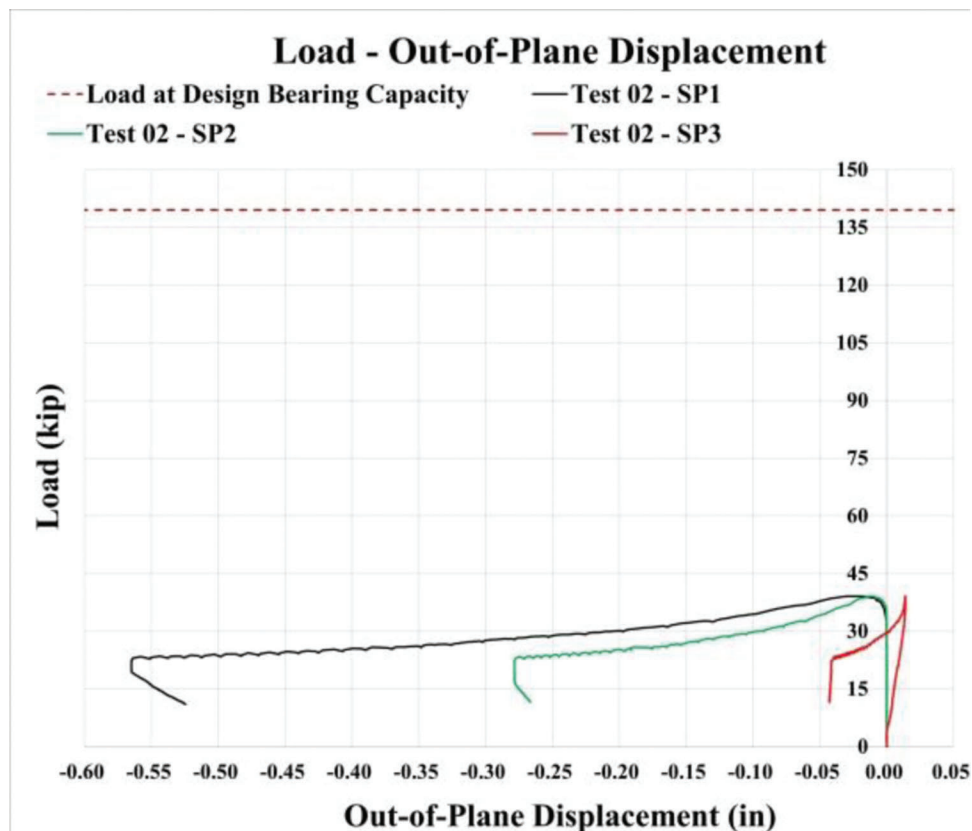


Figure 6.10 Load-OOP displacement plot for Specimen 2.

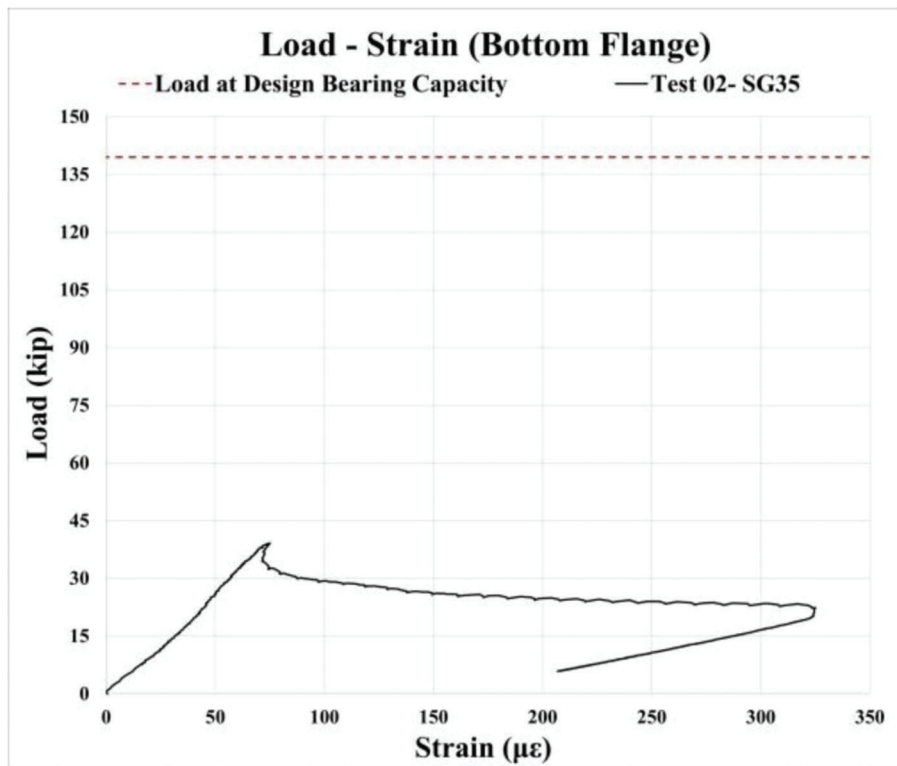


Figure 6.11 Load-strain (bottom flange) plot for Specimen 2.

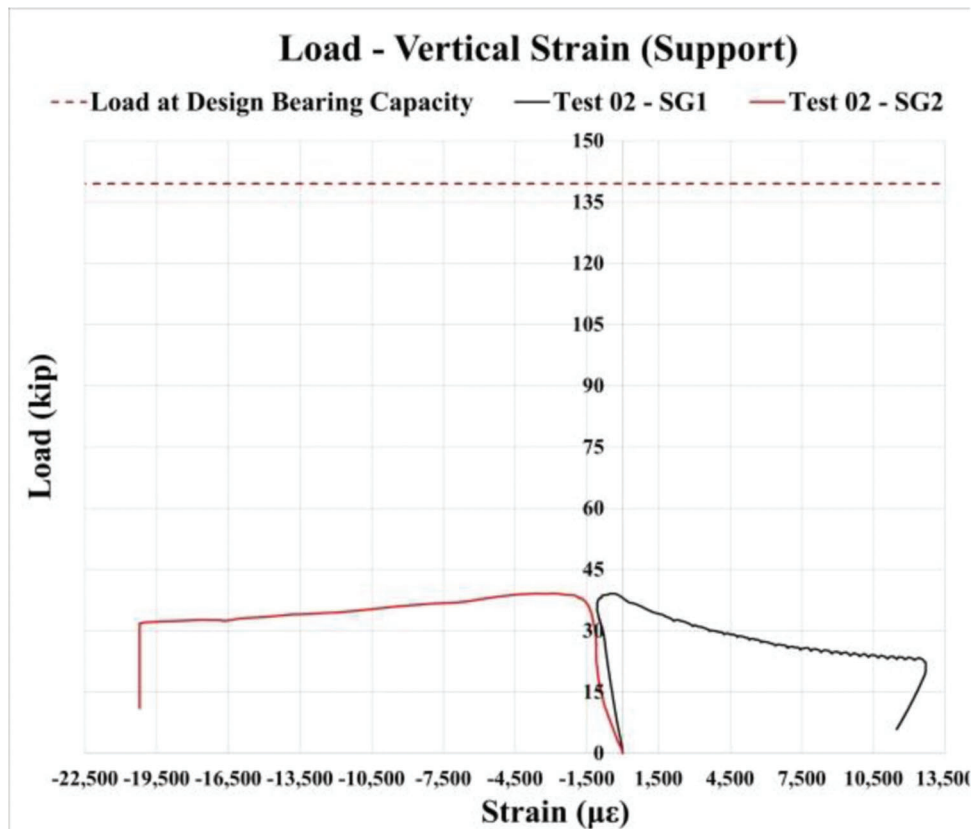


Figure 6.12 Load-vertical strain (support) plot for Specimen 2.



Figure 6.13 Specimen 2: deformations in the corroded region.

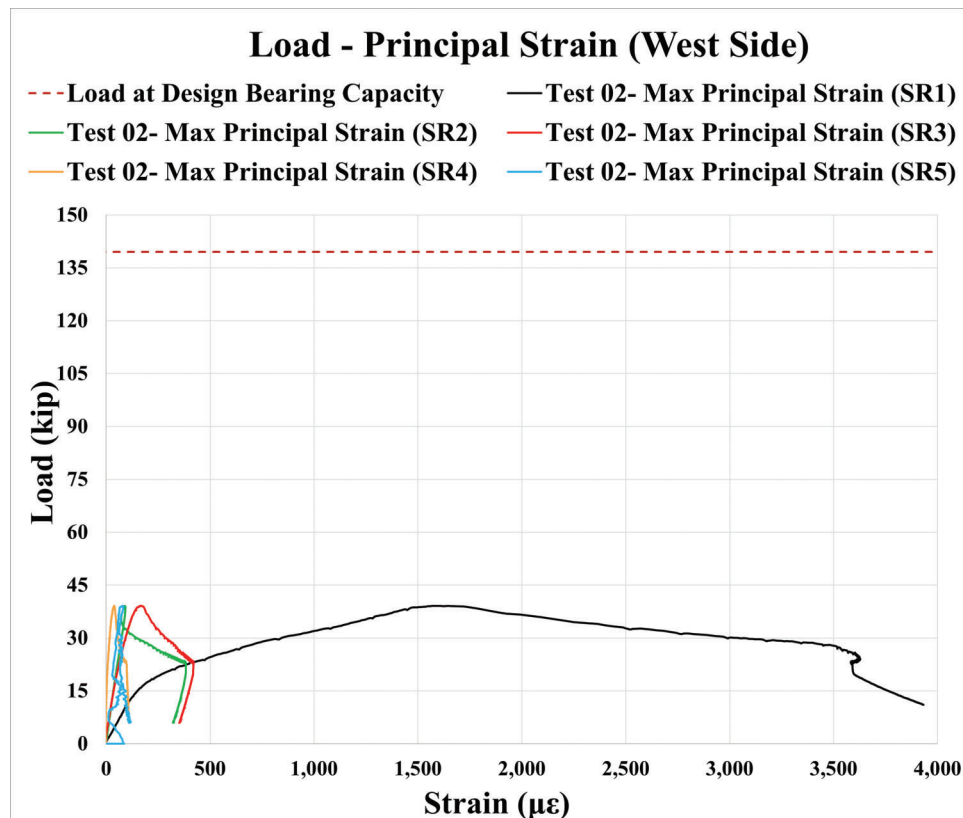


Figure 6.14 Load-maximum principal strain (west side) for Specimen 2.

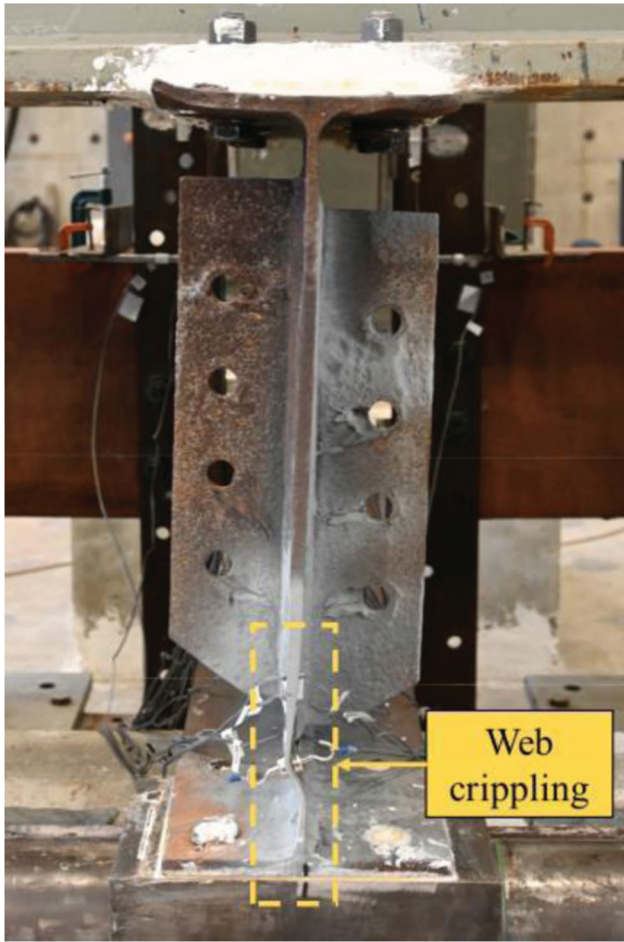


Figure 6.15 Specimen 2: deformed shape.

The deformed shape of Specimen 2 is shown in Figure 6.15 and Figure 6.16. As expected, Specimen 2 ultimately failed in web local crippling since this failure mode generally governs in unstiffened corroded steel girders. In addition, due to excessive tensile deformations, the rupture was noticed in the corroded web (Figure 6.17). While inducing section loss with an angle grinder, this region was ground excessively, resulting in a fragile thin web.

6.3 Specimen 3

The moderately corroded Specimen 3, repaired using the sandwich panel method, reached the maximum load of 79.6 kips and failed in web crippling. A vertical displacement of 0.049" (DT2) and an out-of-plane displacement of 0.102" (SP1) was recorded at the maximum applied load. Even though the girder was repaired using the sandwich panel method, a 43% decrease in the web crippling capacity was observed.

The force-vertical displacement plot is shown in Figure 6.18. The displacement transducer DT2 was positioned beneath the point of applied loading, 16" from the girder end, measuring the displacement of the bottom flange. The force-vertical displacement plot

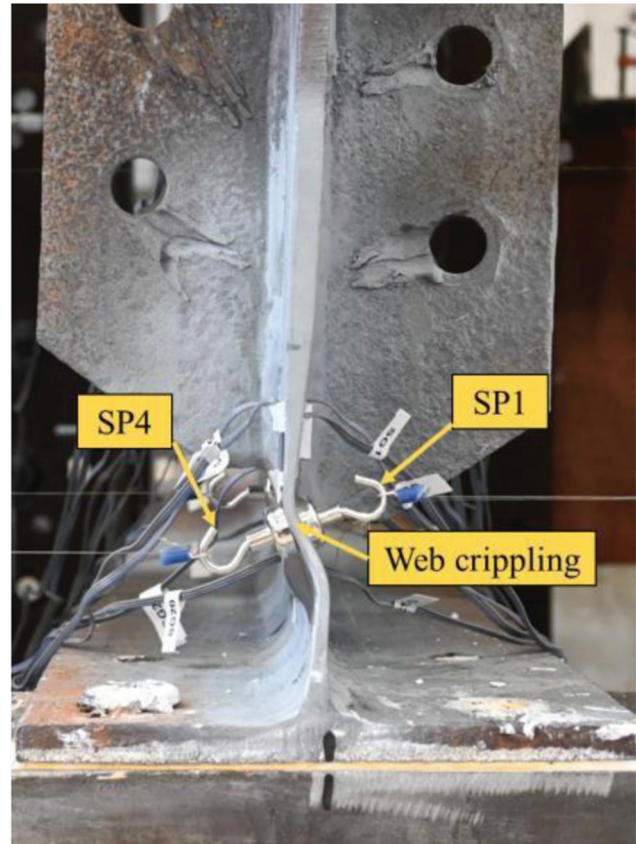


Figure 6.16 Specimen 2: deformed shape. Locations of SP1 and SP4.

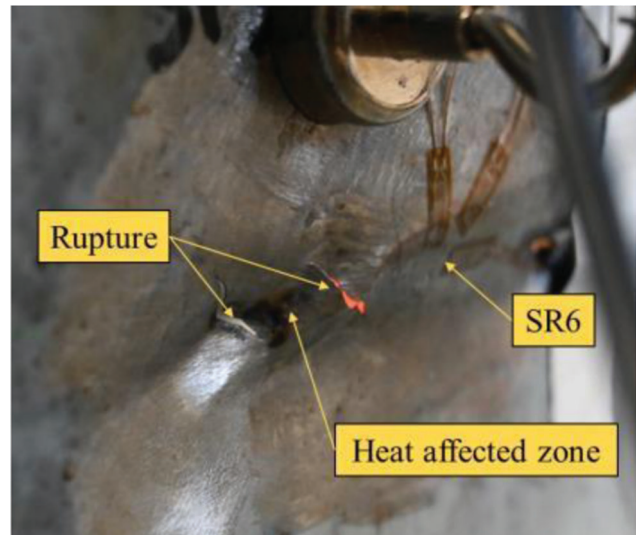


Figure 6.17 Rupture in the artificially corroded web.

shows that up to a load of 48 kips, the graph was linear with an initial stiffness of 3,032 kips/in. Following this loading step, softening behavior was observed. Once the load peaked, the girder underwent deformations but with negative stiffness. Subsequently, the load plateaued at 73 kips with approximately zero stiffness until the experiment was terminated.

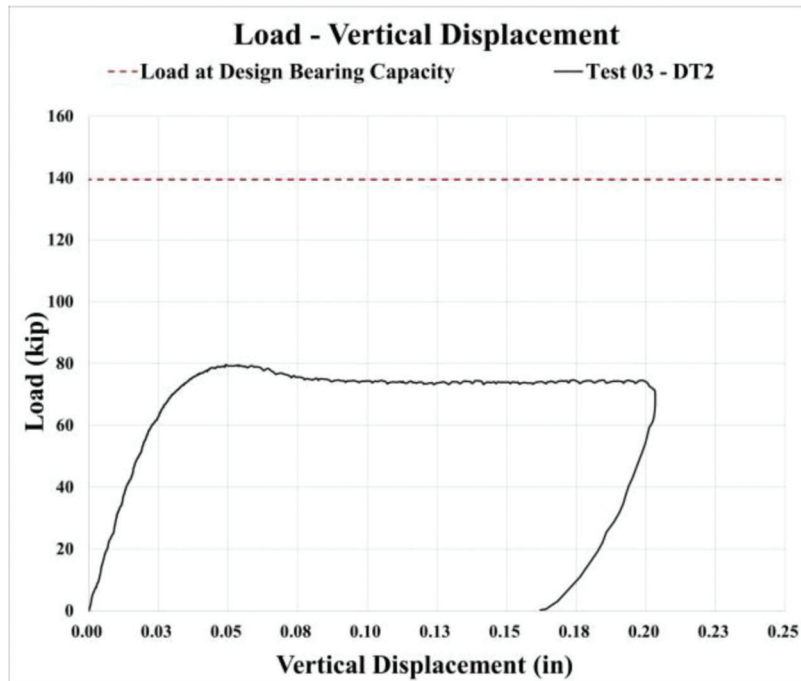


Figure 6.18 Load-vertical displacement plot for Specimen 3.

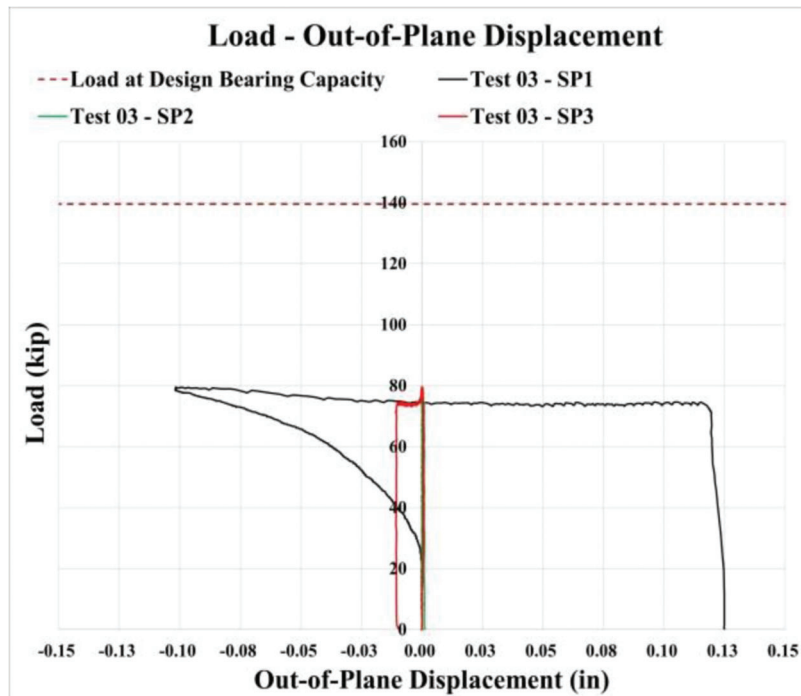


Figure 6.19 Load-OOP displacement plot for Specimen 3.

Out-of-plane (OOP) displacements of repaired Specimen 3 were four times lower than for Specimen 2. According to the data recorded by string potentiometers (Figure 6.19), the most significant out-of-plane displacement occurred at the girder end (SP1), as expected. In contrast, almost no displacement was recorded by SP2 and SP3 (away from the girder end). The peak OOP

displacement recorded by SP1 was 0.13 in. at 73 kips followed by termination of the experiment.

Strains in the bottom flange were recorded by a longitudinally oriented strain gauge (SG35). Figure 6.59 shows that the bottom flange remained within the elastic range, with strain not exceeding the yielding strain $\epsilon_y = 1,550 \mu\epsilon$. However, although the bottom

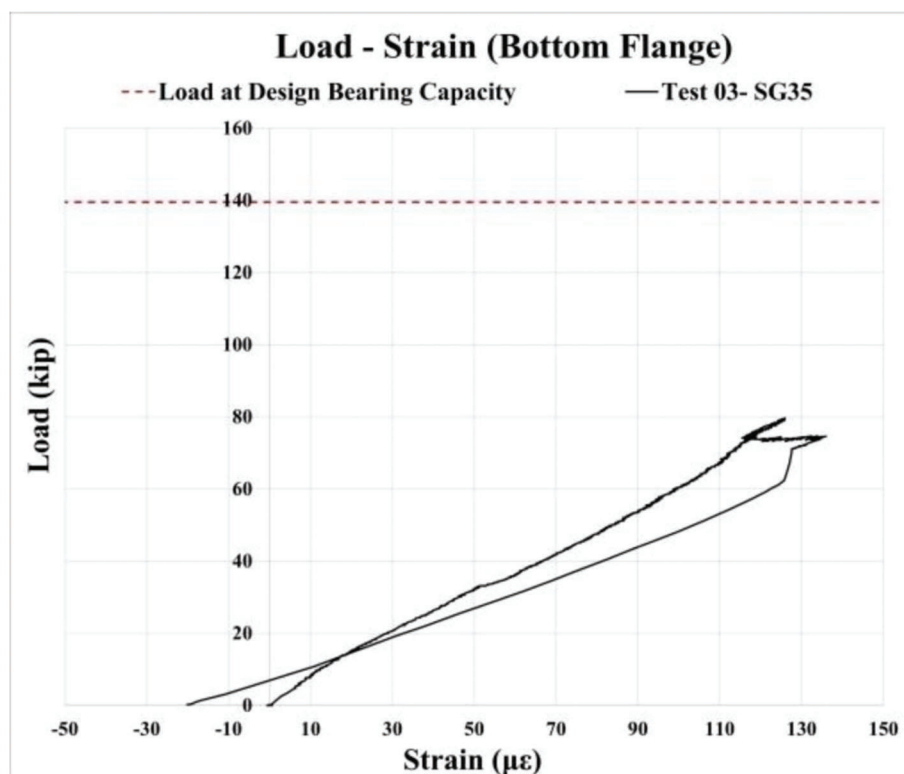


Figure 6.20 Load-strain (bottom flange) plot for Specimen 3.

flange did not yield during the test, the corroded area over the bearing started yielding at 55 kips (SG2), followed by the yielding of SG1 at 68 kips, and finally SG5 at 79 kips a few steps before the specimen reached its maximum loading capacity. Initially, all vertical strain gauges were subjected to compression (Figure 6.21).

However, it is evident that after reaching 40 kips and 60 kips, respectively, SG2 and SG1 changed the direction of deformations from compression to tension. Strang gauge SG5, encased in grout, remained in compression throughout the entire test. Overall, the most significant strains, SG1(SG18) and SG2(SG19) were recorded in the bearing region. Based on data from four strain gauge rosettes located on the west side of the girder web, none of the strain gauge rosettes yielded (Figure 6.22).

The deformed shape of Specimen 3 is shown in Figure 6.23 through Figure 6.27. Specimen 3 ultimately failed in web local crippling, followed by minor cracking of cementitious grout and insignificant bending of threaded rods. After the experiment, one of the steel sheets was removed to observe the cracking pattern in the grout panel. A few cracks were found in the bottom region subjected to tension (Figure 6.65). However, overall, the grout panel remained intact. Additionally, the steel sheet detached from the grout infill and buckled, forming a gap (Figure 6.28). Nevertheless, since the steel sheets served solely as a stay-in-place formwork, this behavior was not a major concern.

6.4 Specimen 4

The moderately corroded Specimen 4 repaired using the sandwich panel method, reached the first peak load of 311 kips. Subsequently, the load dropped to 301 kips, after which the girder continued to carry additional load before reaching an ultimate capacity of 315 kips. Specimen 4 ultimately failed in web local crippling, followed by threaded rod rupture and extensive shear cracking of two grout panels.

At the first peak load, the vertical displacement (DT3) and out-of-plane displacement (SP1) reached 0.203" and 0.596", respectively. At the ultimate loading capacity, the vertical displacement of 0.317 in. (DT3) and out-of-plane displacement of 0.794" (SP1) were reached. Specimen 4 fully restored the targeted value of design bearing capacity, surpassing it by 138% when considering the first peak load of 311 kips. It was not a research objective to recover the design shear capacity of the girder. However, Specimen 4 fully recovered design bearing strength, exceeding this value by 126%.

The force-vertical displacement plot is shown in Figure 6.29. The displacement transducer DT3 was installed 22 in. from the girder end, measuring the vertical displacement of the bottom flange. From the force-vertical displacement plot, it could be observed that up to a load of 131 kips, the graph was linear with an initial stiffness of 4,158 kips/in. After reaching this load level, softening behavior was observed. Once the load reached the first peak, 311 kips, the girder continued to endure deformations but with a negative

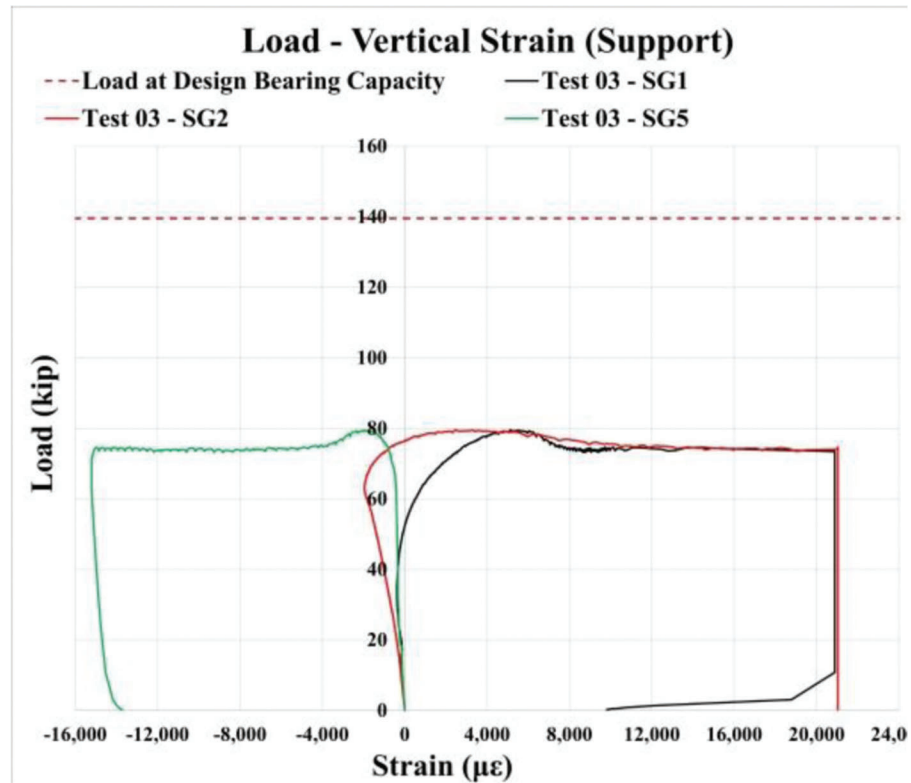


Figure 6.21 Load-vertical strain (support) plot for Specimen 3.

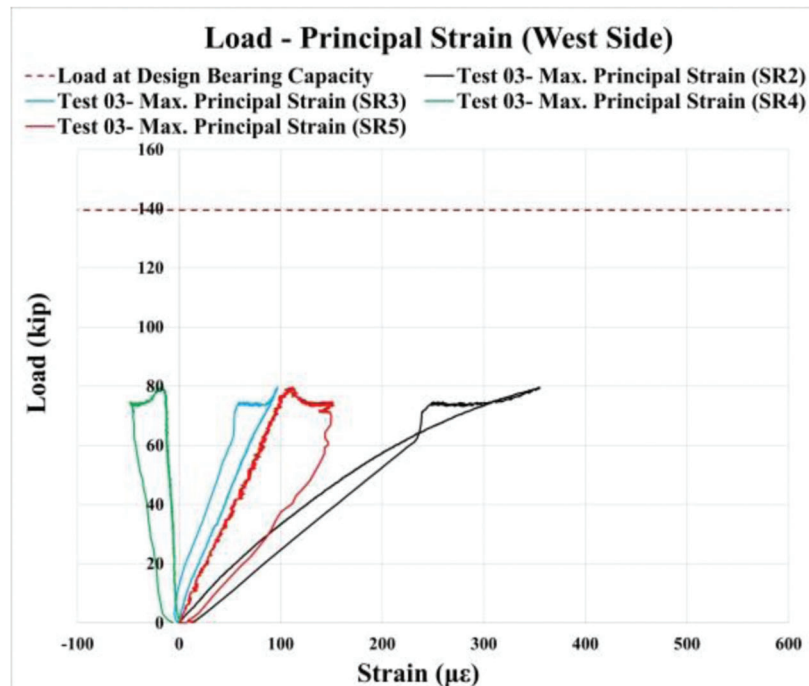


Figure 6.22 Load-maximum principal strain (west side) for Specimen 3.



Figure 6.23 Specimen 3: deformed shape, front view.

stiffness up to the load level of 301 kips. Afterward, the girder resumed carrying the load with a positive stiffness until the second peak of 315 kips. Subsequently, the girder kept undergoing deformations but with a negative stiffness until the test was terminated due to excessive cracking of the grout panels.

Based on the data recorded by string potentiometers (Figure 6.30), the most significant out-of-plane displacement occurred at the corroded girder end (SP1), as expected, because of the increased slenderness of the corroded web. Almost no displacement was recorded by SP2 that was attached to the grout panel. Relatively small lateral displacements were captured by SP3 located on the girder web over the grout panel that did not exceed 0.15". The peak out-of-plane displacement recorded by SP1 was equal to 1" at 270 kips, after which the experiment was terminated.

The deformations in the bottom flange were recorded by a longitudinally oriented strain gauge SG35. Figure 6.31 shows that the bottom flange first yielded at 306 kips after Specimen 4 reached the first peak load. The corroded area over the bearing started yielding at 85 kips (SG2), followed by the yielding of SG5 at 108 kips, and finally, the yielding of SG1 at 121 kips. All vertical strain gauges were subjected to compression throughout the test (Figure 6.32). Based on data from four strain gauge rosettes located on the east side of the girder web, it could be noted that only one strain gauge



Figure 6.24 Specimen 3: deformed shape, front view (enlarged).

rosette, SR8, located over the grout panel yielded (Figure 6.33).

Six longitudinal strain gauges were installed on three threaded rods placed over the bearing and anticipated to undergo the largest deformations (Figure 6.34 and Figure 6.35). Both the top and bottom surfaces of the threaded rods were instrumented, and the sensor layout can be found in Figure 5.28. First, the lowermost threaded rod #1 (SG40 and SG41) was subjected to only elastic tensile deformations throughout the entire test, and no yielding was documented ($\epsilon_{y_rod} = 3,620 \mu\epsilon$).

Furthermore, threaded rod #2 underwent more significant deformations, and SG42 captured the initiation of yielding at 268 kips before Specimen 4 reached ultimate capacity. It can be seen from Figure 6.34 that up to the load of 173 kips, threaded rod #2 was subjected to tension. However, after reaching this load threshold, deformations transitioned into bending, with the bottom side of the rod experiencing tension and the top side being subjected to compression.

Finally, threaded rod #3 was similarly subjected to pure tension up to 176 kips, after which bending deformations took over, and the threaded rod yielded at 266 kips.

The deformed shape of Specimen 4 is shown in Figure 6.36 through Figure 6.44. Specimen 4 failed in web local crippling, followed by threaded rod rupturing

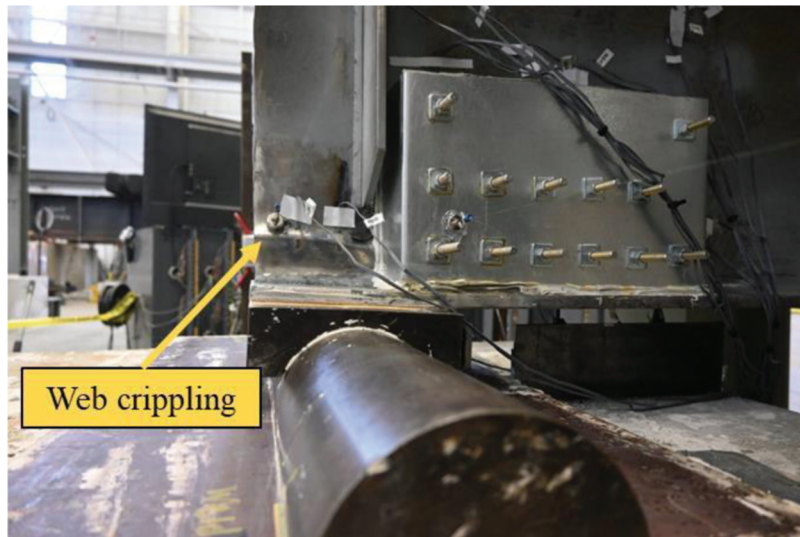


Figure 6.25 Specimen 3: deformed shape, view from the west side.



Figure 6.26 Specimen 3: deformed shape, view from the east side.

and cracking of cementitious grout panels. The failure mode of web local crippling is illustrated in Figures 6.36, 6.37, and 6.38. Despite the specimen being repaired and successfully restoring the bearing capacity, the corroded region that was not encased in the cementitious grout experienced significant lateral displacements. Due to the large forces carried by threaded rods, the bending of square washers was observed (Figure 6.39). The use of thicker and larger square washers might have prevented deformation. However, it would not have significantly affected the repair's capacity, as the primary objective of introducing square washers is to avoid local deformations in steel sheets.

After the experiment, one of the steel sheets was removed to observe the cracking pattern in the grout panel. The entire grout panel was extensively cracked when the experiment was terminated, as shown in

Figure 6.41. Three out of the 13 threaded rods ruptured, all located in the second row. By examining the cross-section surface at the location of a rupture, it can be concluded that the rupture was ductile, indicating that the rod yielded before rupturing.

6.5 Specimen 5

The moderately corroded Specimen 5, repaired using the sandwich panel method, reached its first peak load of 180 kips. Subsequently, the load dropped to 174 kips, after which the girder continued to carry additional load before reaching an ultimate capacity of 340 kips. Specimen 5 eventually failed due to web crippling, with no observed threaded rod rupture or extensive cracking of Kwik Bond PPC-1121 panels. However, web crippling occurred in two regions: the loading and corroded regions.

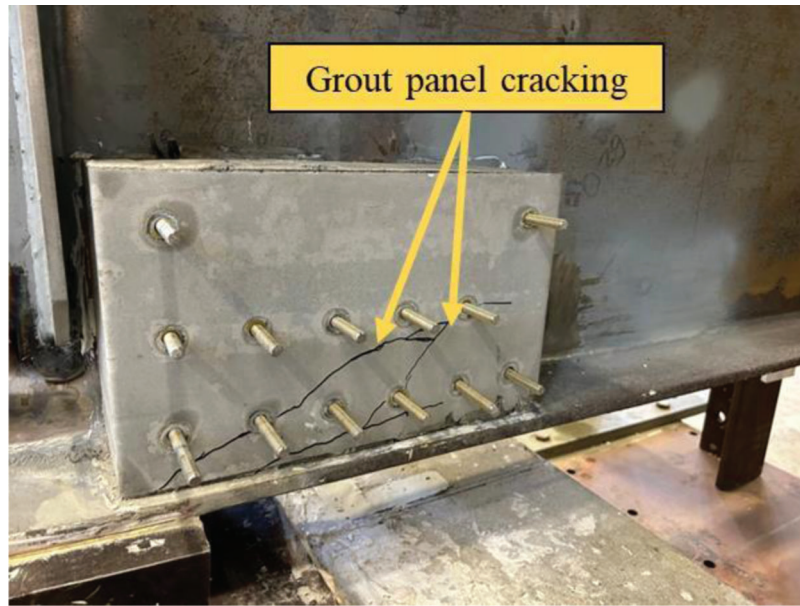


Figure 6.27 Specimen 3: cracks in grout panel.

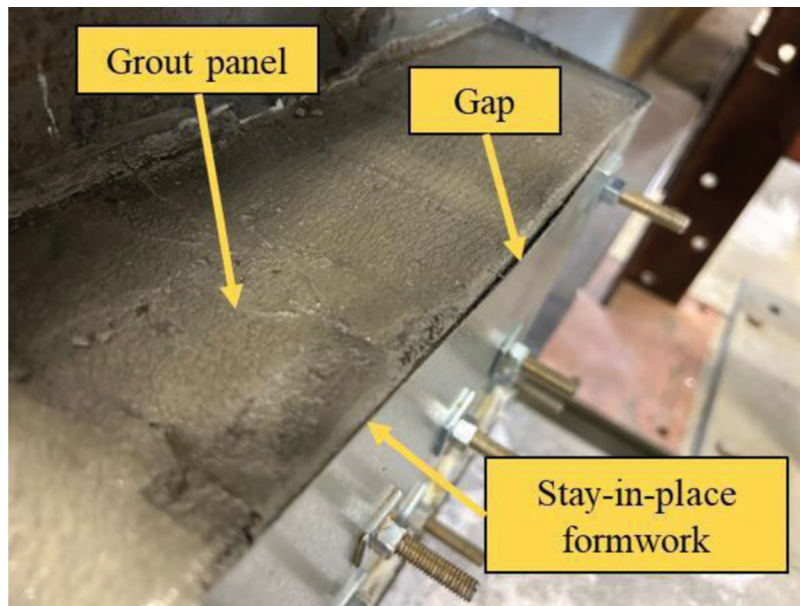


Figure 6.28 Specimen 3: detachment of stay-in-place formwork from grout panel.

At the first peak load, the vertical displacement of 0.041" (DT3) and out-of-plane displacement of 0.143" (SP1) were reached. At the ultimate loading capacity, the vertical displacement of 0.257" (DT3) and out-of-plane displacement of 0.566" (SP1) were observed. Specimen 5 fully restored the targeted design bearing capacity, surpassing it by 29% and 144% at the first and second peak loads of 180 kips and 340 kips, respectively.

The force-vertical displacement plot in Figure 6.45 shows the displacement transducer DT3, installed 22" from the girder end, measuring the vertical displacement of the bottom flange. Up to a load of 175 kips, the graph was linear with an initial stiffness of 4,779 kips/

in. After reaching this load level, a short period of softening behavior was observed, followed by a sudden drop in capacity at 180 kips.

Once the load reached the first peak at 180 kips, the girder endured deformations with negative stiffness up to the load level of 175 kips. Afterward, the girder resumed carrying the load with positive stiffness until the second peak of 315 kips. A sudden, rapid decrease in capacity was observed due to web crippling under the spreader beam, leading to the termination of the experiment.

Based on data recorded by string potentiometers in Figure 6.46, the largest out-of-plane displacement

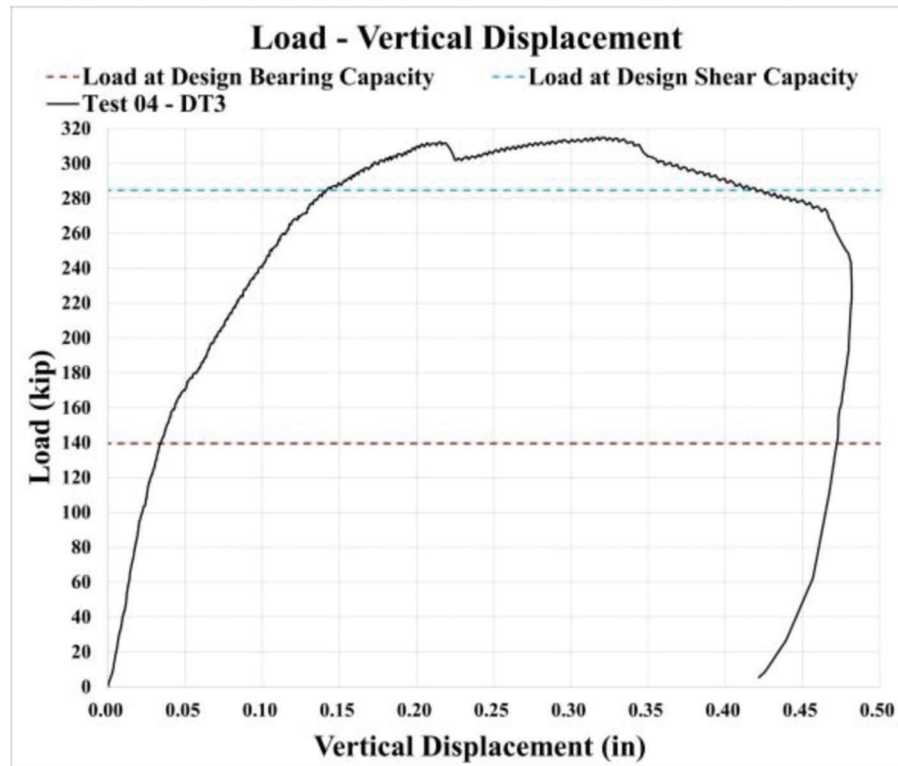


Figure 6.29 Load: vertical displacement plot for Specimen 4.

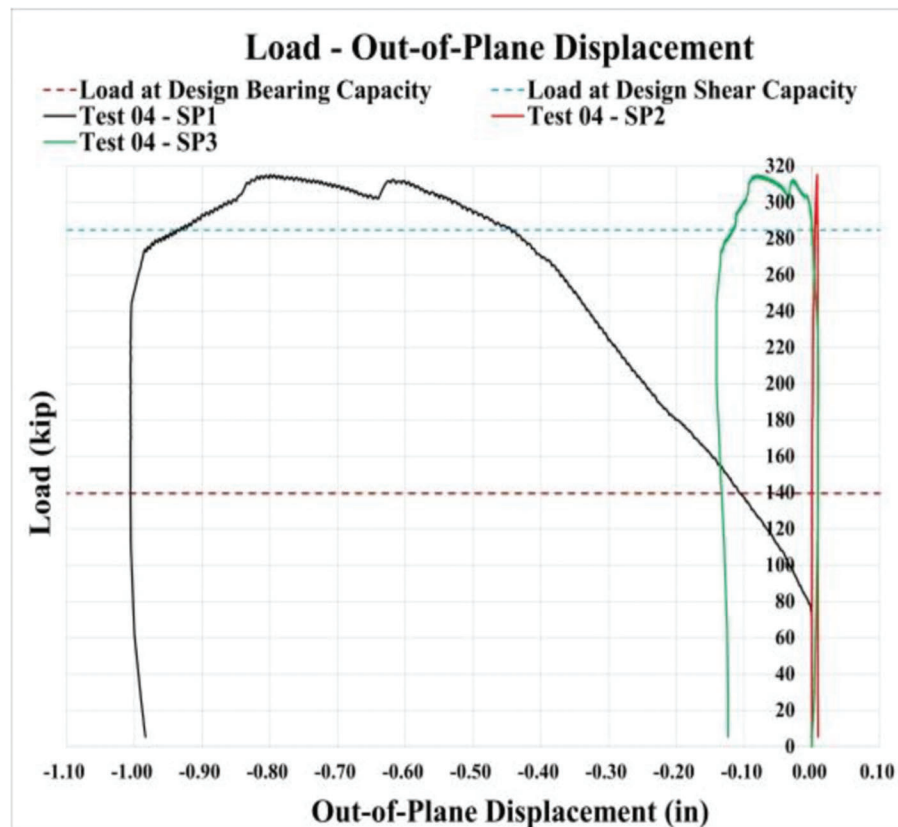


Figure 6.30 Load: OOP displacement plot for Specimen 4.

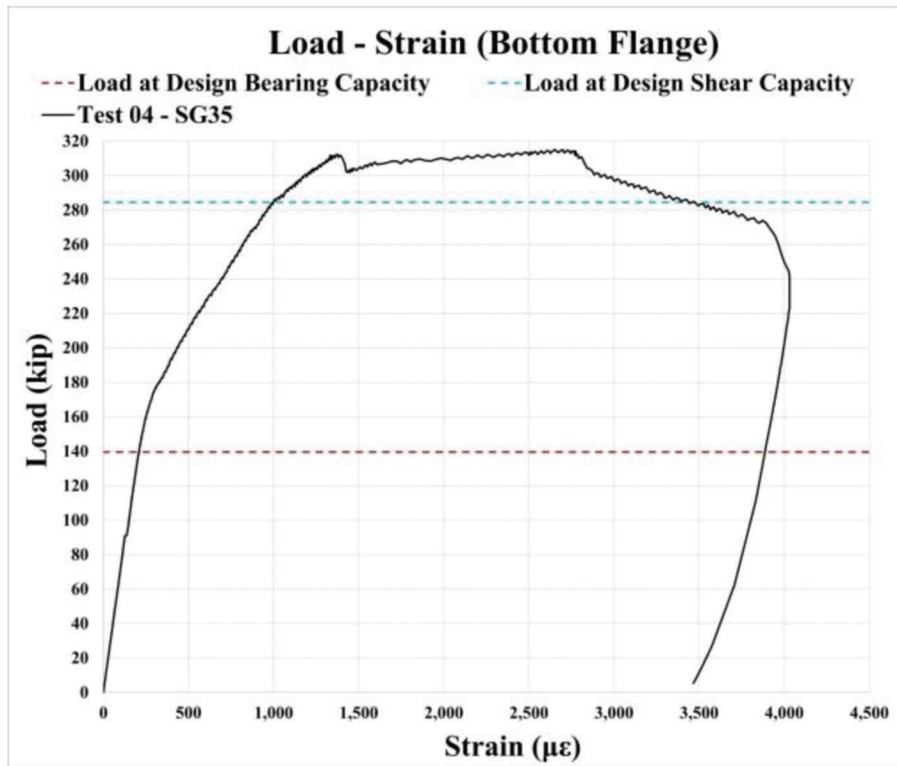


Figure 6.31 Load: strain (bottom flange) plot for Specimen 4.

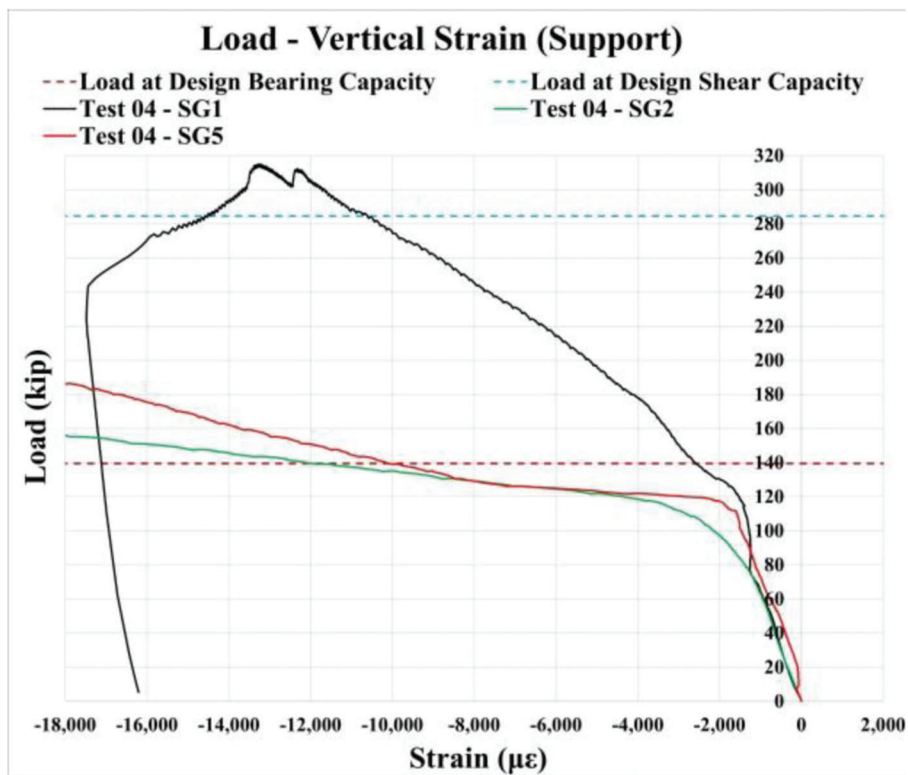


Figure 6.32 Load: vertical strain (support) plot for Specimen 4.

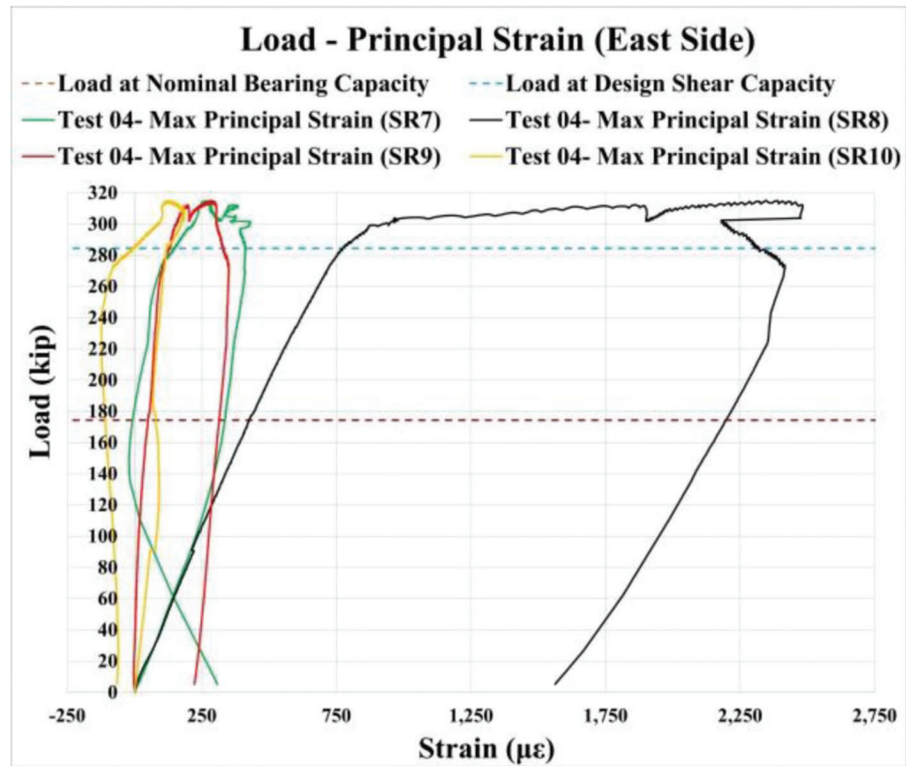


Figure 6.33 Load: maximum principal strain (east side) for Specimen 4.

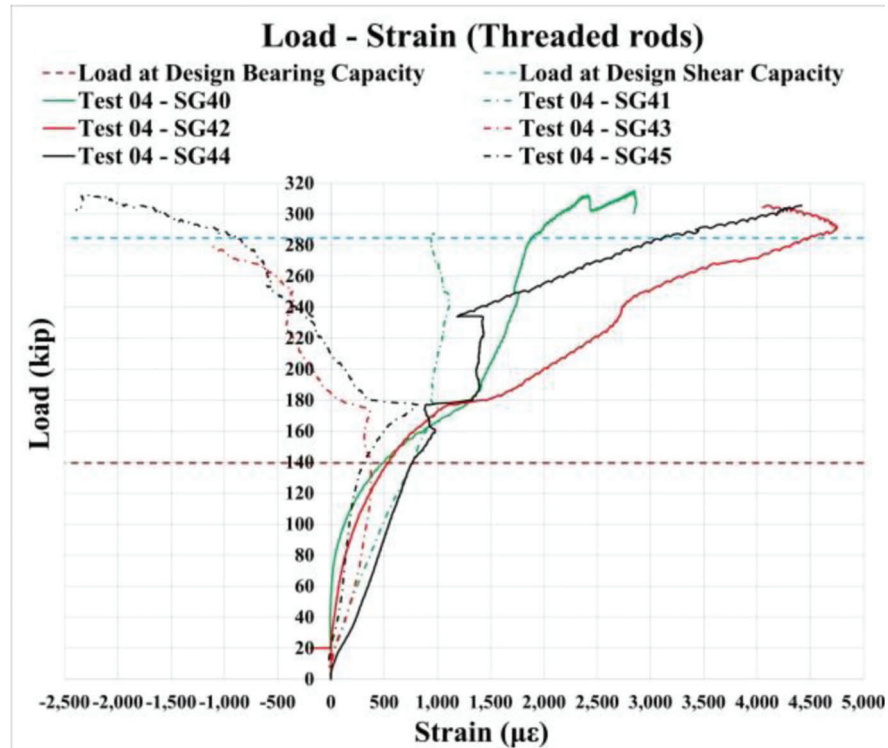


Figure 6.34 Load: strain in threaded rods for Specimen 4.

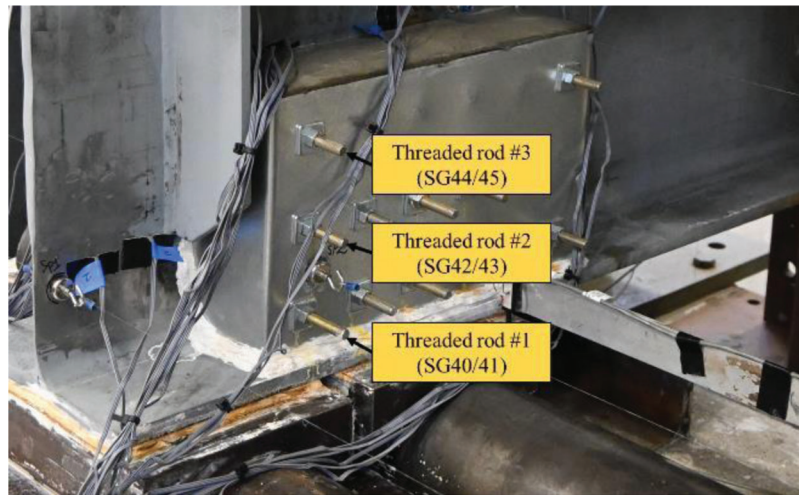


Figure 6.35 Instrumented threaded rods.

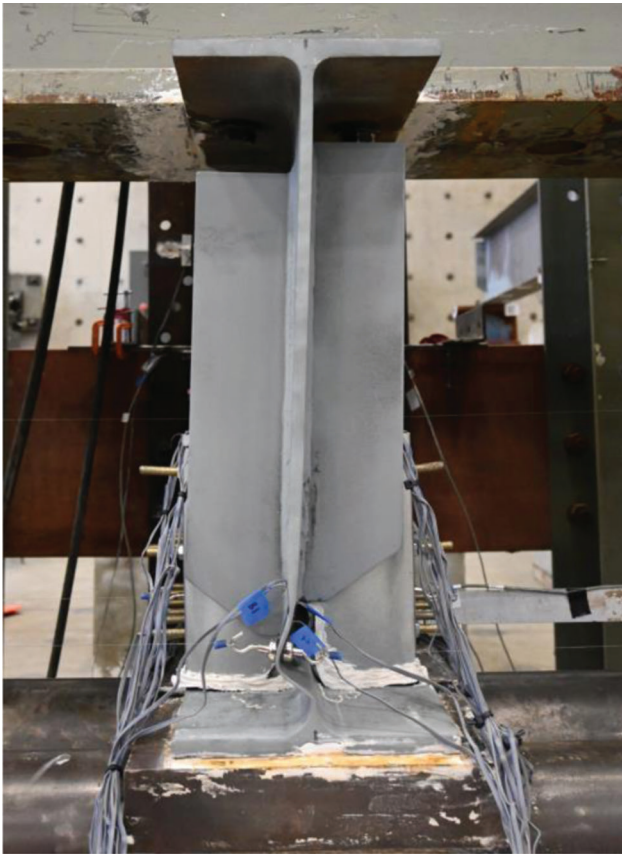


Figure 6.36 Specimen 4: deformed shape, front view.

occurred at the deteriorated girder end (SP1), as expected. In contrast, almost no displacement was recorded by SP2 and SP3, attached to a concrete panel. The peak out-of-plane displacement recorded by SP1 was 0.61" at 230 kips, after which the experiment was terminated. Because the web crippling failure under the spreader beam was an unexpected failure mode, no displacement sensors were installed in this region.

However, visual inspection revealed lateral deformations an order of magnitude higher than those recorded by SP1.

A strain gauge (SG35) oriented longitudinally recorded the deformations in the bottom flange. Figure 6.47 shows that the bottom flange first yielded at 254 kips after Specimen 5 reached the first peak load. The corroded area over the bearing started yielding at 113 kips (SG2), followed by SG5 at 128 kips, and finally SG1 at 310 kips. All vertical strain gauges were subjected to compression throughout the test (Figure 6.48).

Based on data from four strain gauge rosettes located on the west side of the girder web, it can be noted that two strain gauge rosettes (SR2 and SR3) situated over the grout panel extensively yielded (Figure 6.49), indicating significant deformations in the loading area due to web crippling.

Six longitudinal strain gauges were installed on three threaded rods placed over the bearing and anticipated to undergo the largest deformations (Figure 6.50). Both the top and bottom surfaces of the threaded rods were instrumented, and the sensor layout can be found in Figure 5.28. First, the lowermost threaded rod #1 (SG40 and SG41) up to 180 kips (first peak load) underwent insignificant bending deformation, followed by primarily tensile deformations; SG40 recorded the initiation of yielding at 333 kips. Furthermore, threaded rod #2 underwent larger deformations, and SG43 captured the initiation of yielding at 337 kips before Specimen 5 reached its ultimate capacity.

It can be seen from Figure 6.50 that up to the load of 240 kips, the top surface of threaded rod #2 was subjected to tension. However, after reaching this load threshold, deformations transitioned into bending, with the top side of a rod subjected to compression. SG42 malfunctioned during the test; therefore, its data are not presented in Figure 6.50. Finally, threaded rod #3 underwent insignificant bending deformations up to the load of 205 kips. Afterward, threaded rod #3 was subjected to reverse bending: the bottom surface was

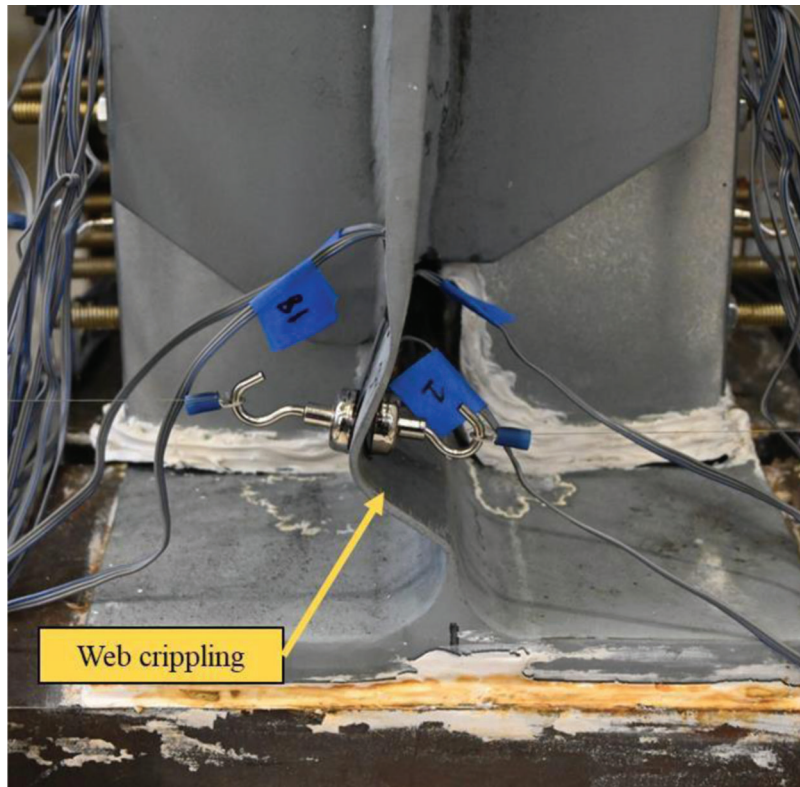


Figure 6.37 Specimen 4: deformed shape, enlarged view.



Figure 6.38 Specimen 4: deformed shape, view from the east side.

subjected to compression (SG44), and the top surface was subjected to tension (SG45). The yielding was recorded at 323 and 310 kips by SG44 and SG45, respectively.

The deformed shape of Specimen 5 is illustrated in Figure 6.51 through Figure 6.56. Specimen 5 experienced

failure in web local crippling in two different zones: bearing and loading regions. Although the specimen was repaired and successfully restored in terms of bearing capacity, the corroded area not encased in the polyester polymer concrete (PPC) exhibited substantial lateral



Figure 6.39 Specimen 4: deformed square washer, view from the west side.

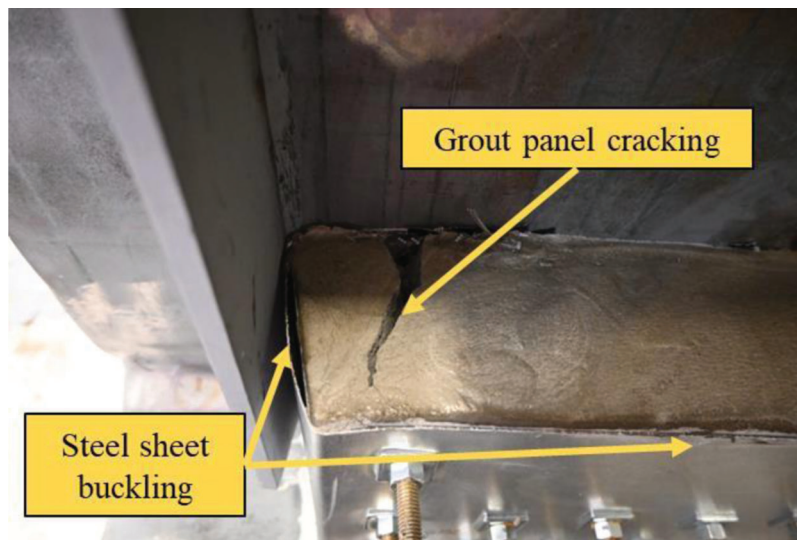


Figure 6.40 Specimen 4: cracks in west panel (top view).

deformations. The unexpected web failure in the loading region occurred due to large compressive forces, resulting in instability, and buckling.

After the experiment, one of the steel sheets was removed to observe the cracking pattern in the Kwik Bond PPC-1121 panel. The panel did not exhibit significant cracking when the experiment was terminated, as depicted in Figure 6.56. This can be attributed to the high tensile strength of the polyester polymer concrete (PPC) compared to conventional cementitious grout. Only a few horizontal cracks were observed in the panel (Figure 6.56).

6.6 Specimen 6

The moderately corroded Specimen 6 was repaired using the sandwich panel method and reached the maximum applied load of 252 kips. Specimen 6 failed in web local crippling, followed by threaded rod yielding, and extensive shear cracking of two grout panels. At the ultimate loading capacity of the repaired specimen, the vertical displacement of 0.286" (DT2) and out-of-plane displacement of 0.019" (SP1) were reached. Specimen 6 fully restored the targeted value of the design bearing capacity, exceeding it by 81%.

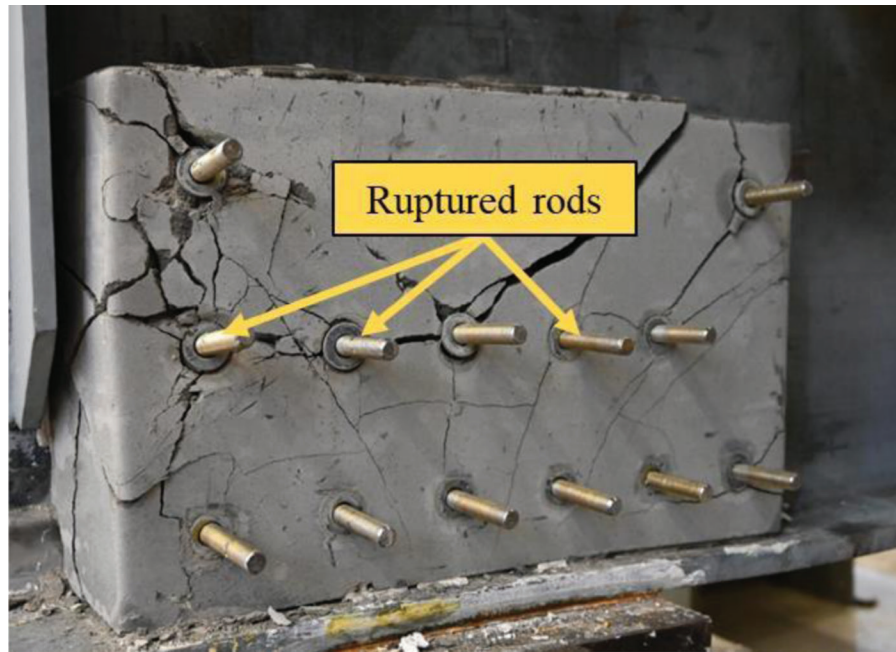


Figure 6.41 Specimen 4: cracking in west panel (elevation view).

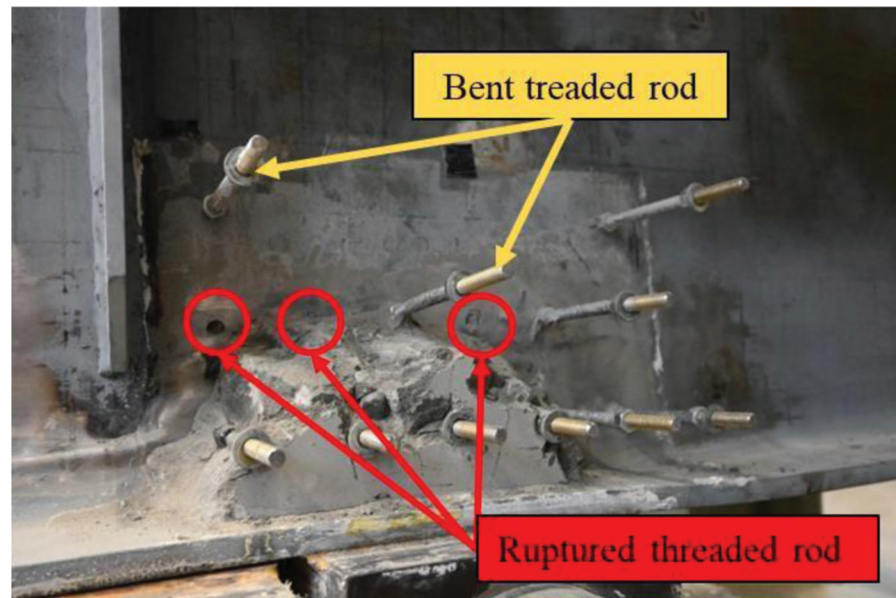


Figure 6.42 Specimen 4: threaded rod deformations (grout panel removed).

The force-vertical displacement plot is shown in Figure 6.57. The displacement transducer DT2 was installed 16" from the girder end, measuring the vertical displacement of the bottom flange. From the force-vertical displacement plot, it could be observed that up to a load of 100 kips, the graph was linear with an initial stiffness of 3,352 kips/in. After reaching this load level, softening behavior was observed. Once the load reached the ultimate load of 252 kips, the girder continued to endure deformations but with negative

stiffness until the test was terminated at 206 kips due to extensive cracking of grout panels.

Based on the data recorded by string potentiometers (Figure 6.58), insignificant out-of-plane displacements were recorded by either SP1, SP2, or SP3. The sensors SP1 and SP2 were connected to the west grout panel and measured the gap opening between the girder web and a grout panel throughout the test. The peak out-of-plane displacement recorded by SP1 was only 0.09" at 206 kips, after which the experiment was terminated.



Figure 6.43 Specimen 4: cross-section of ruptured rods.



Figure 6.44 Specimen 4: three ruptured rods.

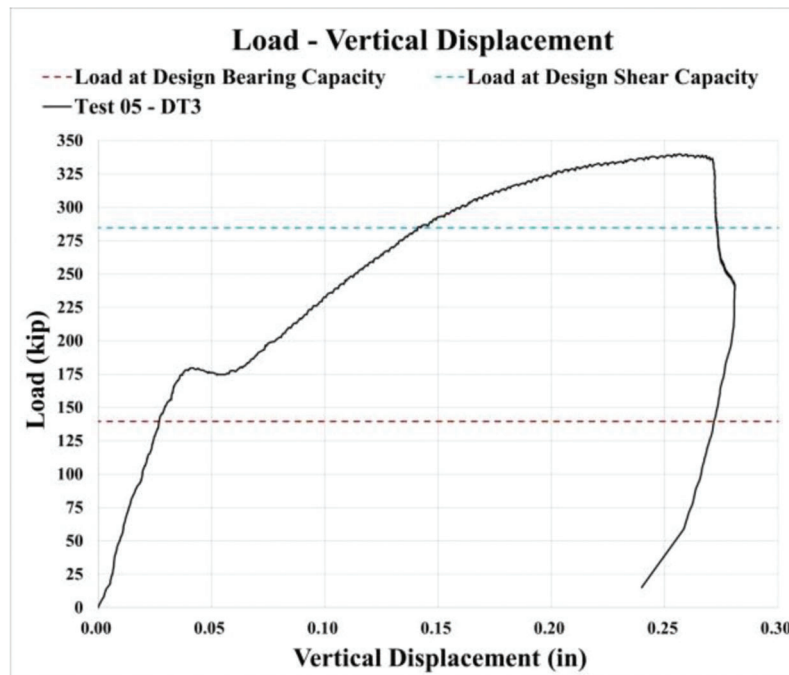


Figure 6.45 Load: vertical displacement plot for Specimen 5.

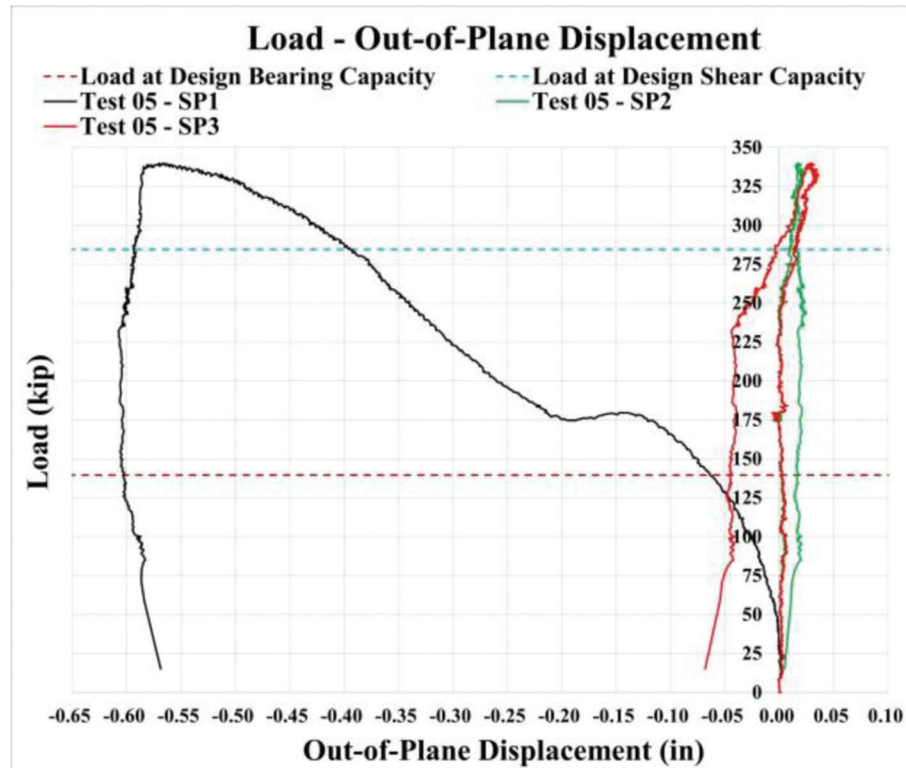


Figure 6.46 Load: OOP displacement plot for Specimen 5.

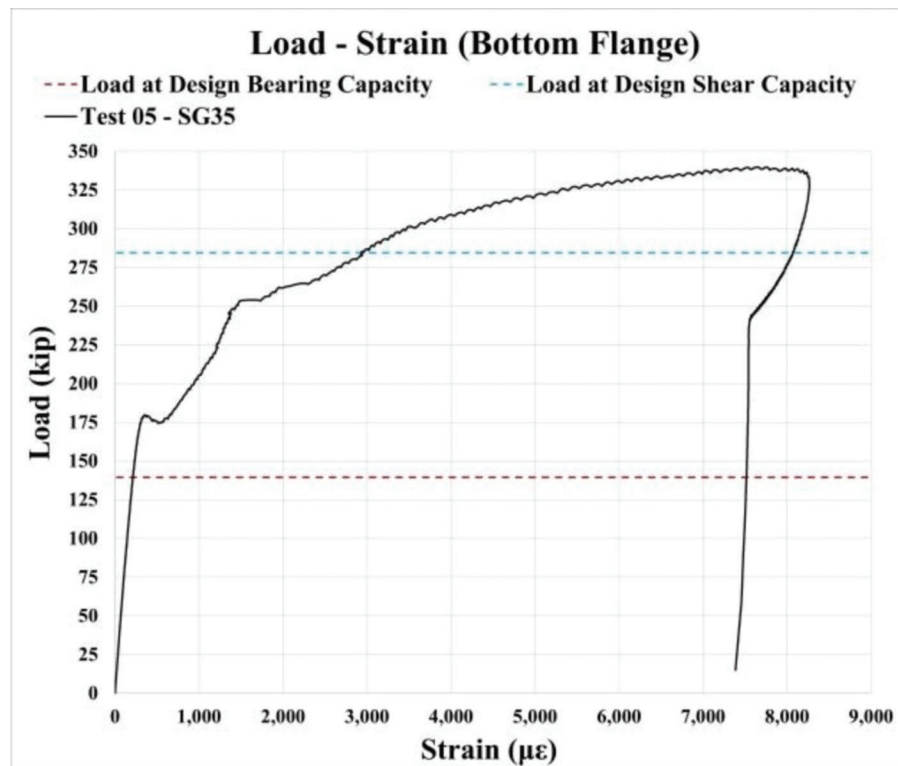


Figure 6.47 Load: strain (bottom flange) plot for Specimen 5.

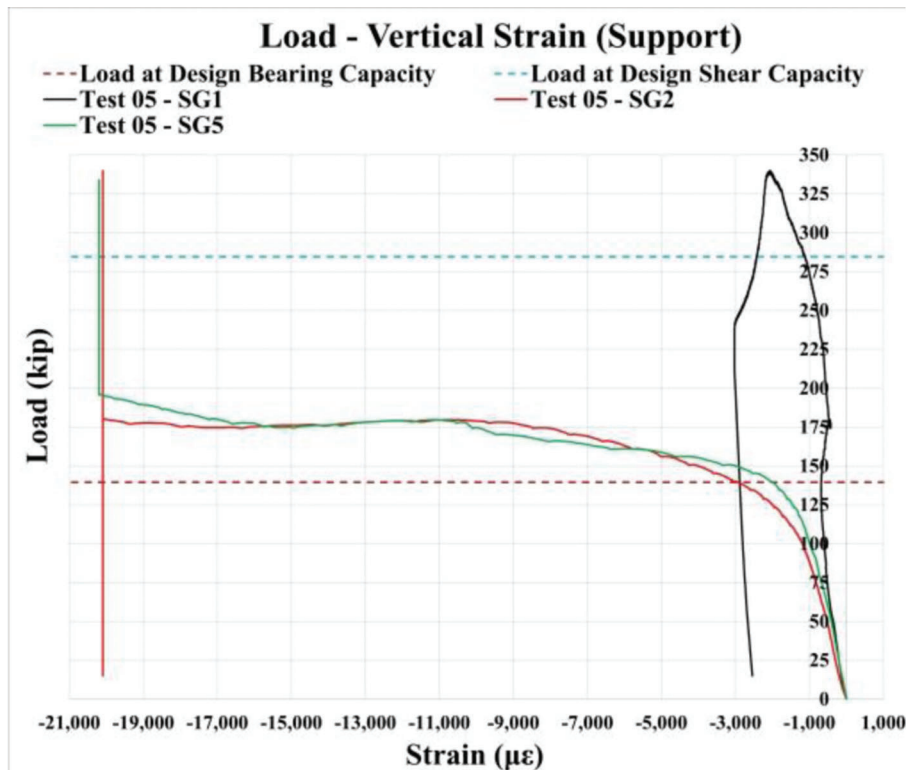


Figure 6.48 Load: vertical strain (support) plot for Specimen 5.

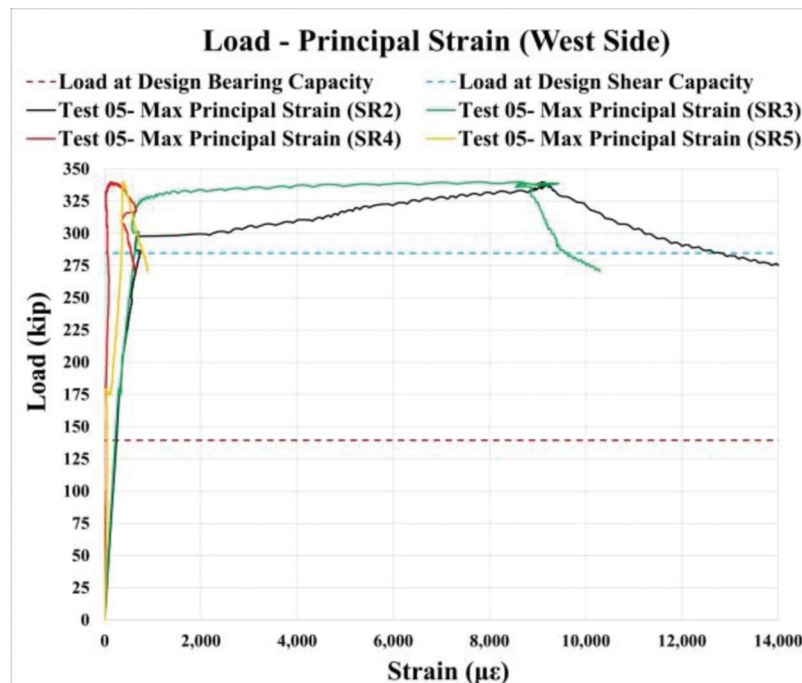


Figure 6.49 Load: maximum principal strain (west side) for Specimen 5.

The lateral displacements were insignificant compared to the previous experiments on repaired Specimen 3—Specimen 5 due to the corroded end being fully encased in this configuration.

A strain gauge (SG35) oriented longitudinally recorded flexural deformations in the bottom flange. Figure 6.59 shows that the bottom flange first yielded at 240 kips after Specimen 6 reached its maximum loading

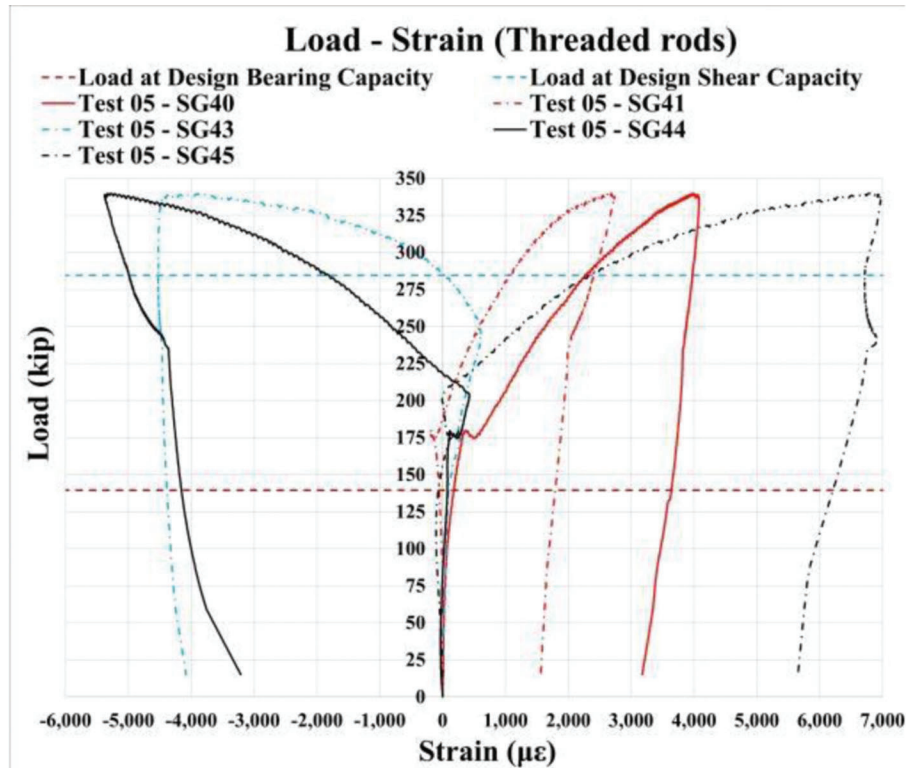


Figure 6.50 Load: strain in threaded rods for Specimen 5.



Figure 6.51 Specimen 5: deformed shape, front view.

capacity. The corroded area over the bearing started yielding at 81 kips (SG1), followed by the yielding of SG2 at 88 kips, and finally, the yielding of SG5 at 117 kips. All vertical strain gauges were subjected to compression throughout the test (Figure 6.60).

Based on data from four strain gauge rosettes located on the west side of the girder web, it could be noted that only one strain gauge rosette (SR2) situated between the grout panel and spreader beam yielded (Figure 6.61).

Six longitudinal strain gauges were installed on the three threaded rods placed over the bearing and anticipated to undergo the largest deformations (Figure 6.62). Both the top and bottom surfaces of the threaded rods were instrumented, and the sensor layout can be found in Figure 5.28. First, the lowermost threaded rod #1 (SG40 and SG41) was subjected to only elastic tensile deformations throughout the entire test, and no yielding was documented ($\epsilon_{y_rod} = 3,620 \mu\epsilon$). Furthermore, the uppermost threaded rod #3 underwent tensile deformations up to 120 kips. Subsequently, threaded rod #3 was subjected to reverse bending: the bottom surface was in compression (SG44), and the top surface was in tension (SG45). The yielding was recorded at 212 kips by SG45 before the specimen reached its ultimate loading capacity.

The deformed shape of Specimen 6 is shown in Figure 6.63 through Figure 6.68. Specimen 6 failed in web local crippling, followed by threaded rod yielding

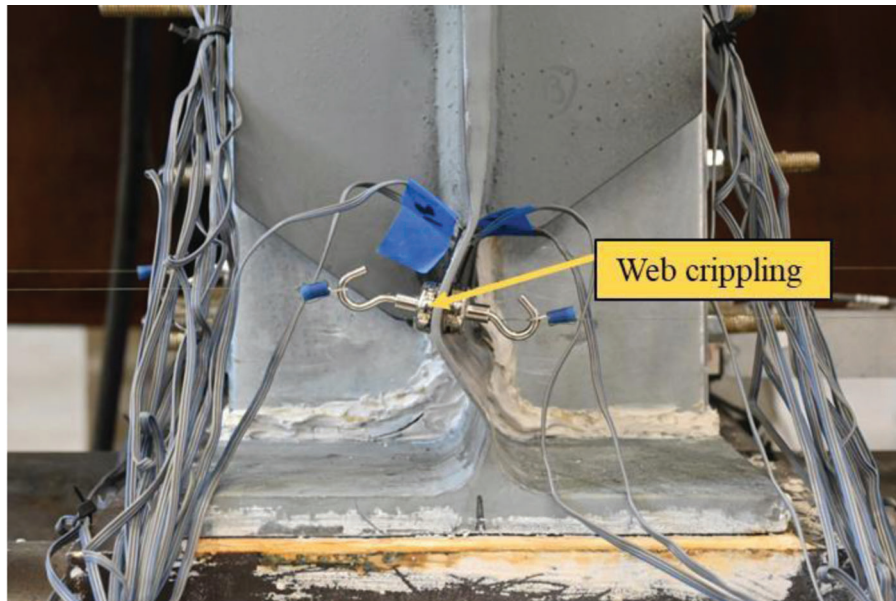


Figure 6.52 Specimen 5: deformed shape, enlarged front view.

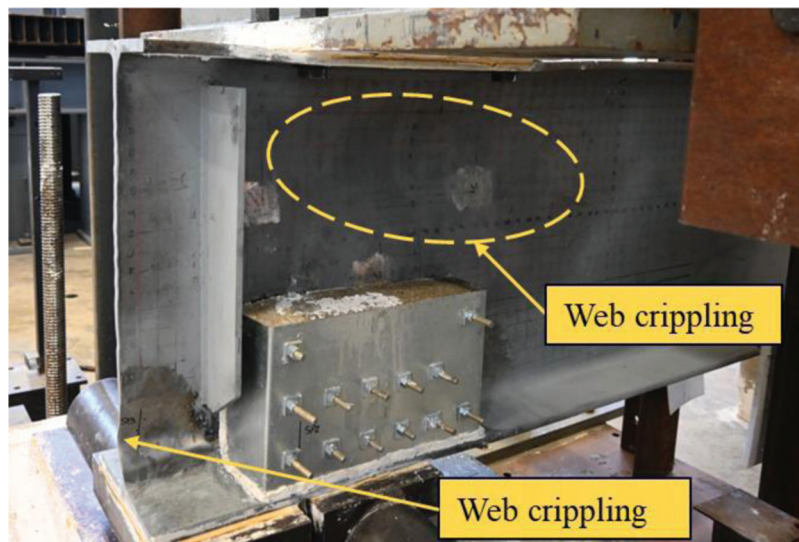


Figure 6.53 Specimen 5: deformed shape, view from the west side.

and cementitious grout panels cracking. After the experiment, one of the steel sheets was removed to observe the cracking pattern in the grout panel. The entire grout panel was extensively cracked when the experiment was terminated.

6.7 Specimen 7

The specimen reached the first peak load of 233 kips. Subsequently, the load dropped to 217 kips, after which the girder continued to carry additional load before reaching an ultimate capacity of 285 kips. Specimen 7 failed in web local crippling combined with threaded rod rupturing and mild cracking of Kwik Bond

PPC-1121 panels. At the first peak load, the vertical displacement of 0.130" (DT2) and out-of-plane displacement of 0.005" (SP1) were obtained. At the ultimate capacity of the repaired specimen, the vertical displacement of 0.369" (DT3) and out-of-plane displacement of 0.032" (SP1) were reached. Specimen 7 fully restored the targeted value of design bearing capacity, surpassing it by 67% when considering the first peak load of 233 kips.

The force-vertical displacement plot is shown in Figure 6.69. The displacement transducer DT2 was installed 16" from the girder end, measuring the vertical displacement of the bottom flange. From the force-vertical displacement plot, it could be observed that up



Figure 6.54 Specimen 5: deformed shape, view from the east side.

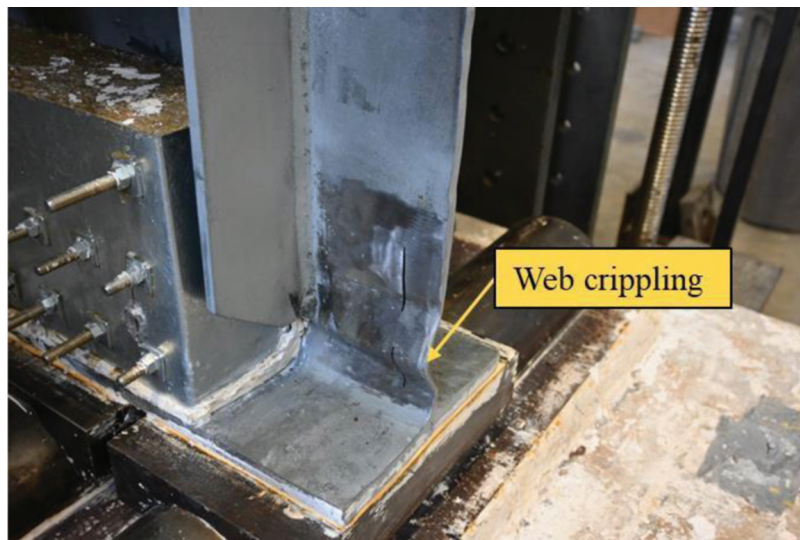


Figure 6.55 Specimen 5: deformed shape, east side view.

to a load of 160 kips, the graph was linear with an initial stiffness of 3,225 kips/in. A softening behavior was observed after reaching this load level, followed by a drop in loading capacity at 233 kips. Once the load reached the first peak, the girder endured deformations but with negative stiffness up to the load level of 217 kips. Afterward, the girder resumed carrying the load with positive stiffness until the second peak of 285 kips. The experiment was terminated at 208 kips when vertical displacement reached 0.61".

Based on the data recorded by string potentiometers (Figure 6.70), insignificant out-of-plane displacements that did not exceed 1/8" were recorded by SP1–SP3 throughout the test. The sensors SP1 and SP2 were connected to the west Kwik Bond panel and measured

the gap opening between the girder web and a grout panel during the test. The peak OOP displacement recorded by SP1 was equal to only 0.112" at 200 kips, after which the experiment was terminated. The lateral displacements were insignificant compared to the previous experiments on repaired Specimens 3 to 5 due to the full encasement of the corroded end in the polyester polymer concrete.

A strain gauge (SG35) oriented longitudinally monitored the deformations in the bottom flange. Figure 6.71 shows that the bottom flange first yielded at 266 kips after Specimen 7 reached the first peak load. The corroded area over the bearing started yielding at 60 kips (SG1), followed by the yielding of SG2 at 80 kips, and finally, the yielding of SG1 at 103 kips. All



Figure 6.56 Specimen 5: cracking in the west Kwik Bond panel.

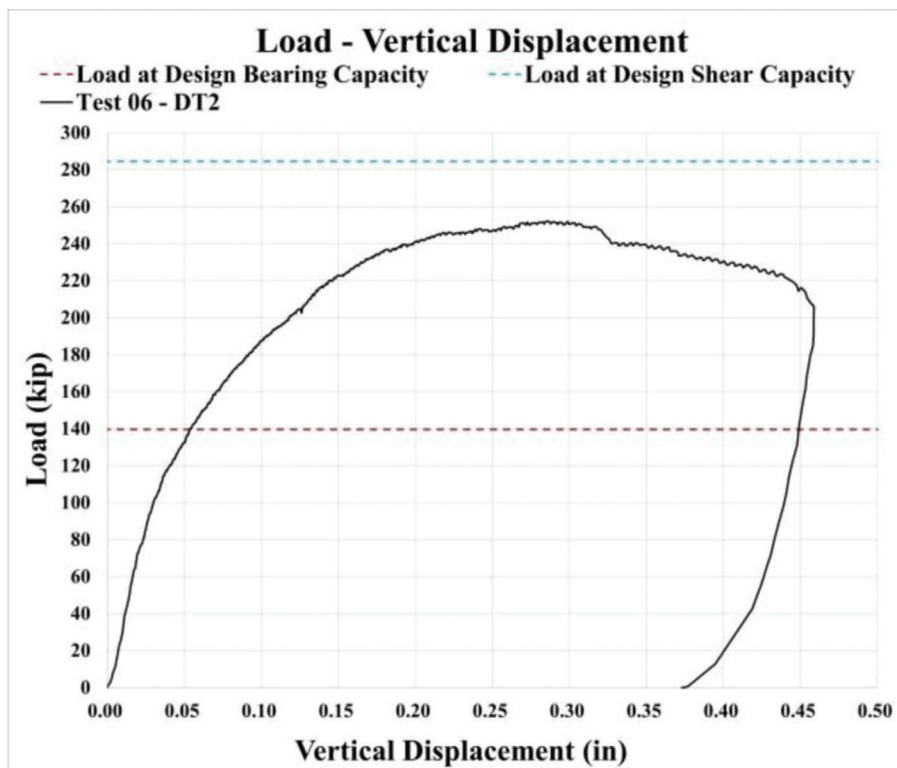


Figure 6.57 Load: vertical displacement plot for Specimen 6.

vertical strain gauges were subjected to compression throughout the test (Figure 6.72). Particularly, strain gauge rosette SR2, positioned between the grout panel and a spreader beam, yielded, while SR3–SR5 underwent only elastic deformations (Figure 6.73).

Six longitudinal strain gauges were installed on the first column of three threaded rods placed over the

bearing and expected to undergo the largest deformations (Figure 6.74). Both the top and bottom surfaces of the threaded rods were instrumented, and the sensor layout can be found in Figure 5.28. The lowermost threaded rod #1 (SG40 and SG41) experienced tensile deformations throughout the entire test; SG40 recorded the initiation of yielding at 236 kips, while SG41 started

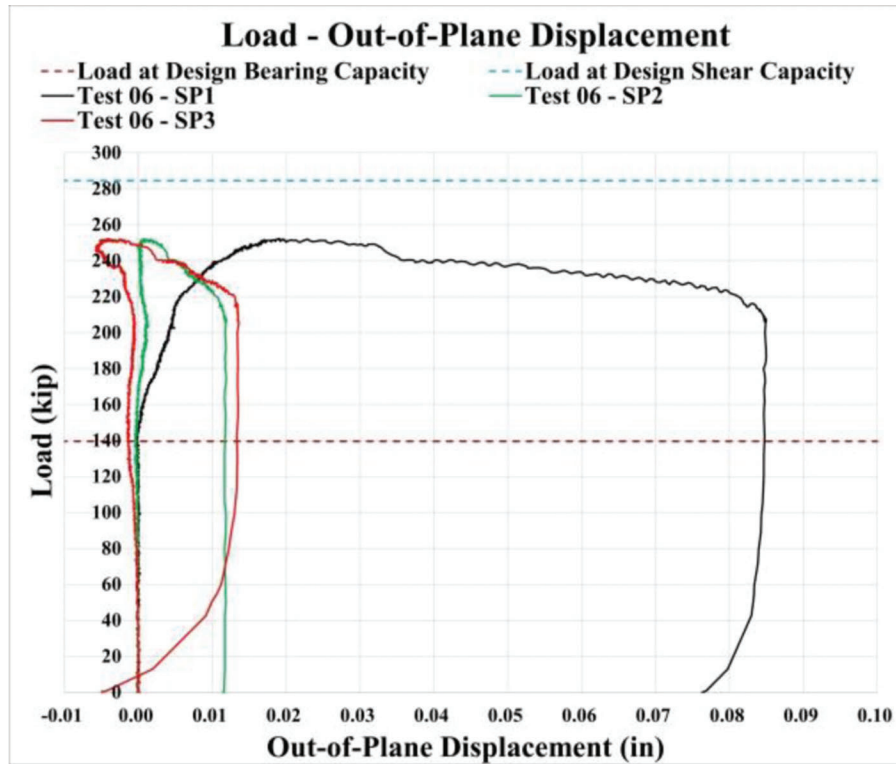


Figure 6.58 Load: OOP displacement plot for Specimen 6.

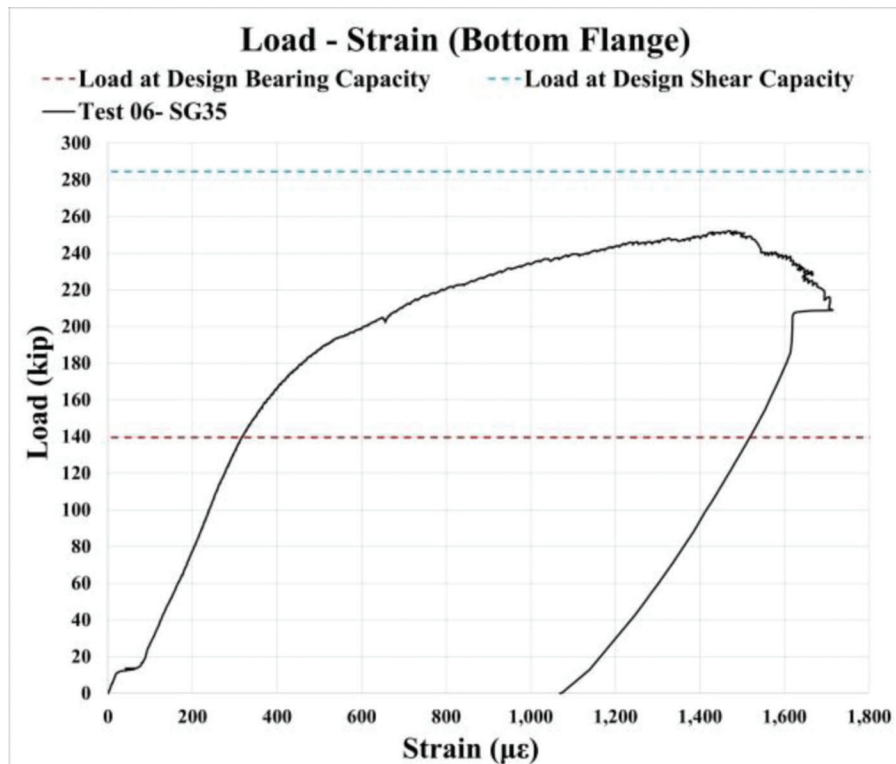


Figure 6.59 Load: strain (bottom flange) plot for Specimen 6.

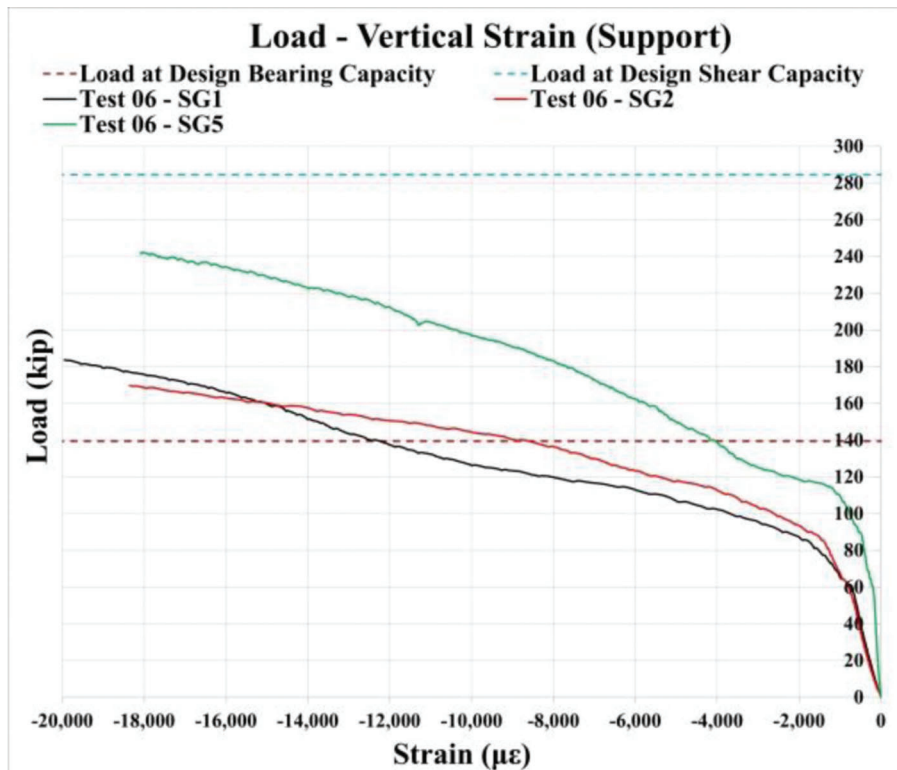


Figure 6.60 Load: vertical strain (support) plot for Specimen 6.

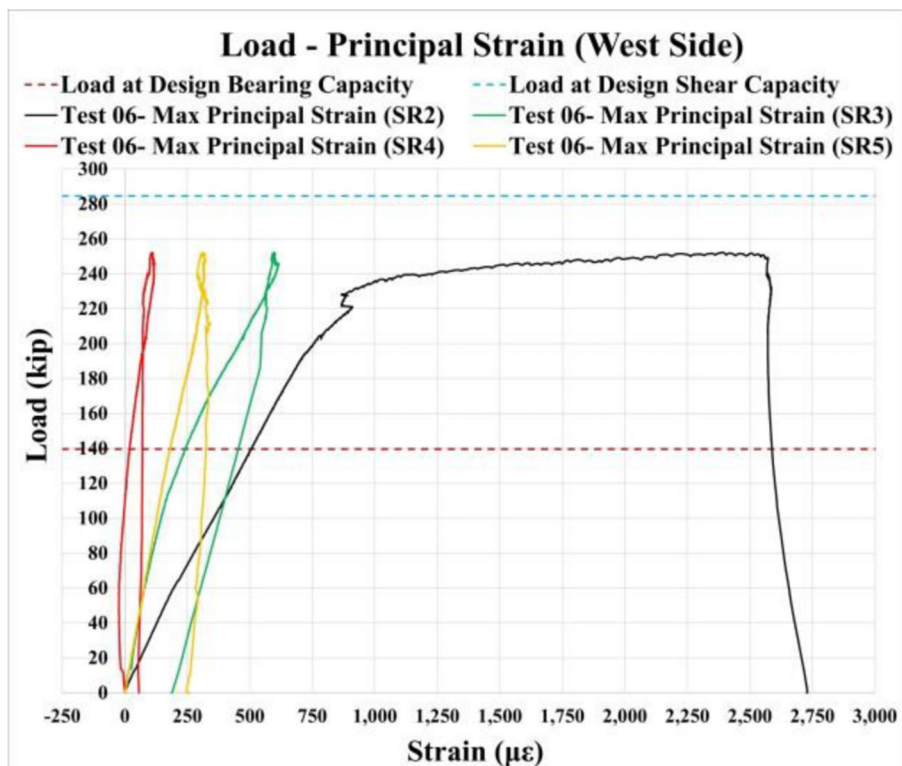


Figure 6.61 Load: maximum principal strain (east side) for Specimen 6.

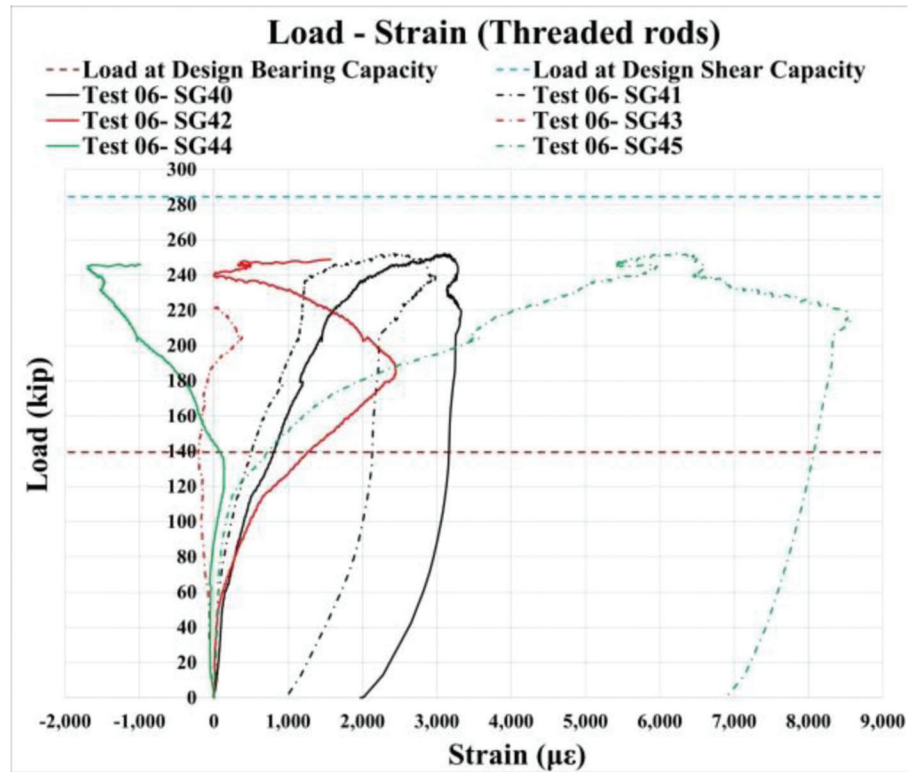


Figure 6.62 Load: strain in threaded rods for Specimen 6.

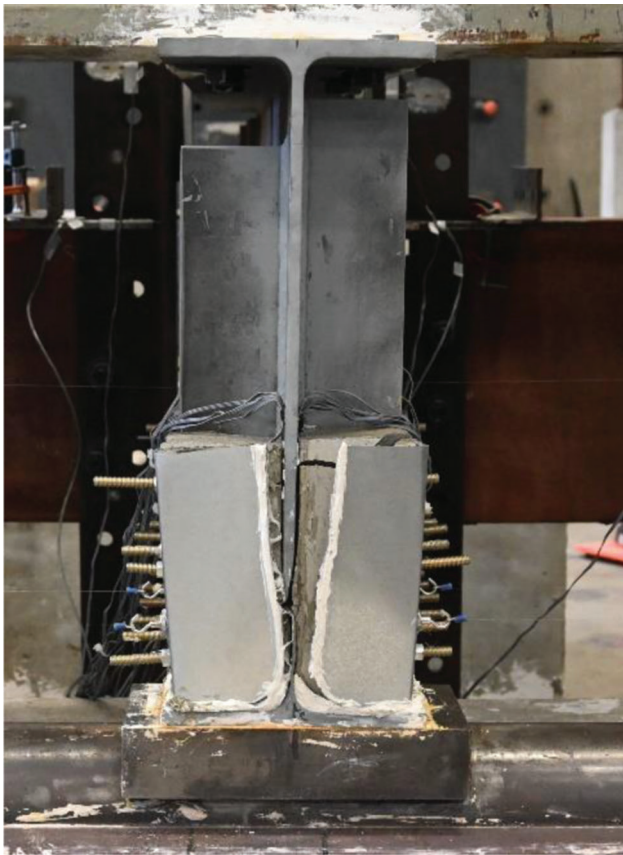


Figure 6.63 Specimen 6: deformed shape, front view.

yielding at 276 kips after the specimen reached its ultimate loading capacity.

It can be observed from Figure 6.74 that up to a load of 250 kips, threaded rod #2 underwent bending with the bottom side of the rod subjected to tensile deformations. However, after reaching this load threshold, deformations transitioned into reverse bending, with the top side of the rod subjected to tension. Both SG42 and SG43 yielded at 217 kips and 282 kips, respectively.

Finally, a similar behavior was noted in threaded rod #3, as it underwent bending deformations up to the first peak load of 230 kips. Subsequently, threaded rod #3 experienced reverse bending, with the bottom surface subjected to compression (SG44) and the top surface subjected to tension (SG45). Yielding was recorded at 280 kips by SG45.

The deformed shape of Specimen 7 is shown in Figure 6.75 through Figure 6.81. Specimen 7 failed in web local crippling, followed by threaded rod rupturing and polyester polymer concrete panel cracking. After the experiment, one of the steel sheets was removed to observe the cracking pattern in the Kwik Bond PPC-1121 panel. Only one major crack was found that propagated from the partial stiffener. Besides that, the panel was not significantly cracked when the experiment was terminated, as shown in Figure 6.78, due to a considerably higher tensile strength of the polymer concrete compared to conventional cementitious grout. In summary, it was found that the infill material can

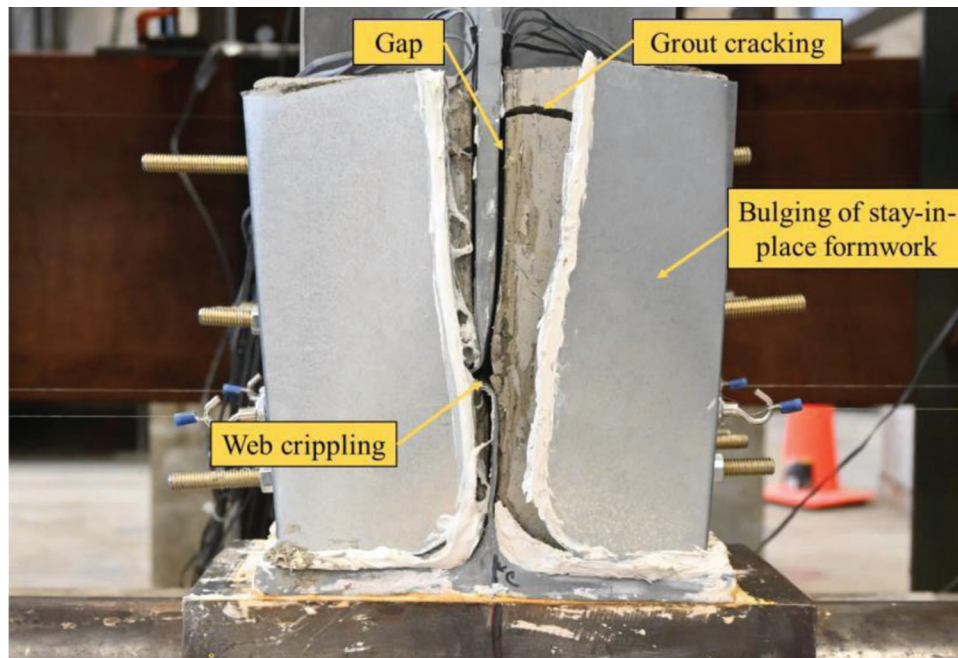


Figure 6.64 Specimen 6: deformed shape, enlarged front view.

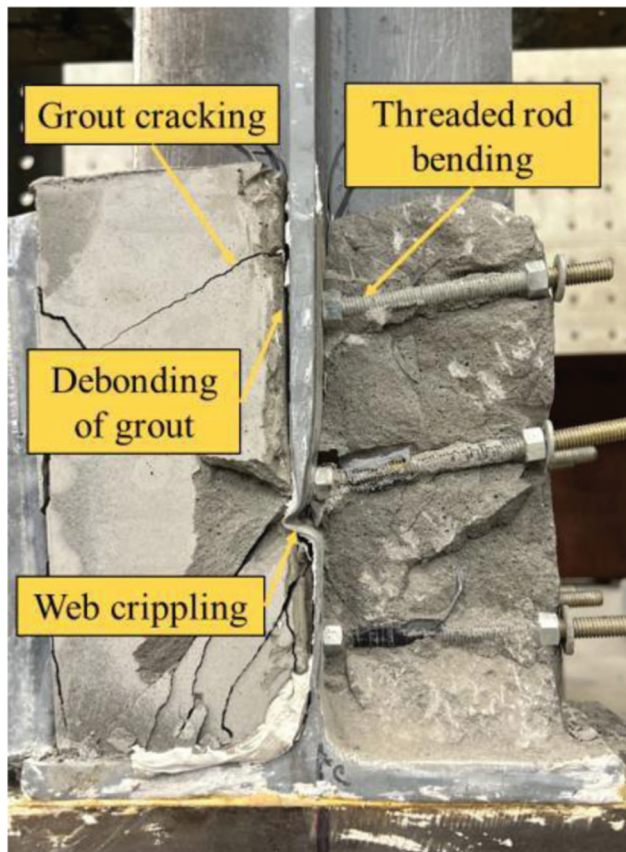


Figure 6.65 Specimen 6: deformed shape and failure

significantly affect the failure mode and the loading capacity of the repaired specimen.

6.8 Summary and Observations

The experimental results from seven large-scale tests, presented in Sections 6.1–6.7, included an undamaged girder, a corroded girder, and five specimens repaired using the sandwich panel method. Both approaches had limitations that the Engineer should consider during the design of the repair. However, Specimen 3 demonstrated that the third option, involving a single support without encasement of the corroded area in the bearing region, would not efficiently recover the design web crippling capacity of the corroded girder.

Table 6.1 illustrates that the post-repair strength of Specimen 4–Specimen 7 exceeded the design web crippling capacity of an intact girder, calculated as per AASHTO provisions (AASHTO, 2020). The bearing arrangement and a visual representation of a test setup for each experiment is included in Table 6.2. The test results demonstrated the efficiency of the novel repair method, as these specimens not only fully recovered but also exceeded the targeted value of the design web crippling capacity. While Specimen 3 exhibited improved strength and performance compared to prior repair state, it did not reach the design web crippling capacity threshold after repair.

The stiffness was calculated using the displacement data from sensor DT3 in all seven tests. The artificially

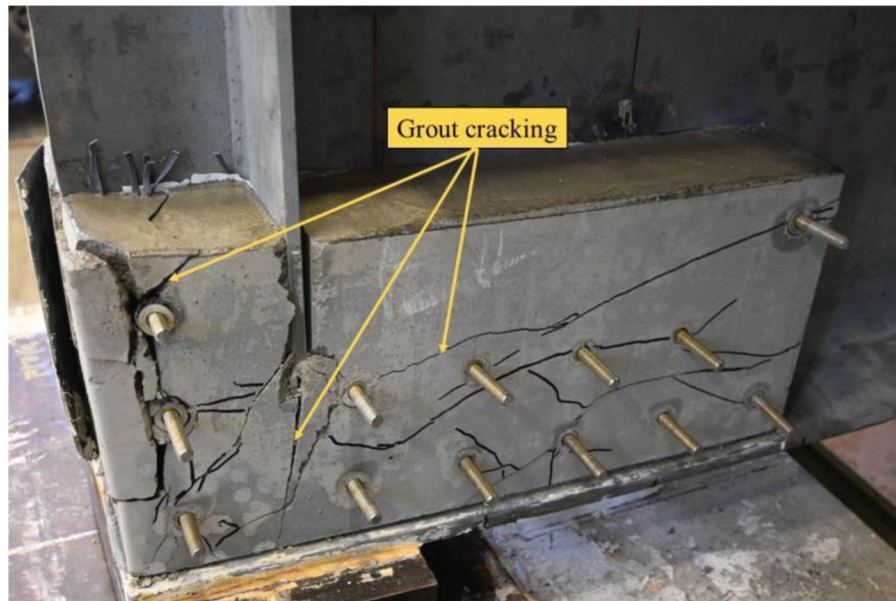


Figure 6.66 Specimen 6: cracking in the west panel.



Figure 6.67 Specimen 6: deformations in threaded rods and grout panels cracking.

corroded Specimen 2 lost roughly 30% of its stiffness from load-vertical displacement response due to section loss. However, after repair, each girder surpassed the initial stiffness values of a non-corroded steel girder. Specimens 4 and 5 showed significantly increased stiffness due to the extended bearing length.

Moreover, the effectiveness of the repair was evident in the strains in the web above the bearing region. The vertical strain gauge at 4" away from the girder end, positioned over the center of the bearing in the section loss region (SG1/SG2), revealed 3 to 7 times decrease in bearing strain for Specimen 3–Specimen 7 compared to the values of Specimen 2, which failed at 39 kips. The reduction in strain values suggested the establishment of an alternative load path, transferring forces from the girder web to the concrete panels

through threaded rods and from concrete panels to the bearing.

Finally, two effective options were investigated for recovering the design web crippling capacity of unstiffened steel girders. The first option involved encasing the corroded web in the bearing region without increasing the bearing length (Specimens 6–7). The second option was to increase the bearing length by installing additional support without encasement of the corroded web in the bearing region (Specimens 4–5). Both approaches had limitations that engineers should consider during the design of repairs. However, Specimen 3 demonstrated that the third option, involving a single support without encasement of the corroded area in the bearing region, would not efficiently recover the design web crippling capacity of the corroded girder.

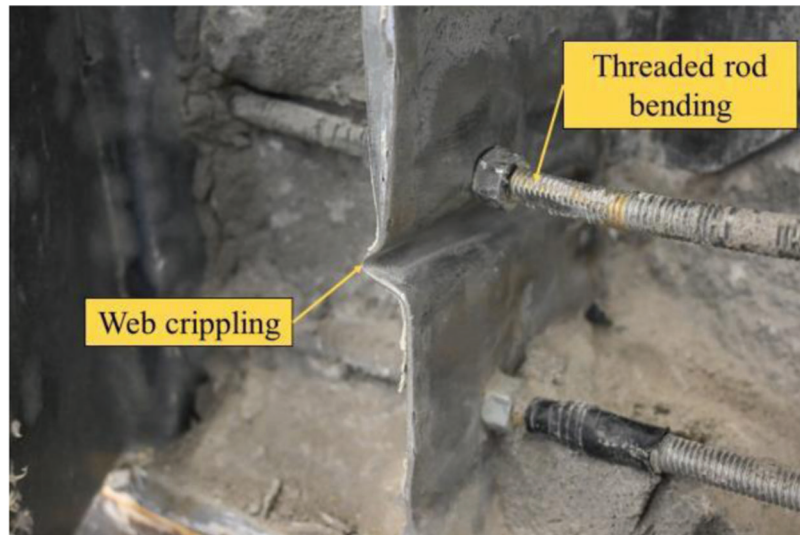


Figure 6.68 Specimen 6: web crippling behind grout panel.

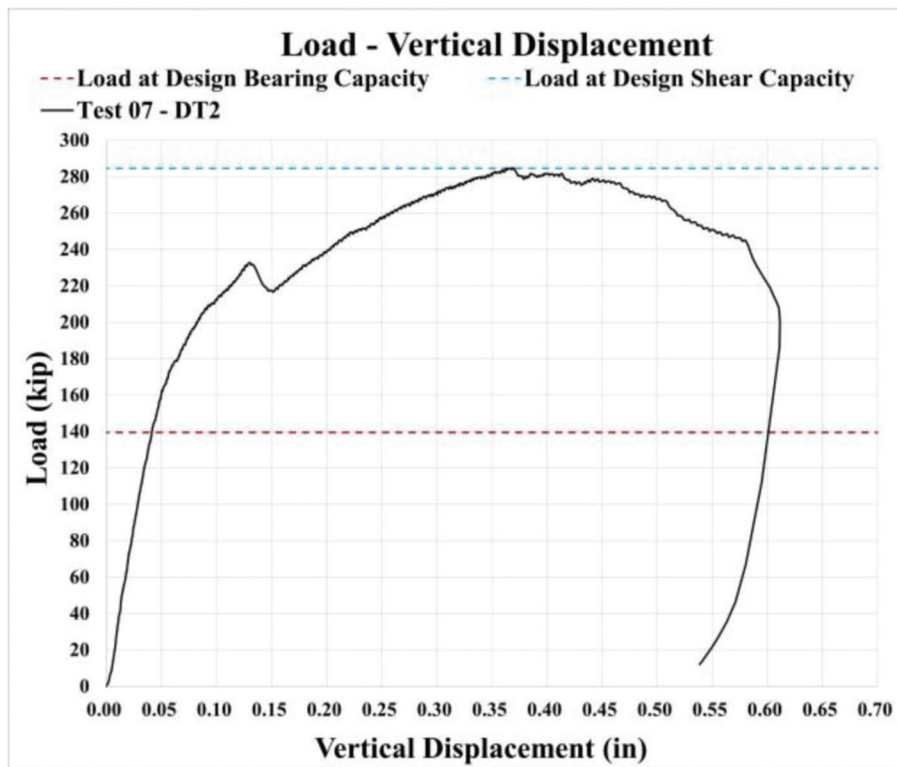


Figure 6.69 Load: vertical displacement plot for Specimen 7.

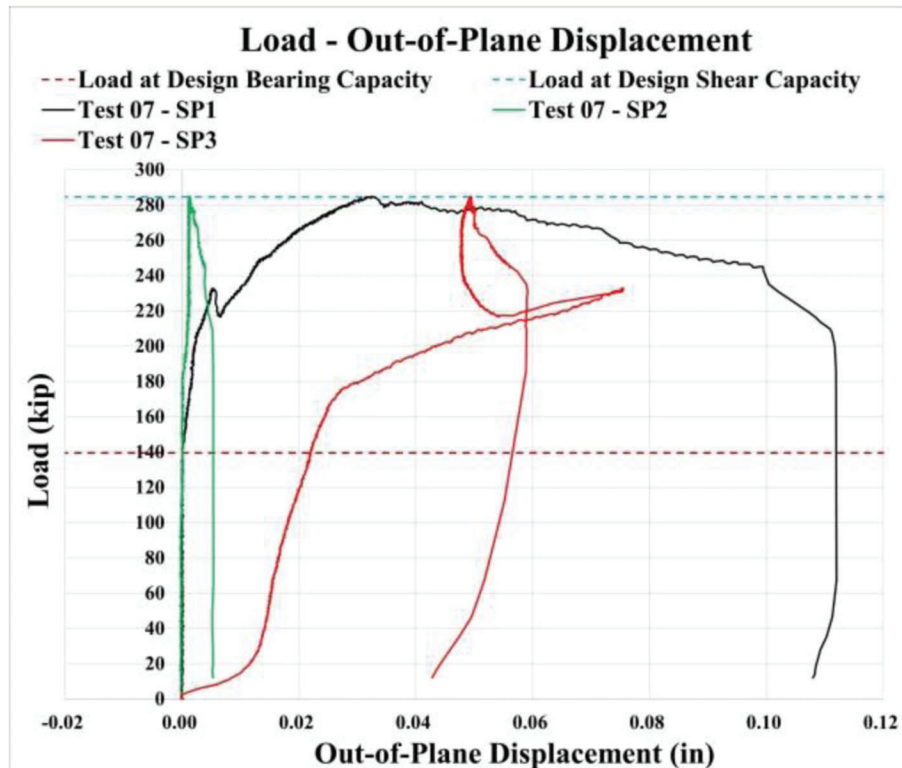


Figure 6.70 Load: OOP displacement plot for Specimen 7.

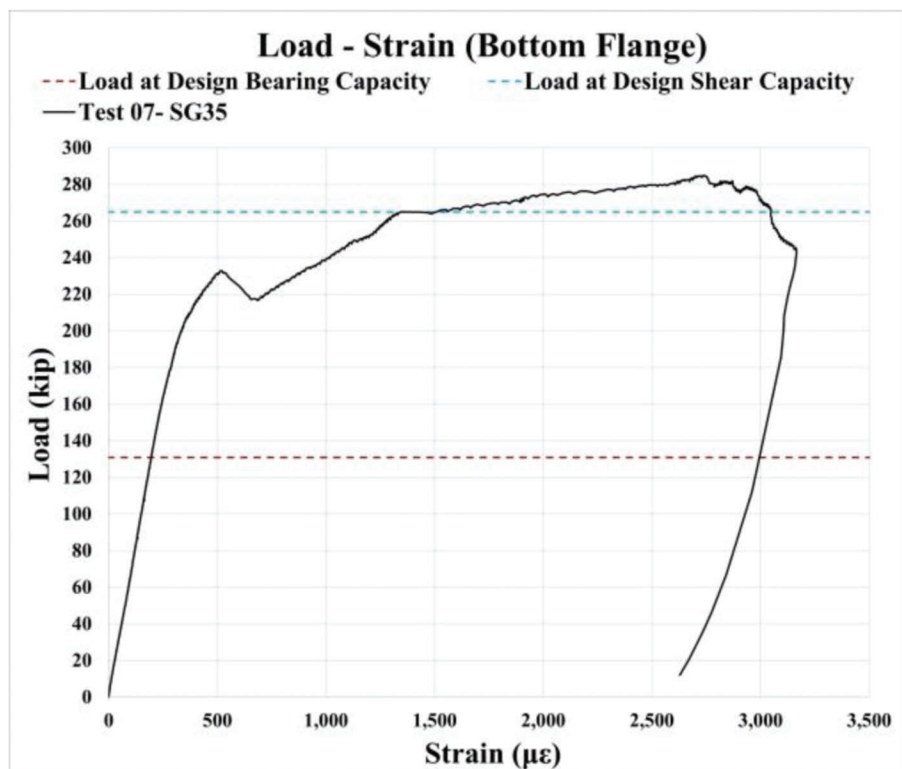


Figure 6.71 Load: strain (bottom flange) plot for Specimen 7.

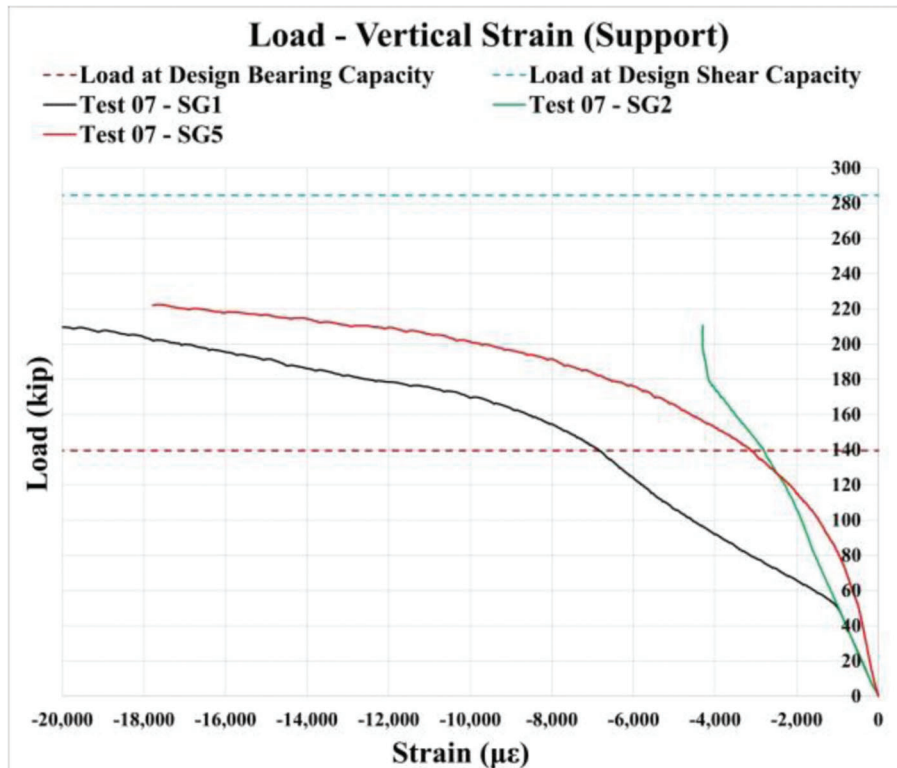


Figure 6.72 Load: vertical strain (support) plot for Specimen 7.

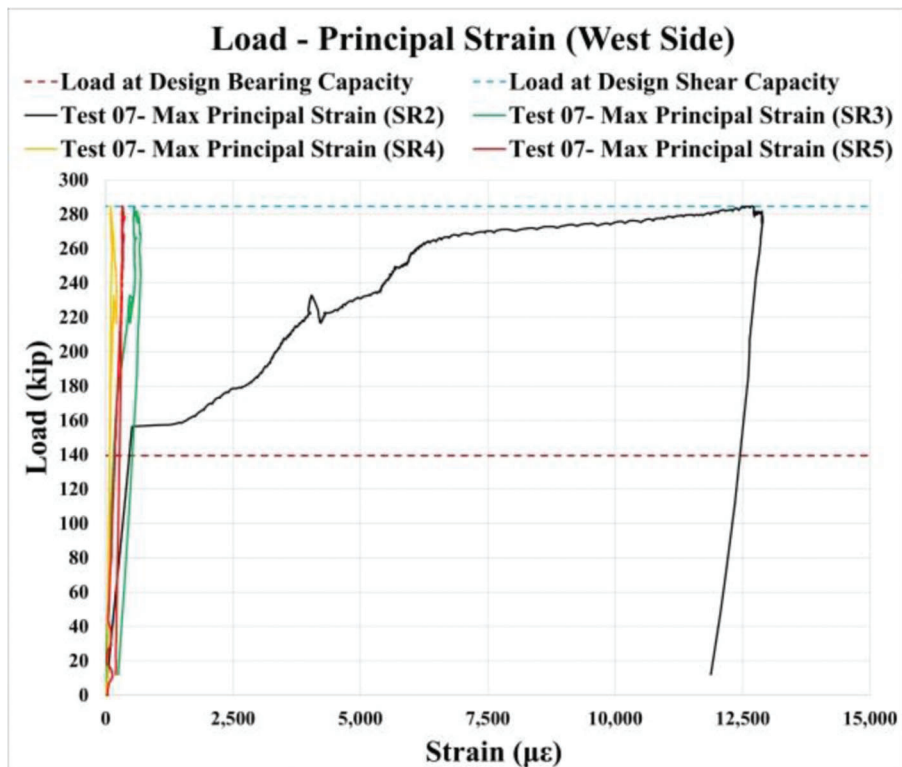


Figure 6.73 Load: maximum principal strain (west side) for Specimen 7.

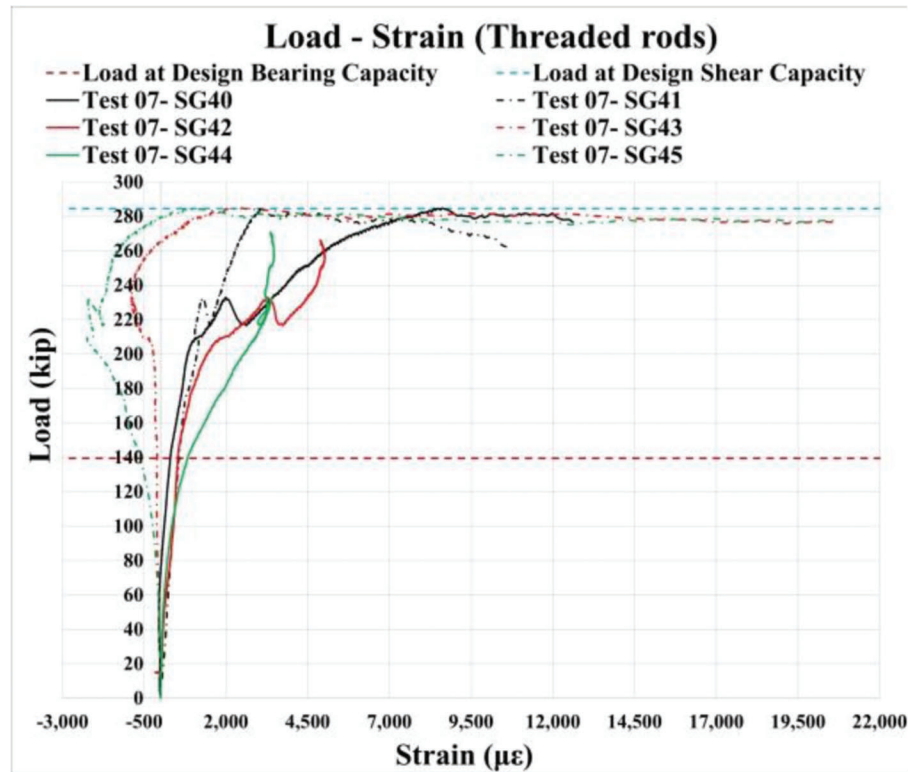


Figure 6.74 Load: strain in threaded rods for Specimen 7.

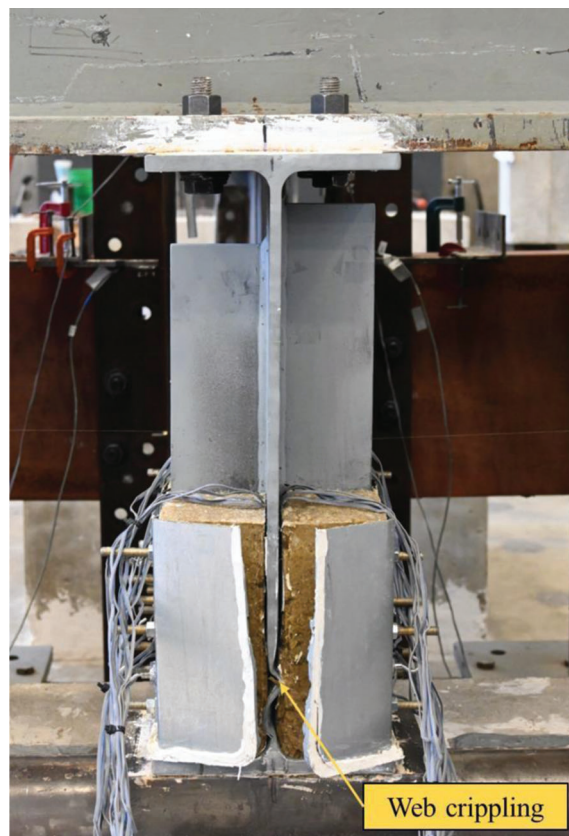


Figure 6.75 Specimen 7: deformed shape.

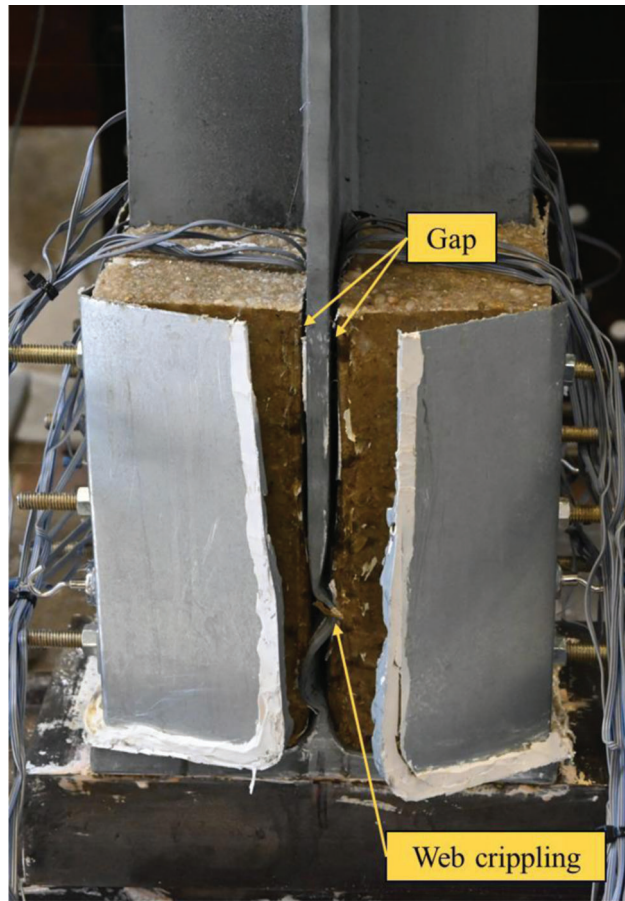


Figure 6.76 Specimen 7: deformed shape, enlarged front view.



Figure 6.77 Specimen 7: deformed shape, east side view.

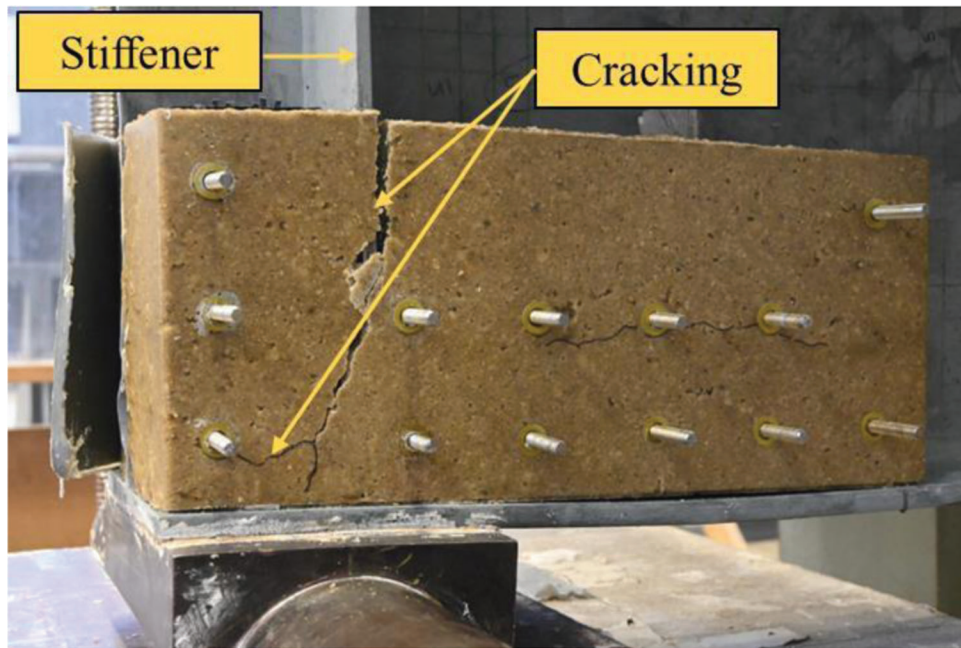


Figure 6.78 Specimen 7: cracking in a west panel.

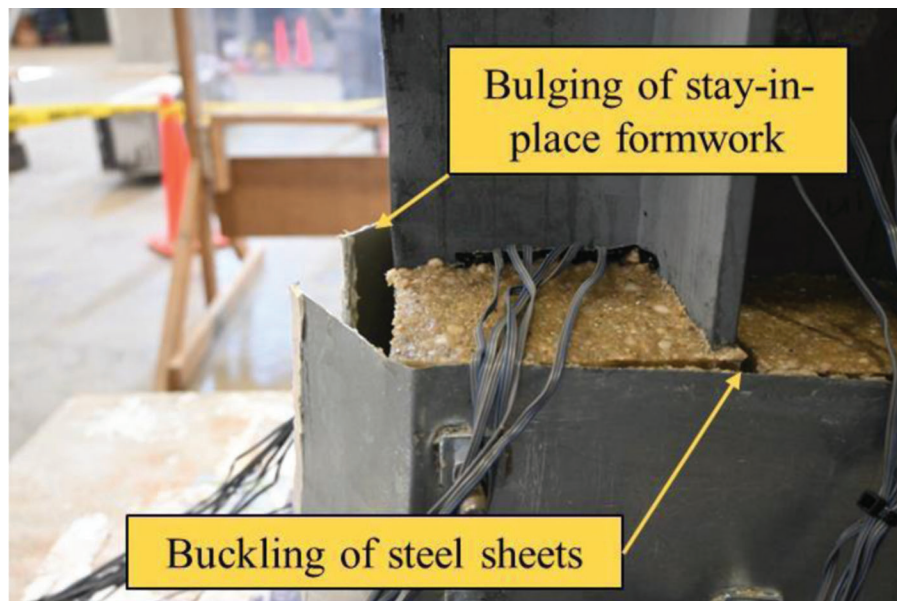


Figure 6.79 Specimen 7: buckling and bulging of steel sheets.

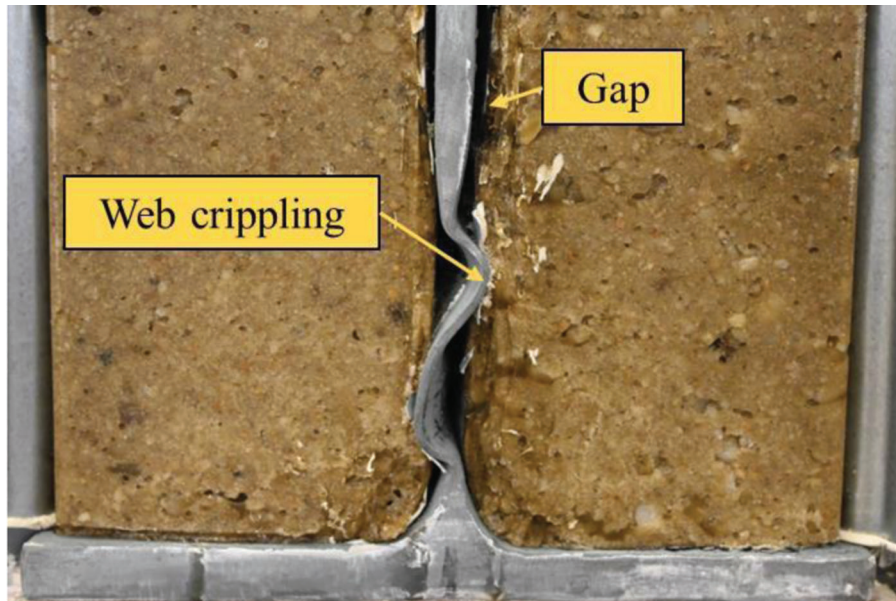


Figure 6.80 Specimen 7: web crippling deformations, front view.



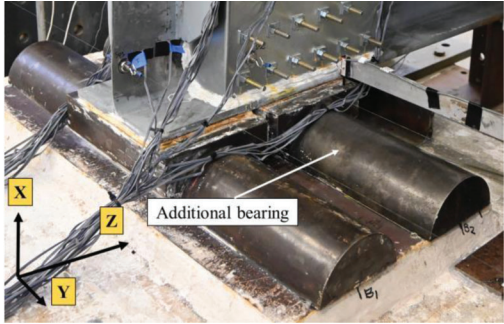



Figure 6.81 Specimen 7: web crippling deformations behind the concrete panel.

TABLE 6.1
Experimental results

Specimen Number	Failure Mode	Maximum Applied Load, kip	Design Web Crippling Capacity, kip	Change in Design Web Crippling Capacity (%)	Stiffness, kip/in. (DT3)	Bearing Strain at 39.1 kips, $\mu\epsilon$
1	Web Crippling	230.7	139.5	65	2,473	-527
2	Web Crippling	39.1		-72	1,722	-2,990
3	Web Crippling	79.6		-43	2,587	-1,003
4	Web Crippling + Threaded Rod Rupture	315.0		126	4,158	-638
5	Web Crippling	339.9	104	144	4,779	-420
6	Web Crippling	252.2		81	2,906	-546
7	Web Crippling + Threaded Rod Rupture	284.8		104	2,839	-779

TABLE 6.2
Test setup and bearing arrangement details

Specimen Number	Bearing Length (in.)	Bearing Arrangement	Visual Representation
1 2 3 6	8		
7		Bearing arrangement for Specimens 1–3, 6–7	Visual representation of the test setup (Specimens 1–3, 6–7)
4 5	17		
		Bearing arrangement for Specimens 4–5	Visual representation of the test setup (Specimens 4–5)

7. FINITE ELEMENT MODELING

Finite element (FE) models for Specimens 1–7 were developed in Abaqus, and the Explicit solver was employed to replicate the behavior observed during the experiments. Developed FE models were validated using the experimental results and used for parametric study (Chapter 8) and verifying the proposed design equations. The following subsections describe the modeling approach for the finite element models of Specimens 1–7, providing details on assembly, material properties, meshing techniques, boundary conditions, loads, interactions, constraints, and imperfections. The modeling approach differed between non-repaired specimens (Specimens 1 and 2) and repaired specimens (Specimens 3–7) and has been described in detail below.

7.1 Modeling Approach: Specimen 1–Specimen 2

7.1.1 Assembly, Boundary Conditions, Interactions, and Load

The assembly for Specimens 1 and 2 consisted of a steel girder with partial-depth transverse stiffeners modeled as one solid part, four steel plates acting as lateral bracings, and two pairs of bearings. The bearings consisted of two solid parts: the bottom half-cylinder and the upper component, which was allowed to rotate (Figure 7.1). The corrosion profile induced in Specimen 2 had smooth transitions to the undamaged web and bottom flange, as shown in Figure 7.1, and Figure 7.2. Specimens 3–7 had a similar approach for incorporating the section loss profile.

The finite element models had simply supported boundary conditions (BC): pin support at one end and roller support at the other end. Pin support was represented by three restrained translational degrees of freedom: $U1 = U2 = U3 = 0$ on the bottom of the half-cylindrical bearing, allowing the top component to rotate. The roller support consisted of a steel plate, a half-cylindrical, and the top parts of the bearing. In this

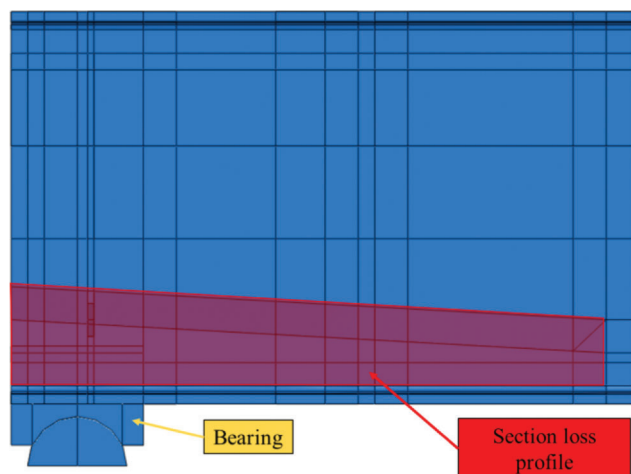


Figure 7.1 Assembly in Abaqus, elevation view.

case, only the bottom steel plate was restrained from movement in three translational degrees of freedom: $U1 = U2 = U3 = 0$. The half-cylindrical part was allowed to slide along the surface of the steel plate, and the upper part was allowed to rotate (Figure 7.3).

General contact (explicit) for the entire model was used with a static steel-to-steel friction coefficient of 0.6 for tangential behavior (The Engineering Toolbox, 2004) and “hard” contact for normal behavior to prevent penetration.

At the location where lateral bracings were installed, 0.75” steel plates were added to restrain out-of-plane movement and prevent lateral torsional buckling. A small 1/8” gap was introduced to represent actual boundary conditions, as small gaps were also present in the test setup (Figure 7.4). A single concentrated vertical load was applied 16” from the girder end to the top. Because the load from the actuator was applied through the spreader beam, the area under the spreader beam deformed instantaneously. To capture similar behavior, a kinematic coupling constraint was used on the top at the location of the spreader beam, allowing this region to deform similarly under the applied load. In the coupling constraint, only translational degrees of freedom $U2 = U2 = U3$ were constrained.

In all FE models, displacement control was used: a 0.5” displacement was applied in the vertical direction to obtain a full force–displacement curve. To apply the load quasi-statically without dynamic amplification, “Smooth Step” was used for the amplitude of the applied load. This allowed the loading to be applied smoothly without causing stress waves. To speed up the

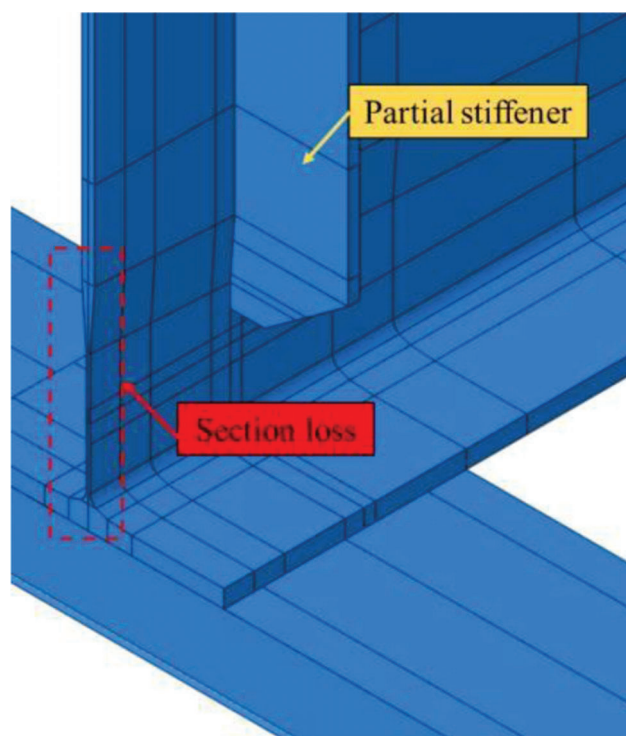


Figure 7.2 Section loss profile.

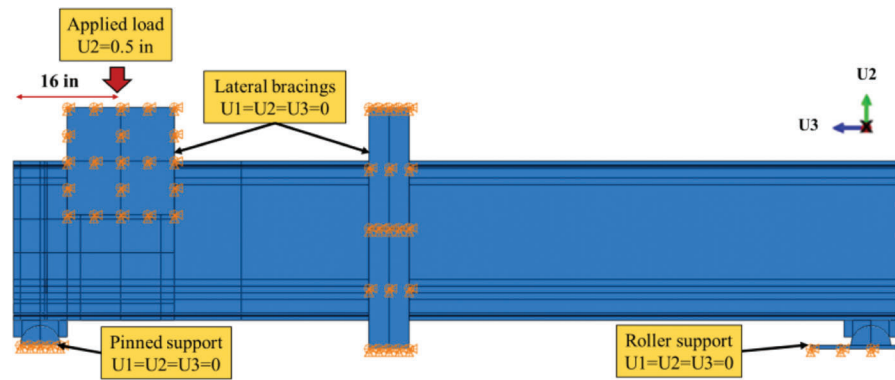


Figure 7.3 Boundary conditions (BC) of the FE model, side elevation view.

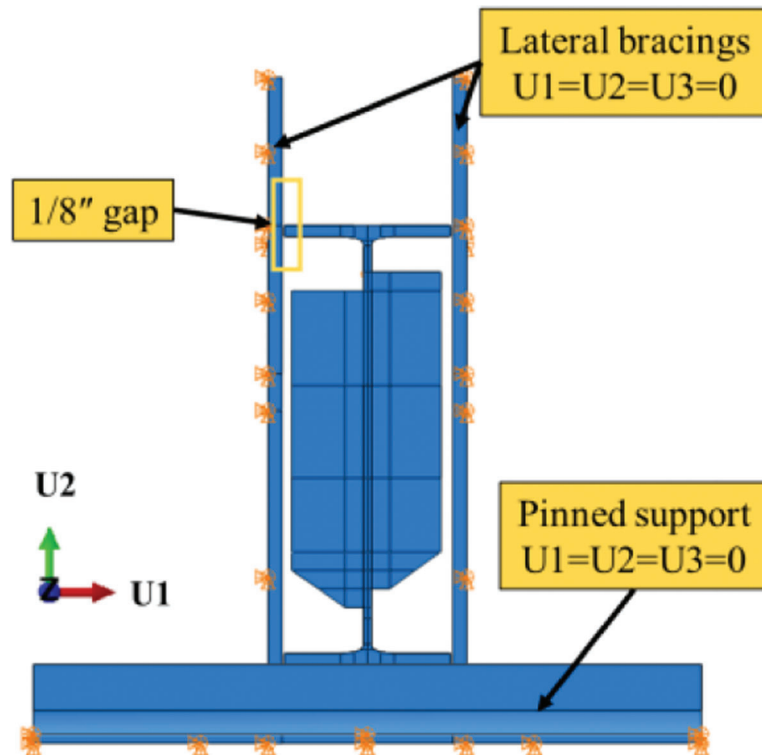


Figure 7.4 BC of the FE model, front view.

analysis, mass scaling was used. However, a thorough investigation was conducted to finalize the appropriate value that would not significantly affect the simulation results by introducing dynamic and inertial effects to the model.

7.1.2 Mesh

Finite element models were developed using solid eight-node brick linear order elements (C3D8I and C3D8R). The critical parts, such as the girder, were modeled using incompatible mode elements (C3D8I). These elements provided more accurate results for elements subjected to bending than simple linear order C3D8 elements because artificial stiffness was elimi-

nated. Incompatible mode elements were more computationally efficient than quadratic elements. Conversely, less critical elements data from which was not extracted, such as bearings, were modeled using reduced integration elements (C3D8R) to accelerate the analysis. Usually, the solid elements that have one integration point (C3D8R) are susceptible to the hourglass effects due to the reduced stiffness of the elements. Enhanced hourglass control was used to prevent the appearance of zero-energy modes, also known as hour glassing. The size of the mesh varied throughout the model: the girder end was meshed using fine elements (0.5–1") to obtain more accurate results, whereas the bearings and lateral bracings had coarser elements (2 × 2"). The standard mesh is shown in Figure 7.5.

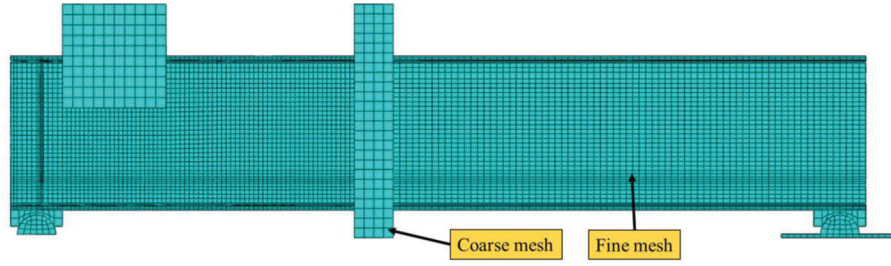


Figure 7.5 Standard mesh: Specimen 1.

7.1.3 Material Properties

7.1.3.1 Structural steel. The precise material properties for the Abaqus input were paramount to achieving results comparable to the experimental data. The material properties of steel were obtained by completing tensile coupon tests following ASTM E8-22 (ASTM, 2022a) specifications. Tensile coupons were cut from steel girders in directions parallel and transverse to the bending stresses and tested in the INSTRON machine. The tested girders were demolished from the same bridge as Kanakamedala, Seo, Varma, Connor, and Tarasova (2023) described in their study; therefore, an identical material model was implemented in this study. It should be noted that the yielding strength of A36 steel greatly exceeded the nominal 36 ksi, reaching approximately 45 ksi. A plastic material model was used to predict the behavior of a steel girder with a measured yield strength of $F_y = 45$ ksi. When identifying plasticity in Abaqus, true stress and strain must be used for the finite element software to interpret the data correctly. Therefore, Equation 7.1–Equation 7.3 were used to convert the measured stress (σ_{eng}) and strain (ϵ_{eng}) to the true stress (σ_{true}) and strain (ϵ_{true}). The equations were taken from the Abaqus manual (Abaqus, 2006b). The true and engineering stress–strain curves for A36 steel are shown in Figure 7.6.

$$\epsilon_{true} = \ln(1 + \epsilon_{eng}) \quad (\text{Eq. 7.1})$$

$$\sigma_{true} = \sigma_{eng}(1 + \epsilon_{eng}) \quad (\text{Eq. 7.2})$$

$$\epsilon_p = \epsilon_{true} - \frac{\sigma_{true}}{E} \quad (\text{Eq. 7.3})$$

7.1.4 Imperfections and Buckling Analysis

To account for the initial out-of-plane straightness of the girders, buckling analysis in Abaqus was performed, and the $0.3t_w$ imperfection value ($0.1245''$) was incorporated in Specimen 1. The $0.1t_w$ imperfection value ($0.0415''$) was used for Specimen 2. The amount of imperfection and the mode shape used were selected to match the experimental results. Girders without full-depth bearing stiffeners were found to be extremely sensitive to imperfections; therefore, when

benchmarking the finite element model to the large-scale experiment, the imperfection value was changed to alter the loading capacity and match it with the experimental data. Therefore, the first buckling shape corresponding to the lowest eigenvalue was incorporated into the parent model of Specimen 1. However, for Specimen 2, a second buckling mode was used. An example of a deformed shape for Specimens 1 and 2 is given in Figure 7.7 and Figure 7.8.

7.2 Modeling Approach: Specimen 3–Specimen 7

7.2.1 Assembly, Boundary Conditions, Load, and Interactions

For repaired specimens (Specimen 3.7), the modeling approach slightly varied from that described in Section 7.1 for non-repaired specimens. The assembly consisted of a corroded girder with holes in the web for threaded rod installation in addition to section loss. Furthermore, two (for Specimen 3, Specimen 6–7) or three (for Specimen 4–5) bearings modeled as two parts, two grout panels, and 13 threaded rod assemblies were present. The threaded rod assembly consisted of two hex nuts, two washers, and a threaded rod. However, they were merged into one solid part to simplify the modeling process. The steel sheets that acted as stay-in-place formwork were not included in the model because they did not affect the repair capacity. The details of the assembly of Specimen 3 are shown in Figures 7.9, 7.10, and 7.11.

Specimens 4–7 had a similar assembly to Specimen 3 that was altered insignificantly. For example, Specimens 4 and 5 had additional bearings installed close to the corroded girder end (Figure 7.12). In contrast, Specimens 6 and 7 had the region of the corroded web on top of the bearing encased in infill material (Figure 7.13). The only difference between Specimens 4 and 5, and Specimens 6 and 7 was the different material properties of the infill material. Specimens 4 and 6 had NS cementitious grout as an infill, whereas Kwik Bond PPC-1121 was used for Specimens 5 and 7.

Boundary conditions for Specimen 3–7 varied from described in Section 7.1 for Specimen 1 and Specimen 2. The steel plates representing the lateral bracings were removed to simplify the model and accelerate the analysis time. Instead, the lateral displacement of the

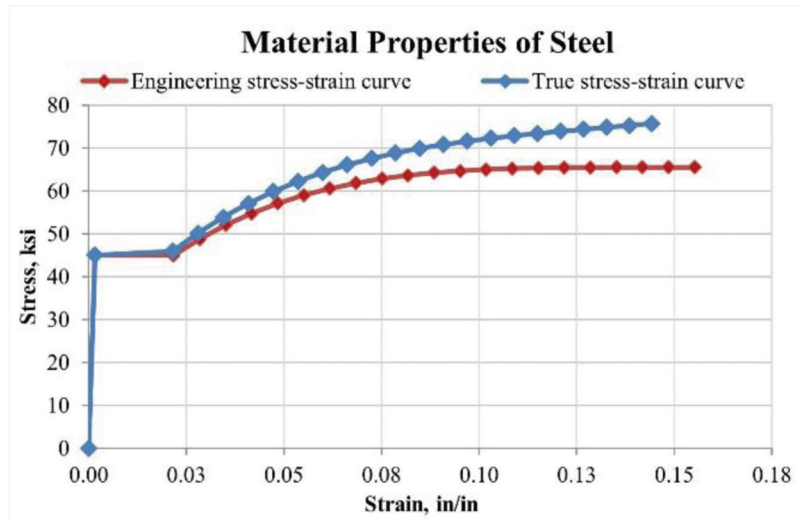


Figure 7.6 Stress-strain curve for steel.

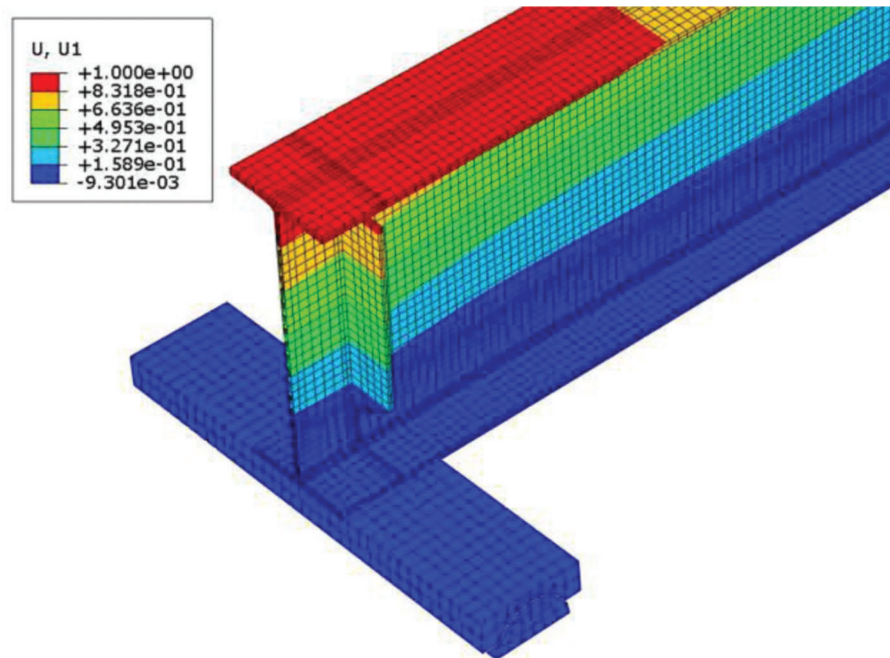


Figure 7.7 First modeshape (Specimen 1).

top and bottom flanges was restrained ($U1 = 0$) in the locations where lateral bracings were installed, as shown in Figure 7.14. The load was similarly applied 16" from the girder end.

Interactions and constraints were altered as new elements were introduced into the model. General contact (explicit) for the whole model was used with static steel-to-steel and steel-to-concrete friction coefficients of 0.6 for tangential behavior. "Hard" contact for normal behavior was used to prevent the penetration of parts into each other. Based on (The Engineering Toolbox, 2004), the static friction coefficient

between steel elements varies between 0.5 and 0.8, whereas the steel-to-concrete friction coefficient varies between 0.57 and 0.7 (Rabbat & Russell, 1985). Therefore, for simplification, the static friction coefficient of 0.6 satisfied both ranges for steel-to-steel and steel-to-concrete element interactions. It was assumed that due to threads on the rod, no slip occurred between the grout panel, and the strains of the steel rods and grout panel was compatible. Therefore, embedded constraints were implemented in Abaqus to represent this behavior, with grout panels acting as the host region and threaded rods as the

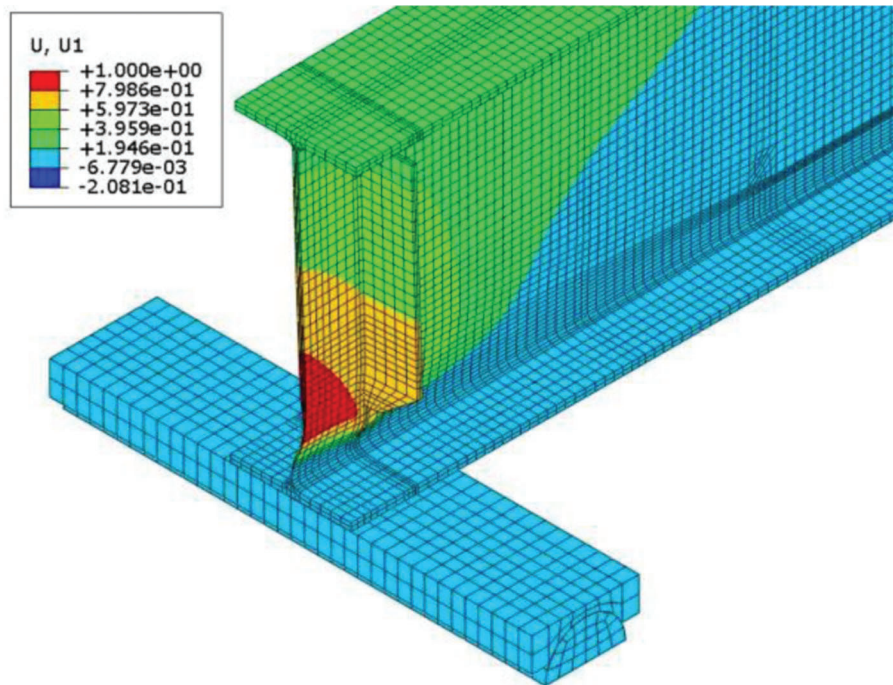


Figure 7.8 Second modeshape (Specimen 2).

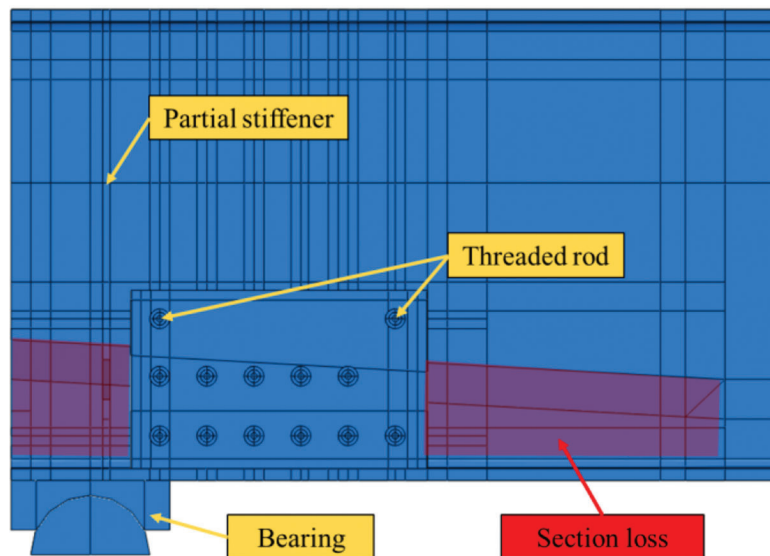


Figure 7.9 Specimen 3 assembly, elevation view

embedded region. Specimens 4–7 had a general contact interaction between the grout/concrete panels and a steel girder web. However, only for Specimen 3 was the steel girder web encased into the grout panel using embedded constraints, as no slip between the grout panels and the steel web was observed during the test.

A kinematic coupling constraint was used on the top at the location of the spreader beam, forcing this region to deform simultaneously under the applied load. In the coupling constraint, only translational degrees of freedom $U2 = U2 = U3$ were restrained.

7.2.2 Mesh

Finite element models for Specimen 3–Specimen 7 were developed using solid eight-node brick linear order elements (C3D8I/C3D8R). The steel girder and threaded rods were modeled using the incompatible mode elements (C3D8I) because these two parts were of primary importance. Incompatible mode elements give more accurate results for elements subjected to bending than simple linear order C3D8 elements and are more computationally efficient than quadratic elements. Parts such as bearings and grout panels were

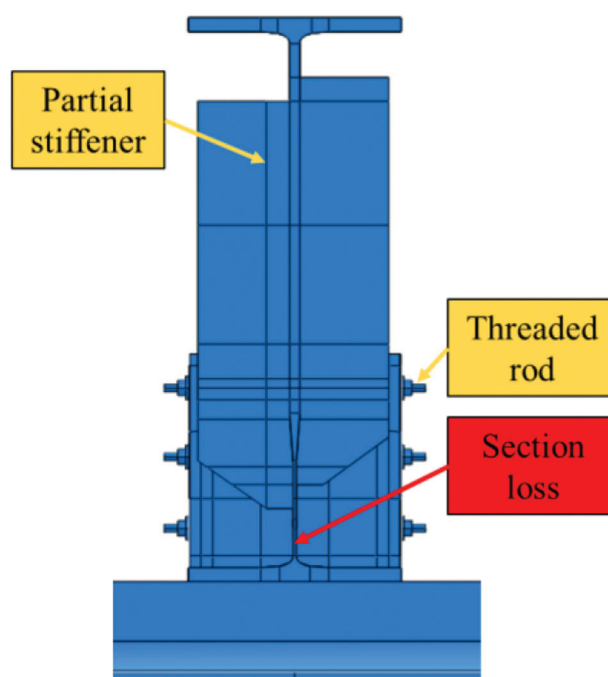


Figure 7.10 Specimen 3 assembly, front view

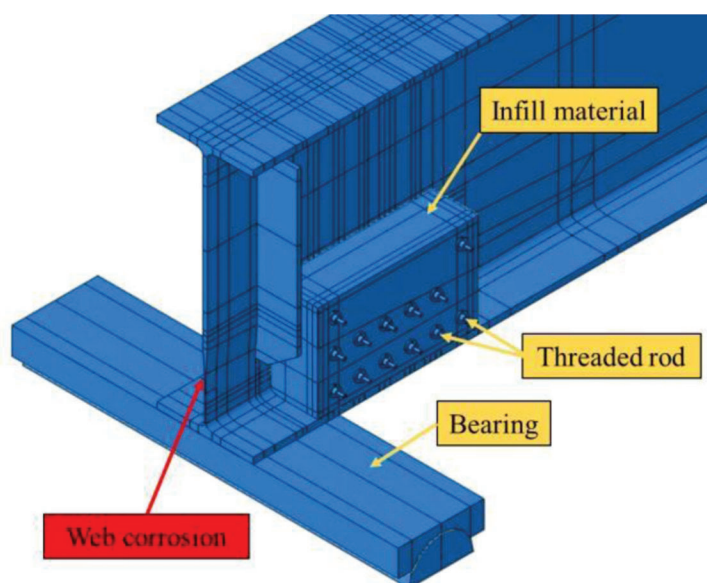


Figure 7.11 Specimen 3 assembly, isometric view.

meshed using reduced integration elements (C3D8R) to accelerate the analysis time. Usually, solid elements that have one integration point (C3D8R) are susceptible to hourglass effects because of the reduced stiffness of the elements. Enhanced hourglass control was used to prevent the appearance of zero-energy modes, also known as hour glassing. The size of the mesh varied throughout the model: the corroded girder end, threaded rods, and grout panels were meshed using fine elements (0.3"–1") to obtain more accurate results, whereas the bear-

ings and non-corroded end of a girder were meshed using coarse elements (2" × 2"). The standard meshing approach used for Specimens 3–7 is shown in Figure 7.15.

7.3 Results

7.3.1 Specimen 1 and Specimen 2

The finite element (FE) model for Specimen 1 was able to accurately predict the web crippling failure

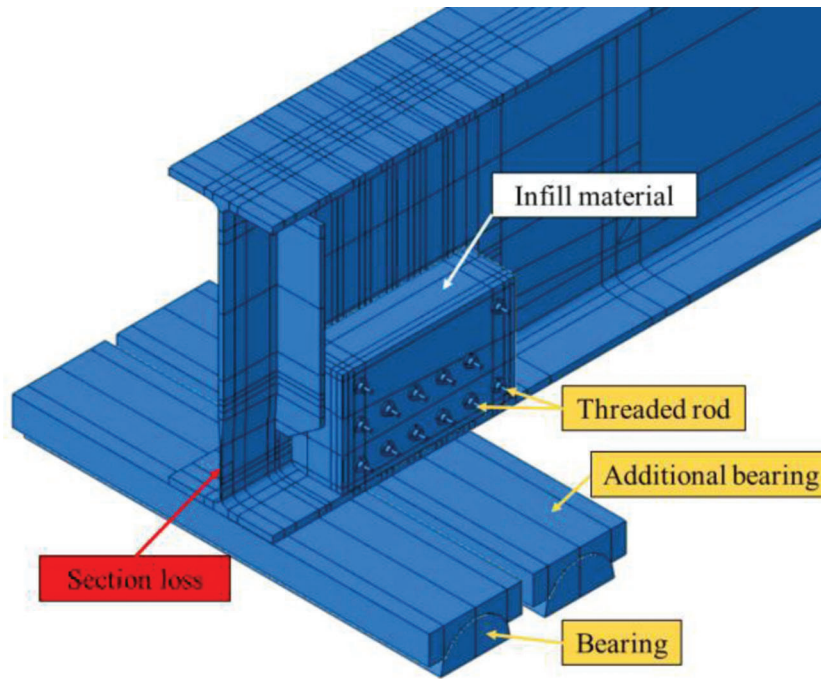


Figure 7.12 Specimen 4 and 5 assemblies.

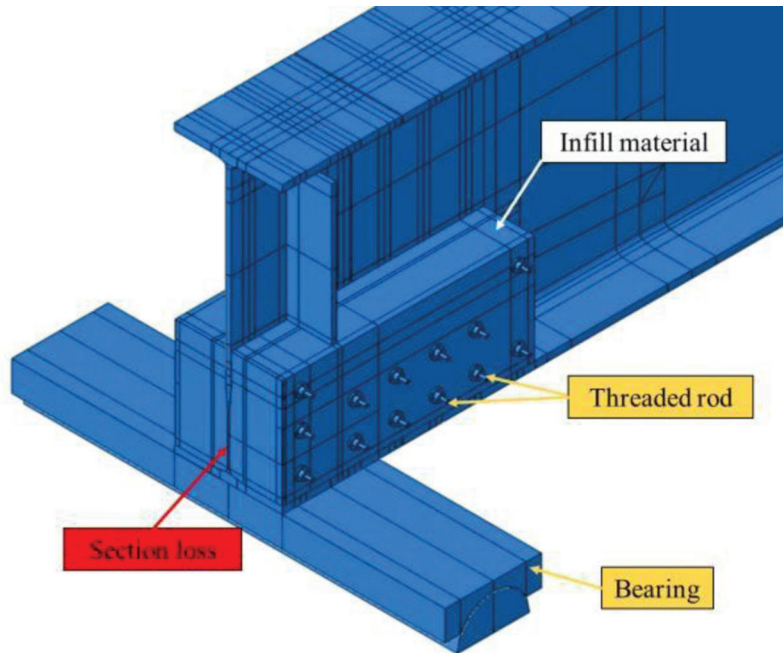


Figure 7.13 Specimen 6 and 7 assemblies.

mode and loading capacity of 241 kips. The difference between the FE model's capacity and the experimental result was only 4%; however, noticeable differences in stiffness (110%) were observed. The primary reasons for significant differences in stiffness could be complex boundary conditions in the test setup or section loss profile. Initially, the settlement of the bearings might have been the problem and was not accounted for in the

FE model. As described in Section 5.1, hydro-stone gypsum cement was used to level concrete blocks and steel plates under the bearings. During the experiment, the hydro-stone compresses as the loading increases, making the relative vertical displacement smaller and causing a softer response. To simplify the FE model, however, those connections were not modeled, and it most likely caused a stiffer response of the FE model.

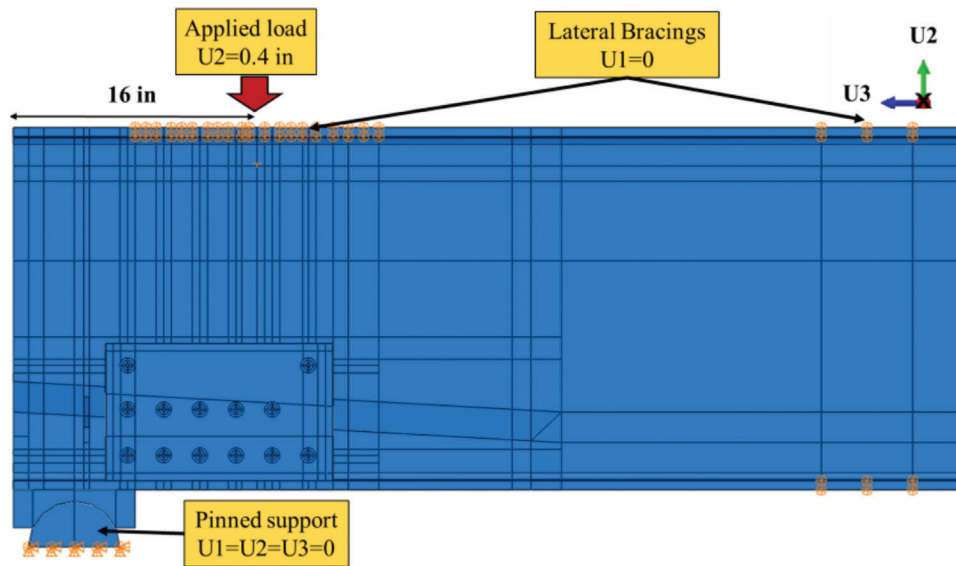


Figure 7.14 Specimen 3–Specimen 7: boundary conditions.

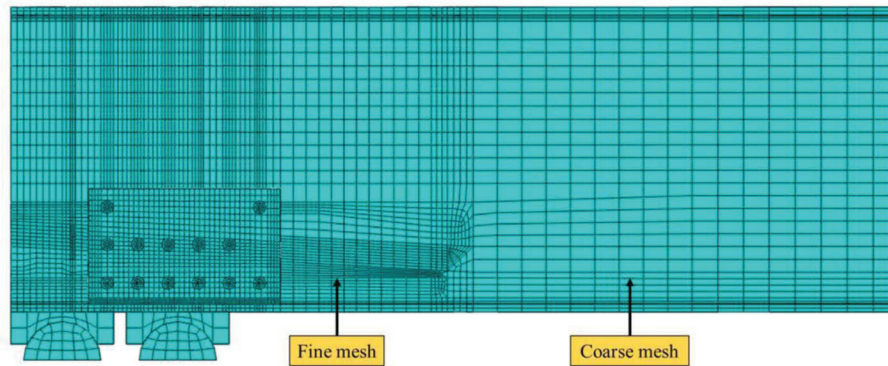


Figure 7.15 Standard meshing approach for Specimen 3–Specimen 7.

Additionally, the finite element model did not have light corrosion in the web's top and bottom parts, which might have affected the stiffness as well. Nonetheless, the maximum applied load and failure mode were captured accurately. Figure 7.16 compares load-vertical displacement responses obtained during the experimental investigation (black curve) and the numerical simulations (green curve).

The finite element model for Specimen 2 was able to capture the web crippling failure mode and loading capacity of 39.6 kips; only a 1% difference from the experimental data was observed. However, like the specimen, the stiffness of the FE model was noticeably higher than the stiffness obtained during the large-scale testing: the FE model overpredicted the stiffness by 85%. In this case, however, the effect of the web thickness was more drastic, and any variation from the design section loss profile would have affected the stiffness value. Because the section loss profile was introduced through metal grinding, the thickness of the corroded region in Specimen 2 was close to the design values but still differed from it. However, the maximum

applied load and failure mode were captured correctly, and Figure 7.17 shows a comparison of load-vertical displacement responses between the FE model (green curve) and test data (black curve).

Finally, the deformed shapes of Specimen 1 and Specimen 2 FE models and their comparison with the experimental data are shown in Figures 7.18, 7.19, 7.20, and 7.21. The FE models captured the web crippling failure mode and deformed shape well. However, in the FE model and Specimens 1 and 2, the web buckled out in opposite directions due to imperfections and minor eccentricities in the test setup. The gray regions on contour plots indicate that at the applied load, the area had yielded ($F_y = 45$ ksi).

7.3.2 Specimen 3

The finite element model for Specimen 3 captured the web crippling failure mode and load-carrying capacity of 72.25 kips. The FE model underpredicted the capacity of the specimen by 9% and overpredicted the stiffness by 52% compared with the experimental data.

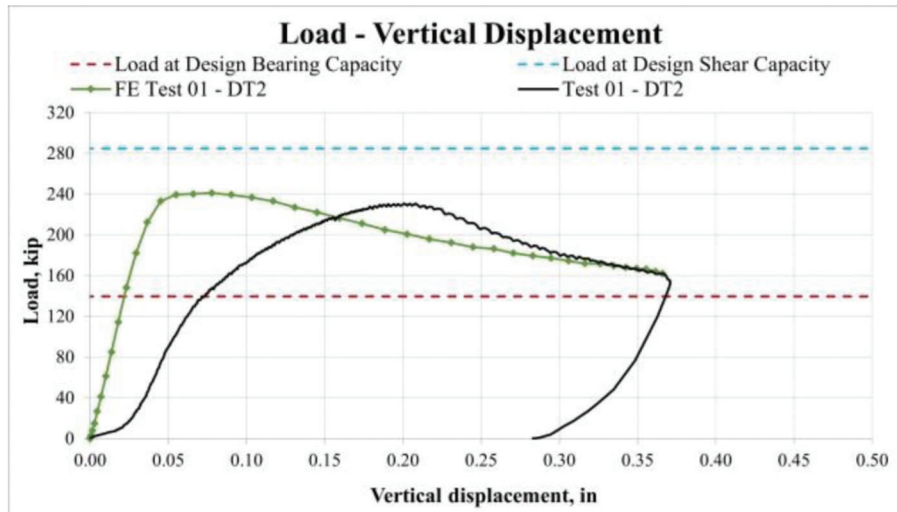


Figure 7.16 Comparison of load-vertical displacement relationship for Specimen 1.

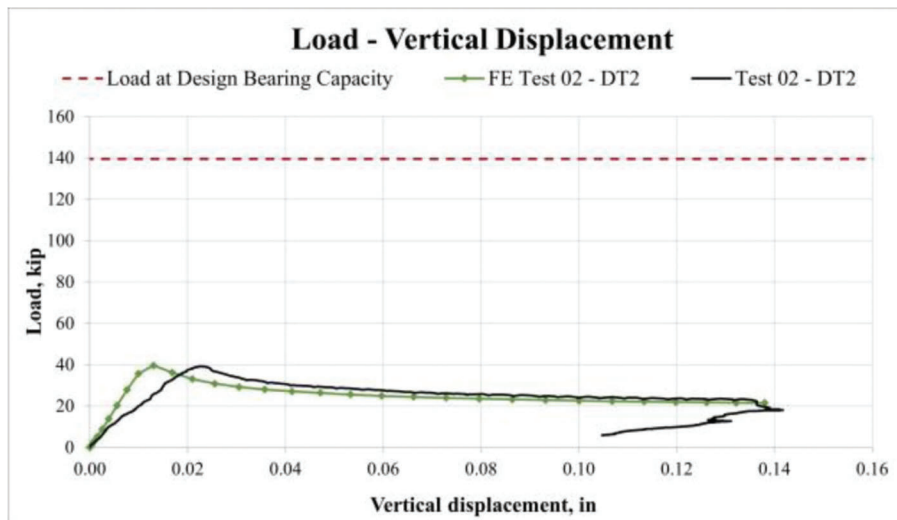


Figure 7.17 Comparison of load-vertical displacement relationship for Specimen 2.

Figure 7.22 compares load-vertical displacement responses between the FE model (green curve) and test data (black curve). Like Specimens 1 and 2, the stiffer response of the FE model might have been caused by differences in boundary conditions and slight variations in the section loss profile. Nevertheless, the FE model and experimental data showed that this configuration for the sandwich panel repair method would not recover the design bearing capacity that was the target value. The proposed configuration was inefficient due to threaded rods located far away from the bearing with a large eccentricity to the center of the bearing that reduced their capacity. In addition, the corroded region over the bearing was not encased, allowing for significant out-of-plane displacements.

Finally, the Specimen 3 FE model's deformed shape compared with the experimental data is shown in Figures 7.23, 7.24, 7.25, and 7.26. The finite element

model captured the web crippling failure mode and deformed shape accurately. It can be seen from Figure 7.26 that threaded rods did not deform significantly, and no yielding was observed. This indicated the inefficiency of threaded rods in transferring forces from the girder web to the grout panel and eventually to the bearing. Overall, the significant deformations and stress concentrations were limited to the corroded region over the bearing, and the rest of the girder underwent minor deformations. The gray regions on contour plots indicate that at the applied load, the area yielded ($F_y = 45$ ksi for the girder and $F_y = 105$ ksi for the threaded rods).

7.3.3 Specimen 4

The FE model developed to capture the performance of Specimen 4 was able to precisely predict the maximum loading capacity with only 2% underpredic-

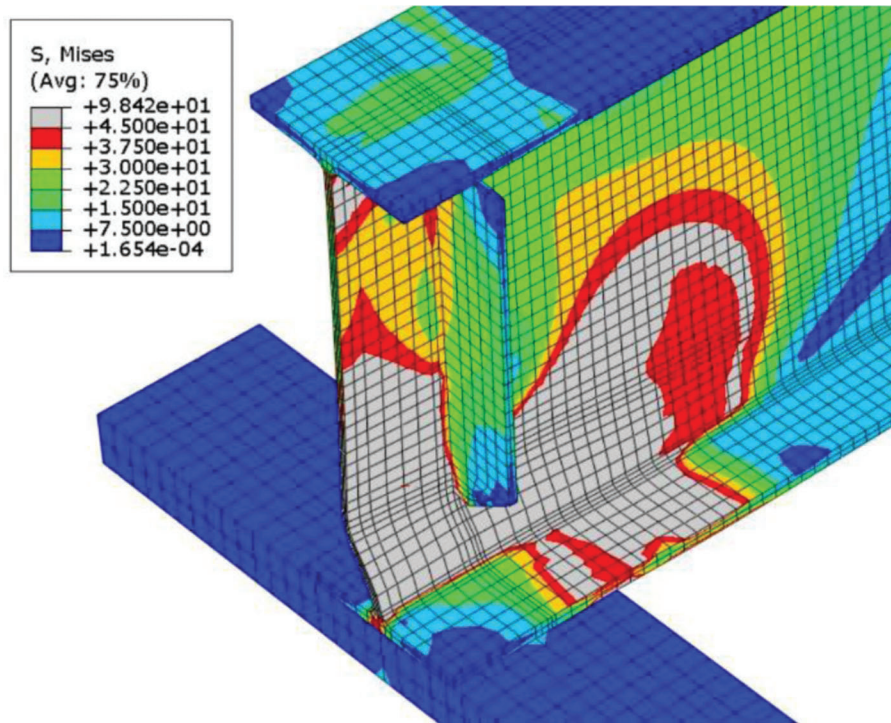


Figure 7.18 Deformed shape of Specimen 1 (FE model, post-peak load = 162.1 kips).



Figure 7.19 Deformed shape of Specimen 1 (experiment).

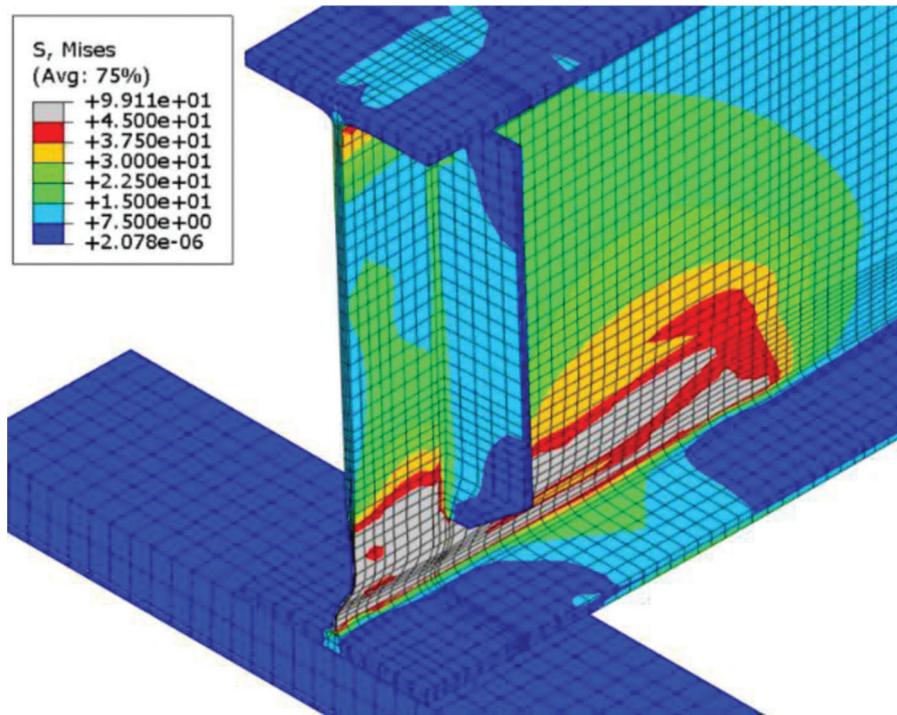


Figure 7.20 Deformed shape of Specimen 2 (FE model, post-peak load = 21.5 kips).



Figure 7.21 Deformed shape of Specimen 2 (experiment).

tion compared to the experimental data; the FE model reached a maximum loading capacity of 310.2 kips. A stiffer behavior was observed in the finite model during the elastic response range, exceeding the experimental value by 77%. The significant difference in stiffness might be due to complicated boundary conditions in the test setup and deviation from the design section loss profile, as described in detail in Section 7.3.1. The numerical model anticipated the change in stiffness at 127 kips, whereas, during the large-scale testing, a softer response was noticed at 131 kips, which agreed well with the FE model. Furthermore, the stiffness of the softening branch of the load-vertical displacement curve for the finite element model was like the experimental data. The FE model displayed comparable ductility of the test specimen: the vertical displacement at the first peak load for both cases was approximately 0.21 in.; the post-peak behavior was also accurately captured by the FE model. The curves representing the behavior of Specimen 4 are shown in Figure 7.27 with green and black lines corresponding to numerical simulations and experimental data, respectively.

Finally, the deformed shape of the Specimen 4 FE model and its comparison with the experimental data are shown in Figures 7.28, 7.29, 7.30, and 7.31. The FE model captured the web crippling failure mode and deformed shape accurately. However, the FE model and Specimens 4 web buckled out in opposite directions due to initial imperfections and minor eccentricities in the

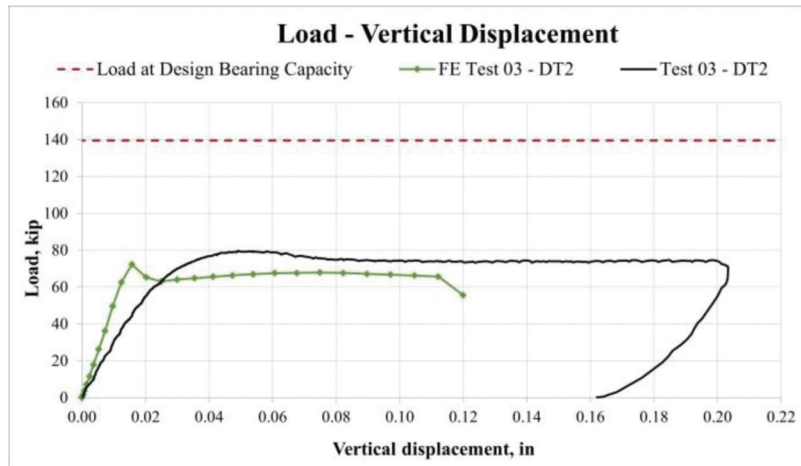


Figure 7.22 Comparison of load-vertical displacement relationship for Specimen 3.

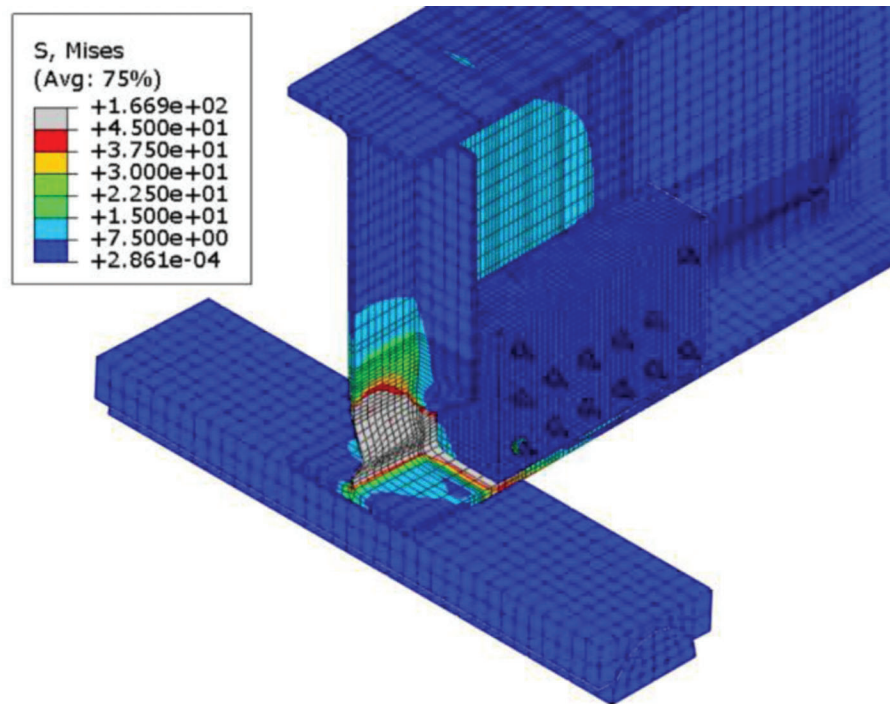


Figure 7.23 Deformed shape of Specimen 3 (FE model, post-peak load = 55.6 kips).

test setup. The FE model correctly captured the deformations of threaded rods embedded in the grout panels: the bottom threaded rod stayed in tension the entire time, whereas the remaining two rods were subjected to bending. The finite element model for Specimen 4 did not incorporate element deletion and damage model features; therefore, excessive deformations of threaded rods occurred in the center instead of rupture (Figure 7.31). Plastic deformations were detected in threaded rods from both the FE model and the experimental data. The area highlighted in gray indicates that the region reached the yielding strength of the material, 105 ksi. Overall, Specimen 4 was successfully benchmarked and used to conduct a parametric study.

7.3.4 Specimen 5

The finite element model developed for Specimen 5 predicted the maximum load-carrying capacity and displayed a 10% difference from the experimental data. The FE model reached a maximum capacity of 307.3 kips (339.9 kips during the experiment), and stiffer behavior was observed, overprediction the experimental value by 51%. The significant difference in stiffness might be due to complicated boundary conditions in the test setup and deviation from the design section loss profile, as described in Section 7.3.1. The finite element model did not fail in web local crippling of the loading region; therefore, more ductile behavior without a rapid



Figure 7.24 Deformed shape of Specimen 3 (experiment).

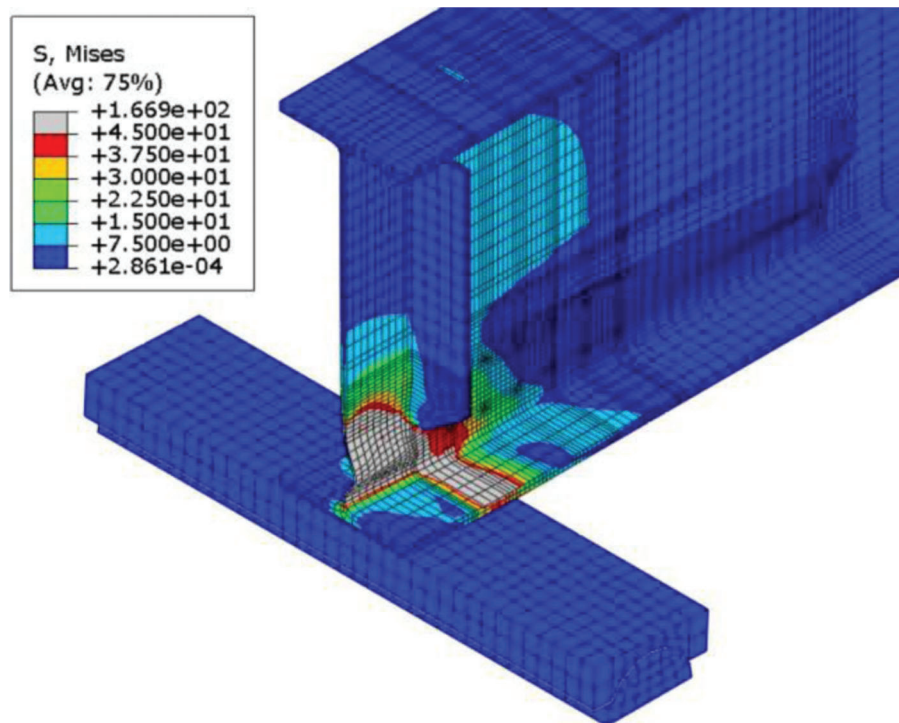


Figure 7.25 Specimen 3: corroded web yielding (FE model, post-peak load = 55.6 kips).

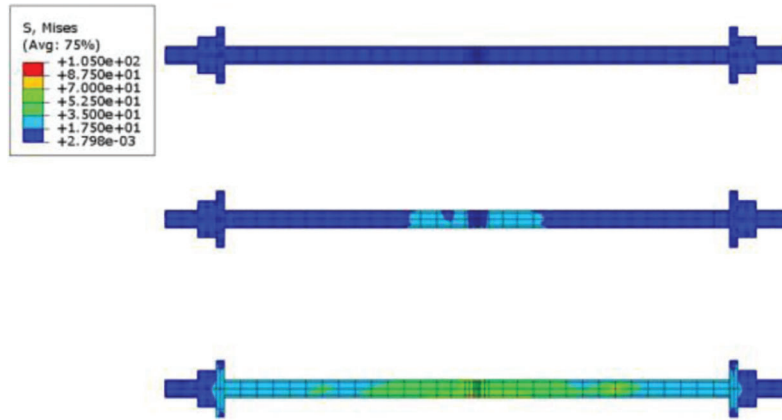


Figure 7.26 Stress distribution in threaded rods. No yielding was observed (post-peak load = 55.6 kips).

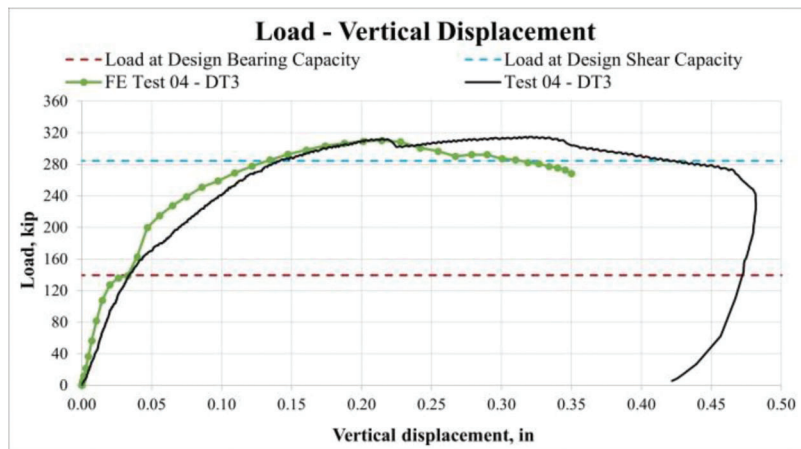


Figure 7.27 Comparison of load-vertical displacement relationship for Specimen 4.

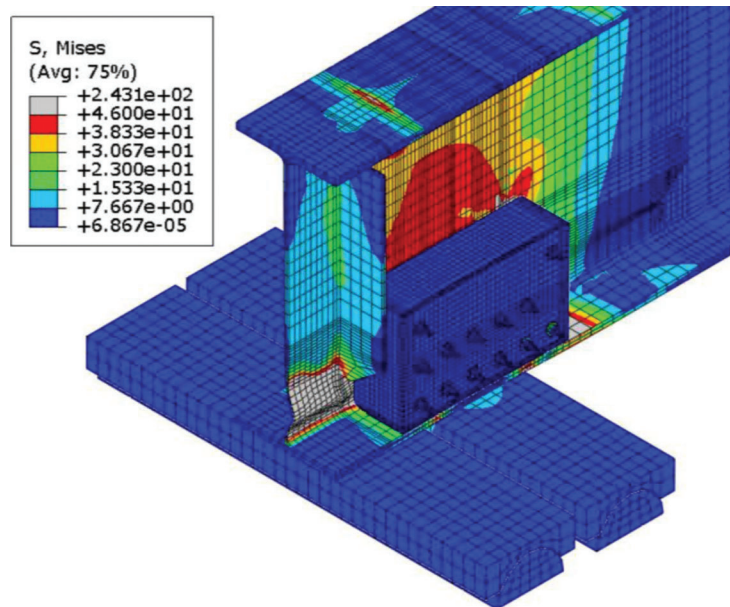


Figure 7.28 Deformed shape of Specimen 4 (FE model, peak load = 310.2 kips).



Figure 7.29 Deformed shape of Specimen 4 (experiment).

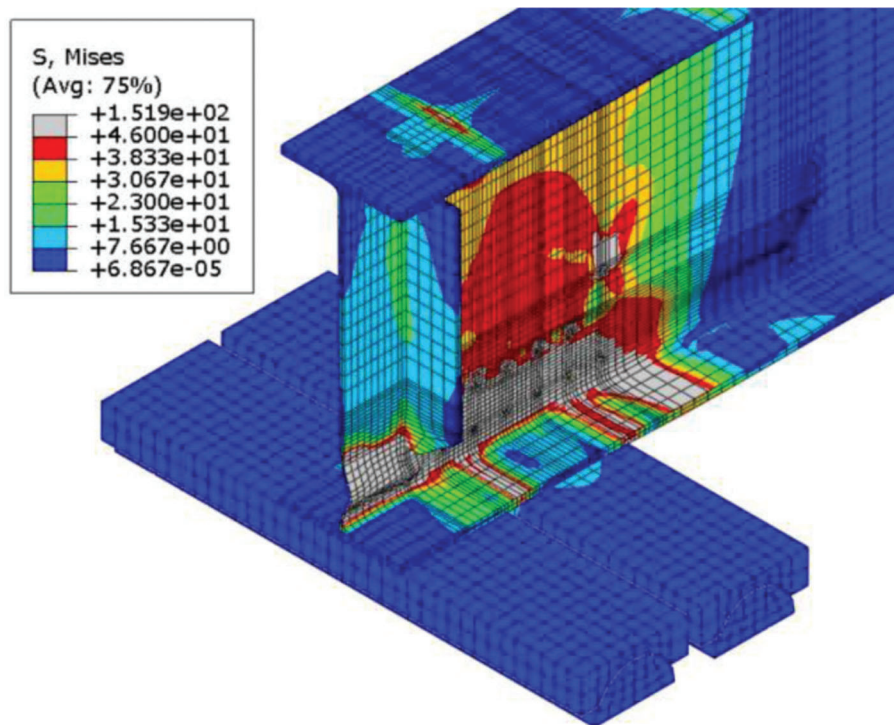


Figure 7.30 Specimen 4: corroded web yielding (FE model, peak load = 310.2 kips).

capacity drop was attained. The curves representing the behavior of Specimen 5 are shown in Figure 7.32 with green and black lines corresponding to numerical simulations and experimental data, respectively.

The deformed shape of the Specimen 5 FE model and its comparison with the experimental data are shown in Figures 7.33, 7.34, 7.35, and 7.36. The web crippling failure of the corroded region was captured accurately by the finite element model. However, in the FE model and Specimen 5, the web buckled out in opposite directions due to initial imperfections and minor eccentricities in the test setup. In addition, due to large compression forces in the loading region and imperfections, web local buckling occurred in Specimen 5 that the FE model could not capture. Plastic deformations were detected in threaded rods from both the FE model and the experimental data. The area highlighted in gray indicates that the region reached the yielding strength of the material: 105 ksi for threaded rods (Figure 7.36).

Due to difficulties in developing a material model for polyester polymer concrete (Kwik Bond PPC-1121),

the FE model for Specimen 5 did not accurately reflect the behavior observed during the large-scale testing. Therefore, it was decided not to implement this model for parametric study because additional studies are required on that topic.

7.3.5 Specimen 6

The FE model developed to capture the behavior of Specimen 6 was able to accurately predict the maximum loading capacity with only 9% underprediction compared with the experimental data; the FE model reached a maximum loading capacity of 228.7 kips. In addition, the stiffness of the finite model in the elastic range of response aligned well with the experimental data, exceeding it by 36%. The numerical model anticipated the change in stiffness at 87 kips, whereas, during the large-scale testing, a softer response was noticed at 100 kips, which agreed well with the FE model. Furthermore, the stiffness of the softening branch of the load-vertical displacement curve was accurately captured by the FE model and aligned well

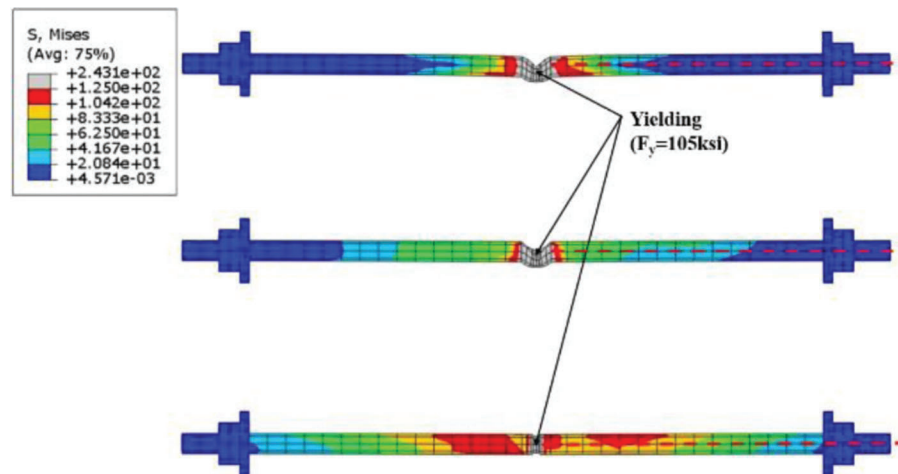


Figure 7.31 Specimen 4: threaded rod deformations (FE model, peak load = 310.2 kips).

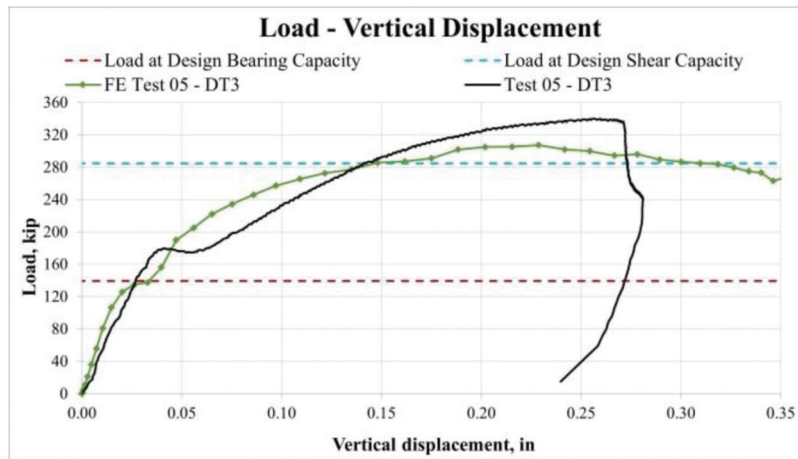


Figure 7.32 Comparison of load-vertical displacement relationship for Specimen 5.

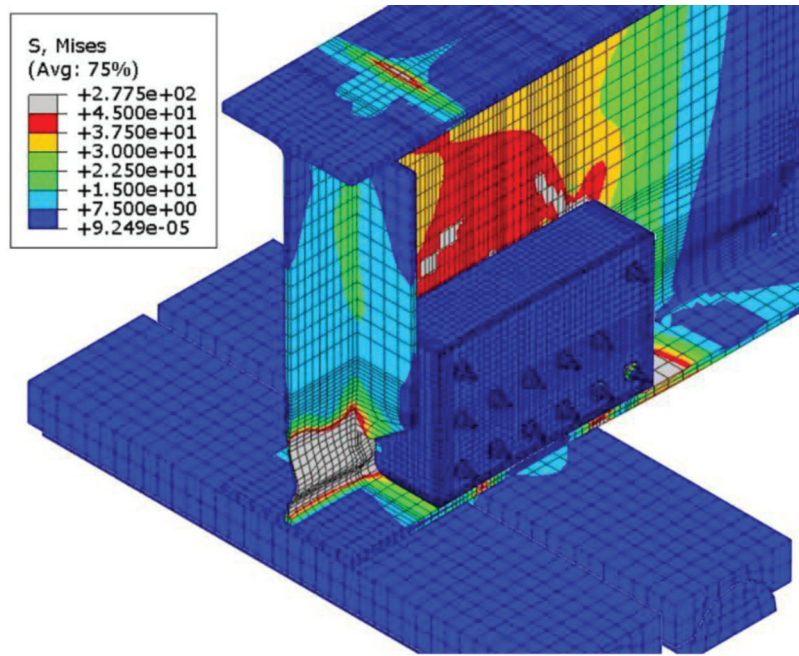


Figure 7.33 Deformed shape of Specimen 5 (FE model, peak load = 307.3 kips).

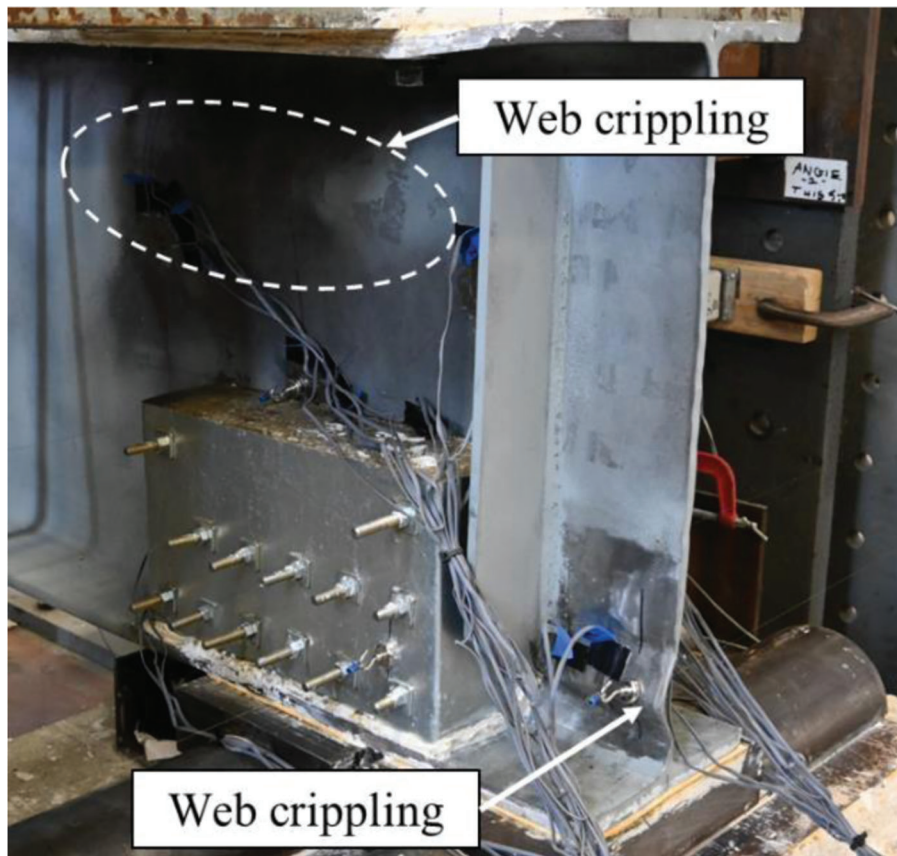


Figure 7.34 Deformed shape of Specimen 5 (experiment).

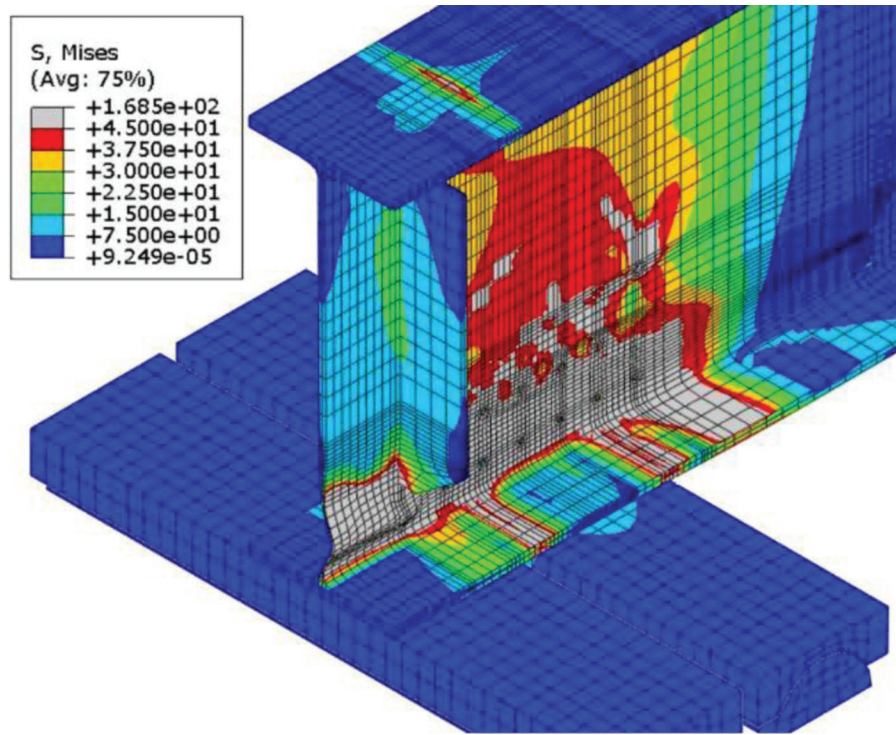


Figure 7.35 Specimen 5: corroded web yielding (FE model, peak load = 307.3 kips).

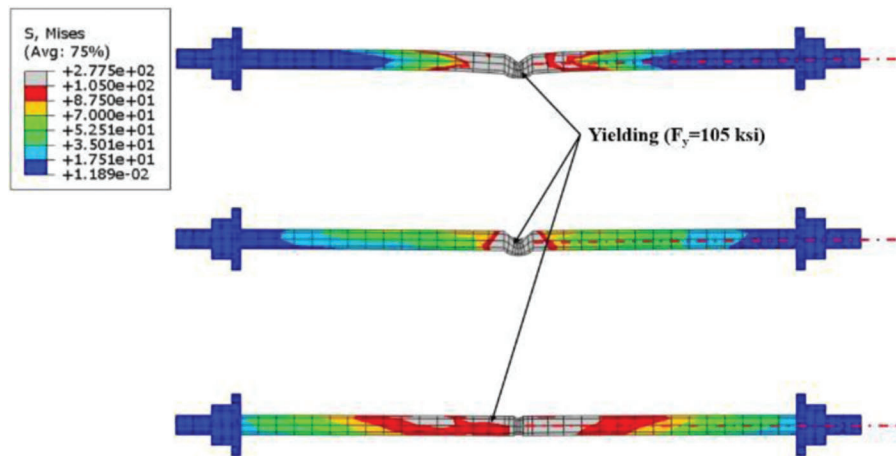


Figure 7.36 Specimen 5: threaded rod deformations (FE model, peak load = 307.3 kips).

with the experimental data up to a load of 228.7 kips. However, the FE model displayed less ductile behavior than that observed during the experimental evaluation, with the vertical displacement at the peak load being only 0.2 in. The curves representing the behavior of Specimen 6 are shown in Figure 7.37, with green and black lines corresponding to numerical simulations and experimental data, respectively.

The deformed shape of the FE model for Specimen 6 and its comparison with the experimental data are shown in Figures 7.38, 7.39, and 7.40. Plastic deformations were detected in both steel girders and threaded

rods; the area highlighted in gray indicates that the region reached the yielding strength of the material: 45 ksi and 105 ksi for steel girders and threaded rods, respectively (Figure 7.39 and Figure 7.40). Most of the corroded region that experienced 70% section loss yielded by the time Specimen 6 reached its maximum loading capacity. Overall, Specimen 6 was successfully benchmarked, and therefore, the developed FE model was used to conduct a further parametric study where threaded rod layouts and their material properties were altered to study their effect on the repair performance.

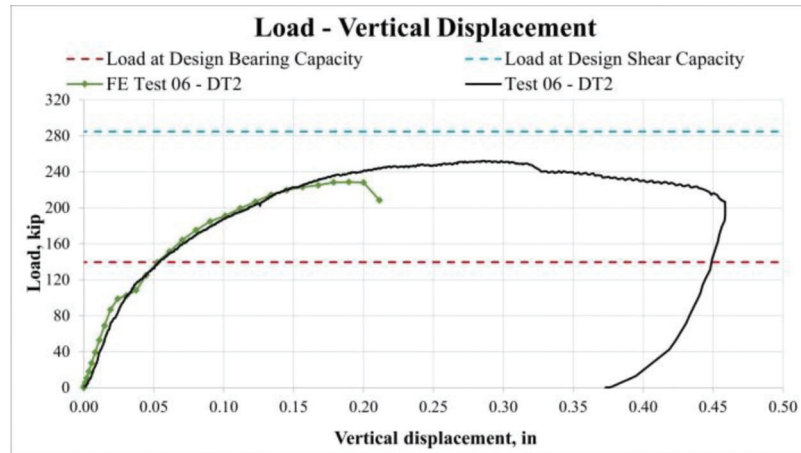


Figure 7.37 Comparison of load-vertical displacement relationship for Specimen 6.

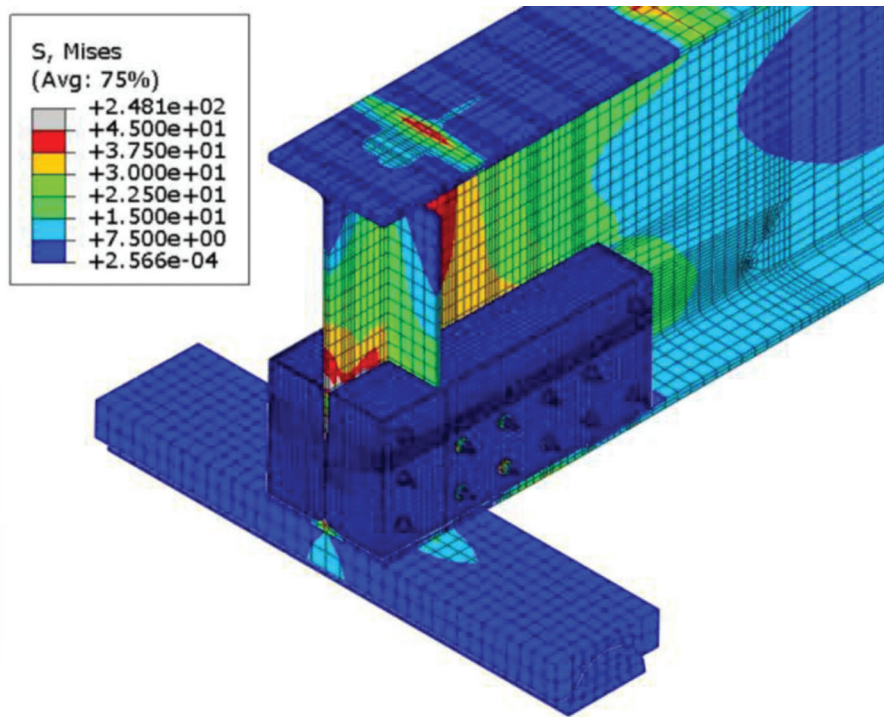


Figure 7.38 Specimen 6: stress distribution (FE model, peak load = 228.7 kips).

7.3.6 Specimen 7

The FE model developed to capture the behavior of Specimen 7 was able to accurately predict the maximum loading capacity with only 5% underprediction compared with the experimental data; the FE model reached a maximum loading capacity of 271.4 kips. In addition, the stiffness of the finite element model in the elastic range of response aligned comparatively well with the experimental data, exceeding it by 45%. The FE model precisely captured the first peak load of 239 kips, which was only 2.5% higher than that observed during the experiment. Furthermore, the stiffness of the softening branch of the load-vertical displacement curve aligned

well with the experimental data up to a load of 271.4 kips; however, the post-peak behavior was not predicted accurately. The FE model displayed less ductile behavior than that observed during the experimental evaluation, with the vertical displacement at the peak load being only 0.21 in. The curves representing the behavior of Specimen 7 are shown in Figure 7.41, with green and black curves corresponding to numerical simulations and experimental data, respectively.

Overall, Specimen 7 was successfully benchmarked, and the first and second peak loads were accurately predicted by the FE model as well as a corroded region's web local crippling failure mode. A substantial area of the web in the loading region and the bearing region that

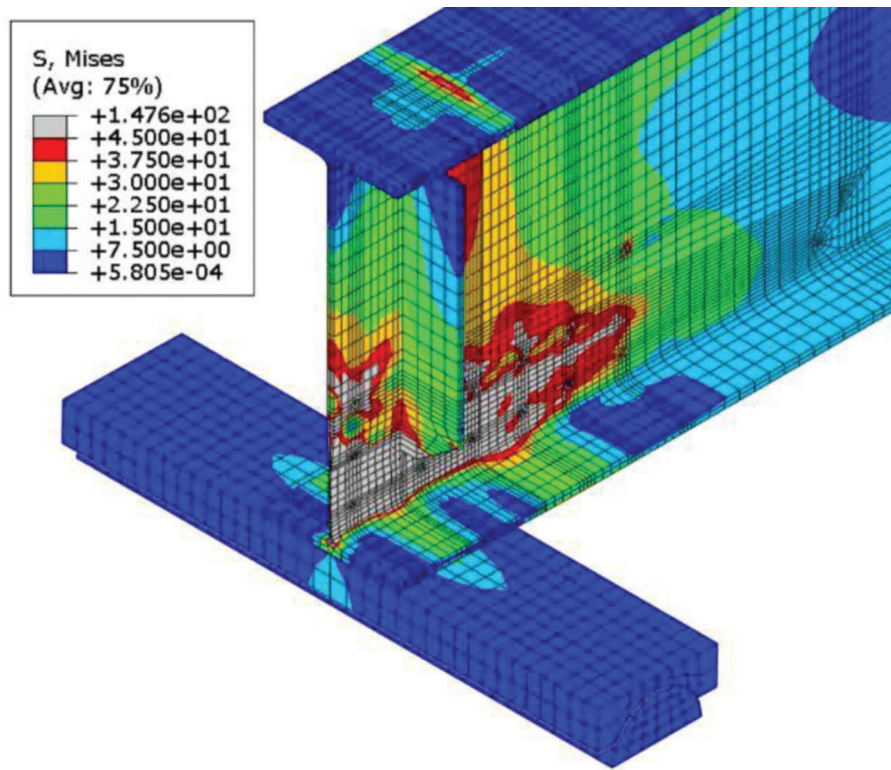


Figure 7.39 Specimen 6: corroded web yielding (FE model, peak load = 228.7 kips).

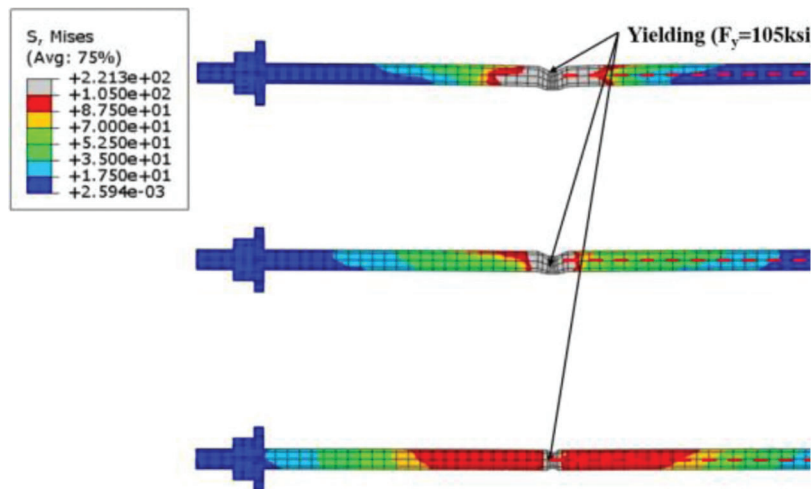


Figure 7.40 Specimen 6: stress distribution in threaded rods (FE model, peak load = 228.7 kips).

had 70% section loss yielded by the time Specimen 7 reached its maximum loading capacity (Figure 7.42 and Figure 7.43). Plastic deformations were also detected in threaded rods in both the FE model and the experimental data. The area highlighted in gray indicates that the region reached a yielding strength of 105 ksi (Figure 7.44). Due to insignificant information on the tensile properties of Kwik Bond-PPC 1121 to accurately develop a material model in Abaqus, it was

decided not to use this FE model for further parametric study.

7.3.7 Summary

In conclusion, seven finite element models were developed and verified using experimental data. The FE models predicted failure modes and load-carrying capacity (LCC) accurately, with a variation of LCC of

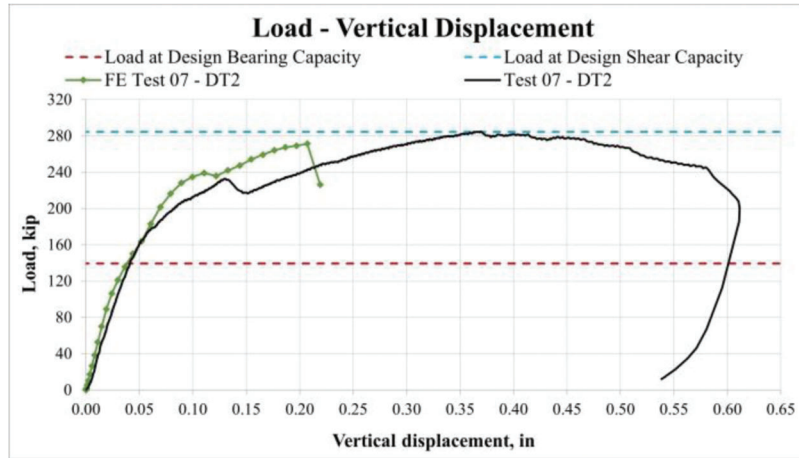


Figure 7.41 Comparison of load-vertical displacement relationship for Specimen 7.

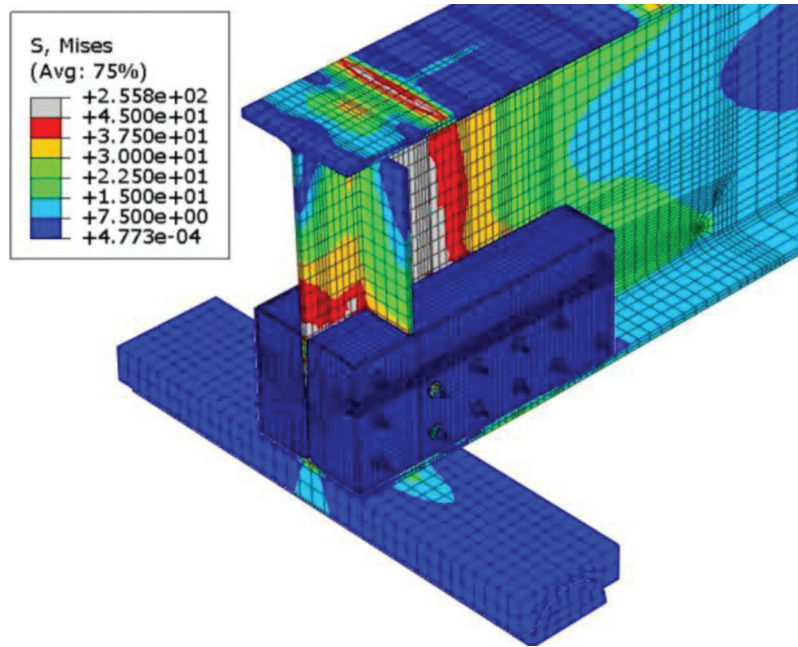


Figure 7.42 Specimen 7: stress distribution (FE model, peak load = 271.4 kips).

10%. The significant difference in stiffness was caused by complicated boundary conditions imposed by the test setup and deviation from the design section loss profile that tested specimens had. Two models were selected for a parametric study: Specimen 4 and Specimen

6 because their load-vertical displacement curves most precisely matched the experimentally obtained values of maximum applied load and stiffness. The results of the finite element simulations are presented in Table 7.1.

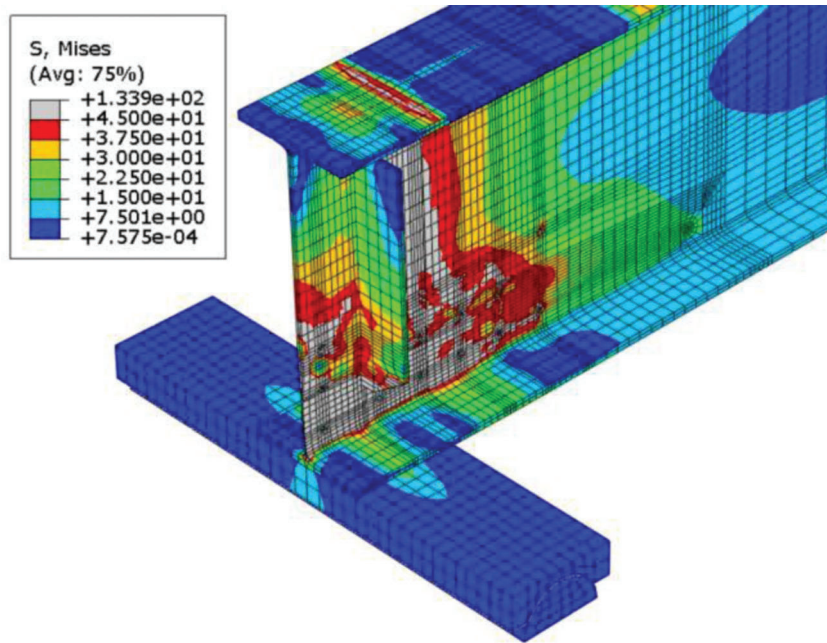


Figure 7.43 Specimen 7: corroded web yielding (FE model, peak load = 271.4 kips).

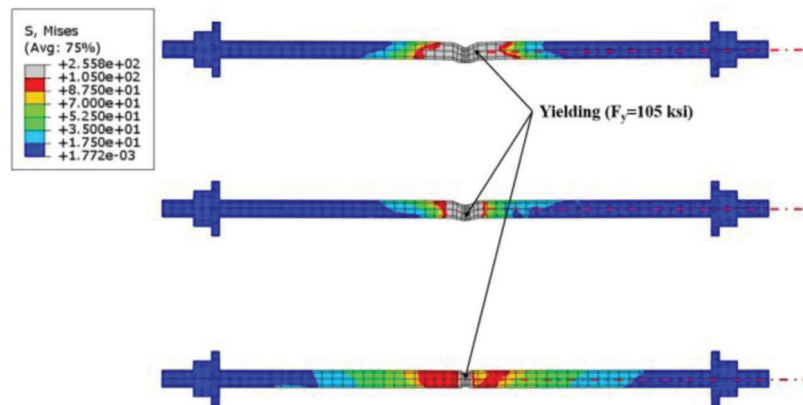


Figure 7.44 Specimen 7: deformations in threaded rods (FE model, peak load = 271.4 kips).

TABLE 7.1
Comparison between FE simulations and experimental data

Specimen Number	Maximum Applied Load (Test), kip	Maximum Applied Load (FE Model), kip	Difference (%)	Stiffness (Test), kip/in.	Stiffness (FE Model), kip/in.	Difference (%)
1	230.7	241.0	4	2,955	6,195	110
2	39.1	39.6	1	1,939	3,578	85
3	79.6	72.3	-9	3,032	4,597	52
4	315.0	310.2	-2	4,158	7,343	77
5	339.9	307.3	-10	4,779	7,227	51
6	252.2	228.7	-9	3,352	4,545	36
7	284.8	271.4	-5	3,225	4,685	45

8. PARAMETRIC STUDY

The parametric study investigated the impact of a number of threaded rods and their tensile strength on the post-repair capacity of the girder after applying the sandwich panel repair method. Additionally, the layout variations were examined to understand the influence of the location of threaded rods on the girder's post-repair strength and ductility. The developed matrix for the parametric study is shown in Table 8.1. The parametric study comprised 33 models, each designated with a specific naming convention. For example, Model #1 had an Identification Number of I-G-16-150, indicating that the model had 16 effective threaded rods with tensile strength (F_u) of 150 ksi encased in cementitious grout (G). The naming convention was as follows.

- (I): Case number (I, II, or III)
 - Case number I: Extended bearing length and encasement do not include the corroded web behind the partial stiffener.

- Case number II: Encasement includes the entire corroded region.
- Case III: Effective threaded rods were concentrated in the bearing region to investigate if the capacity of the threaded rod decreases with increasing eccentricity.
- (G): Infill material (cementitious grout)
- (N): Number of “effective” threaded rods
- (F_{u_tr}): Tensile strength of a threaded rod (Three grades: Grade 1, Grade B7, and Grade 8)

8.1 Parametric Study: Case I

8.1.1 Threaded Rod Layouts

Finite element models for Case I were based on the Specimen 4 FE model and validated using experimental data (Section 7.3.3). Additional support was provided to extend the bearing length but the web that had an artificially induced section loss behind the partial stiffener remained unencased.

TABLE 8.1
Parametric study matrix

Model Number	Identification Number	Configuration	Infill Material	Number of Effective Threaded Rods	Threaded Rods Material (F_u), ksi
1	I-G-16-150	Case I: Additional support + no encasement behind a stiffener	Cementitious grout	16	150 (Grade 8)
2	I-G-11-150			11	
3	I-G-7.1-150			7	
4	I-G-7.2-150			7	
5	I-G-16-125			16	125 (Grade B7)
6	I-G-11-125			11	
7	I-G-7.1-125			7	
8	I-G-7.2-125			7	
9	I-G-16-60			16	60 (Grade 1)
10	I-G-11-60			11	
11	I-G-7.1-60			7	
12	I-G-7.2-60			7	
13	II-G-16-150	Case II: One support + encasement behind a stiffener	Cementitious grout	16	150 (Grade 8)
14	II-G-11-150			11	
15	II-G-7.1-150			7	
16	II-G-7.2-150			7	
17	II-G-16-125			16	125 (Grade B7)
18	II-G-11-125			11	
19	II-G-7.1-125			7	
20	II-G-7.2-125			7	
21	II-G-16-60			16	60 (Grade 1)
22	II-G-11-60			11	
23	II-G-7.1-60			7	
24	II-G-7.2-60			7	
25	III-G-15-150	Case III: One support + encasement behind a stiffener (updated threaded rod layouts)	Cementitious grout	15	150 (Grade 8)
26	III-G-9-150			9	
27	III-G-6-150			6	
28	III-G-15-125			15	125 (Grade B7)
29	III-G-9-125			9	
30	III-G-6-125			6	
31	III-G-15-60			15	60 (Grade 1)
32	III-G-9-60			9	
33	III-G-6-60			6	

The threaded rod layouts for Case I are shown in Figures 8.1, 8.2, 8.3, and 8.4, with the number of effective threaded rods varying from 7 to 16. The threaded rod was called effective if considered in design calculations to achieve the desired post-repair strength. However, besides the effective threaded rods that acted as a structural component, more threaded rods were utilized for constructibility reasons. Those threaded rods were called non-structural and their location is indicated in Figure 8.1 to Figure 8.4. The primary purpose of non-structural threaded rods was to secure the location of stay-in-place formwork. Additionally, for the model with 7 effective threaded rods, two scenarios were presented—Option 7: middle, and Option 7: bottom (Figure 8.3 and Figure 8.4). For Option 7:

middle, four threaded rods were placed in the middle row of the grout panel, 5.25" away from the bottom flange. However, Option 7: bottom had four threaded rods shifted downward by 3". It was essential to examine whether the vertical location of threaded rods affected the post-repair capacity to develop design guidelines for the sandwich panel repair and provide recommendations on effective redistribution of the threaded rods along the length of the grout/concrete panel.

8.1.2 Case I: Results and Discussion

Case I consisted of 12 models and the results were arranged into the following two groups to investigate.

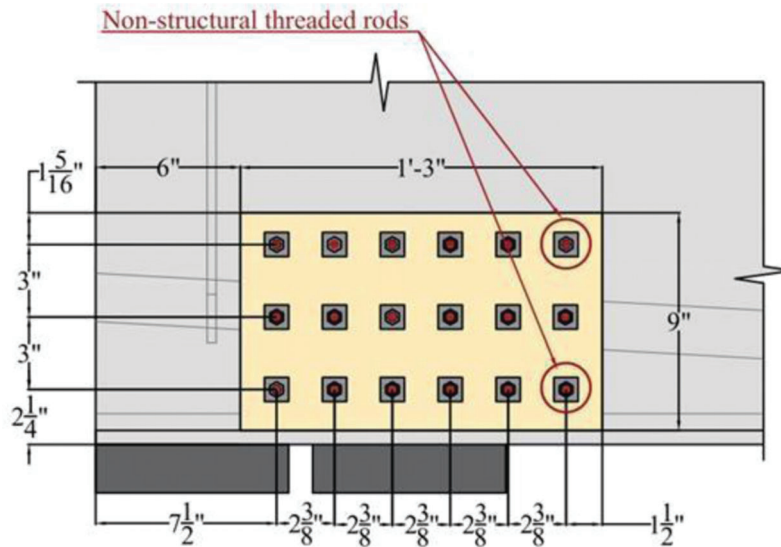


Figure 8.1 Case I: threaded rod layout with 16 effective threaded rods (I-G-16).

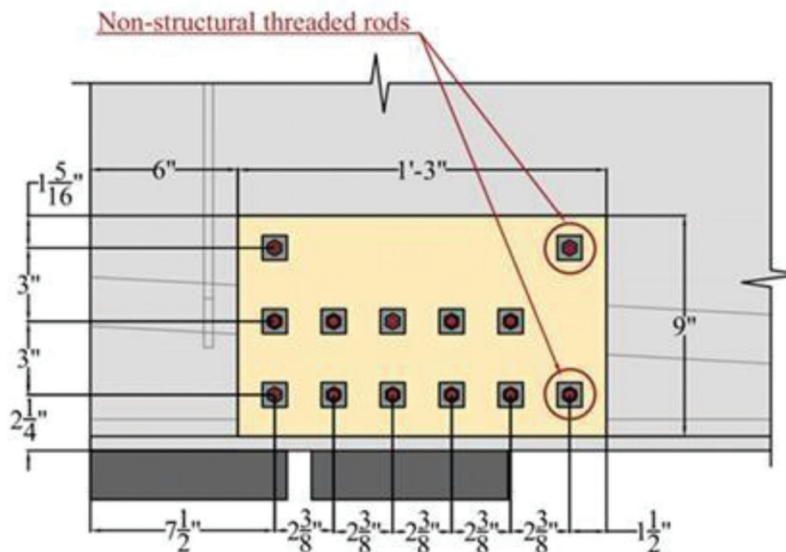


Figure 8.2 Case I: threaded rod layout with 11 effective threaded rods (I-G-11).

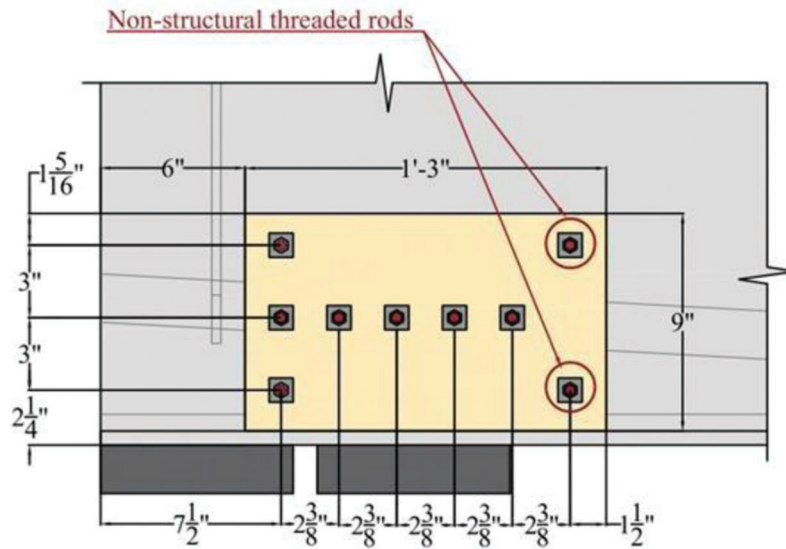


Figure 8.3 Case I: threaded rod layout with 7 effective threaded rods. Option 7: Middle (I-G-7.1).

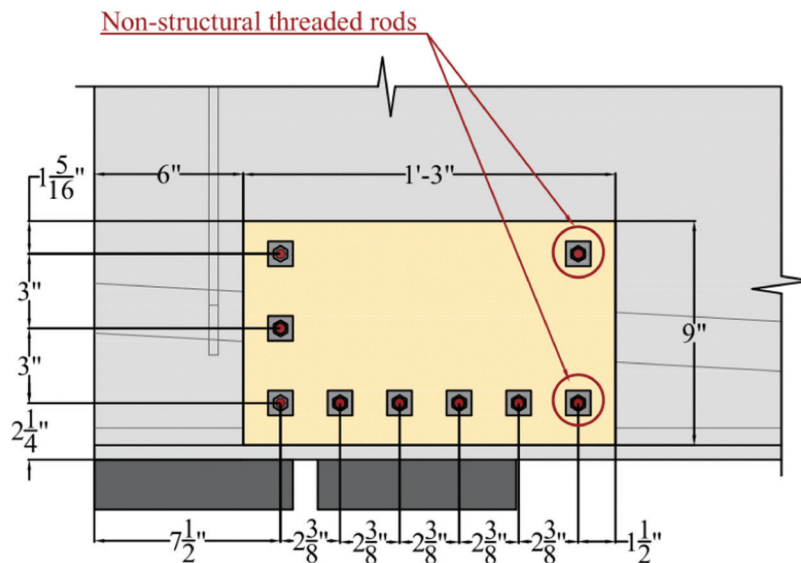


Figure 8.4 Case I: threaded rod layout with 7 effective threaded rods. Option 7: bottom.

1. Impact of threaded rod material on the post-repair capacity with a constant number of “effective” threaded rods (Figures 8.5, 8.6, 8.7, and 8.8).
2. Impact of the number of threaded rods on post-repair capacity with constant material properties (Figures 8.9, 8.10, and 8.11).

8.1.2.1 Impact of threaded rod material on the repair capacity. The parametric study comprised 12 distinct finite element models featuring different threaded rod materials, including Grade 1, Grade B7, and Grade 8. All finite element analyses demonstrated the complete recovery of the web’s crippling capacity. Additionally, the study revealed a clear correlation between the strength of the threaded material and the post-repair capacity of the FE model.

Figure 8.5 highlights that model I-G-16-150, with 16 effective threaded rods made of Grade 8 steel, achieved the highest capacity of 417.7 kips. This model not only fully recovered the design bearing strength but also exceeded the design shear capacity by 47%. The failure mode observed included web crippling of the corroded region in the steel girder, rupturing of threaded rods, and concrete crushing.

Model I-G-16-125 which had a similar number of threaded rods but with lower-grade material (Grade B7, F_u equals; 125 ksi), achieved a slightly lower capacity of 388.0 kips. Finally, model I-G-16-60, utilizing Grade 1 ($F_u = 60$ ksi) threaded rods, reached the lowest capacity of 277 kips among the discussed finite element models in the parametric study.

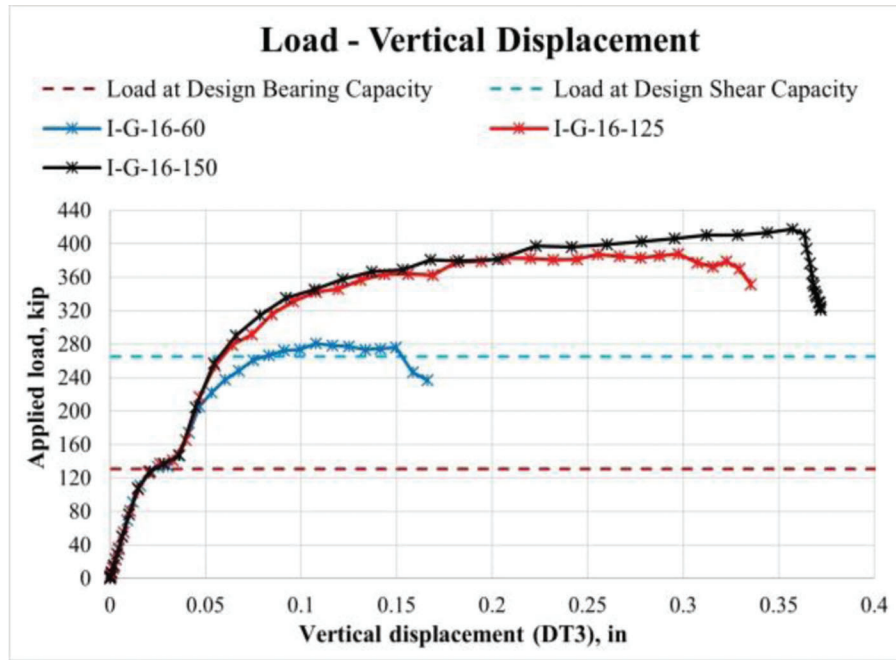


Figure 8.5 Impact of threaded rod material on the repair capacity (Case I: 16 effective threaded rods).

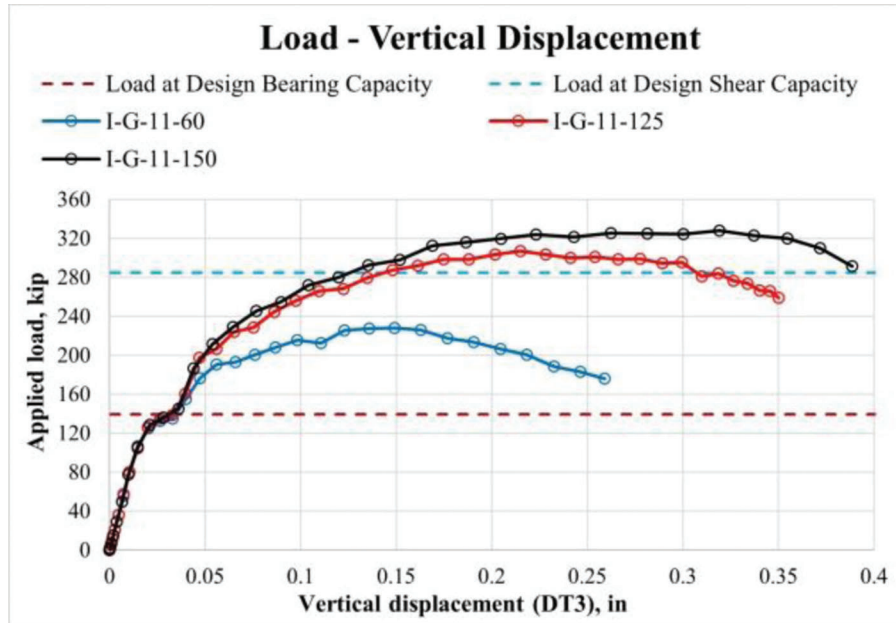


Figure 8.6 Impact of threaded rod material on the repair capacity (Case I: 11 effective threaded rods).

A consistent trend of higher threaded rod grade correlating with increased post-repair strength was observed for the models that had 11 and 7 effective threaded rods (Option 7: bottom and Option 7: middle), as shown in Figures 8.6, 8.7, and 8.8. In addition, high-strength threaded rods demonstrated a more ductile response compared to their lower-grade counterparts.

8.1.2.2 Impact of the number of threaded rods on the repair capacity. The parametric study for Case I

included the investigation of the influence of the number of threaded rods on the post-repair capacity. A comparison of the models with the same grade for threaded rods (Grade 1, Grade B7, or Grade 8), but a varied number of rods, indicated a more ductile response and higher post-repair strength for the models with a larger number of threaded rods (Figures 8.9, 8.10, and 8.11).

Additionally, different behavior was observed in Option 7: bottom and Option 7: middle, due to the

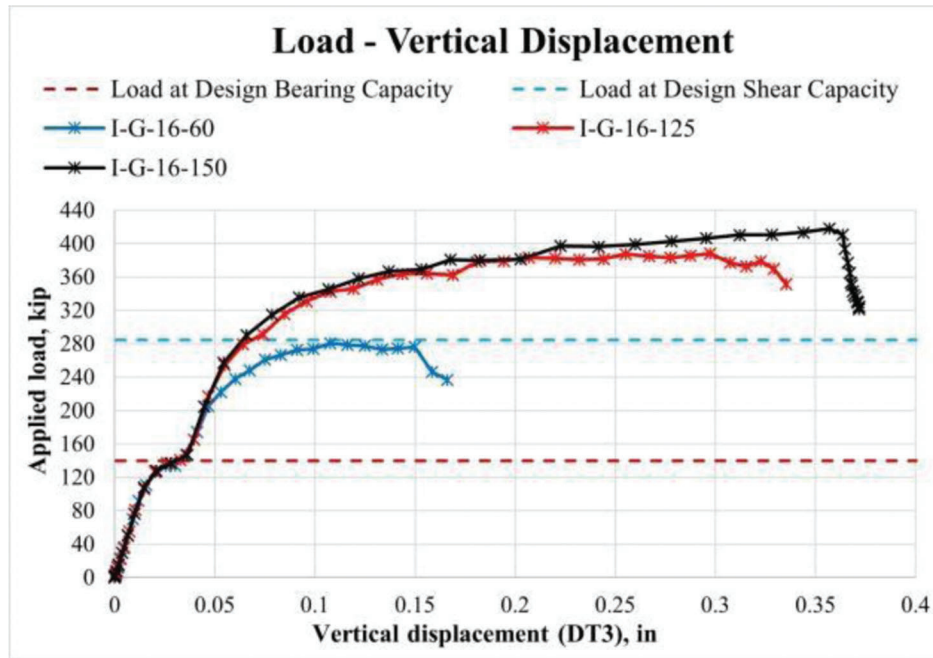


Figure 8.7 Impact of threaded rod material on the repair capacity (Case I: 7 effective threaded rods, Option 7: middle).

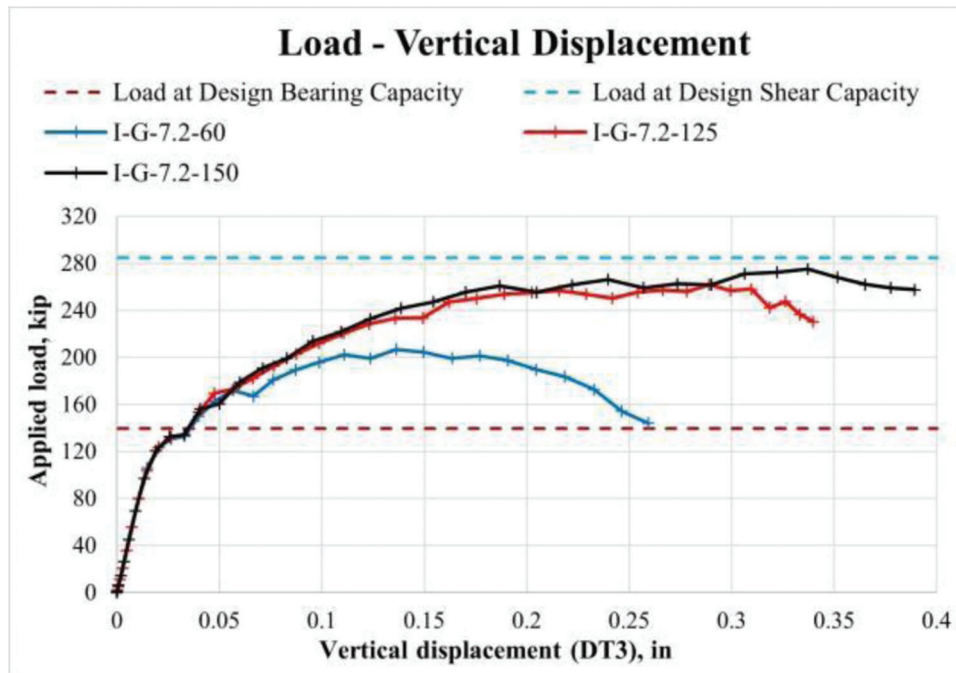


Figure 8.8 Impact of threaded rod material on the repair capacity (Case I: 7 effective threaded rods, Option 7: bottom).

threaded rods' location in different areas of the corroded web. Option 7: bottom, with multiple threaded rods installed in the bottom row, showed more ductile behavior than Option 7: middle. However, their loading capacities did not differ substantially. For example, models I-G-7.1-60 and I-G-7.2-60 reached comparable capacities of 191.5 kips and 206.9 kips, respectively, which varied by less than 10%. However,

I-G-7.2-60 exhibited a more ductile post-peak response, whereas I-G-7.1-60 experienced a sudden drop in capacity after reaching the peak (Figure 8.9).

The parametric study provided insights into failure mode and effective distribution of threaded rods over the corroded area when detailing the repair. The standard failure mechanism for girders with a portion of corroded region unencased was web local crippling

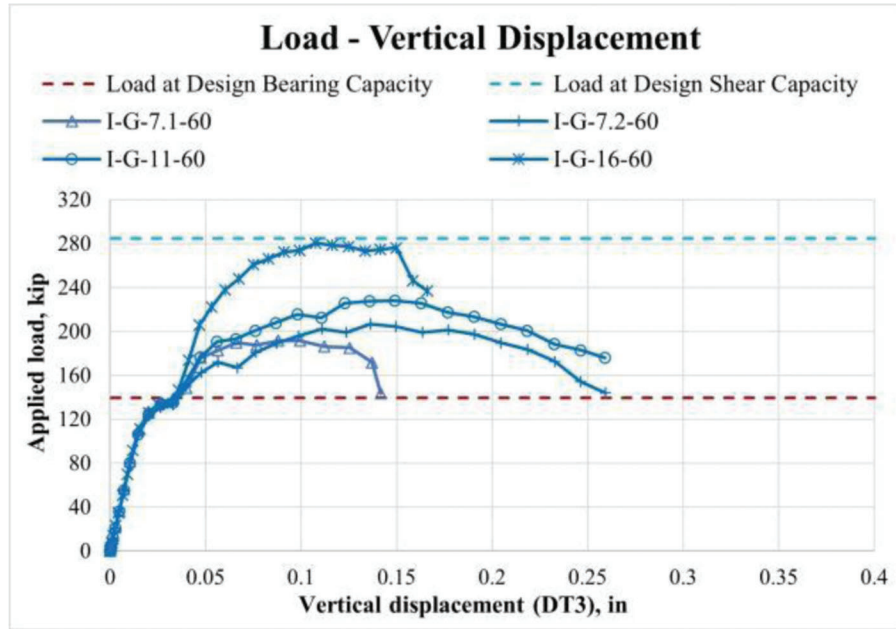


Figure 8.9 Impact of the number of threaded rods on the repair capacity (Case I: $F_u = 60$ ksi).

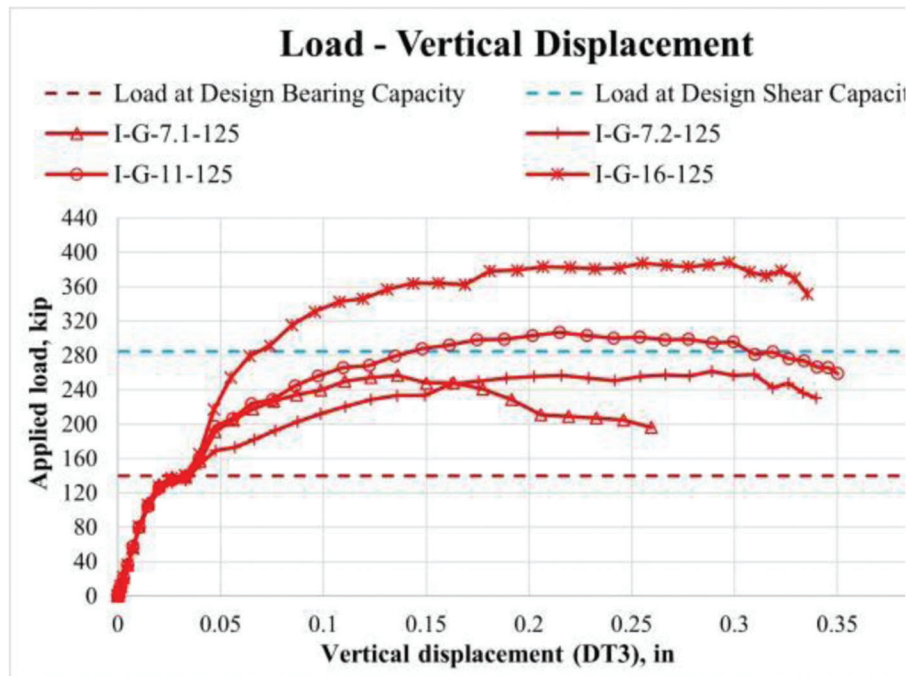


Figure 8.10 Impact of the number of threaded rods on the repair capacity (Case I: $F_u = 125$ ksi).

followed by threaded rod rupturing and grout panel cracking. Only model I-G-16-150 failed in web local crippling in the loading region. However, the large force applied to the top may not truly represent the loading that the bridge would typically experience.

The finite element simulation results from 12 models for the Case I configuration are presented in Table 8.2. The parametric study conclusively demonstrated that the number of threaded rods and their material

properties play a vital role in influencing the repair capacity. Consequently, in scenarios where space for threaded rod installation is constrained, employing higher-grade rods becomes a viable strategy to restore the required strength of the girder.

The success of the repair of $W24 \times 68$ was contingent on one key criterion: achieving the recovery of the design bearing strength (139.5). However, an additional requirement of recovering at least 85% of the design

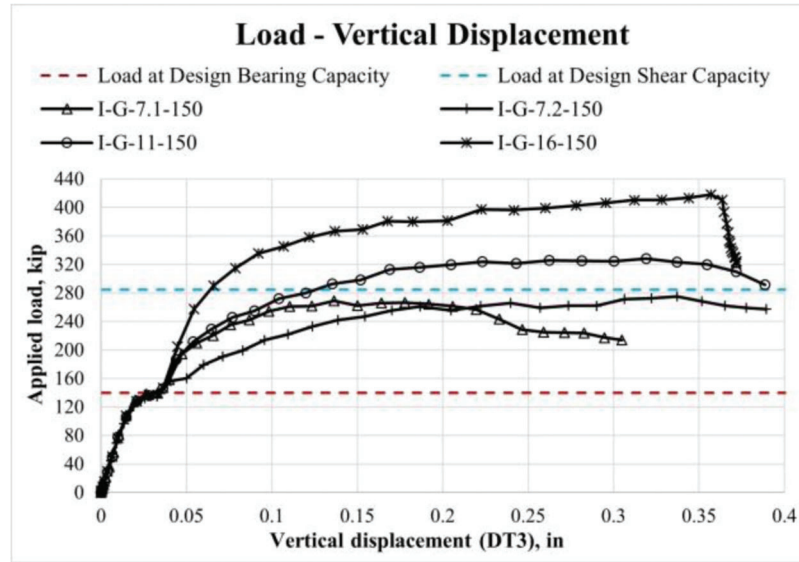


Figure 8.11 Impact of the number of threaded rods on the repair capacity (Case I: $F_u = 150$ ksi).

TABLE 8.2
Case I: FE simulations results

Name	Infill Material	Number of Threaded Rods	Threaded Rods Material, F_u , ksi	Loading Capacity, kip	Design Bearing Capacity Recovered?	85% of the Design Shear Capacity Recovered?
I-G-16-150	Grout	16	150	417.7	Yes	Yes
I-G-11-150	Grout	11	150	328.0	Yes	Yes
I-G-7.1-150	Grout	7	150	268.6	Yes	Yes
I-G-7.2-150	Grout	7	150	275.0	Yes	Yes
I-G-16-125	Grout	16	125	388.0	Yes	Yes
I-G-11-125	Grout	11	125	306.8	Yes	Yes
I-G-7.1-125	Grout	7	125	256.6	Yes	Yes
I-G-7.2-125	Grout	7	125	261.6	Yes	Yes
I-G-16-60	Grout	16	60	280.5	Yes	Yes
I-G-11-60	Grout	11	60	227.9	Yes	No
I-G-7.1-60	Grout	7	60	191.5	Yes	No
I-G-7.2-60	Grout	7	60	206.9	Yes	No

shear capacity (218.5 kips) was established. All models except I-G-11-60, I-G-7.1-60, and I-G-7.2-60 with low-strength threaded bars satisfied this additional condition.

8.2 Parametric Study: Case II

8.2.1 Threaded Rod Layouts for Case II

Finite element models for Case II were based on the benchmarked Specimen 6 FE model using experimental data (Section 7.3.5). Models in this case included the encasement of the corroded region behind the partial stiffener. Unlike the previous parametric study, there was no additional support provided, leading to a lower post-repair capacity for Case II models compared to Case I, despite having the same number of threaded rods. Previous research confirmed that eccentrically loaded shear studs do not reach their full plastic

capacity (Kruszewski et al., 2018a, 2018b), and these discoveries were projected to predict the behavior of threaded rods encased in the grout that were similarly used to transfer shear forces.

The threaded rod layouts for Case II are shown in Figures 8.12, 8.13, 8.14, and 8.15. Similar to Case I, two scenarios were presented for the model with seven effective threaded rods: Option 7: Middle and Option 7: bottom. For Option 7: middle, four threaded rods were placed in the middle of the grout panel, 5.25" from the bottom, while Option 7: bottom, had four threaded rods at 2.25" from the bottom. Due to partial stiffeners, the first two columns of threaded rods had a 4.5" spacing, in contrast to a consistent 3.375" spacing between the remaining columns. The effect of threaded rod location on the repair capacity was examined to develop design guidelines for the repair and provide recommendations for efficient distribution of threaded rods.

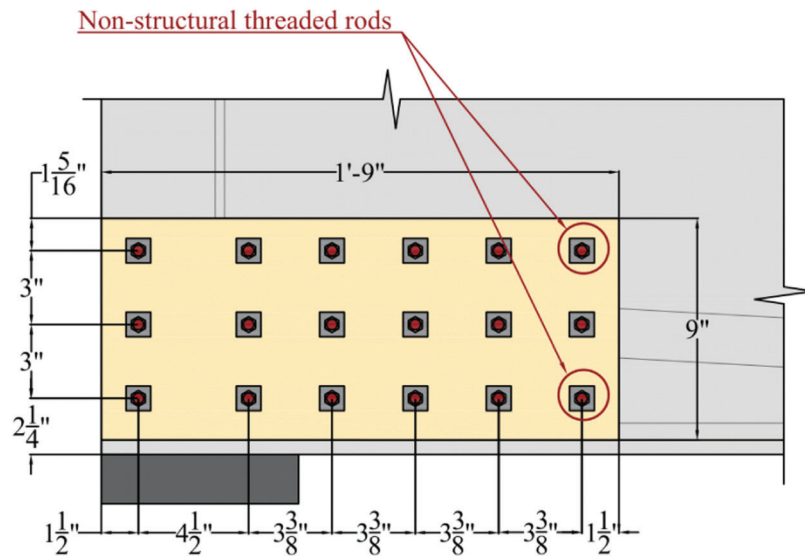


Figure 8.12 Case II: threaded rod layout with 16 effective threaded rods (II-G-16).

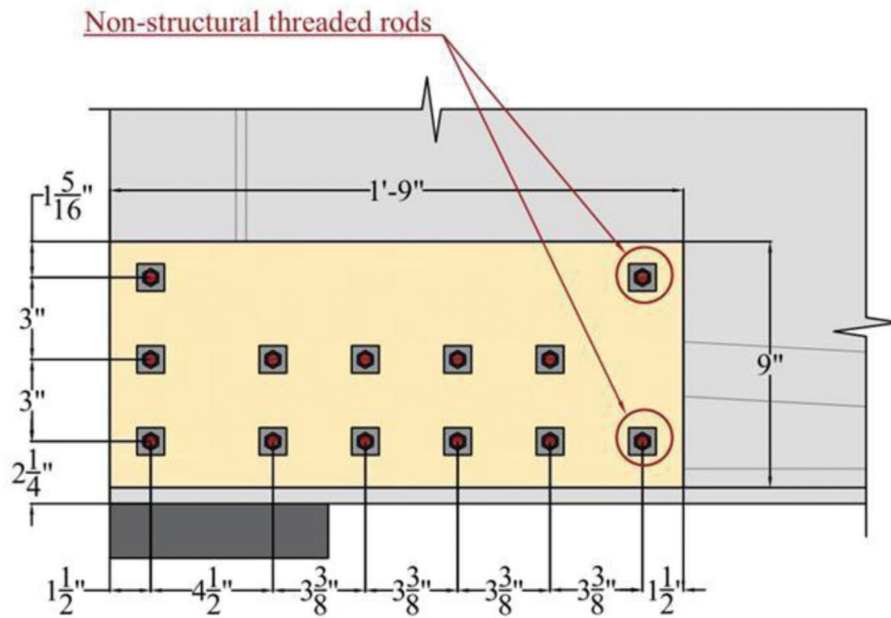


Figure 8.13 Case II: threaded rod layout with 11 effective threaded rods (II-G-11).

8.2.2 Case II: Results and Discussion

Case II consisted of 12 models, and the results were arranged into two major groups to examine the influence of the number of threaded rods and their material properties on the capacity of the repair separately.

1. Impact of threaded rod material on the post-repair capacity with a constant number of “effective” threaded rods (Figures 8.16, 8.17, 8.18, and 8.19).
2. Impact of the number of threaded rods on post-repair capacity with constant material properties (Figures 8.20, 8.21, and 8.22).

A significant difference from the Case I study was the encasement of the corroded region over the bearing and the absence of additional support.

8.2.2.1 Impact of threaded rod material on the repair capacity. The parametric study comprised 12 distinct FE models featuring different threaded rod materials, including Grade 1, Grade B7, and Grade 8. All finite element analyses demonstrated the complete recovery of the design bearing capacity (139.5 kips). Additionally, the study revealed a clear correlation between the strength of the threaded material and the post-repair strength of the girder.

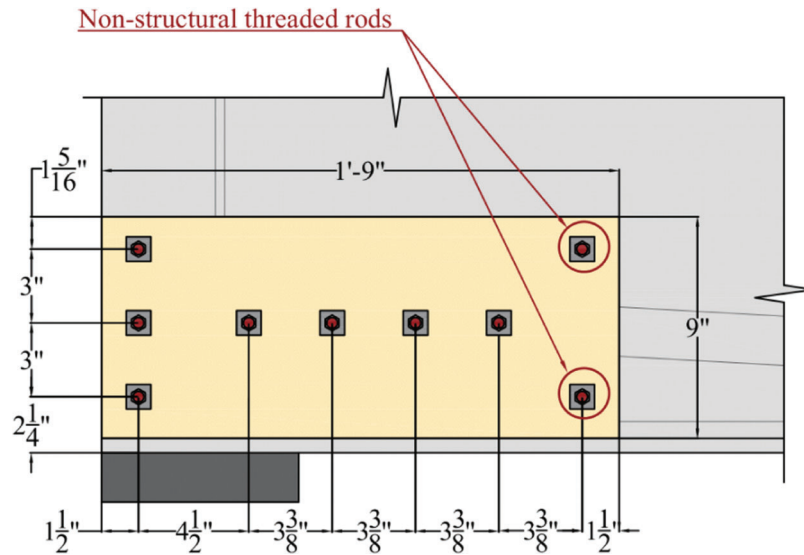


Figure 8.14 Case II: threaded rod layout with 7 effective threaded rods. Option 7: middle (II-G-7.1).

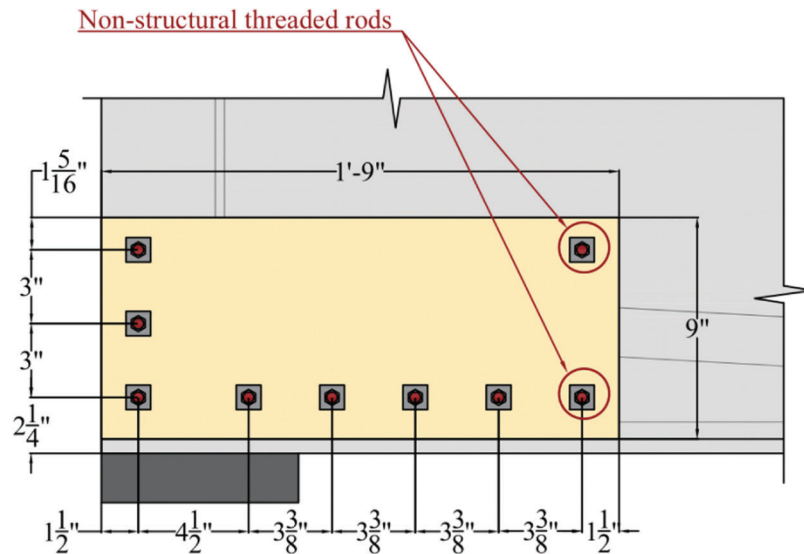


Figure 8.15 Case II: threaded rod layout with 7 effective threaded rods. Option 7: bottom (II-G-7.2).

Figure 8.16 highlights that model II-G-16-150, with 16 effective threaded rods made of Grade 8 steel, achieved the highest capacity of 264.0 kips. This model not only fully recovered the design bearing strength but also the design shear capacity. After reaching a peak load, a rapid drop in capacity was observed because of a substantial relative slip between the bottom of the repaired specimen and the bearing. The FE model was not able to accurately predict the post-peak behavior. Therefore, a rapid drop in capacity was observed from the load-vertical displacement plot. However, during the experiment, the observed behavior was significantly more ductile. The failure mode encompassed corroded web yielding in the steel girder, threaded rod rupturing, and concrete crushing.

Model II-G-16-125, with a similar number of threaded rods but with lower-grade material (Grade B7, $F_u = 125$ ksi), achieved a slightly lower capacity of 251.5 kips. Finally, model II-G-16-60, utilizing Grade 1 ($F_u = 60$ ksi) threaded rods, reached the lowest capacity of 191.6 kips among the discussed finite element models in the parametric study.

A similar trend of higher rod grade causing higher repair capacity was observed for the models with 11 and 7 effective threaded rods (Option 7: middle and Option 7: bottom), as shown in Figure 8.16 through Figure 8.19.

8.2.2.2 Impact of the number of threaded rods on the repair capacity. The parametric study for Case II included the investigation of the influence of the

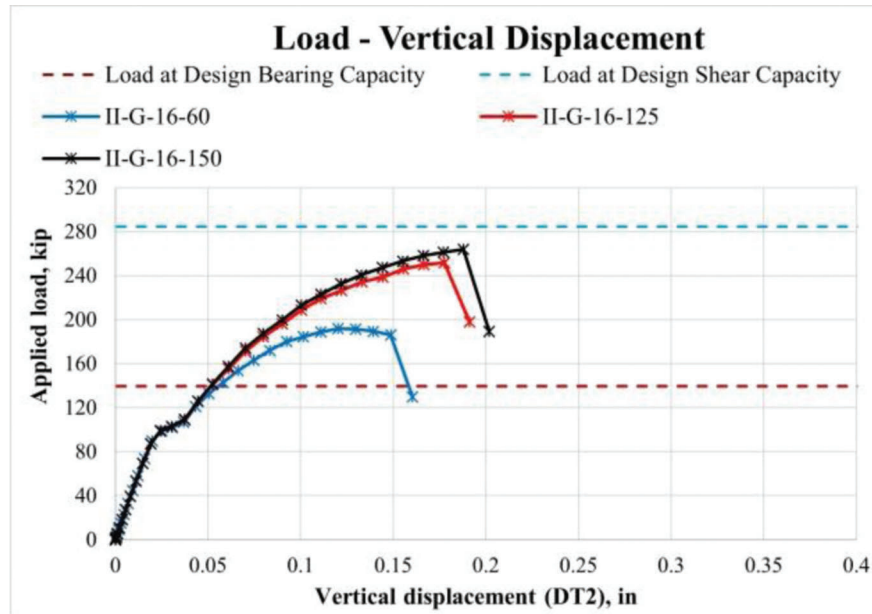


Figure 8.16 Impact of threaded rod material on the repair capacity (Case II: 16 effective threaded rods).

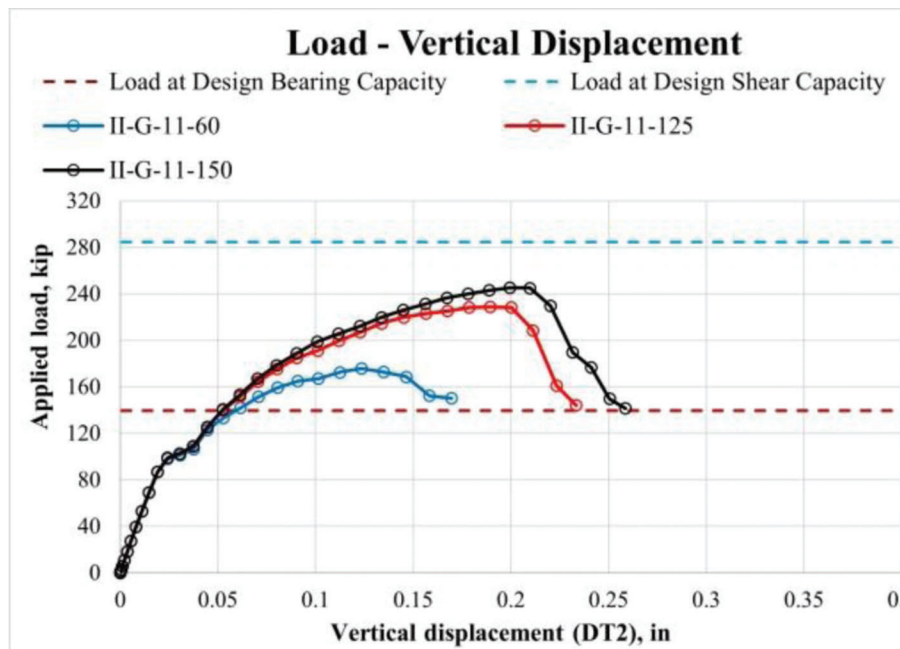


Figure 8.17 Impact of threaded rod material on the repair capacity (Case II: 11 effective threaded rods).

number of threaded rods on the post-repair capacity. Comparison of the models with the same grade for threaded rods (Grade 1, Grade B7, or Grade 8), but various numbers of rods, indicated a higher post-repair capacity with a larger number of rods (Figure 8.20 through Figure 8.22) and, in contrast to Case I, a more brittle response.

Additionally, different behavior was observed in Option 7: middle and Option 7: bottom, due to location in different areas of the corroded web. As a result, Option

7: bottom, which had the most of effective threaded rods installed in the bottom row, showed a more ductile response than Option 7: middle. However, their loading capacities did not differ significantly. For example, models II-G-7.1-150 and II-G-7.2-150 reached comparable capacities of 231.5 and 227.1 kips, respectively.

However, II-G-7.2-150 was more ductile and reached a vertical displacement of 0.238 in. at the peak load, whereas the vertical displacement of II-G-7.1-150 was only 0.2 in. (Figure 8.22).

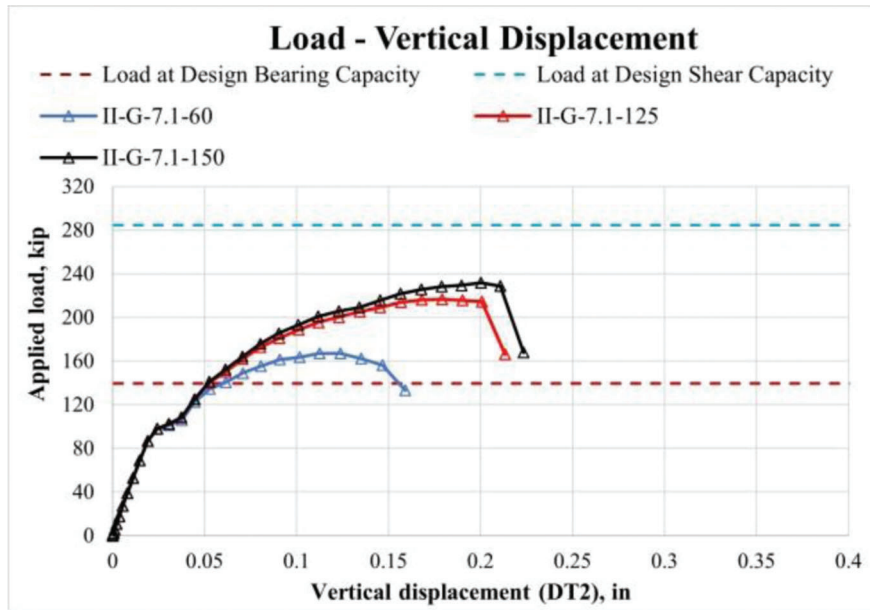


Figure 8.18 Impact of threaded rod material on the repair capacity (Case II: 7 effective threaded rods. Option 7: middle).

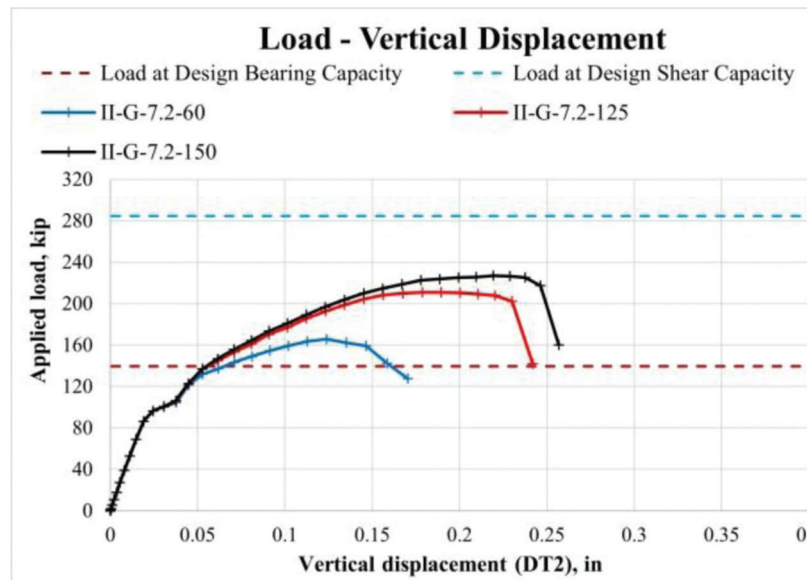


Figure 8.19 Impact of threaded rod material on the repair capacity (Case II: 7 effective threaded rods. Option 7: bottom).

The parametric study provided insights into failure mode and effective distribution of threaded rods over the corroded area when detailing the repair. The standard failure mechanism for all models was yielding the corroded region combined with threaded rod rupturing and grout panel cracking.

The finite element simulation results from 12 models for the Case II configuration are presented in Table 8.3. The parametric study conclusively demonstrated that the number of threaded rods and their material properties play an important role in influencing the repair capacity. Consequently, in scenarios

where space for threaded rod installation is constrained, employing higher-grade rods becomes a viable strategy to restore the required strength of the girder.

The success of the repair of $W24 \times 68$ was contingent on one key criterion: achieving the recovery of the design bearing strength (139.5 kips). However, an additional requirement of recovering at least 85% of the design shear capacity was set. Only three models (II-G-16-150, II-G-11-150, II-G-16-125) with high-strength and medium-strength threaded rods satisfied this additional condition.

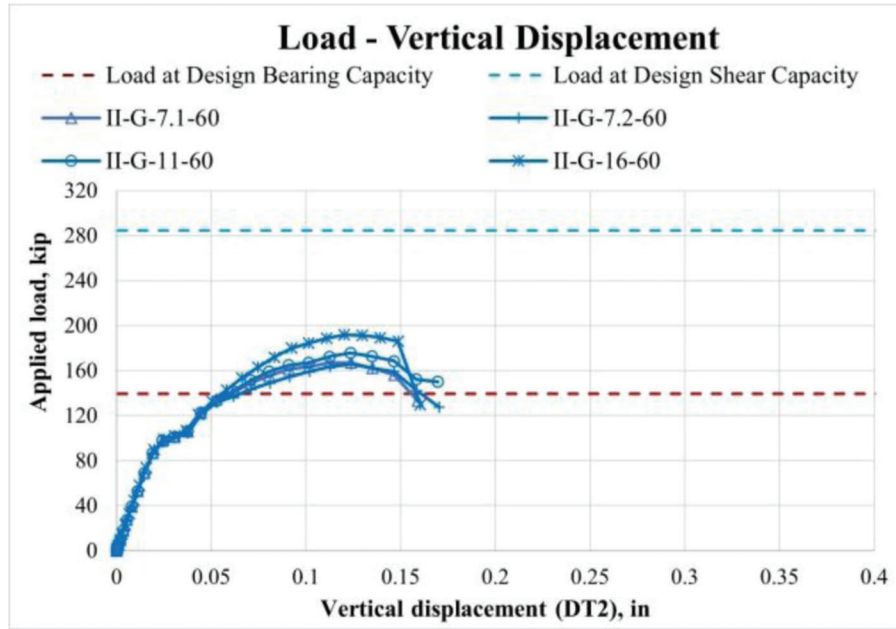


Figure 8.20 Impact of the number of threaded rods on the repair capacity (Case II: $F_u = 60$ ksi).

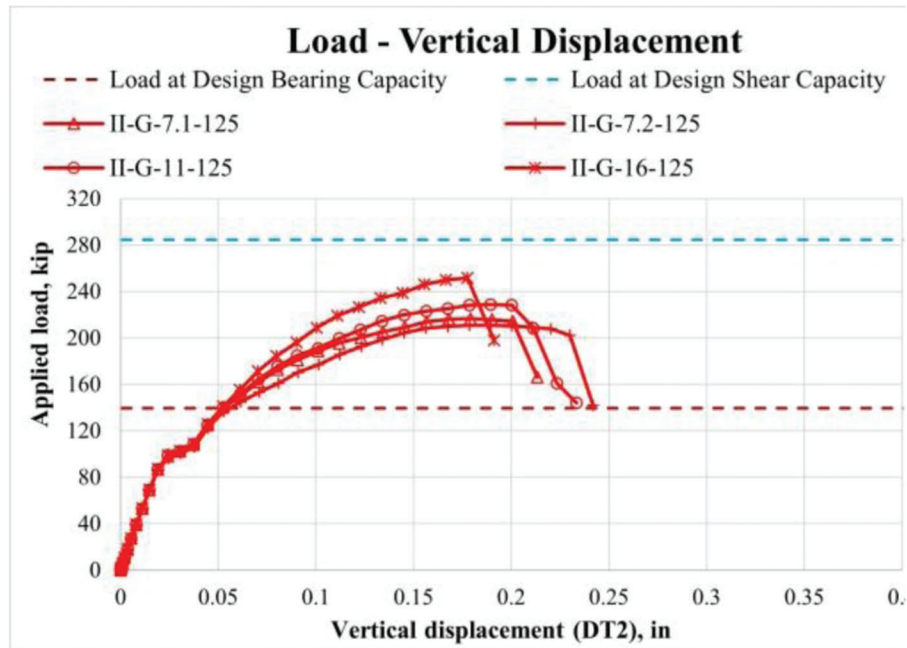


Figure 8.21 Impact of the number of threaded rods on the repair capacity (Case II: $F_u = 125$ ksi).

8.3 Parametric Study: Case III

8.3.1 Threaded Rod Layouts for Case III

Similar to Case II, finite element models for Case III were based on the Specimen 6 FE model, validated using experimental data (Section 7.3.5). However, the updated threaded rod layouts for Case III were developed with the majority of threaded rods concentrated in the bearing

region (Figure 8.23 to Figure 8.25). Because of the presence of partial stiffeners, threaded rods were not evenly distributed in the bearing region, and the distance between the second and third columns of threaded rods was 3.125". In contrast, the remaining columns were spaced evenly at 1.625". However, if no complex geometry is present, it is recommended to distribute threaded rods evenly in the bearing region because eccentrically installed rods do not develop their full capacity.

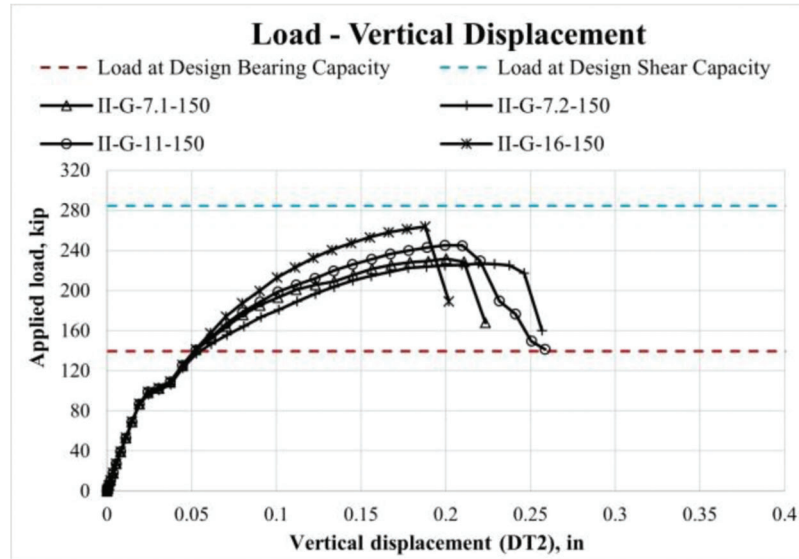


Figure 8.22 Impact of the number of threaded rods on the repair capacity (Case II: $F_u = 150$ ksi).

TABLE 8.3
Case II: FE simulation results

Name	Infill Material	Number of Threaded Rods	Threaded Rods Material, F_u , ksi	Loading Capacity, kip	Design Bearing Capacity Recovered?	85% of the Design Shear Capacity Recovered?
II-G-16-150	Grout	16	150	264.0	Yes	Yes
II-G-11-150	Grout	11	150	245.0	Yes	Yes
II-G-7.1-150	Grout	7	150	231.5	Yes	No
II-G-7.2-150	Grout	7	150	227.1	Yes	No
II-G-16-125	Grout	16	125	251.5	Yes	Yes
II-G-11-125	Grout	11	125	228.7	Yes	No
II-G-7.1-125	Grout	7	125	216.5	Yes	No
II-G-7.2-125	Grout	7	125	211.0	Yes	No
II-G-16-60	Grout	16	60	191.6	Yes	No
II-G-11-60	Grout	11	60	175.6	Yes	No
II-G-7.1-60	Grout	7	60	167.0	Yes	No
II-G-7.2-60	Grout	7	60	165.6	Yes	No

8.3.2 Case III: Results and Discussion

Case III of the parametric study consisted of 9 finite element models, and the results were arranged into two groups to investigate.

1. Impact of threaded rod material on the post-repair capacity with a constant number of “effective” threaded rods (Figure 8.26 through Figure 8.28).
2. Impact of the number of threaded rods on post-repair capacity with constant material properties (Figure 8.29 through Figure 8.31).

8.3.2.1 Impact of threaded rod material on the repair capacity. The parametric study comprised 9 distinct finite element models featuring different threaded rod materials, including Grade 1, Grade B7, and Grade 8. All finite element analyses demonstrated the complete

recovery of the design bearing capacity. Additionally, the study revealed a clear correlation between the strength of the threaded material and the post-repair strength.

Figure 8.26 highlights that model III-G-15-150, with 15 effective threaded rods made of Grade 8 steel, achieved the highest capacity of 302.6 kips. This model not only fully recovered the design bearing strength but also reached the design shear capacity. The failure mode observed included corroded web yielding in the steel girder, threaded rod rupturing, and concrete crushing. No web crippling and significant lateral deformations were observed. The FE model did not accurately predict post-peak behavior. Therefore, a rapid drop in capacity was observed from the load-vertical displacement plot. However, during the experiment, the behavior of the specimen was significantly more ductile.

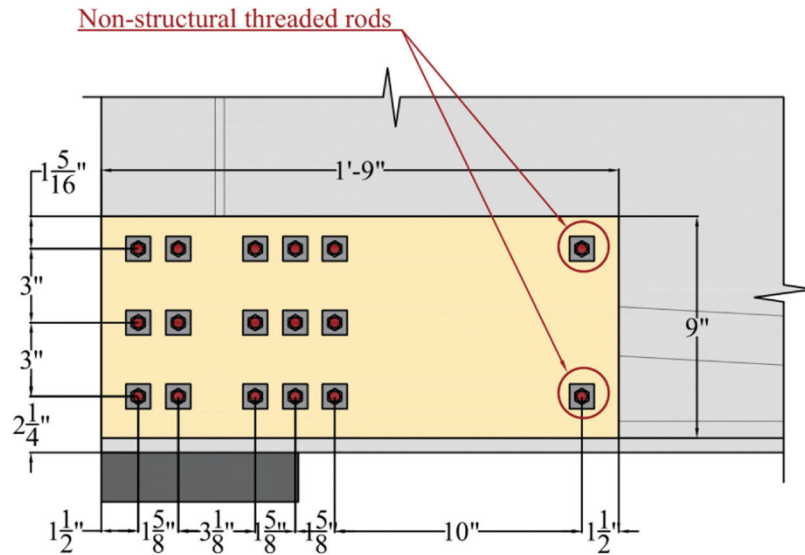


Figure 8.23 Case III: threaded rod layout with 15 effective threaded rods (III-G-15).

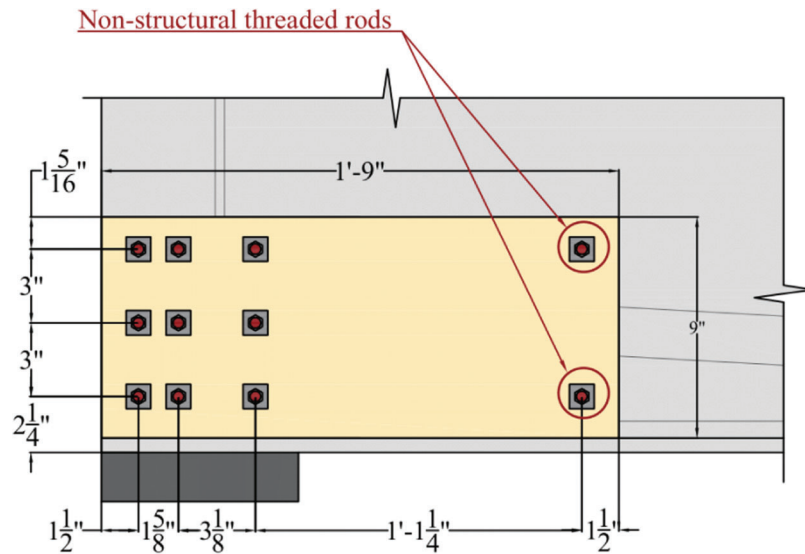


Figure 8.24 Case III: threaded rod layout with 9 effective threaded rods (III-G-9).

Model III-G-15-125, with a similar number of threaded rods but with lower-grade material (Grade B7, $F_u = 125$ ksi), achieved a slightly lower capacity of 299.7 kips. Finally, model III-G-15-60, utilizing Grade 1 ($F_u = 60$ ksi) threaded rods, reached the lowest capacity of 237.1 kips among the discussed finite element models in the parametric study.

A consistent trend of higher threaded rod grade correlating with increased post-repair strength was observed for the models that had 9 and 6 threaded rods, as shown in Figure 8.27 and Figure 8.28.

8.3.2.2 Impact of the number of threaded rods on the repair capacity. The parametric study for Case III included the investigation of the influence of the

number of threaded rods on the post-repair capacity. Comparison of the models with the same grade for threaded rods (Grade 1, Grade B7, or Grade 8), but various numbers of rods, indicated a higher post-repair capacity with a larger number of rods (Figure 8.29 through Figure 8.31).

The finite element simulation results from 9 models for the Case III configuration are presented in Table 8.4. The parametric study conclusively demonstrated that the number of threaded rods and their material properties play an important role in influencing the post-repair capacity. Consequently, in scenarios where space for threaded rod installation is constrained, employing higher-grade rods becomes a viable strategy to restore the required strength of the girder.

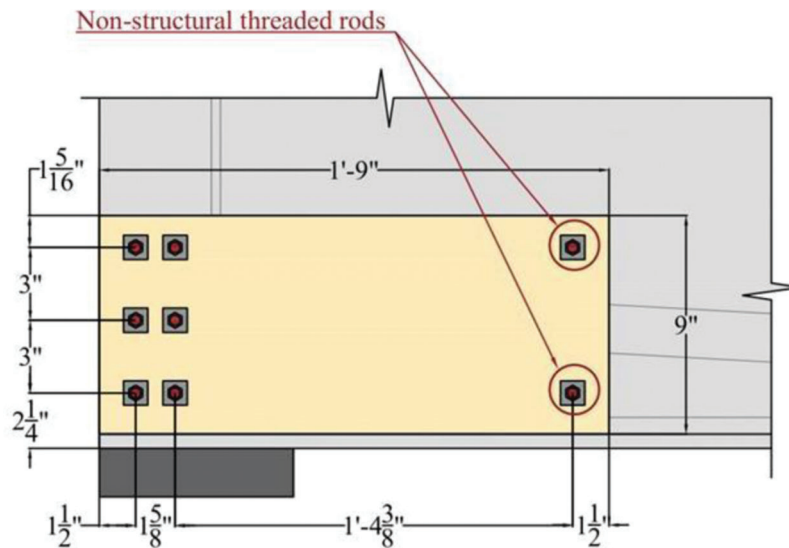


Figure 8.25 Case III: threaded rod layout with 6 effective threaded rods (III-G-6).

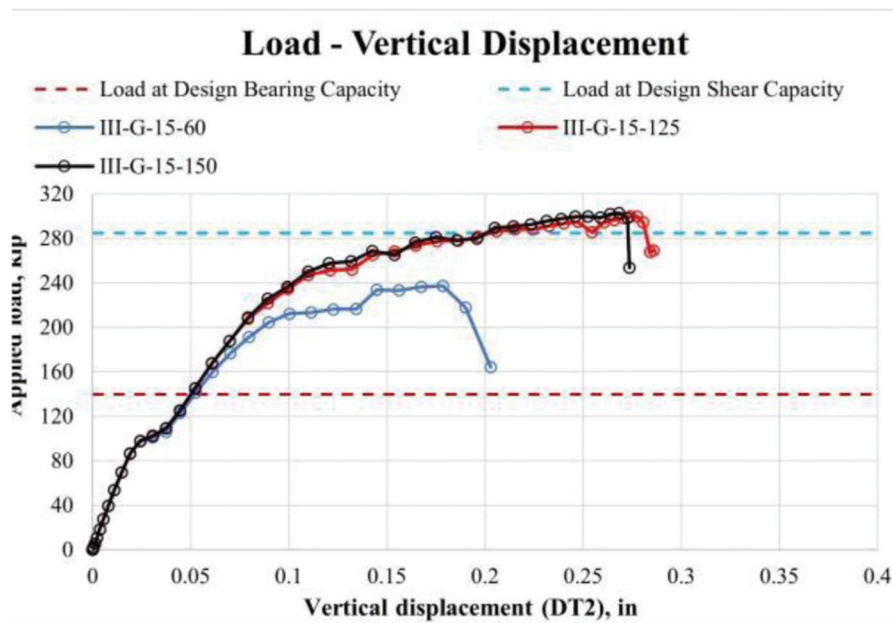


Figure 8.26 Impact of threaded rod material on the repair capacity (Case III: 15 effective threaded rods).

The summary of the finite element simulation results from 9 models for Case III configuration are presented in Table 8.4. It was concluded from this part of the study that the number of threaded rods and their material properties directly affect the capacity of the repair. Therefore, if the limited space for threaded rod installation is available, the higher-grade rods could be used to restore the required strength of the girder.

The success of the repair of the W 24 × 68 section was contingent on one key criterion: achieving the recovery of the design bearing strength. However, an additional requirement of restoring at least 85% of the design shear capacity was set. Therefore, the number of

accepted threaded rod configurations for the sandwich panel repair method decreased notably. Four models, III-G-6-125, III-G-15-60, III-G-9-60, and III-G-6-60 did not satisfy this additional condition. Those four models were assembled with either low-strength threaded rods (Grade 1) or only 6 medium-strength threaded rods (Grade B7). Overall, the finite element models built for Case III proved that the threaded rods are the most effective in the region right above the bearing. Threaded rods installed with substantial eccentricities concerning the bearing do not significantly contribute to the strength of the sandwich panel repair.

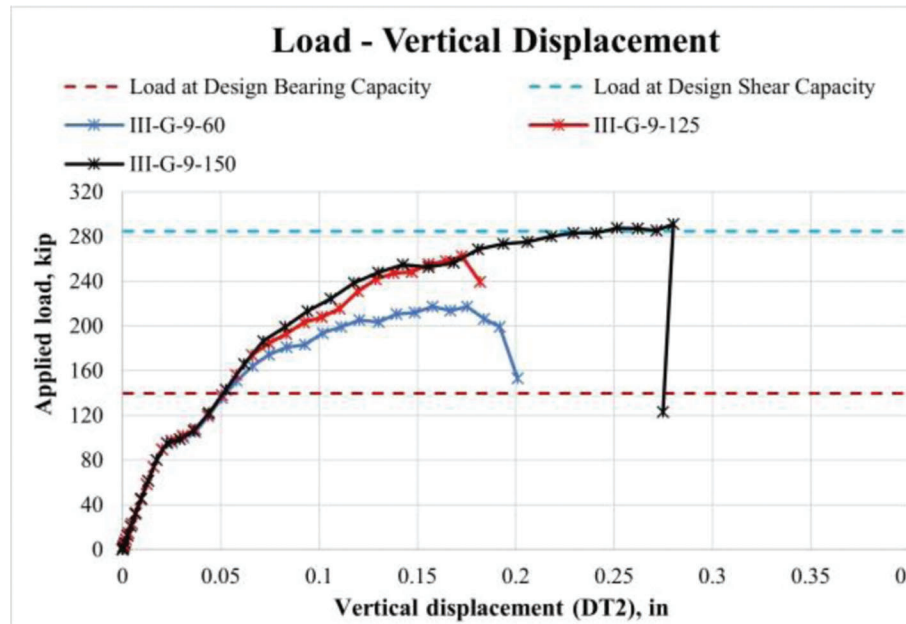


Figure 8.27 Impact of threaded rod material on the repair capacity (Case III: 9 effective threaded rods).

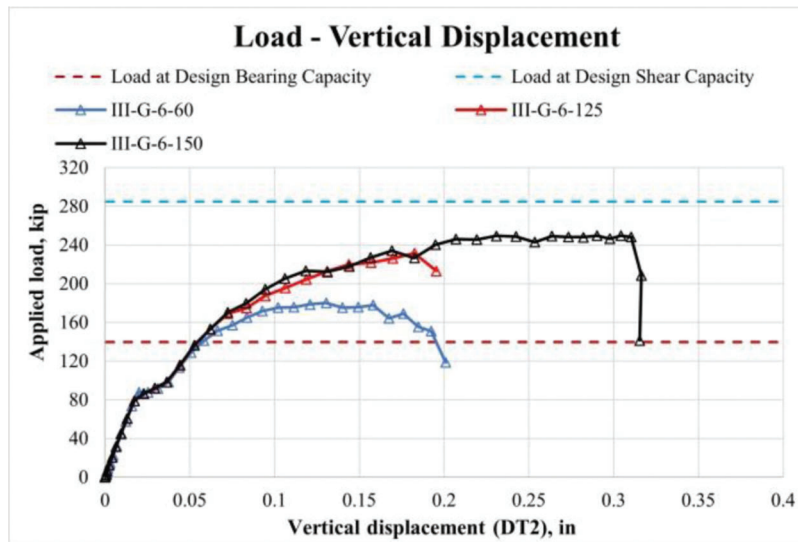


Figure 8.28 Impact of threaded rod material on the repair capacity (Case III: 6 effective threaded rods).

8.4 Summary

To summarize the findings from a comprehensive parametric study involving 3 different cases and 33 solid finite element models, a few significant conclusions were made.

1. Threaded rods should be considered effective only when located in the bearing region and subjected to primarily concentric forces. Threaded rods lose their effectiveness in recovering capacity proportionally to the eccentricity value with respect to the bearing location. Hence,

threaded rods become less efficient the farther they are positioned from the bearing. Future studies are required to quantitatively measure the decrease in the capacity of threaded rods due to eccentric loading.

2. The material property and number of threaded rods directly affect the capacity of the repaired girder. Therefore, implementing high-strength threaded rods would be the most effective repair strategy when a substantial amount of capacity is lost due to corrosion. Opting for a larger number of medium-strength threaded rods could serve as an alternative if high-strength rods are not readily available.

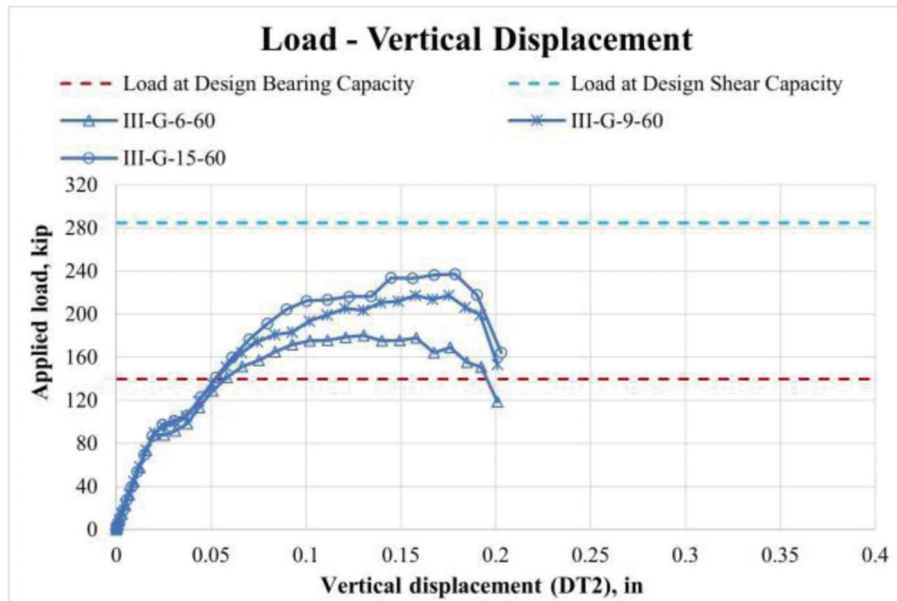


Figure 8.29 Impact of the number of threaded rods on the repair capacity (Case II; $F_u=60$ ksi).

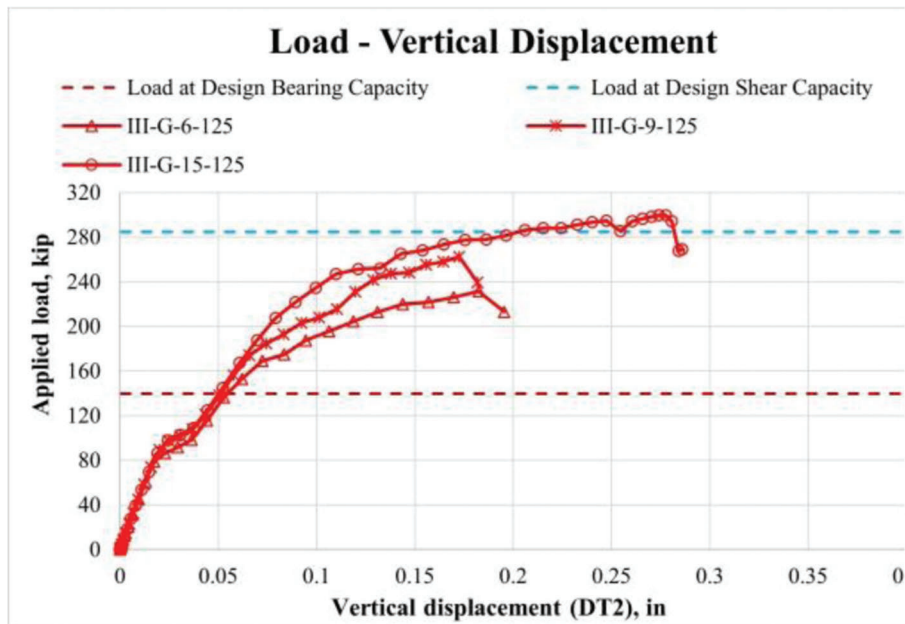


Figure 8.30 Impact of the number of threaded rods on the repair capacity (Case II; $F_u=125$ ksi).

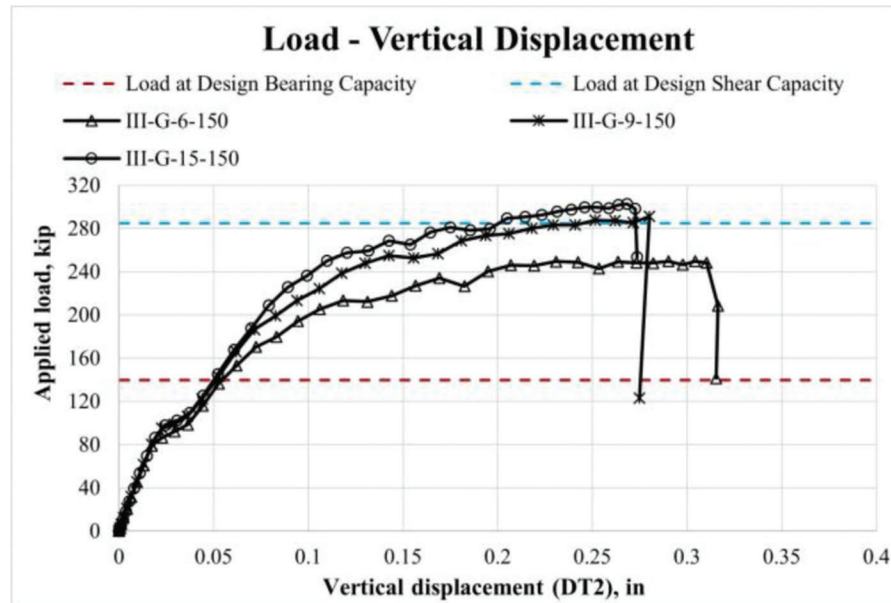


Figure 8.31 Impact of the number of threaded rods on the repair capacity (Case III: $F_u = 150$ ksi).

TABLE 8.4
Case III: FE simulation results

Name	Infill Material	Number of Threaded Rods	Threaded Rods Material, F_u , ksi	Loading Capacity, kip	Design Bearing Capacity Recovered?	85% of the Design Shear Capacity Recovered?
III-G-15-150	Grout	15	150	302.6	Yes	Yes
III-G-9-150	Grout	9	150	291.1	Yes	Yes
III-G-6-150	Grout	6	150	249.8	Yes	Yes
III-G-15-125	Grout	15	125	299.7	Yes	Yes
III-G-9-125	Grout	9	125	262.5	Yes	Yes
III-G-6-125	Grout	6	125	231.4	Yes	No
III-G-15-60	Grout	15	60	237.1	Yes	No
III-G-9-60	Grout	9	60	217.3	Yes	No
III-G-6-60	Grout	6	60	180.2	Yes	No

9. RECOMMENDATIONS FOR DESIGN AND APPLICATION

In the following Sections 9.1–9.8, recommendations for the design and application of the sandwich panel repair method are presented. The recommendations encompass the selection of the sandwich panel repair configuration, an equation to determine the required number of threaded rods, the arrangement of threaded rod layout, the selection of infill material, and guidelines for fabrication and assembly. The developed repair method is limited to only steel girder members that were subjected to end corrosion.

9.1 Selection of the Repair Configuration

The initial step in designing the repair involves selecting one of two presented configurations (Option 1 or Option 2) that best align with the project require-

ments. Option 1, represented by Specimens 6 and 7 (Sections 6.6 and 6.7) preserves the existing bearing, with the region behind a partial stiffener encased in grout/concrete. Option 2, represented by Specimens 4 and 5 (Sections 6.4 and 6.5) requires the installation of additional support but eliminates the need for encasement of the corroded region behind partial stiffener. When selecting between two configurations, the parameters listed in Subsections 9.1.1–9.1.3 must be considered.

9.1.1 Presence of the Diaphragm and its Depth

The first parameter that must be taken into account when selecting between the two configurations is the depth of the diaphragm, if applicable. Diaphragms in steel bridges are structural elements that serve as lateral bracings and prevent torsional buckling failure. However, depending on the diaphragm dimensions,

the repair complexity varies. Deep diaphragms that limit access to the corroded region, as shown in Figure 9.1, might have to be temporarily removed during the repair. Additionally, re-bolting the diaphragm becomes necessary, with the added requirement of cutting a portion to accommodate the altered geometry of the steel girder following the application of the sandwich panel repair.

9.1.2 Diaphragm Condition

The next essential parameter is the condition of the diaphragm. If the diaphragm is severely corroded (Figure 9.2) and must be replaced, then the new diaphragm should be designed shallower to allow for corroded girder end encasement using the sandwich panel method. As shown in Figure 9.2, the space



Figure 9.1 Non-corroded diaphragm in a steel bridge.

between the bottom flange of the diaphragm and the girder's bottom flange is insufficient to perform the repair.

9.1.3 Available Space for Additional Support

Finally, the last parameter that must be considered is the space availability underneath the corroded girder end. Option 2 entails the placement of one additional bearing, and it is vital to have sufficient space for its installation. Figure 9.3 illustrates abundant space available for accommodating an additional bearing.

To conclude, within the scope of the study, two configurations (Option 1 or Option 2) were extensively studied. If the bridge geometry prohibits the use of either Option 1 or Option 2, an alternative conventional repair method should be considered.

9.2 Calculation of Required Number of Threaded Rods

The process of determining the minimum required number of threaded rods consists of four steps. They include determining the web crippling capacities of both non-corroded and corroded girders, along with the tensile resistance of a single threaded rod. The four steps were explained in Subsections 9.2.1–9.2.4, and accompanied by example calculations for Specimen 6. During the experimental investigation, Specimen 6 exhibited the full recovery of the design web crippling capacity and 89% of the design shear capacity, validating the efficacy of the developed equation. The recovery of 89% of the design shear capacity also proved the conservativeness of the developed equation, as the target was to reach only the design web crippling capacity after performing the repair.



Figure 9.2 Severely corroded diaphragms.

9.2.1 Step 1: Determine the Required Capacity

The sandwich panel repair method applies to both stiffened and unstiffened girders. However, this study focused primarily on experimental and numerical evaluation of girders without full-depth transverse stiffeners. Additionally, unstiffened girders are more susceptible to significant capacity loss resulting from corrosion. As the web local crippling (WLC) capacity governs the design of unstiffened girders, the required capacity that must be restored was established as the design web local crippling capacity of the undamaged girder. The web local crippling capacity was calculated following AASHTO LRFD 2020 provisions (AASHTO, 2020). Depending on the bearing length and distance of the applied load from the end of the member either Equation 9.1 (AASHTO, 2020; D6.5.3-2), Equation 9.2 (AASHTO, 2020; D6.5.3-3), or Equation 9.3 (AASHTO, 2020; D6.5.3-4) were used in the design process.

If the concentrated load is applied at a distance greater than or equal to $d/2$ from the girder end, then:

$$R_{n_WLC} = .08t_w^2 \left[1 + 3 \left(\frac{N}{d} \right) \left(\frac{t_w}{t_f} \right)^{1.5} \sqrt{\frac{EF_{yw}t_f}{t_w}} \right] \quad (\text{Eq. 9.1})$$

Otherwise, is if $\frac{N}{d} \leq 0.2$, then:

$$R_{n_WLC} = .04t_w^2 \left[1 + 3 \left(\frac{N}{d} \right) \left(\frac{t_w}{t_f} \right)^{1.5} \sqrt{\frac{EF_{yw}t_f}{t_w}} \right] \quad (\text{Eq. 9.2})$$

is if $\frac{N}{d} > 0.2$, then:

$$R_{n_WLC} = .04t_w^2 \left[1 + 3 \left(\frac{4N}{d} - 0.2 \right) \left(\frac{t_w}{t_f} \right)^{1.5} \sqrt{\frac{EF_{yw}t_f}{t_w}} \right] \quad (\text{Eq. 9.3})$$

In this study, the target capacity after repair application was aimed to achieve the design web crippling capacity. Consequently, the R_n value was multiplied by the resistance factor $\phi_w = 0.8$ (AASHTO, 2020; Section 6.5.4.2). The tested specimens had a bearing length ($N = 8 \text{ in.}$) ratio over the overall depth of the girder ($d = 23.73 \text{ in.}$) more than 0.2. Therefore, Equation 9.4 was utilized to evaluate the design web crippling capacity of the W24 \times 68 section, incorporating the values of modulus of elasticity ($E = 29,000 \text{ ksi}$), yield strength ($F_{yw} = 45 \text{ ksi}$), and, finally, web thickness ($t_w = 0.585 \text{ in.}$). The values of design web crippling and shear capacities of corroded and non-corroded specimens are presented in Table 9.1.

$$R_u = \phi_w \cdot R_{n_WLC} \quad (\text{Eq. 9.4})$$

TABLE 9.1
Shear and bearing capacities of W24 \times 68 girder

Capacity	Value
Design Shear Capacity	257.0 kips
85% of Design Shear Capacity	218.5 kips
Nominal Web Local Crippling Capacity	157.6 kips
Design Web Local Crippling Capacity	126.0 kips
Residual Web Local Crippling Capacity (Specimen 4)	49.2 kips
Factored Web Local Crippling Capacity (Specimen 4)	39.4 kips
Residual Web Local Crippling Capacity (Specimen 6)	31.1 kips
Factored Web Local Crippling Capacity (Specimen 6)	24.9 kips

Substituting the given values into the equation yields:

$$R_u = 0.8 \cdot 0.4 \cdot 0.415 \text{ in}^2 \left[1 + 3 \left(\frac{4 \cdot 8 \text{ in}}{23.73 \text{ in}} - 0.2 \right) \left(\frac{0.415 \text{ in}}{0.585 \text{ in}} \right)^{1.5} \right] \sqrt{\frac{29,000 \text{ ksi} \cdot 45 \text{ ksi} \cdot 0.585 \text{ in}}{0.415 \text{ in}}} = 126 \text{ kip}$$

9.2.2 Step 2: Determine the Residual Capacity

To calculate the residual capacity of a corroded girder, the modifications were applied to the web local crippling capacity equation as outlined in Equation 9.5. Two major adjustments were introduced: firstly, the nominal web thickness (t_w) was substituted with the average residual web thickness (t_{w_r}). The average residual thickness should be determined within a critical section above the bearing up to 2–3 in. above the k-area in hot-rolled steel sections as described by Kanakamedala, Seo, Varma, Connor, and Tarasova (2023).

Secondly, the overall depth of the girder was replaced by the d_0 value, which is the average unsupported depths of the web (d_1 , d_2) as shown in Figure 9.4 ($d_0 = 3 \text{ in.}$). The measurements of unsupported web depth were taken from the upper surface of the bottom flange to the lower surface of the partial stiffener. As stiffeners are typically installed asymmetrically, the average value d_0 was introduced. The primary rationale behind implementing the value of unsupported web depth is, firstly, the contribution of partial depth stiffeners to the web crippling capacity of the girder. Additionally, for corroded girders, web crippling deformations are localized to the corroded region because of its increased slenderness. Consequently, employing the entire girder depth for calculating the residual web crippling capacity would be excessively conservative.

The reduced factored residual web crippling capacity of W24 \times 68 was calculated using Equation 9.6. The residual web thickness was experimentally measured using the ultrasonic thickness gauge, yielding the value of $t_{w_r} = 0.125 \text{ in.}$ A strong correlation was noted



Figure 9.3 Placement of an additional bearing.

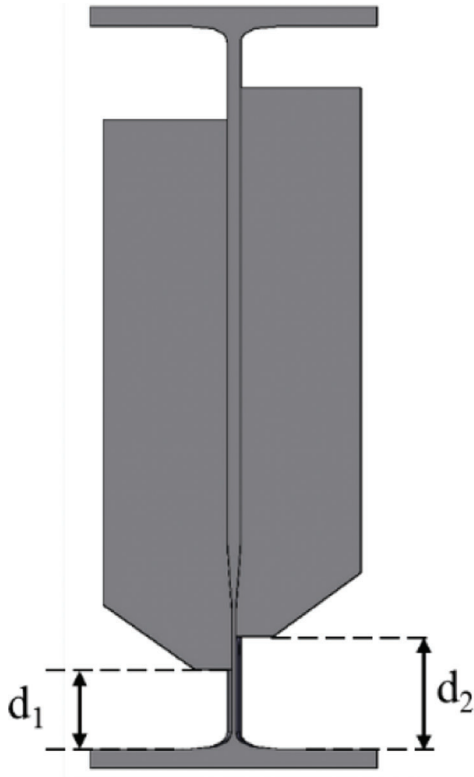


Figure 9.4 Definition of d_1 and d_2 values.

between the nominal residual web crippling capacity estimated using Equation 9.5 and the maximum applied load that Specimen 2 reached during the large-scale test. The load-carrying capacity of Specimen 2 was equal to 39 kips, exceeding the calculated value by 26%, thus affirming the conservative nature of Equation 9.5.

$$R_{n_WLC_r} = 0.4 t_{w_r}^2 \left[1 + 3 \left(\frac{4N}{d_0} - 0.2 \right) \left(\frac{t_{w_r}}{t_f} \right)^{1.5} \sqrt{\frac{E F_{yw} t_f}{t_{w_r}}} \right] \quad (\text{Eq. 9.5})$$

Substituting the given values into the equation yields

$$R_{n_WLC_r} = 0.4 \cdot 0.125 \text{ in}^2 \left[1 + 3 \left(\frac{4 \cdot 8 \text{ in}}{3 \text{ in}} - 0.2 \right) \left(\frac{0.125 \text{ in}}{0.585 \text{ in}} \right)^{1.5} \sqrt{\frac{29,000 \text{ ksi} \cdot 45 \text{ ksi} \cdot 0.585 \text{ in}}{0.125 \text{ in}}} \right] = 31 \text{ kip}$$

$$R_{u_r} = \phi_w \cdot R_{n_WLC_r} \quad (\text{Eq. 9.6})$$

Substituting the given values into the equation yields

$$R_{u_r} = 0.8 \cdot 31 = 25 \text{ kip}$$

9.2.3 Step 3: Determine the Tensile Resistance of a Threaded Rod

The third step in the calculation of the required number of threaded rods involves determining the nominal tensile resistance of an individual rod (Equation 9.7). The area of the threaded rod (A_{rod}) is calculated using the value of the nominal diameter (d), including threads provided by the manufacturer (Equation 9.8). Additionally, the ultimate tensile strength (F_u) a crucial parameter in the design calculations. The specimens that were tested experimentally implemented Grade B7 threaded rods with $F_u = 125 \text{ ksi}$. To obtain the design tensile capacity, T_{n_rod} value is multiplied by the resistance factor $\phi_t = 0.8$ (AASHTO, 2020; Section 6.5.4.2) as indicated Equation 9.9.

$$T_{n_rod} = 0.76 \cdot A_{rod} \cdot F_u \quad (\text{Eq. 9.7})$$

$$A_{rod} = \pi \cdot d^2 / 4 \quad (\text{Eq. 9.8})$$

$$T_{u_rod} = \phi_t \cdot T_{n_rod} \quad (\text{Eq. 9.9})$$

Substituting the given values into the equation yields:
 $T_{u_rod} = 0.8 \cdot 0.76 \cdot 0.11 \text{ in}^2 \cdot 125 \text{ ksi} = 8.39 \text{ kip}$

9.2.4 Step 4: Determine the Minimum Required Number of Threaded Rods

Finally, the last step of calculating the number of required rods involves subtracting the residual web crippling capacity value of the corroded specimen from the targeted capacity of the rehabilitated specimen. The difference is then multiplied by the strength reduction factor ϕ_w and divided by the design tensile resistance of a single threaded rod as shown in Equation 9.10. The number of threaded rods value (N_{rod}) must be rounded up to the next closest integer.

$$\frac{N_{rod} = \phi_w \cdot (R_{n_WLC} - R_{n_WLC_r})}{\phi_t \cdot T_{n_rod}} \quad (\text{Eq. 9.10})$$

Using the provided values

$$N_{rod} = \frac{126 \text{ kip} - 25 \text{ kip}}{8.39 \text{ kip}} = 12.04 \approx 13 \text{ rods}$$

To conclude, the minimum required number of threaded rods to recover the design bearing capacity of the medium-level corroded specimen is equal to 13. It is essential to ensure the even distribution of these threaded rods across the bearing region. The definition of the bearing region is provided in Section 9.3.

9.3 Development of Threaded Rod Layout

It was confirmed during the parametric study that was extensively detailed in Chapter 8, that the layout of threaded rods is pivotal in achieving the desired strength recovery. The threaded rods should be installed in the bearing region over the support, ensuring concentric loading that allows a threaded rod to develop its full capacity (Equation 9.7). The length of the bearing region is equal to the length of the support (N). The height of the bearing region extends from the bottom flange to the top flange (Figure 9.5). The threaded rod is considered to be subjected to concentric loading if installed in the region right above the existing bearing. Threaded rods installed with significant eccentricities (far away from the bearing) do not drastically contribute to the capacity of the repair.

For instance, models II-G-11-150 (Figure 8.17) and III-G-6-150 (Figure 8.25) exhibited capacities of 245

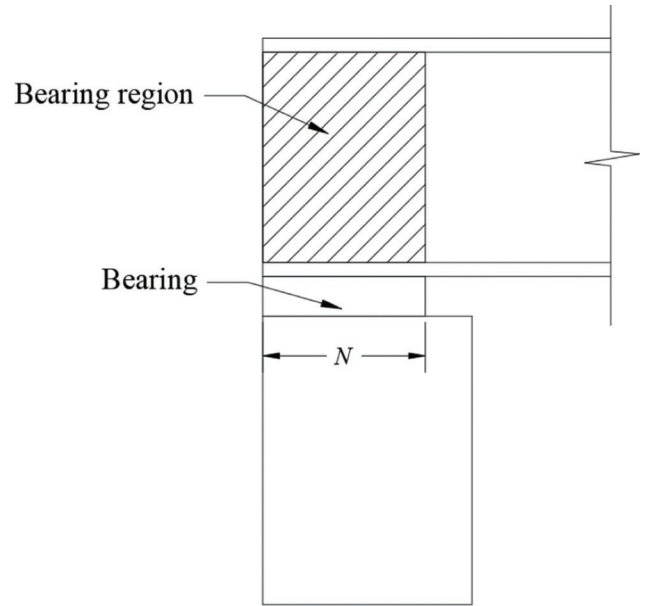


Figure 9.5 Definition of the bearing region.

kips and 250 kips, respectively. Despite a drastic change in the overall number of threaded rods used in repairs (13 and 8, respectively), the capacities differed by only 2%. The most crucial conclusion from the parametric study was that only the number of threaded rods located in the bearing region contributed to strength recovery. From Figure 8.17 and Figure 8.25, it can be observed that the number of threaded rods located right above the bearing was 5 and 6 for models II-G-11-150 and III-G-6-150, respectively. That explained the small difference in load-carrying capacities of these two models.

Once the required number of threaded rods is determined, it is crucial for the Engineer to evenly distribute them in the bearing region. Additionally, for constructability reasons, more threaded rods than the calculated minimum would be necessary to secure the location of stay-in-place formwork.

9.4 Selection of the Infill Material

Once the required number of threaded rods is calculated, the engineer must finalize the choice of filler material. Within the scope of this study, two materials were employed for infill to repair W24×68 girders: cementitious NS Grout and Kwik Bond-PPC 1121. The respective advantages and drawbacks of these materials are elaborated in Subsections 9.4.1–9.4.8.

9.4.1 Workability

9.4.1.1 Kwik Bond-PPC 1121. The polyester polymer concrete (PPC 1121) produced by Kwik Bond Polymers exhibits a variable working time ranging from 15 to 30 minutes. It was confirmed experimentally that adjusting the amount of added catalyst (MEKP) allows for con-

trol over the working time. Additionally, the working time correlates with the ambient temperatures: the higher the ambient temperature, the smaller the period within which concrete can be transported and cast. For detailed information and mixing recommendations, it is recommended to contact the manufacturer.

9.4.1.2 Cementitious NS Grout. In contrast to Kwik Bond–PPC 1121, the working time of cementitious NS Grout remains unalterable and is approximately 15 minutes. The “fluid” consistency of NS Grout allows for a slightly longer working time compared to the “flowable” consistency due to the increased water content. However, grouts with a higher water/cement ratio exhibit reduced compressive strength.

9.4.2 Mixing Complexity

9.4.2.1 Kwik Bond–PPC 1121. The mixing complexity of Kwik Bond–PPC 1121 is moderate, and, therefore, it can be mixed in 5-gal. buckets when the amount of concrete required for the repair is small (Figure 9.6 through Figure 9.12). Proper training is essential for accurate mixing, as the concrete’s working time is highly sensitive to the amount of added catalyst. Personal protective equipment (PPE) requirements include a respirator with an organic vapor cartridge and goggles due to a strong resin smell during mixing that can also cause eye irritation. The required components and the mixing process of Kwik Bond–PPC 1121 in a 5-lb. bucket are shown in Figure 9.6 through Figure 9.12.

9.4.2.2 Cementitious NS Grout. The mixing process for NS Grout is simple and straightforward (Figure 9.13 through Figure 9.15). Cementitious grout can be easily mixed in 5-gal. buckets using a mixing paddle attached to a heavy-duty power drill. No special training is required, and an N-95 mask is adequate as PPE to prevent dust inhalation.

9.4.3 Setting Time and Traffic Return

The significant advantage of using Kwik Bond–PPC 1121 for sandwich panel repair is the quick 2-hour traffic return. In contrast, NS Grout has a final setting time of 4–6 hours, requiring an extended traffic closure when used as the infill material.

9.4.4 Tensile Strength

9.4.4.1 Kwik Bond–PPC 1121. The value of tensile strength (f'_t) of Kwik Bond–PPC 1121, as per a technical data sheet, is 0.8 ksi. Additionally, insignificant cracking was observed in Specimens 5 and 7 after failure, indicating a relatively high tensile strength (Figure 9.16).



Figure 9.6 Polyester binder resin.

9.4.4.2 Cementitious NS Grout. The technical data sheet for NS Grout does not provide a value for tensile strength (f'_t). However, extensive cracking was observed in Specimen 4 and Specimen 6 after failure (Figure 9.17), demonstrating a significantly lower value of tensile strength compared to Kwik Bond–PPC 1121.

9.4.5 Price and Procurement

Kwik Bond–PPC 1121 is 20% more expensive than NS Grout with prices at 80\$/pcf and 67\$/pcf, respectively (as of 06/2022). Kwik Bond–PPC 1121 could be procured directly from Kwik Bond Polymers, whereas the NS Grout is procured through multiple distributors across the U.S.

To conclude, Kwik Bond–PPC 1121 has outstanding characteristics of tensile strength that positively influence loading capacity after repair, and a quick setting time. The working time could be controlled by adjusting the amount of added catalyst. However, the mixing procedures are more complicated, and the material is more expensive compared to conventional cementitious NS Grout (Table 4.10).

9.5 Components Required for Sandwich Panel Repair

To assemble a sandwich panel repair multiple components are required, and the selection of corrosion-resistant materials is paramount to prevent post-repair corrosion and ensure its prolonged durability. The recommended components for the sandwich panel repair method are described in Subsections 9.5.1–9.5.2.

9.5.1 Stay-in-Place Formwork

In the case of stay-in-place formwork, zinc-galvanized low-carbon steel sheets with a minimum thickness of 0.024" are recommended for use instead of steel plates because they are utilized only as a non-structural component that does not carry any loads. Thicker steel



Figure 9.7 MEKP catalyst.



Figure 9.10 Process of adding MEKP catalyst to binder resin.



Figure 9.8 KBP.



Figure 9.11 Mixing MEKP catalyst and binder resin (15 seconds).



Figure 9.9 KBP blended PPC sand.

sheets are permitted; however, thicker steel sheets impose a more complex bending process. Finally, it is essential to employ corrosion-resistant steel sheets in wet environments to prevent post-repair corrosion.

Upon casting concrete or grout, hydrostatic pressure is applied to the steel sheets. Hence, it is recommended

to clamp them at the bottom and top to prevent formwork damage. The mock-up specimen is illustrated in Figure 9.18, where bar clamps were utilized to secure the stay-in-place formwork and were removed once the filler material had cured.

9.5.2 Washers

Square zinc-plated washers (corrosion-resistant) are used for stress redistribution on the outer side of a stay-in-place formwork (Figure 9.19). While thicker and larger washers would potentially distribute stresses induced by deforming threaded rods more effectively, the impact of washer dimensions on the loading capacity of the repaired girder and cracking patterns has not been studied extensively. Additionally, the increased dimensions of square washers substantially increase the repair cost.

General-purpose zinc yellow-chromate washers (circular shape) are installed inside the stay-in-place formwork to minimize the localized deformations in the steel sheets and redistribute the pressure (Figure 9.20).



Figure 9.12 Mixing aggregates with catalyzed binder resin (2 minutes).

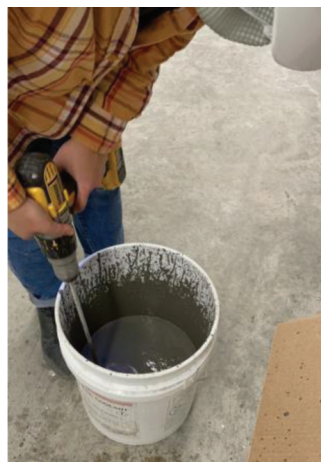


Figure 9.15 Mixing of NS Grout.



Figure 9.13 Water required for NS Grout mixing (5 lb.).



Figure 9.14 NS Grout powder (25 lb.).



Figure 9.16 Cracking pattern: Kwik Bond-PPC 1121.



Figure 9.17 Cracking pattern: NS Grout.

9.5.3 Threaded Rods

For threaded rods, zinc yellow-chromate plated threaded rods that are corrosion-resistant in wet environments are recommended. The grade and diameter of the threaded rod depend on the calculations performed during the design process of the sandwich panel repair to achieve the desired strength recovery.

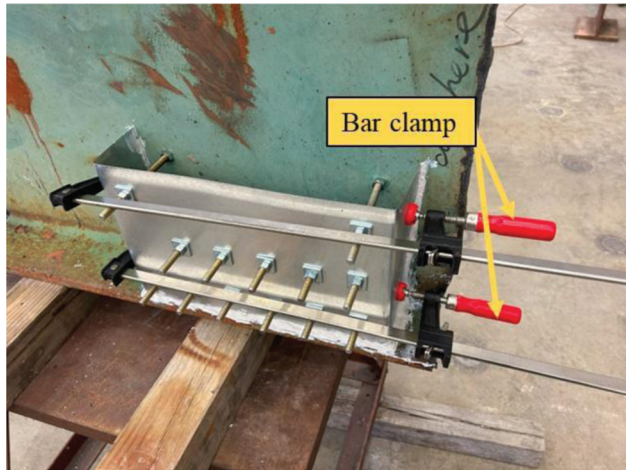


Figure 9.18 Sandwich panel repair mock-up specimen. Clamped stay-in-place formwork.

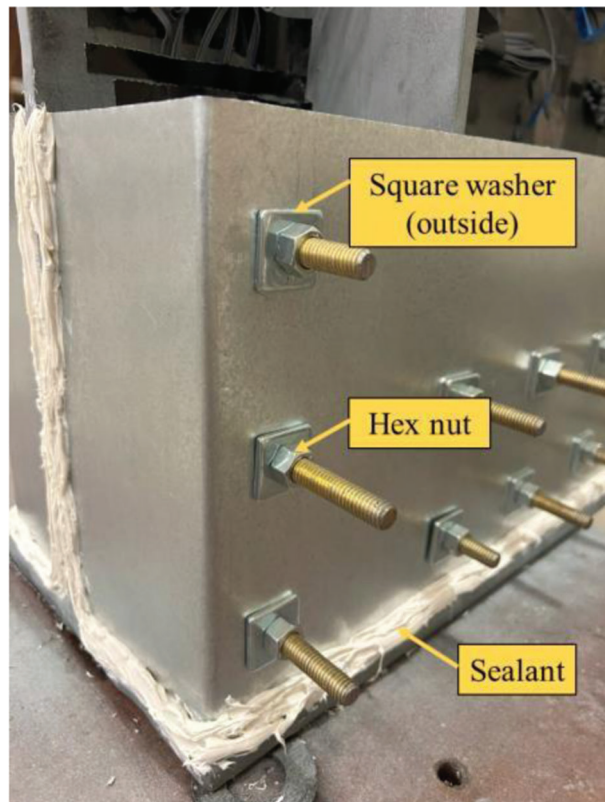


Figure 9.19 Square washers and hex nuts used in the repair (outer side).

9.5.4 Hex Nuts

Hex nuts are employed to securely attach threaded rods to the girder web and stay-in-place formwork, ensuring robustness and stability during the casting process (Figure 9.19). Like threaded rods and steel sheets, hex nuts must be corrosion-resistant in wet environments.

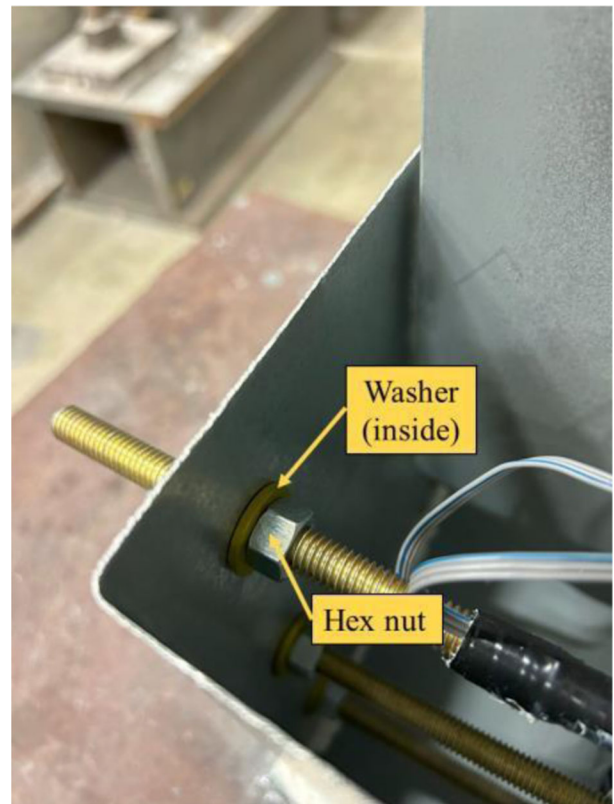


Figure 9.20 Standard washers and hex nuts used in the repair (inner side).

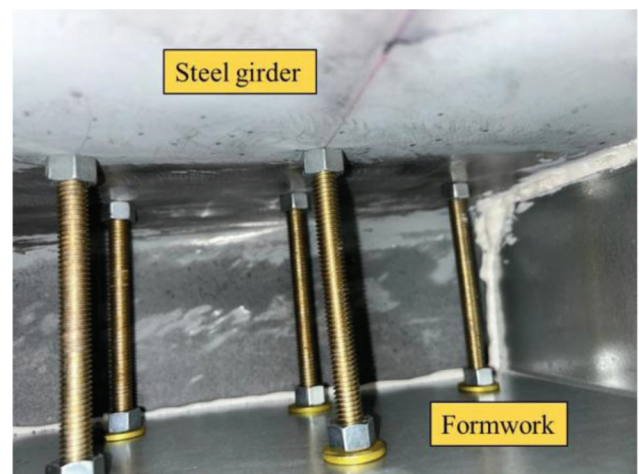


Figure 9.21 Connection of threaded rods to steel girder web and to stay-in-place formwork.

9.6 Fabrication Guidelines

9.6.1 Drilling Holes

To streamline the assembly process and meet tolerance requirements, it is recommended that the diameter of holes drilled in steel sheets exceed the threaded rod diameter by 1/4". One major potential challenge is misalignment between threaded rods already affixed to the girder web and the steel sheets with pre-drilled holes. Therefore, the holes in steel sheets should have a larger diameter than that of the threaded rod. Furthermore, to enhance the hole-drilling process and reduce misalignments, the development of a template is suggested. A cordless 20V drill could be used to drill the holes since the thickness of steel sheets is extremely small.

9.6.2 Metal Sheet Bending

To bend steel sheets, a hydraulic press could be used. Alternatively, one side of the steel sheet could be inserted into a bench vise followed by applying pressure to the opposite side to achieve a 90-degree angle. This process must be repeated for the other side of the steel sheet. The selection between these methods depends on the availability of equipment.

9.6.3 Clipping

The final step in the fabrication of the stay-in-place formwork involves clipping the edges of the steel sheets to ensure a proper fit within the k-region of the hot-rolled steel girder. This step may be omitted for plate girders that do not have a k-region.

9.7 Assembly Guidelines

9.7.1 Installation of Threaded Rods

The threaded rods must be installed and secured by affixing one hex nut on each side of the girder web and stay-in-place formwork, as shown in Figure 9.21. A snug-tight condition must be ensured; however, no pretension is mandatory.

9.7.2 Installation of Metal Steel Sheets

To install steel sheets on both sides of the girder web nuts and washers must be utilized. Minor adjustments to the alignment of threaded rods are acceptable if they do not align well with the holes in the steel sheets due to uneven web surfaces caused by corrosion. For instance,

a threaded rod may be slightly bent to fit the hole in the steel sheet. The snug-tight condition of the nuts supporting the steel sheets must be guaranteed.

9.7.3 Formwork Sealing

To seal all gaps and to prevent leakage of grout and binder resin, a fast-curing, heavy-duty construction adhesive is recommended (Figure 9.22 and Figure 9.23). If a non-fast-curing adhesive is used, it could significantly delay the casting of filler material.

9.8 Long-Term Performance

To ensure the repair's durability, preventing further deterioration is critical. Corrosion of the sandwich panel repair components is avoided by using corrosion-resistant materials (zinc-galvanized steel sheets, zinc-plated nuts and washers, zinc yellow-chromate plated threaded rods). However, water pooling in the repaired area could lead to deterioration after performing the repair. Therefore, the final three steps of the sandwich panel repair involve slope forming, painting, and drip bead placement.

9.8.1 Slope Forming

To prevent water pooling on the top surface of grout/concrete, model a 1%–2% slope through either grinding or top forming procedures based on available equipment.

9.8.2 Painting

The cleaned area above the sandwich panel repair must be painted to prevent deterioration of this region. The painting procedure involves corrosion-inhibiting primer application to enhance the adhesion of the paint. It is followed by applying multiple coats of corrosion-resistant paint as recommended by the manufacturer.

9.8.3 Drip Bead Placement

To minimize water storage in the repaired region the drip bead detail is recommended for use. INDOT Standard Drawing E619-PRWS-01 (INDOT, 2011) shows the drip bead detail (Figure 9.24 and Figure 9.25). Caulk shall be placed on the painted surface at the painted/unpainted interface and is intended to function as a drip bead. The implementation of this detail will reduce the amount of water entering the repaired region and reduce water pooling.

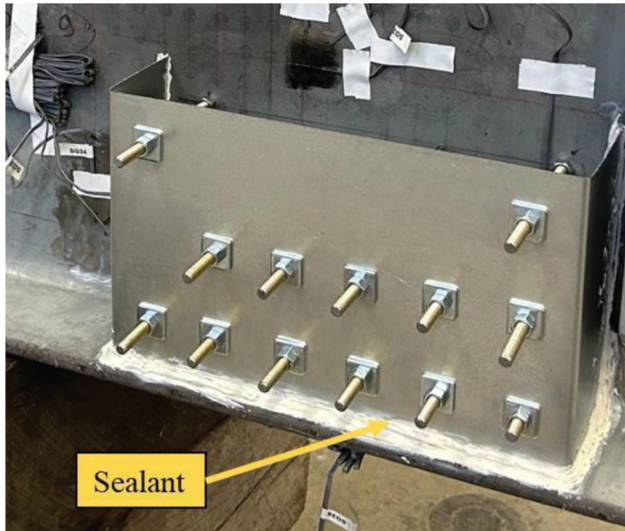


Figure 9.22 Sealed stay-in-place formwork, side view.

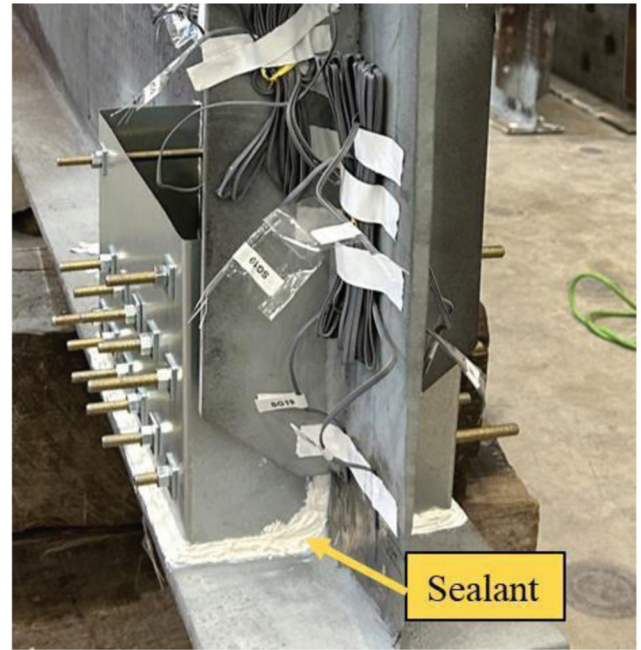


Figure 9.23 Sealed stay-in-place formwork, front view.

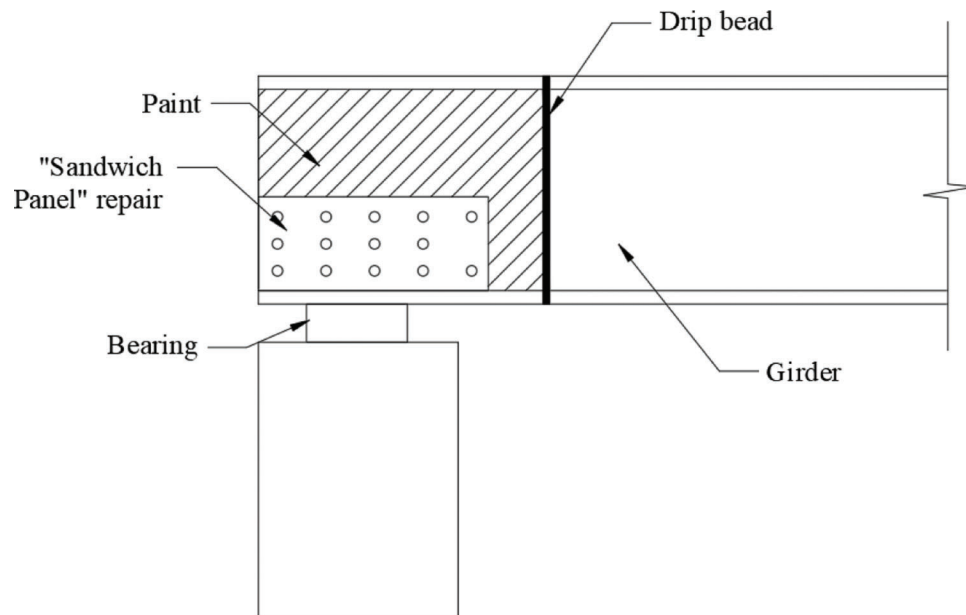


Figure 9.24 Elevation view. Girder at end-bent support.

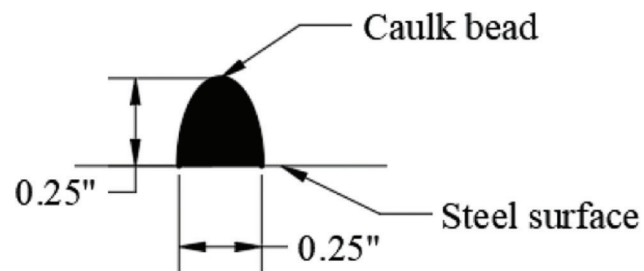


Figure 9.25 Caulk bead detail.

10. SUMMARY AND CONCLUSIONS

A comprehensive study was conducted on developing innovative repair method for rehabilitating corroded girder ends. The study evaluated existing novel repair methods proposed by other researchers as well as newly developed methods utilizing the House of Quality Matrix, ultimately selecting the sandwich panel repair method. Subsequently, experimental, and numerical investigations were performed on the sandwich panel method, followed by a parametric study consisting of multiple scenarios of bearing condition, threaded rod layouts, and material properties of steel rods. The study was completed with the formulation and verification of an equation to calculate the minimum required number of threaded rods, along with recommendations for the optimal configuration of threaded rod layout.

Except for Specimen 3, all repaired specimens exhibited full recovery of the design bearing capacity and at least 85% of the design shear capacity. Specimen 3 exhibited improved strength and performance compared to non-repaired girder; however, it did not reach the design bearing capacity threshold after repair. Therefore, the sandwich panel method was found to be effective for rehabilitating corrosion-damaged steel bridge girders. Experimental data was used to validate the results of finite element simulations. The developed finite element models deviated from the experimental data by no more than 10% in terms of load-carrying capacity.

An extensive numerical parametric study comprised three cases with more than 30 solid finite element models. The parametric study revealed the effect of the number of threaded rods used in repair, their arrangement, and material properties on the load-carrying capacity of the repaired girder. Following the numerical and experimental studies, the equation to calculate the minimum required number of threaded rods was formulated (Equation 9.10) and verified. The required number of threaded rods depended on the desired post-repair capacity, the residual capacity of the corroded girder, and the sectional and material properties of the threaded rod.

Finally, recommendations on the optimal configuration of the threaded rod layout were provided. The primary (also known as effective) threaded rods were found to be the most effective when located in the bearing region as they were able to develop their full capacity. Additionally, recommendations for selecting the filler material were given, as the experimental investigation revealed that the infill material impacted the specimen's failure mode, load-carrying capacity, and cracking pattern.

However, this study had several limitations. Therefore, more in-depth investigations are required for the sandwich panel method. The limitations are as follows.

1. Findings presented in the report are based on a controlled environment (laboratory).

2. Additional experimental and numerical investigations are required to verify the force transfer mechanism between the girder web, threaded rods, and grout/concrete panels. Based on the obtained data, the equation for calculating the minimum required number of threaded rods must be calibrated to account for shear deformations occurring in steel rods.
3. Further experimental evaluation is needed that includes a wider variety of threaded rod layouts, threaded rod grades, and diameters. Additionally, the influence of the height and length of the grout/concrete encasement panel on the repair capacity shall be examined. Moreover, the repair should be performed on unstiffened girders of various dimensions to ensure their efficacy on both larger and smaller W-sections.
4. The effectiveness of the method on severely corrosion-damaged sections needs to be evaluated experimentally and numerically.
5. The applicability of the proposed sandwich panel repair method for plate girders should be investigated experimentally and numerically.
6. A series of push-out tests must be performed, incorporating concentrically and eccentrically loaded rods with diverse rod layouts and infill materials. The contribution of the material infill can be calculated and accounted for in the developed equation, making it less conservative. Additionally, the minimum and maximum allowed spacing of threaded rods and clear cover requirements for the durability of the repair must be specified.
7. The cost-effectiveness of the repair method can only be evaluated through implementing the method to real bridges. Therefore, a sequel study on the field implementation of the sandwich panel repair method is required. Although effective and easily implemented in laboratory conditions, additional challenges could be revealed while performing the sandwich panel repair in the field.
8. The effect of vibrations caused by traffic on the bridge during the infill material curing must be analyzed. If vibrations do not have a detrimental impact on the compressive strength of the filler material, the traffic closure requirement could be eliminated.
9. The long-term durability of the method needs to be investigated.
10. The fatigue performance of the sandwich panel method must be investigated since the behavior under cyclic loading is unknown.

REFERENCES

- AASHTO. (2018/2020). *The manual for bridge evaluation, 3rd edition, with 2020 and 2022 interim revisions*. American Association of State Highway and Transportation Officials.
- AASHTO. (2020). *LRFD bridge design specifications, 9th Edition*. American Association of State Highway and Transportation Officials.
- ABAQUS. (2006a). *Concrete damaged plasticity* (Version 6.6-1). Retrieved October 20, 2023, from <https://classes.engineering.wustl.edu/2009/spring/mase5513/abaqus/docs/v6.6/books/usb/default.htm?startat=pt05ch18s05abm36.html>
- ABAQUS. (2006b). *Plasticity in ductile metals* (Version 6.6-1). Retrieved October 20, 2023, from [162](https://classes.engineer-</p></div><div data-bbox=)

- ing.wustl.edu/2009/spring/mase5513/abaqus/docs/v6.6/books/gss/default.htm?startat=ch08s02.html
- Ahn, J.-H., Kainuma, S., Yasuo, F., & Takehiro, I. (2013). Repair method and residual bearing strength evaluation of a locally corroded plate girder at support. *Engineering Failure Analysis*, 33, 398–418.
- ASCE. (2021). *2021 Report card for America's infrastructure*. American Society for Civil Engineers. Retrieved October 9, 2023, from <https://infrastructurereportcard.org/cat-item/bridges-infrastructure/>
- ASTM. (2017). *ASTM C1856/C1856M-17: Standard practice for fabricating and testing specimens of ultra-high performance concrete*. ASTM International.
- ASTM. (2020). *ASTM C1437-20: Standard test method for flow of hydraulic cement mortar*. ASTM International.
- ASTM. (2021a). *ASTM C39/C39M-21: Standard test method for compressive strength of cylindrical concrete specimens*. ASTM International.
- ASTM. (2021b). *ASTM C109/C109M: Standard test method for compressive strength of hydraulic cement mortars (using 2-in. or [50-mm] cube specimens)*. ASTM International.
- ASTM. (2021c). *ASTM C1611/C1611M-21: Standard test method for slump flow of self-consolidating concrete*. ASTM International.
- ASTM. (2022a). *ASTM E8/E8M-22: Standard test methods for tension testing of metallic materials*. ASTM International.
- ASTM. (2022b). *ASTM C469/C469M-22: Standard test method for static modulus of elasticity and poisson's ratio of concrete in compression*. ASTM International.
- ASTM. (2022c). *ASTM C939/C939M-22: Standard test method for flow of grout for preplaced-aggregate concrete (flow cone method)*. ASTM International.
- Bilal, K. A., Mahamid, M., Hariri-Ardebili, M. A., Tort, C., & Ford, T. (2023). Parameter selection for concrete constitutive models in finite element analysis of composite columns. *Buildings*, 13(7), 1759.
- CTDOT. (2022). *Guidelines for the utilization of ultra-high performance concrete in the rehabilitation of steel bridge girder ends*. <https://aii.transportation.org/Documents/CTDOT%20UHPC%20Beam%20End%20Repair%20Design%20Guidelines.pdf>
- The Engineering Toolbox. (2004). *Friction – Friction coefficients and calculator* [Webpage]. Retrieved October 18, 2023, from https://www.engineeringtoolbox.com/friction-coefficients-d_778.html
- Euclid Chemical. (n.d.a). *Hi-flow grout* [Webpage]. Retrieved October 13, 2023, from <https://www.euclidchemical.com/products/construction-products/grouts/cementitious/hi-flow-grout/>
- Euclid Chemical. (n.d.b). *NS grout*. [Webpage]. Retrieved October 13, 2023, from <https://www.euclidchemical.com/products/construction-products/grouts/cementitious/ns-grout/>
- Euclid Chemical. (n.d.c). *Tammsgrout supreme* [Webpage]. Retrieved October 13, 2023, from <https://www.euclidchemical.com/products/construction-products/grouts/cementitious/tammsgrout-supreme/>
- Fan, Z., Huang, W., & Negoita, A. (2022). Repairing steel girder end corrosion using ultra-high-performance concrete. *Journal of Bridge Engineering*, 27(1).
- FDOT. (2018). Chapter 11 - Superstructure. In *Bridge Maintenance Reference Manual*. Retrieved September 20, 2023, from https://fdotwww.blob.core.windows.net/sitefinity/docs/default-source/maintenance/str/bi/reference-manual/chapter-11-superstructure.pdf?sfvrsn=8c13f0d7_0
- FHWA. (n.d.). *LTBP infobridge analytics* [Webpage tool]. U.S Department of Transportation Federal Highway Administration. <https://infobridge.fhwa.dot.gov/BarStackChart>
- Five Star Products. (n.d.). *Hybrid grout* [Webpage]. Retrieved October 16, 2023, from <https://www.fivestarproducts.com/hybrid-grout.html>
- GDOT. (2012). *Bridge structure maintenance and rehabilitation repair manual* (Version 06.01.12). Georgia Department of Transportation. Retrieved September 20, 2023, from <http://www.dot.ga.gov/investsmart/bridgeprograms/bridgeprograms/bridgerepairmanual.pdf>
- Gerasimidis, S., Breña, S., & Tzortzinis, G. (2021). *Improved load rating procedures for deteriorated steel beam ends with deteriorated stiffeners* (Report No. 21-02). Massachusetts Department of Transportation.
- Haber, Z. B., Foden, A., McDonagh, M., Ocel, J., Zmetra, K., & Graybeal, B. (2022, May). *Design and construction of UHPC-based bridge preservation and repair solutions* (Publication No. FHWA-HRT-22-065). <https://www.fhwa.dot.gov/publications/research/infrastructure/structures/bridge/22065/22065.pdf>
- Hain, A., & Zaghi, A. E. (2021). Learnings from the field implementation of a novel ultra-high performance concrete beam end repair on a corroded steel girder bridge in Connecticut. *Transportation Research Record*, 2675(9), 703–714.
- Hauser, J. R., Griffin, A., Klein, R. L., Katz, G. M., & Gaskin, S. P. (2010). Quality function deployment (QFD). In *Wiley International Encyclopedia of Marketing*. John Wiley & Sons, Ltd.
- He, J., Liu, Y., Chen, A., & Yoda, T. (2012). Shear behavior of partially encased composite I-girder with corrugated steel web: Experimental study. *Journal of Constructional Steel Research*, 77, 193–209.
- He, J., Liu, Y., Lin, Z., Chen, A., & Yoda, T. (2012). Shear behavior of partially encased composite I-girder with corrugated steel web: Numerical study. *Journal of Constructional Steel Research*, 79, 166–182.
- IDOT. (2017, June). *Structural services manual*. Illinois Department of Transportation. Retrieved September 20, 2023, from <https://idot.illinois.gov/content/dam/soi/en/web/idot/documents/doing-business/reports/highways/bridges/20170630---revised-structural-services-manual.pdf>
- INDOT. (2011). *Painting requirements for weathering steel (Standard drawing E619-PRWS-01)*. Indiana Department of Transportation. <https://www.in.gov/dot/div/contracts/standards/drawings/sep22/600e/e600%20combined%20pdfs/E619-PRWS.pdf>
- International Federation for Structural Concrete. (2013). *Fib model code for concrete structures 2010*. Ernst & Sohn.
- Jagtap, P. R., & Pore, S. M. (2021). Strengthening of fully corroded steel I-beam with CFRP laminates. *Materials Today: Proceedings*, 43(2), 2170–2175.
- Javier, E. M., III., Hebdon, M. H., & Provines, J. T. (2021, October). *Methods for evaluation of the remaining shear capacity in steel bridge beams with section losses attributable to corrosion damage* (Report No. FHWA/VTRC 22-R4). Virginia Transportation Research Council. <https://vtrc.virginia.gov/media/vtrc/vtrc-pdf/vtrc-pdf/22-R4.pdf>
- Kanakamedala, D., Seo, J., Varma, A. H., Connor, R. J., & Tarasova, A. (2023). *Shear and bearing capacity of corroded steel beam bridges and the effects on load rating* (Joint Transportation Research Program Publication No. FHWA/IN/JTRP-2023/11). West Lafayette, IN: Purdue University. <https://doi.org/10.5703/1288284317634>

- Kayser, J. R. (1988). *The effects of corrosion on the reliability of steel girder bridges* [Doctoral dissertation, University of Michigan]. <https://hdl.handle.net/2027.42/161817>
- Kayser, J. R., & Nowak, A. S. (1989). Capacity loss due to corrosion in steel-girder bridges. *Journal of Structural Engineering*, 115(6), 1525–1537.
- Kruszewski, D., Wille, K., & Zaghi, A. E. (2018a). Push-out behavior of headed shear studs welded on thin plates and embedded in UHPC. *Engineering Structures*, 173, 429–441.
- Kruszewski, D., Wille, K., & Zaghi, A. E. (2018b). Design considerations for headed shear studs embedded in ultra-high performance concrete as part of a novel bridge repair method. *Journal of Constructional Steel Research*, 149, 180–194.
- Kruszewski, D., & Zaghi, A. E. (2019). Design of various shear connectors for repair of corroded steel girders with ultra-high performance concrete. *Transportation Research Record*, 2673(2), 521–530.
- Kruszewski, D., Zaghi, A. E., & Wille, K. (2019). Finite element study of headed shear studs embedded in ultra-high performance concrete. *Engineering Structures*, 188, 538–552.
- KwikBond Polymer. (n.d.a). *HCSC: Hybrid composite synthetic concrete* [Webpage]. Retrieved October 18, 2023, from <https://www.kwikbondpolymers.com/products/hcsc/>
- KwikBond Polymers. (n.d.b). *PPC 1121: Polyester polymer concrete* [Webpage]. Retrieved October 18, 2023, from <https://www.kwikbondpolymers.com/products/ppc-1121/>
- Lassy, B., Hain, A., Zaghi, A. E., Kanyo, Z. M., Chuong, B. K., & Cardinali, A. (2023). Rehabilitation of corroded steel bridge girder ends using partial-height ultra-high-performance concrete encasement. *Transportation Research Record*, 2678(6), 178–195.
- Lee, J., & Fenves, G. L. (1998). Plastic-damage model for cyclic loading of concrete structures. *Journal of Engineering Mechanics*, 124(8), 892–900.
- Lubliner, J., Oliver, J., Oller, S., & Onate, E. (1989). A plastic-damage model for concrete. *International Journal of Solids and Structures*, 25(3), 299–326.
- McMullen, K. F., & Zaghi, A. E. (2020). Experimental evaluation of full-scale corroded steel plate girders repaired with UHPC. *Journal of Bridge Engineering*, 25(4).
- Miyashita, T., Nagai, M., Wakabayashi, D., Hidekuma, Y., Kobayashi, A., Okuyama, Y., Koide, N., & Horimoto, W. (2015, August 21–22). *Repair method for corroded steel girder ends using CFRP sheet* [Conference presentation]. IABSE-JSCE Joint Conference on Advances in Bridge Engineering-III, Dhaka, Bangladesh.
- Müller, H. S. (2008). *Constitutive modelling for high strength high performance concrete* (Fib Bulletin No. 42). International Federation for Structural Concrete.
- Nakamura, S. I., & Narita, N. (2003). Bending and shear strengths of partially encased composite I-girders. *Journal of Constructional Steel Research*, 59(12), 1435–1453.
- Ogami, H., Fujii, K., Yamada, T., & Iwashaki, H. (2015). Renovation of corroded girder end in plate girder bridge with resin and rebars. Edited by S. Saha, Y. Zhang, S. Yazdani, & A. Singh (Eds.), *Implementing Innovative Ideas in Structural Engineering and Project Management*, pp. 187–192. ISEC Press.
- Rabbat, B. G., & Russell, H. G. (1985, March). Friction coefficient of steel on concrete or grout. *Journal of Structural Engineering*, 111(3), 505–515.
- Steelike Inc. (2023). *Steelike UHPC*. Retrieved October 18, 2023, from <https://steelike.com/product/product-data-sheet/>
- Tarasova, A., Kanakamedala, D., Varma, A. H., Seo, J., & Connor, R. J. (2023). Assessment of innovative repair methods for corroded steel girder bridges using the house of quality matrix. *Transportation Research Record*, 2678(2), 563–573.
- Tokyo Measuring Instruments Laboratory Co. (n.d.). *Concrete material use strain gauge* [Webpage]. Retrieved October 20, 2023, from https://tml.jp/e/product/strain_gauge/concrete.html
- Tzortzinis, G., Gerasimidis, S., Brena, S., & Knickle, B. (2019). *Development of load rating procedures for deteriorated steel beam ends* (Report No. 19008). Massachusetts Department of Transportation. https://www.mass.gov/files/documents/2019/11/13/BeamEndsFinalReportOct_2019.pdf
- Vishay Precision Group. (n.d.). *Strain gage installations for concrete structures* (Application Note TT-611). https://intertechnology.com/Vishay/pdfs/TechNotes_TechTips/TT-611.pdf
- Wakabayashi, D., Miyashita, T., Okuyama, Y., Koide, N., Kobayashi, A., Hidekuma, Y., Horimoto, W., & Nagai, M. (2019). *Study on repair method using CFRP for corroded steel girder ends*. https://www.pwri.go.jp/eng/ujnr/tc/g/pdf/28/28-11-3_Wakabayashi.pdf
- Wheelwright, S. C., & Clark, K. B. (1992). *Revolutionizing product development: Quantum leaps in speed, efficiency, and quality*. Free Press.
- WisDOT. (2024, July). *WisDOT bridge manual*. Retrieved September 20, 2023, from <https://wisconsindot.gov/dtsdManuals/strct/manuals/bridge/ch40.pdf>
- Zhao, X. L., & Al-Mahaidi, R. (2009). Web buckling of lightsteel beams strengthened with CFRP subjected to end-bearing forces. *Thin-Walled Structures*, 47(10), 1029–1036.
- Zmetra, K. M., McMullen, K. F., Zaghi, A. E., & Wille, K. (2017). Experimental study of UHPC repair for corrosion-damaged steel girder ends. *Journal of Bridge Engineering*, 22(8).

APPENDICES

Appendix A. Evaluation Results for Innovative Repair Methods

Appendix B. Section Loss Measurements for Specimens 1–7

Appendix C. Sandwich Panel Repair Details

APPENDIX A. EVALUATION RESULTS FOR INNOVATIVE REPAIR METHODS

Table A.1 Evaluation results for the UHPC beam end repair method

Requirement	Performance Level	Explanation
Loading Capacity	Strong	Extensive laboratory large-scale tests at the University of Connecticut proved a significant increase in the design capacity of the girder after repair.
Corrosion Prevention	Strong	Encasement of the corroded part prevents any liquid from leaking into the corroded area.
Behavior Under Low Temperature	Medium	No information is available on behavior under low temperatures.
Material	Medium	UHPC is moderately priced and commercially available.
Fabrication & Construction	Medium	Welding of shear studs is required in the field, as well as concrete mixing and casting. However, even though UHPC mixing is elaborated, the shear studs welding could be done quickly with a welding gun within a short period.
Jacking of the Structure	Strong	Jacking is not needed.
Corrosion Removal	Medium	Corrosion should be removed before performing the repair; however, the surface should be ground only at the locations where shear studs are to be welded.
Paint Removal	Medium	The paint should be removed; however, the area that must be cleaned is small.
Drilling and Bolting	Strong	Neither drilling nor bolting is required.
Welding	Medium	Welding of shear studs is required; however, using a stud welding gun is relatively simple.
Formwork Construction	Weak	Formwork construction is required for casting.
Concrete or Grout Casting	Weak	Concrete casting is required.
Construction Time	Medium	The repair requires surface preparation, welding, and curing. However, the repair could be completed in a few days, depending on the number of deteriorated beams that must be rehabilitated.
Adaptability in Design	Medium	There are existing material standards for UHPC as well as DOT design guidelines. However, they have not been developed for every state, and the research is still ongoing.
Technology Maturity	Medium	Repairs of steel girder bridges using UHPC in laboratory and field conditions were completed. However, their amount is significantly smaller than conventional maintenance performed.

Table A.2 Evaluation results for the strengthening the corroded part with CFRP method

Requirement	Performance Level	Explanation
Loading Capacity	Medium	The design loading capacity of the non-corroded girder is restored. However, no significant increase is observed.
Corrosion Prevention	Strong	CFRP layers are tightly attached to the corroded area of the web/flange and prevent fluid leakage.
Behavior Under Low Temperature	Medium	No information is available on behavior under low temperatures.
Material	Weak	CFRP is an expensive material.
Fabrication and Construction	Medium	No prefabrication is required. However, all CFRP layers must be attached to the girder in the field.
Jacking of the Structure	Strong	No jacking is required.
Corrosion Removal	Weak	Corrosion should be removed entirely before performing the repair, and the surface must be polished for good bonding between steel and CFRP layers.
Paint Removal	Weak	The paint should be removed completely.
Drilling and Bolting	Strong	Neither drilling nor bolting is required.
Welding	Strong	No welding is required.
Formwork Construction	Strong	Formwork construction is not required.
Concrete or Grout Casting	Strong	Concrete casting is not required.
Construction Time	Weak	The repair requires surface preparation, attaching several CFRP layers with consequent curing of each, and is a highly time-consuming process.
Adaptability in Design	Medium	There are existing material standards and a few research studies that could be used as a reference (Ahn et al., 2013; Jagtap & Pore, 2021; Miyashita et al., 2015).
Technology Maturity	Medium	This type of repair has not been implemented on steel girder bridges in the United States. However, there is existing data on laboratory testing.

Table A.3 Evaluation results for the sandwich panel repair method

Requirement	Performance Level	Explanation
Loading Capacity	Strong	Composite action between threaded rods and filler material significantly increases the loading capacity of the girder (based on preliminary numerical simulations).
Corrosion Prevention	Strong	Encasement of the corroded part prevents contaminants from leaking into the corroded area.
Behavior Under Low Temperature	Strong	No decrease in loading capacity under low temperatures is expected.
Material	Strong	There are various inexpensive encasement materials that are not proprietary, such as cementitious grout or polymer-based concretes.
Fabrication and Construction	Medium	Steel plates could be prefabricated; however, assembly and casting in the field are required.
Jacking of the Structure	Strong	No jacking of the superstructure is required.
Corrosion Removal	Medium	The surface should be cleaned, and corrosion products should be removed before repair; however, the surface need not be polished.
Paint Removal	Strong	The paint does not have to be removed.
Drilling and Bolting	Weak	Drilling and bolting are required.
Welding	Strong	No welding is required.
Formwork Construction	Strong	Formwork construction is not required because steel plates function as formwork.
Concrete or Grout Casting	Weak	Concrete casting is required.
Construction Time	Medium	The repair requires casting and curing and cannot be completed in 1 day. A few days are needed.
Adaptability in Design	Medium	There are existing material standards for infill materials such as cementitious grout, conventional concrete, or UHPC. However, DOT design guidelines to perform such types of repairs have not been developed.
Technology Maturity	Medium	Similar repair procedures such as UHPC beam end repair (Lassy et al., 2023) and “Conventional Bolted Angles” were performed before (FDOT, 2018; GDOT, 2012; IDOT, 2017).

Table A.4 Evaluation results for the improved bolted angles repair method

Requirement	Performance Level	Explanation
Loading Capacity	Strong	The design capacity of the corroded girder is recovered based on the implementation experience of the similar conventional repair method widely used in the US.
Corrosion Prevention	Medium	The fluids are prevented from leaking into the deteriorated region. However, angle sections are made of steel and may potentially corrode over time.
Behavior Under Low Temperature	Strong	No decrease in loading capacity under low temperatures is expected.
Material	Medium	Epoxy resin is a moderately expensive and non-proprietary material.
Fabrication & Construction	Medium	Angle sections could be prefabricated. However, sealing of the gaps with epoxy resin in the field is required.
Jacking of the Structure	Strong	No jacking is required.
Corrosion Removal	Medium	Corrosion should be removed before repair, but the surface must not be polished.
Paint Removal	Weak	The paint should be removed entirely for good epoxy resin adhesion to the girder web.
Drilling and Bolting	Weak	Drilling and bolting are required.
Welding	Strong	No welding is required.
Formwork Construction	Strong	No formwork construction is required.
Concrete or Grout Casting	Strong	No concrete casting is required.
Construction Time	Medium	The repair cannot be performed in 1 day since repair procedures require the curing of epoxy resin.
Adaptability in Design	Medium	Standards and guidelines exist for similar "Conventional Bolted Angles" repair method. However, the system's behavior with epoxy resin between angles and the girder web must still be studied.
Technology Maturity	Medium	A similar conventional repair method is widely used in the US (FDOT, 2018; GDOT, 2012; IDOT, 2017). However, no repairs were performed with the epoxy resin as a filler material between angles and the web.

Table A.5 Evaluation results for the web strengthening with diagonally oriented angles method

Requirement	Performance Level	Explanation
Loading Capacity	Medium	The design capacity is not recovered after the repair based on preliminary numerical simulations. However, the repaired girder shows an improved behavior under significant vertical displacements.
Corrosion Prevention	Weak	Corrosion propagation is not prevented due to the gaps present between the web and installed angle sections where moisture can potentially accumulate.
Behavior Under Low Temperature	Medium	No information is available on behavior under low temperatures.
Material	Strong	Steel is widely available and a non-proprietary material.
Fabrication and Construction	Strong	Angle sections could be prefabricated, and a template could be used for hole drilling in the field.
Jacking of the Structure	Strong	No jacking is required.
Corrosion Removal	Medium	Corrosion should be removed before performing the repair. However, the quality of the prepared surface can be imperfect.
Paint Removal	Strong	The paint does not have to be removed.
Drilling and Bolting	Weak	Drilling and bolting are required to install steel angles.
Welding	Strong	No welding is required.
Formwork Construction	Strong	No formwork construction is required.
Concrete or Grout Casting	Strong	No concrete casting is required.
Construction Time	Strong	The repair could be performed in 1 day since repair procedures are similar to conventional repair methods (FDOT, 2018; GDOT, 2012; IDOT, 2017) and are well-known by bridge maintenance personnel.
Adaptability in Design	Medium	There are standards and guidelines for similar “Conventional Bolted Angles” repair method. However, the orientation of angles differs.
Technology Maturity	Medium	A similar conventional type of repair is widely used in the US. However, there were no repairs performed with the diagonal angle orientation.

APPENDIX B. SECTION LOSS MEASUREMENTS FOR SPECIMENS 1–7

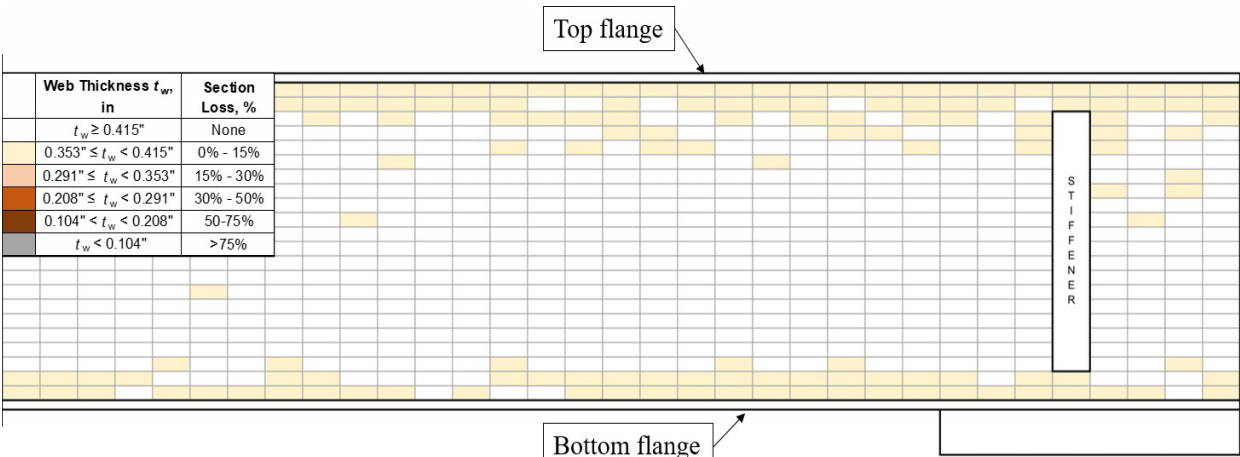


Figure B.1 Section loss measurements for Specimen 1.

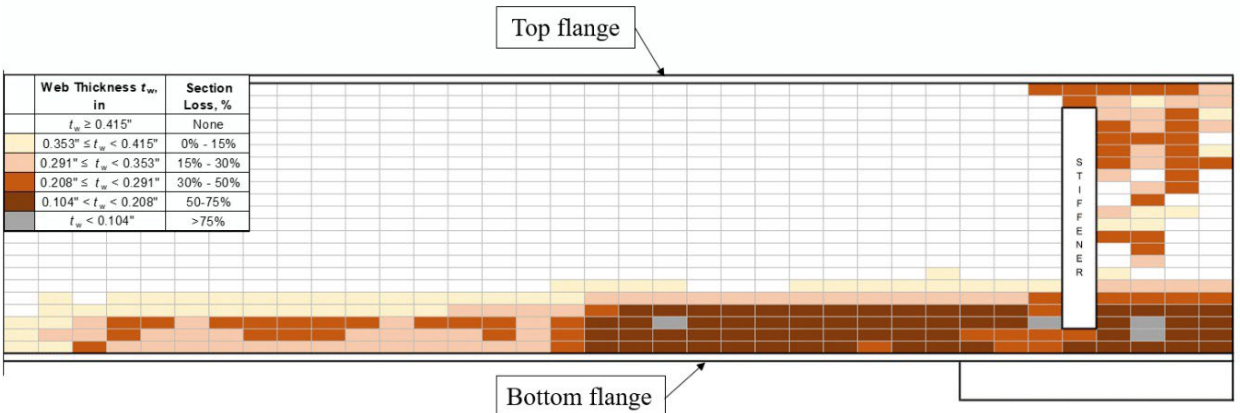


Figure B.2 Section loss measurements for Specimen 2.

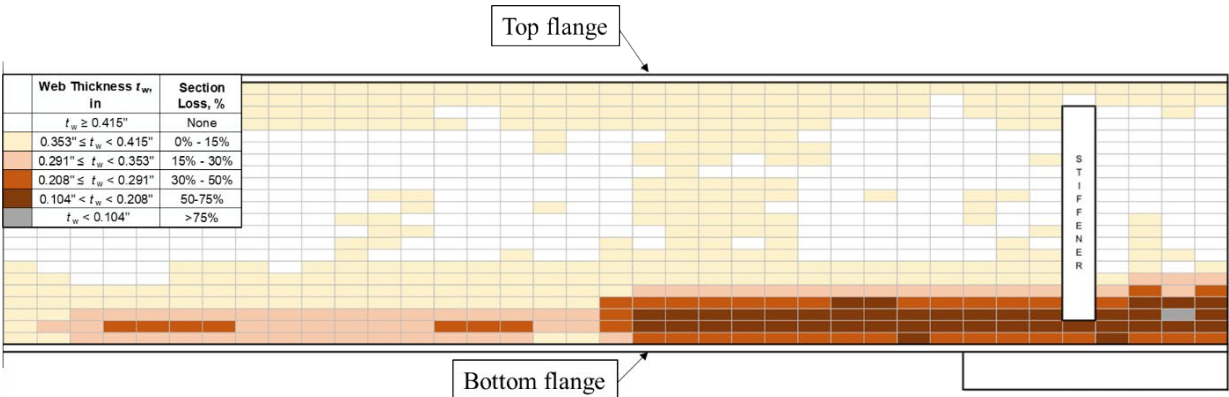


Figure B.3 Section loss measurements for Specimen 3.

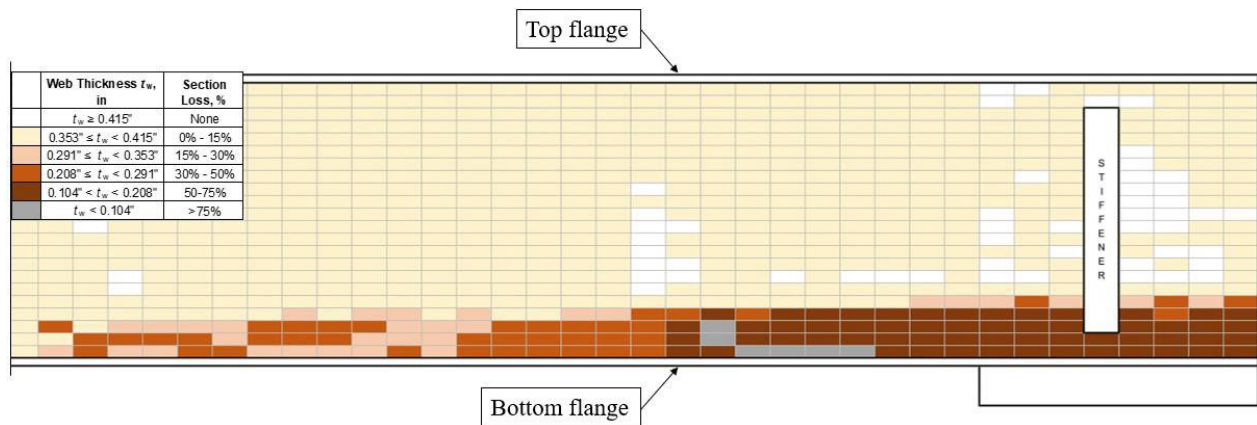


Figure B.4 Section loss measurements for Specimen 4.

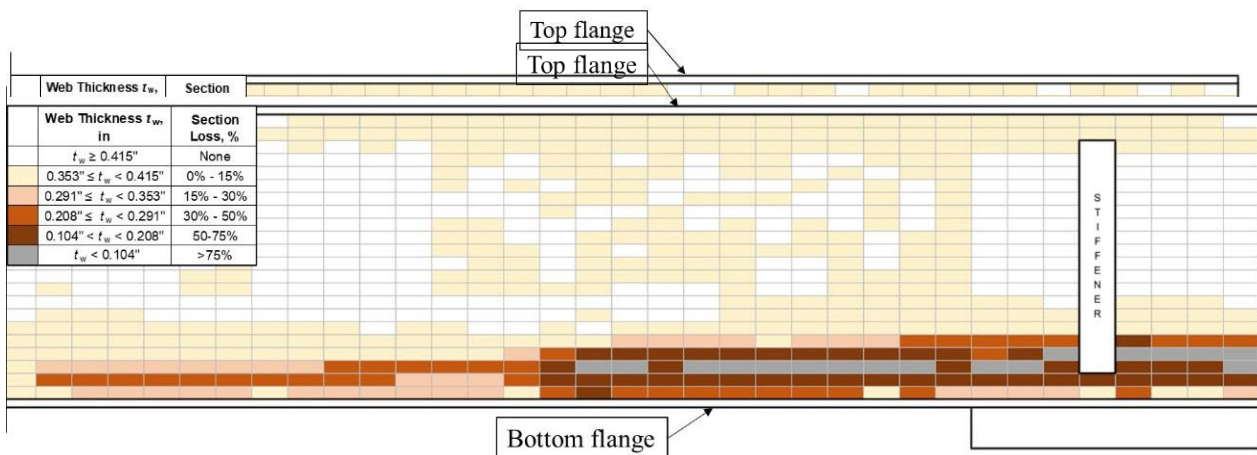


Figure B.6 Section loss measurements for Specimen 6.

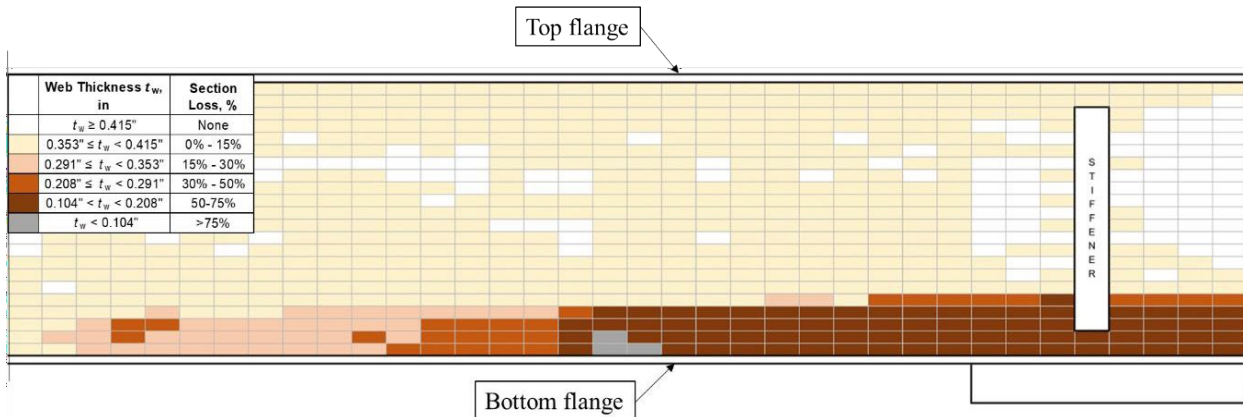


Figure B.7 Section loss measurements for Specimen 7.

APPENDIX C. SANDWICH PANEL REPAIR DETAILS

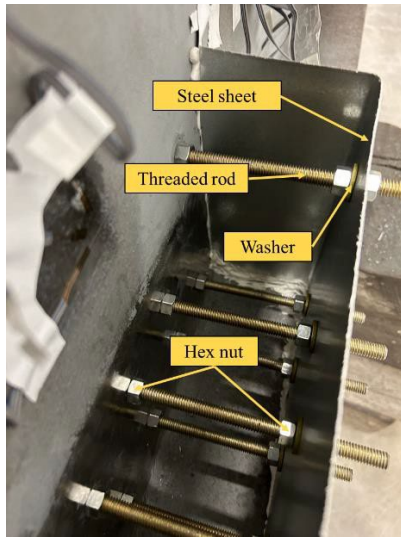


Figure C.1 Specimen 3. Details of Sandwich Panel repair assembly.

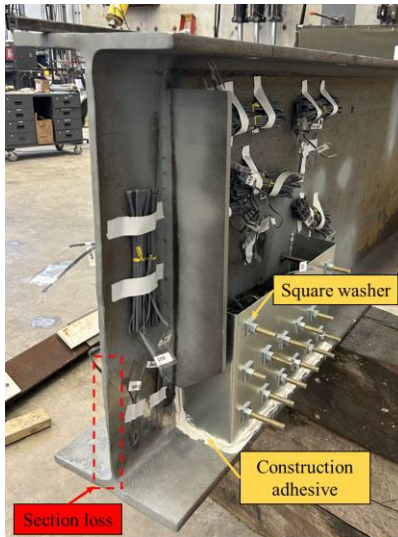


Figure C.2 Specimen 3 before casting.

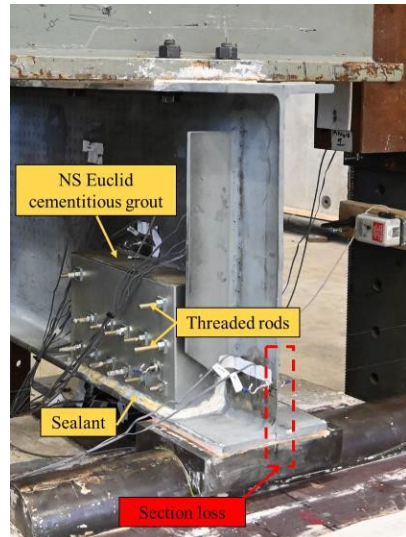


Figure C.3 Specimen 3 after casting and curing grout.

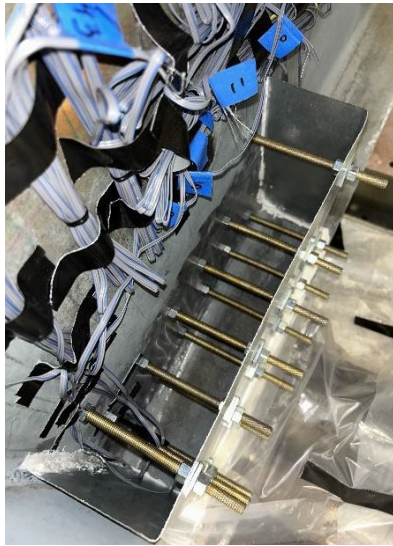


Figure B.4 Specimen 4. Details of Sandwich Panel repair assembly.



Figure B.5 Specimen 4 before grout casting.



Figure B.6 Specimen 4 after casting and curing grout.

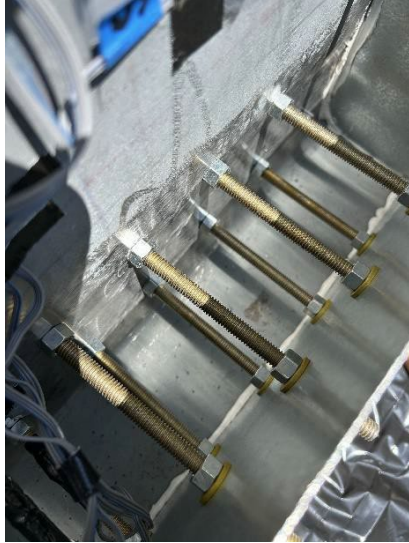


Figure C.7 Specimen 5.
Details of Sandwich Panel
repair assembly.



Figure C.8 Specimen 5 before
casting.



Figure C.9 Specimen 5 after
casting and curing Kwik Bond
PPC-1121.



Figure C.10 Specimen 6. Details
of Sandwich Panel repair assembly.



Figure C.11 Specimen 6 before
casting.



Figure C.12 Specimen 6 after
casting and curing grout.



Figure C.13 Specimen 7. Details of Sandwich Panel repair assembly.



Figure C.14 Specimen 7 before casting.



Figure C.15 Specimen 7 after casting and curing PPC-1121.

About the Joint Transportation Research Program (JTRP)

On March 11, 1937, the Indiana Legislature passed an act which authorized the Indiana State Highway Commission to cooperate with and assist Purdue University in developing the best methods of improving and maintaining the highways of the state and the respective counties thereof. That collaborative effort was called the Joint Highway Research Project (JHRP). In 1997 the collaborative venture was renamed as the Joint Transportation Research Program (JTRP) to reflect the state and national efforts to integrate the management and operation of various transportation modes.

The first studies of JHRP were concerned with Test Road No. 1 — evaluation of the weathering characteristics of stabilized materials. After World War II, the JHRP program grew substantially and was regularly producing technical reports. Over 1,600 technical reports are now available, published as part of the JHRP and subsequently JTRP collaborative venture between Purdue University and what is now the Indiana Department of Transportation.

Free online access to all reports is provided through a unique collaboration between JTRP and Purdue Libraries. These are available at <http://docs.lib.purdue.edu/jtrp>.

Further information about JTRP and its current research program is available at <http://www.purdue.edu/jtrp>.

About This Report

An open access version of this publication is available online. See the URL in the citation below.

Tarasova, A., Kanakamedala, D., Seo, J., Varma, A. H., & Connor, R. J. (2024). *New repair strategies for life-cycle extension of corroded steel girder bridges* (Joint Transportation Research Program Publication No. FHWA/IN/JTRP-2024/15). West Lafayette, IN: Purdue University. <https://doi.org/10.5703/1288284317748>